Controlling the Dielectric Behavior of Organic Electronic Devices

Dissertation

Soh Kushida

Dissertation

Submitted to the
Combined Faculty of Natural Sciences and Mathematics
Heidelberg University, Germany
for the degree of Doctor of Natural Sciences (Dr. rer. nat.)

Presented by
M. Eng. Soh Kushida
from Hyogo, Japan

Oral examination: March 13rd, 2020

Printed and published with the support of the German Academic Exchange Service

Controlling the Dielectric Behavior of Organic Electronic Devices

Gutachter: Prof. Dr. Uwe H. F. Bunz

Prof. Dr. Petra Tegeder

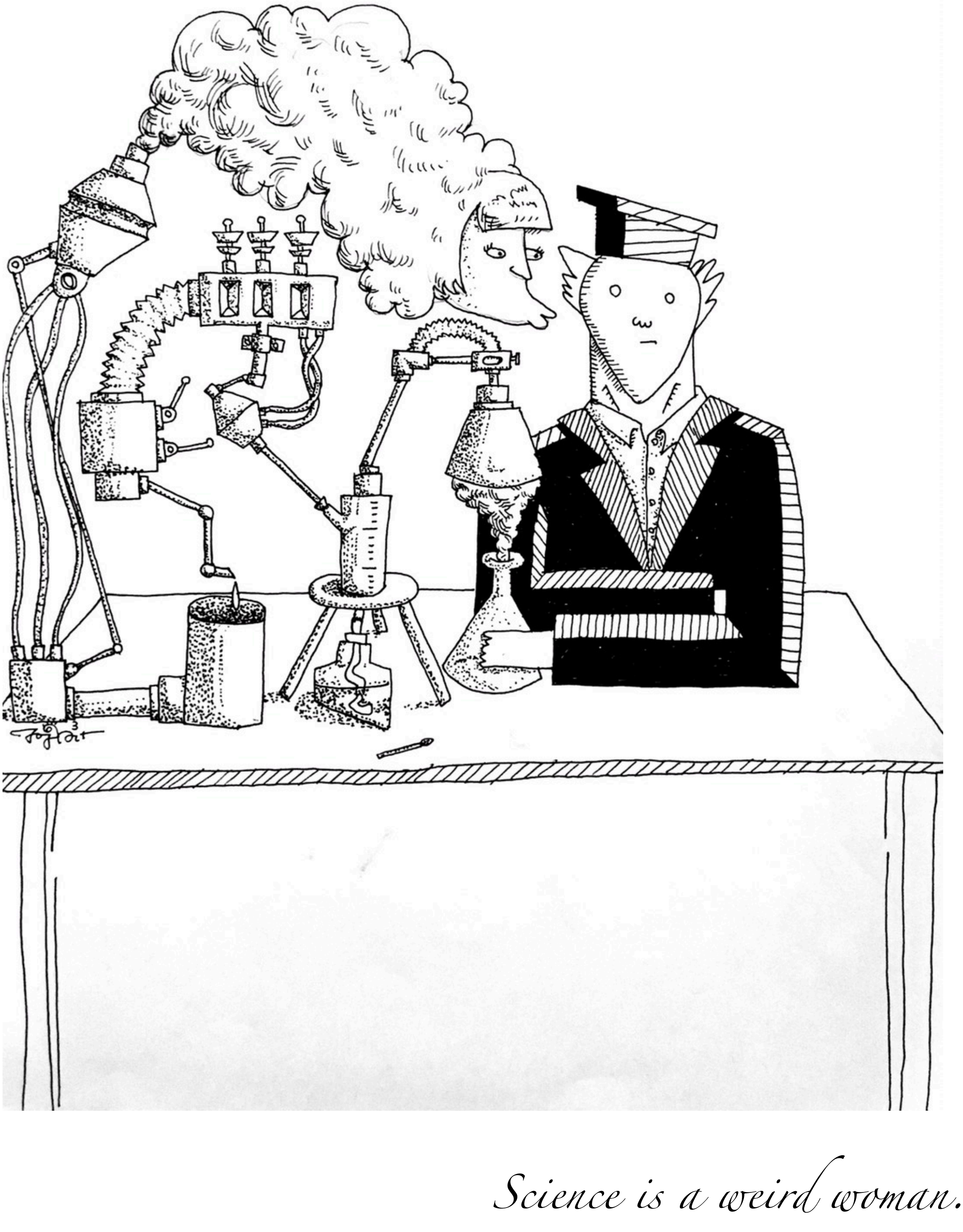

Science is a weird woman.

She sometimes kisses you but never loves you.

Parts of this thesis were already published:

Publications in journals:

Soh Kushida, Emanuel Smarsly, Lisa Veith, Irene Wacker, Rasmus R. Schröder, Uwe H. F. Bunz,
"Solid-State Gels of Poly(p-phenyleneethynylene)s by Solvent Exchange"
Macromolecules **2017**, *50*, 7880–7886.

Soh Kushida, Emanuel Smarsly, N. Maximilian Bojanowski, Irene Wacker, Rasmus R. Schrçder, Osamu Oki, Yohei Yamamoto, Christian Melzer, Uwe H. F. Bunz,
"Dipole-Switchable Poly(para-phenyleneethynylene)s: Ferroelectric Conjugated Polymers"
Angew. Chem. Int. Ed. **2018**, *57*, 17019 –17022.

Soh Kushida, Sebastian Kebrich, Emanuel Smarsly, Karl-Philipp Strunk, Christian Melzer, Uwe H. F. Bunz,
"Light-Emitting Electrochemical Cells Based on Conjugated Ion Gels“
Submitted.

(4) Soh Kushida, Emanuel Smarsly, Uwe H. F. Bunz,
"π-Ion Gel Transistors“
In preparation.

Oral Presensations in Conferences:
Soh Kushida,
"Gelation and Device Application of Poly (p-phenyleneethenylene)s"
π-System Figuration German-Japanese Workshop, Heidelberg (Germany), November **2017.**

Soh Kushida, Uwe H. F. Bunz,
"Organic Field Effect Transistor Based on π-ion Gel"
π-System Figuration Europian-Japanese Workshop, Zabrze (Poland), November **2019**.

Posters:
Soh Kushida, Emanuel Smarsly, Karl-Philipp Strunk, Christian Melzer, Uwe H. F. Bunz,
"Ferroelectric Poly-(p-Phenyleneethynelene)"
CEMSupra2018, Tokyo(Japan), January **2018**.

Soh Kushida, Emanuel Smarsly, Irene Wacker, Rasmus R. Schröder, Christian Melzer, Uwe H. F. Bunz,

"Dipole switchable Poly-(p-Phenyleneethynelene)"

π-System Figuration European-Japanese W orkshop, Dubrovnik(Croatia), November **2018.**

Soh Kushida, Uwe H. F. Bunz,

"π-Ion Gel OFET"

CEMSupra2019, Tokyo(Japan), December **2019**.

Contributions to further published projects:

Sae Nakajima‡, Ken Albrecht‡, Soh Kushida‡, Eiji Nishibori, Takashi Kitao, Takashi Uemura, Kimihisa Yamamoto, Uwe H. F. Bunz, Yohei Yamamoto,

"A fluorescent microporous crystalline dendrimer discriminates vapour molecules" *Chem. Commun*. **2018**, *54*, 2534–2537. ‡: contribution equal

Sebastian N. Intorp, Soh Kushida, Evgenia Dmitrieva, Alexey A. Popov, Frank Rominger, Jan Freudenberg, Felix Hinkel, and Uwe H. F. Bunz,

"True Blue Through Oxidation—A Thiaazulenic Heterophenoquinone as Electrochrome"

Chem. Eur. J. **2019**, accepted.

Manuela Casutt, Benedikt Dittmar, Hanna Makowska, Tomasz Marszalek, Soh Kushida, Uwe H. F. Bunz, Jan Freudenberg, Daniel Jänsch, Klaus Müllen,

"A Diketopyrrolopyrrole-Based Dimer as a Blue Pigment"

Chem. Eur. J. **2019**, *25*, 2723 – 2728.

Jinsong Han, Benhua Wang, Markus Bender, Soh Kushida, Kai Seehafer, Uwe H. F. Bunz,

"Poly(aryleneethynylene) Tongue That Identifies Nonsteroidal Anti-Inflammatory Drugs in Water: A Test Case for Combating Counterfeit Drugs"

ACS Appl. Mater. Interfaces **2017**, *9*, 790–797.

Abstract

In this thesis, the dielectric behavior including dielectric constants and dielectric characteristics of poly-(*p*-phenyleneethynylene)s (PPEs) and their influence on organic electronic devices are investigated.

In the first part, a method to create gels that compose of PPE and an ionic liquid was invented and named π-ion gels. π-ion gels exhibit a high dielectric constant so that excellent performances are displayed when π-ion gels are applied to the light-emitting electrochemical cells (LECs). The turn-on time, the brightness, the current density of LECs based on π-ion gels are improved by 10 times (0.7~2 s), four times, and 10 times (~20 A/cm^2) in comparison to LECs fabricated by a drop-casting method, respectively. Furthermore, π-ion gels are applied to a new type of transistors, π-ion gel transistors (PIGTs). PIGTs display the on/off ratio of ~10^5, the hole carrier mobility of (0.4 cm^2/V s), and the response time of ~20 µs, respectively. Especially, the response time of 20 µs is the fastest among electrochemical based transistors.

In the second part, a novel concept for the control of dielectric properties was developed. dipolar units of *o*-difluorobenzene were incorporated in both poly-(*p*-phenyleneethynylene)s (PPEs) and liquid-crystalline oligo-(*p*-phenyleneethynylene)s (PEs). When *o*-difluorobenzene is introduced in PPEs, ferroelectric behavior is observed as the first example of ferroelectric conjugated polymer based on molecular rotations. Furthermore, a liquid-crystalline PE forms a dipole-aligned crystal *via* a dual control of the electric field and the temperature (called 2D control). In both cases, the compounds are applied to metal-insulator-metal (MIM) diodes, exhibiting anisotropic currents.

Overall, the approaches to control dielectric constants and dielectric characteristics are beneficial for organic electronic devices. The concept is novel and feasible to apply to other materials.

Zusammenfassung

In dieser Arbeit wurden die dielektrischen Eigenschaften von PPEs und die Auswirkungen dieser auf Anwendungen in der organischen Elektronik untersucht.

Im ersten Teil wurden Gele bestehend aus einer ionischen Flüssigkeit und einem PPE hergestellt, welche als π-Ionengele bezeichnet wurden. π-Ionengele zeigen eine hohe Dielektrizitätskonstante welches sich als vorteilhaft für die Anwendung in LECs zeigte. Im Vergleich zu LECs, die im Drop-Casting-Verfahren hergestellt wurden, konnte die Anschaltgeschwindigkeit der Bauteile so um das bis zu zehnfache auf 0.7-2 s verkürzt werden, während die Helligkeit ebenfalls um den Faktor zehn auf 20 A/cm^2 erhöht werden konnte. Weiterhin wurden die π-Ionengele in einer neuen Art von Transistoren, den π-Ionengel-Transitoren (PIGTs - π-Ionengel-Transistor) verwendet. Diese zeigten eine hohes An/Aus-Verhältnis von 10^5, eine Lochmobilität von 0.4 cm^2/Vs und eine Reaktionszeit von 20 µs, welches die schnellste bis hierhin gemessene Zeit ist.

Im zweiten Teil der Arbeit wurde ein neues Konzept für die Kontrolle von dielektrischen Eigenschaften entwickelt. Dipolare Einheiten von o-Difluorbenzol wurden in Oligomere und Polymere aus Phenylenethinylene eingegliedert. Für die PPEs konnten hierdurch die ersten Beispiele ferroelektrischer konjugierter Polymeren durch molekulare Rotation gezeigt werden. Für die PEs konnte ein Dipol-ausgerichteter Flüssigkristall durch duale Steuerung des elektrischen Feldes und der Temperatur erzeugt werden (2D Kontrolle). PPEs und PEs wurden in MIM Dioden eingesetzt, welche beide anisotrope Ströme zeigten.

Zusammenfassend wurde gezeigt, dass die Kontrolle der dielektrischen Eigenschaften einen Vorteil für die Anwendungen in ßder organischen Elektronik zeigt. Dieses Konzept ist neuartig und übertragbar auf andere Materialien.

Contents

1 Introduction

Rapid developments on the technologies that are supported by silicon-based inorganic semiconductors bestow a great impact on humans' lives. Triggered by the invention of transistors in 1947, the industry of semiconductors exploded and myriads of silicon-based electronic devices were developed. Transistors are central to integrated circuits (ICs). When we look around the today's society, ICs are inserted into most of the electronic applications such as computers, smartphones, and so on.

The field of organic electronics also appeared after the discovery of organic semiconducting properties in 1948. [1-3] Organic semiconductors have unique properties and great advantages over inorganic semiconductors, such as flexibility and solution-processability. [4-5] These characteristics allow for the applications of printed electronics and wearable devices as known as state of art devices.

However, when we focus on device properties such as carrier mobility and stability, organic electronics have not surpassed the inorganic electronics, yet. [5] The organic field-effect transistors (OFETs) exhibit mobilities of around 1-10 cm^2 V^{-1} s^{-1}, while inorganic transistors have shown mobilities as high as 370 cm^2 $V^{-1}s^{-1}$. [6] Organic electrical pumping lasers have been achieved in 2019, [7] while a variety of electrically pumped inorganic lasers with superior stability have already been used for years. Many researchers dedicate their work to understanding and improving the organic electronic device properties. Nowadays, comprehensive understandings of the basic charge transport and other electronic functions have been generalized step by step. Molecular design has been studied to satisfy a lot of parameters including molecular packings, energy levels, molecular wettability, and dielectric constants to optimize FETs. [5,8,9] The author of this thesis focuses on dielectric constants of organic materials. Despite it being a critical factor, only a few studies have focused on this topic due to the difficulties of controlling the intrinsic dielectric permittivity of organic semiconductors. [10, 11]

This thesis is a trajectory of the author to improve the organic electronic devices by controlling the dielectric behavior. The thesis comprises mainly two strategies to control the dielectric behavior of the semiconductors. In chapters 4-6, a strategy of "molecular assemblies" is employed to realize organic semiconductors in high dielectric constant media. Formation of π-conjugated polymer gels enclosing an ionic liquid (IL), which exhibits a high dielectric constant, is investigated. The gels are nano-composite materials of a semiconductor in a high dielectric medium. The resulting net dielectric constant is higher than that of bare conjugated polymer films. The gels are applied to light-emitting devices and transistor devices. In chapters 7-8, a strategy of “molecular designs” to functionalize the spontaneous dipole moments in the backbones of conjugated molecules is presented. When the dipole units are incorporated into a conjugated polymer, a ferroelectric is observed. Furthermore, a method to form dipole-oriented crystals of small molecules is invented. In both strategies, unique properties are observed.

2 Theoretical Background

2.1 Organic Semiconductors

The conductivity of organic semiconductors is based on the delocalization of π-electrons in their conjugated systems. [12] Organic semiconductors are composed of carbons and hydrogens and can be heteroatoms such as Sulfur, Nitrogen, Phosphorus, etc.

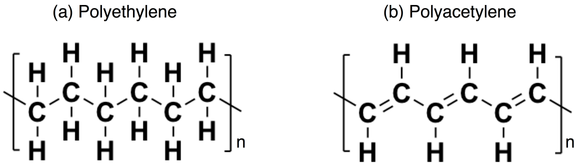
(a) Polyethylene

(b) Polyacetylene

Figure 2-1. Molecular structures of polyethylene (a) and polyacetylene (b)

Hydrogen-saturated hydrocarbons such as Polyethylene do not exhibit conducting properties because all electrons of carbons are incorporated into four different σ-bonds in the SP^3 orbitals, arresting them in place. Polyethylene is an insulator. A prerequisite for (semi-) conducting properties are alternating double bonds within the molecular structure of the material. polyacetylene is the corresponding hydrocarbons that satisfy the requirement. In the case of polyacetylene, an electron of a carbon atom is transferred to $2p_z$ orbital, which is vertical to the σ bonds, and form π-bonds meanwhile the other three electrons form sp^2 orbital to form σ bonds. The electron is called a π electron. The π orbitals overlap each other, allowing for the delocalization of π-electrons. *Upon* charge carrier doping, polyacetylene becomes a conductor although polyacetylene is still an insulator or a poor semiconductor in a neutral state. Repeating of single and double(triple) bonds is also found in other molecules and they are π-conjugated molecules. [12, 13] The π-conjugated molecules can be sorted into two groups; small molecules and polymers. Some examples that have been commonly applied in organic electronic devices are shown in Figure 2-2. Both material classes have individual advantages and disadvantages, but these molecules all have alternating single–double bond structures and overlapping of π-orbitals.

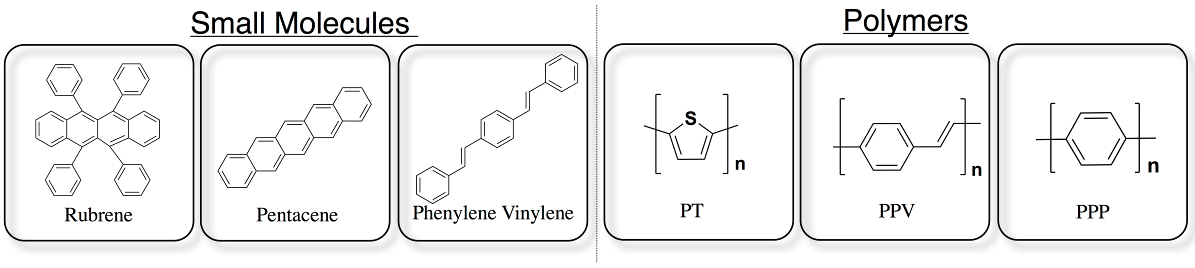

Figure 2-2. Examples of π-conjugated molecules.

To understand carrier transport, the energetic structure of a material is important (Figure 2-3). In a ground state, the electrons occupy the energetically lower orbitals. Between the energetically Highest Occupied Molecular Orbital (HOMO) and the energetically lowest Occupied Molecular Orbital (LUMO) there is a bandgap, which defines how much energy is needed to excite one electron from HOMO to LUMO, forming an excited state (Figure 2-3, right).

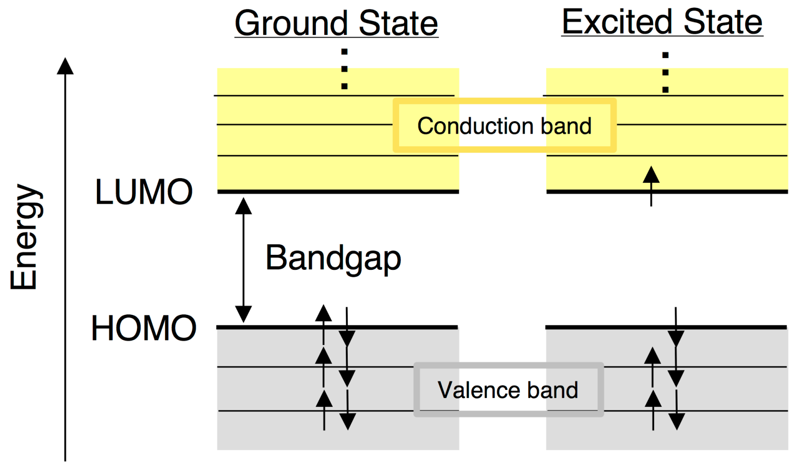

Figure 2-3. Energy diagrams of a semiconductor in a ground state (a) and in an excited state (b).

The electrons in the HOMO can be excited by light or heat, usually into an anti-bonding π*orbital. The size of the bandgap can be controlled by altering the size of the delocalized system. With increasing conjugation, the bandgap becomes smaller. The excited electrons are mobile in LUMO and the orbitals above LUMO (conduction band), although excited states relax to the ground state thermodynamically. Electrons occupying the orbitals below HOMO (valence band) are binding. Carrier transport cannot happen in the ground state. To obtain steady conductivity, the molecules need to be doped. Doing includes p-doping, which is withdrawing electrons from the valence band, and n-doping, which is donating electrons into the conduction band. The conduction band and valence band are quasi-continuous. In the cases of inorganic semiconductors and some specific organic semiconductors (e.g. a single crystal of Rubrene), the carrier transportation takes place based on the delocalization over the whole conduction band. [4,14-17] However, carrier transportation of most organic semiconductors is rather complicated. Because most organic semiconductors assemble with weak interactions between molecules and are often affected by phonon vibrations, carriers are transported *via* the hopping mechanism. [18] The details are discussed in the next section.

2.2 Charge Carrier Transfer in Organic Semiconductors

Charge carrier transport is accomplished when a carrier travels from an electrode to another electrode. Among the process, there are mainly 3 types of resistances. The first one is the contact resistances that arise at the interface between electrodes and semiconductors. The energy barrier (Schottky barrier) is determined by the potential of semiconductors and electrodes. Adjusting the energy level of the molecules to that of the electrode material is an important approach. The second one is inter-grain resistances since organic semiconductors form several crystalline domains in a device. [25] Carriers travel from a grain to a grain by percolation. The resistance of percolation is larger than that of hopping in a grain. Consequently, growing crystal domains is important to reduce the inter-grain resistances. The third one is bulk resistances, which are supposed to be the resistances that described as a hopping model as discussed below.

The charge carrier mobility (μ) is a parameter to express the behavior of charge carrier transport. μ is described as

$$\upsilon = \mu E \qquad (\mathrm{eq.}\,2-1)$$

Whereas υ and E are the speed of the charge carrier and the electric field, respectively. Furthermore, the current density (j) is expressed as

$$\mathrm{j} = \mathrm{qn}\upsilon = qn\mu E = \sigma E \qquad (\mathrm{eq.}\,2-2)$$

with the charge carrier density (n) and the charge amount per carrier (q). The charge carrier mobility is proportional to the conductivity (σ) so that an important intrinsic parameter of materials.

The charge carrier transport in most organic semiconductors can be described using the hopping model. The hopping mechanism was first suggested in Marcus theory. [19,20] The theory describes charge carrier transport between two molecules, a carrier donor and an acceptor. The transfer rate (k_{ET}) is described as

$$k_{ET} = \frac{2\pi J^2}{\hbar}\sqrt{\frac{1}{4\pi\lambda k_B T}}\, exp\left[-\frac{(\lambda+\Delta G)^2}{4\lambda k_B T}\right] \qquad (\mathrm{eq.}\,2-3)$$

with the reduced Plank constant ($\hbar$), Boltzmann constant (k_B) and temperature (T). J is the Hamiltonian of the electronic coupling of two molecules. λ and ΔG are the reorganization energy and Gibbs free energy difference between the initial state and the transferred state. As seen eq.2-

3, temperature dependency is more emphasized in the case of organic semiconductors. In most cases, the mobility increases as elevating temperature, in contrast to inorganic semiconductors. [21,22] J is an important parameter to increase $k_{ET.}$ J can be increased by tuning the distance between molecules. This is a reason why molecular packings are well pronounced to improve the charge carrier mobility. Another parameter that stands out in eq.2-3 is the reorganization energy (λ). λ is not constant and affected by the surrounding conditions. λ can be described as

$$\lambda = e^2\left[\frac{1}{2r_D}+\frac{1}{2r_A}-\frac{1}{r_D+r_A}\right]\left[\frac{1}{\varepsilon_{op}}-\frac{1}{\varepsilon_{ST}}\right] \qquad (\text{eq.}\,2-4)$$

whereas the radius of the molecular wave function of the donor is r_D and that of the acceptor is r_A. ε_{op} and ε_{ST} are the dielectric constant in an optical range and the static dielectric constant. With the combination of eq.2-3 and eq.2-4, it is obvious that ε_{ST} is an important parameter to control k_{ET}. Noteworthy is that the model discussed here is a very simple and fundamental part and the model has been improved in several ways to adapt individual experimental results. [23, 24]

Furthermore, the existence of energetic trap sites diminish carrier transport. [11,26] Defects, impurities and adhering solvents can be trap sites. Charge carriers are bound in trap sites. These effects are significant in the case of organic semiconductors. The interaction to the charge carrier can be expressed as Coulomb interaction E_b and described as

$$E_b = \frac{e^2}{4\pi\varepsilon\varepsilon_0 r} \qquad (\text{eq.}\,2-5)$$

with the dielectric constant (ε), the vacuum constant (ε_0), the distance (r), and the elementary charge (e). The dielectric constant is inverse proportional to the dielectric constant. Therefore, the negative interaction can be reduced simply by increasing the dielectric constant.

2.3 Dielectric Constants

The dielectric constant (ε_r) or relative permittivity to the permittivity in vacuum express a parameter that defines how many charges are induced under an electric field. The dielectric constant is measured with capacitors, which are sandwich structures of two conductive plates and a dielectric material in between. (Figure 2-4c)

Capacitance is described as

$$C = \varepsilon_r\varepsilon_0\frac{A}{T} \qquad (\text{eq.}\,2-6)$$

whereas ε_0 is the vacuum constant and A is the area of the capacitor. T is the thickness of two plates. As seen in eq.2-6, capacitance is proportional to the dielectric constant.

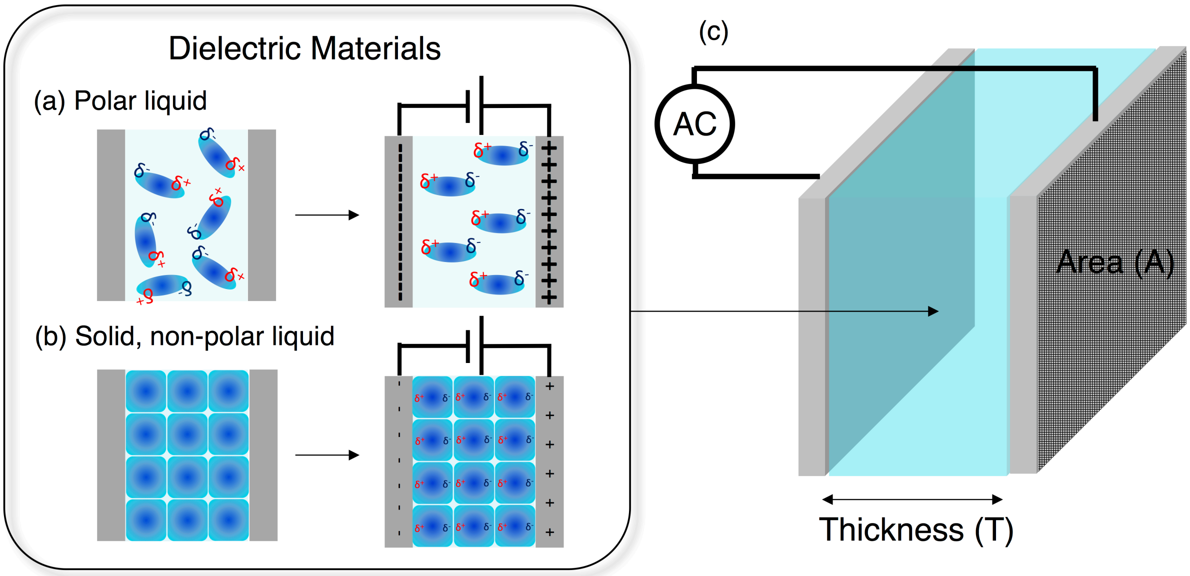

Figure 2-4. Dielectric responses of a polar liquid (a) and a solid or a non-polar liquid(b). (c)A schematic illustration of a dielectric capacitor.

The value of the dielectric constant refers to the dielectric polarization. In the case of polar liquids, the dielectric response is associated with the reorganization of molecules (Figure 2-4a). In this case, the dynamic motion of dipoles in the capacitor takes place, resulting in a large response. This is a reason why polar molecules such as water and methanol have large dielectric constants (water: ~80, methanol: ~30). [27] When a liquid material is non-polar, the dielectric response is much smaller and stabilizes less charge carriers on the surfaces of the capacitor (Figure2-4b). In this case, the polarization stems from the slight deformation of electron density in the molecules. Consequently, the dielectric constant is small (benzene: ~2). In the case of solid materials, the dielectric constant is small even if there are dipole moments because the motions are restricted by the packing except for specific cases. [28] The dielectric responses of solid materials are also based on the deformation of electron density in the molecules. The dielectric constants of the solid materials depend on the density of the electrons. Therefore, large atoms containing materials such as inorganic crystals have a relatively larger dielectric constant than that of organic molecules. (silicon crystals: ~12, conjugated polymers: ~4).

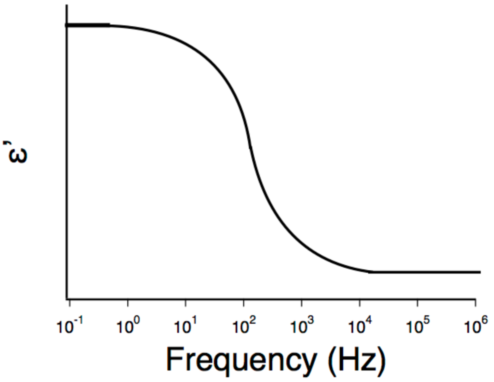

Figure 2-5. An example of dielectric constant as a function of frequency.

The dielectric constant is dependent on the frequency of the applied electric field (Figure2-5). At higher frequencies, the dipoles cannot follow the electric field, resulting in a low dielectric constant while the dipoles can follow the electric field at a lower frequency. The depletion point and saturation point depend on the materials.

2.4 Ferroelectric Materials

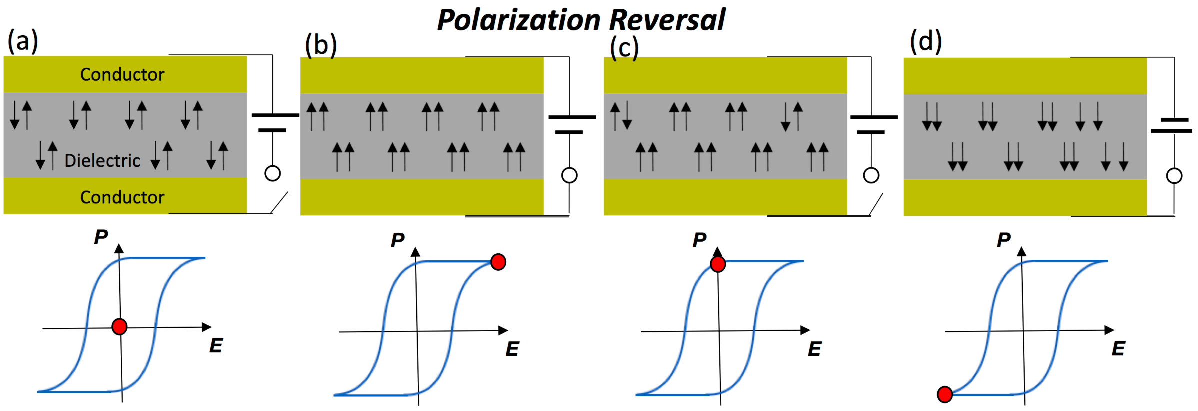

Figure 2-6. Schematic Illustrations of a capacitor of a ferroelectric material and its polarization- Electric field (P-E) plots. When the capacitor is prepared, the dipole moments compensate each other (a). When the sufficient electric bias is applied, the dipole moment aligns with the field direction (b). After removal of the bias, the dipole moments sustain (c). When the bias is applied to the other direction, the dipole moments align to the direction.

Although it is difficult to increase the dielectric constants of conjugated polymers directly, controlling dielectric responses is possible in different ways. Ferroelectricity is a dielectric characteristic in which remnant polarization can be controlled by an external voltage. This phenomenon is often seen in inorganic dielectric crystals, but rarely seen in organic materials. [29,30] For the appearance of the ferroelectric phase, the molecules or crystals need asymmetric dipole moments. Ferroelectric materials are not polarized as prepared because the molecules assemble to compensate each dipole (Figure 2-6a). When the external voltage exceeds the coercive electric field, the polarization of the film orients accordingly (Figure 2-6b). This is called polarization or poling. After removal of the electric bias, the material still preserves the polarization (Figure 2-6c). By applying an opposite voltage above the coercive voltage, the polarization is reversed (Figure 2-6d). Ferroelectric materials are often applied to memory devices. [31,32]

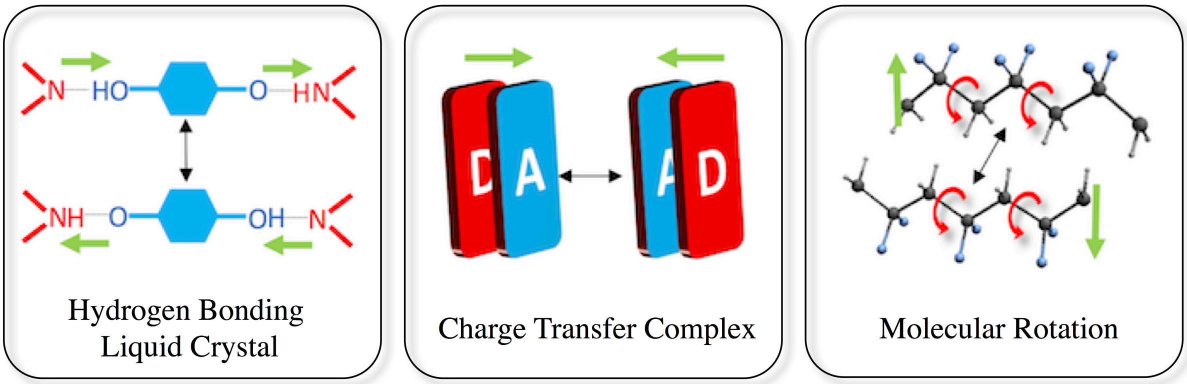

Figure 2-7. Existing ferroelectric mechanisms of organic materials.

There are different mechanisms for organic ferroelectric effects that include hydrogen bonding, [33–35] liquid crystalline ordering, [36] charge-transfer complexes, [37, 38] and molecular rotation. [39, 40] (Figure 2-7). The easiest one to achieve is the hydrogen bonding type. The polarization is induced by the asymmetric localization of protons. Because the protons are mobile within the film, switching is easy. Charge-transfer types are realized based on the electron-donating and –accepting process, which would not require a large motion. A lot of examples of ferroelectric materials based on this mechanism are also reported. [37,38] The most difficult type to realize is the molecular rotation based mechanism, because the dipolar part of the molecule is required to rotate in the solid state, which means it needs space to move, but at the same time, it needs to be locked to sustain the polarization. There are two examples of this type of ferroelectric materials. [39, 40]

2.5 Organic Electronic Devices and Ferroelectric Materials

Organic electronic devices contain organic semiconductors. The main advantages of organic devices are solution-processability and flexibility, which can hardly be achieved by inorganic devices. [4] Although there are many types of devices based on organics, organic field-effect transistors (OFETs), [41] organic light-emitting diodes (OLEDs), [42] and organic photovoltaics (OPVs) [43] are representative. Here, OFETs and OLEDs shall be introduced.

2.5.1 Organic Field-Effect Transistors

OFETs are often used as switches in logic circuits. When an electric field is applied, a current is obtained. OFET is composed of a gate, a source contact, a drain contact, a dielectric layer, and an active layer.

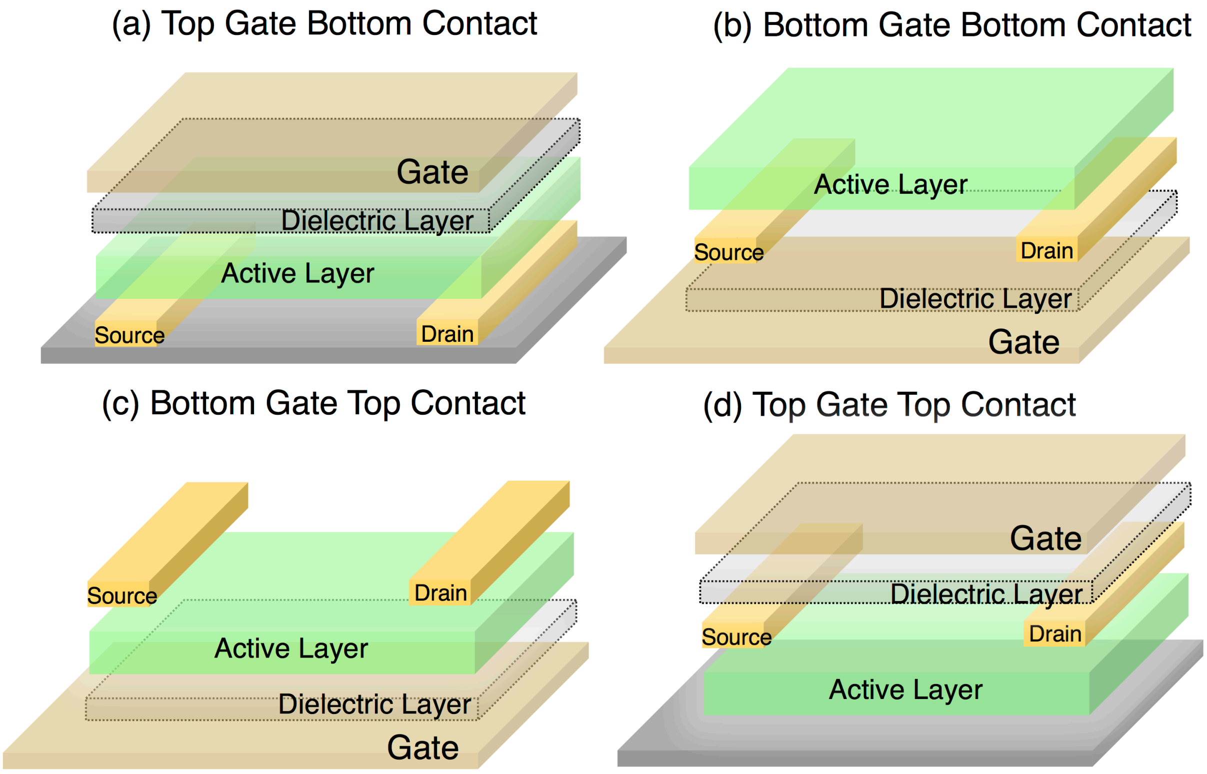

Figure 2-8. Four types of device configurations of OFETs

There are typically four types of architectures of OFETs (Figure 2-8). In all cases, a dielectric layer is sandwiched in between the gate contact and source-drain contacts to form a capacitor structure. When that capacitor is biased, charge carriers are induced at the interface between a dielectric layer and the active layer. The bias is called a gate voltage. The induced carriers make the interface conductive and the carriers are transported by the applied drain voltage. The quantity of induced carriers depends on the capacitance of the dielectric layer. Accordingly, the high capacitance of a dielectric layer results in high drain currents. [44] According to eq.2-6, the capacitance increases inverse proportionally to the thickness of the dielectric layer. However, when the insulator is too thin, current leakage becomes significant. Utilizing high dielectric constant materials is also a strategy to obtain high drain currents. Depending on the processability of materials, the appropriate device architecture is determined. For example, bottom gate bottom contact OFET has the advantage of the simplicity of fabrication. On the other hand, both top gate bottom contact and bottom gate top contact structures are more ideal to induce charge carriers. They often show higher charge carrier mobilities. Each architecture has individual advantages and disadvantages.

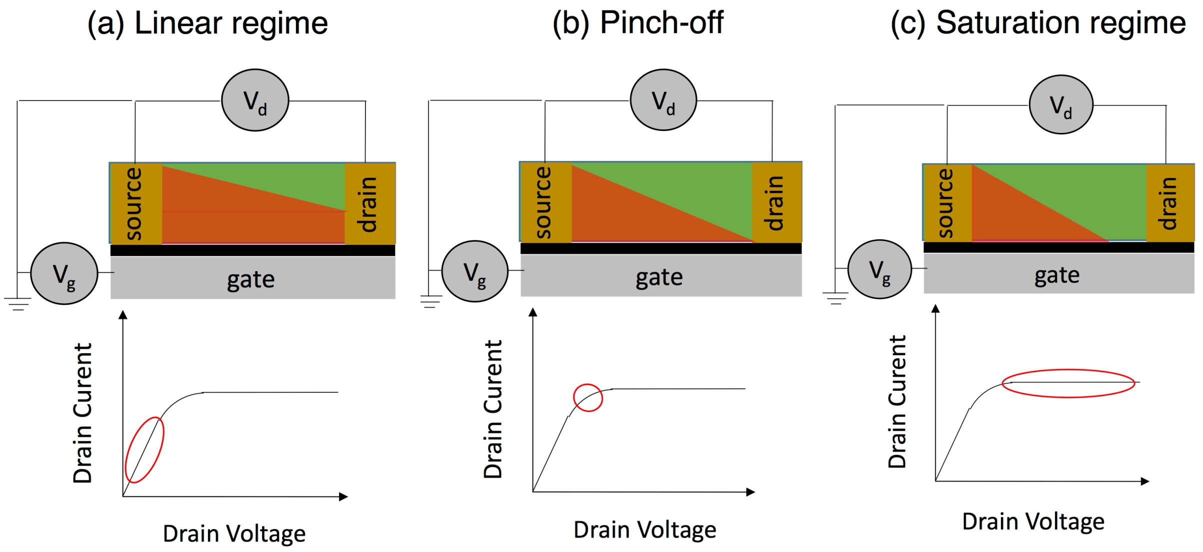

Figure 2-9. Schematic illustrations of channel formation while increasing a drain voltage. Green: semiconductor, Red: potential of an electric field.

The space between source and drain is called a channel. Here, the basic behavior of the channel is briefly introduced. [46] Under the gate bias, the drain current increases proportionally to the drain voltage (linear regime, Figure 2-9a). When the bias reaches the net value of the gate bias, the current saturates because the bias drops to zero between source and drain (Figure 2-9b). This is as known as the pinch-off. Under the drain voltage above the pinch-off, the drain current is constant (saturation regime, Figure 2-9c).

The Shockley equation describes the current in linear regime ($I_{D,lin}$) and in saturation regime ($I_{D,sat}$) as

$$\mathrm{I}_{D,lin} = \frac{C\,W\,\mu_{lin}}{L}\left[\left(V_g - V_{th}\right)V_d - \frac{V_D^2}{2}\right] \qquad (\mathrm{eq.}\,2-7)$$

for $|V_g - V_{th}| \geq V_d$ and

$$\mathrm{I}_{D,sat} = \frac{C\,W\,\mu_{sat}}{2L}\left(V_g - V_{th}\right)^2 \qquad (\mathrm{eq.}\,2-8)$$

for $V_d > |V_g - V_{th}| > 0$

with the mobility of linear regime (μ_{lin}) and saturation regime (μ_{sat}), the channel length (L), the channel width (W), the capacitance per area (C), the threshold gate voltage (V_{th}), the gate voltage (V_g) and the drain voltage (V_d). the equations are also further described as

$$\mu_{lin} = \frac{L}{CWV_d}\frac{\partial I_{D,lin}}{\partial V_g} \qquad (\text{eq. } 2-9)$$

$$\mu_{sat} = \frac{2L}{CW}\left(\frac{\partial\sqrt{I_{D,lin}}}{\partial V_g}\right)^2 \qquad (\text{eq. } 2-10)$$

Accordingly, the mobility can be calculated from the transfer curve, which shows the drain current over the gate voltage.

2.5.2 Organic Light-emitting Diodes

OLEDs are well known organic electronic devices because OLEDs are already applied to practical uses such as TVs and smartphones.[47] The one of the best advantages of OLEDs over the inorganic LEDs is the realization of a variety of colors due to the feasible color tuning of organic semiconductors.

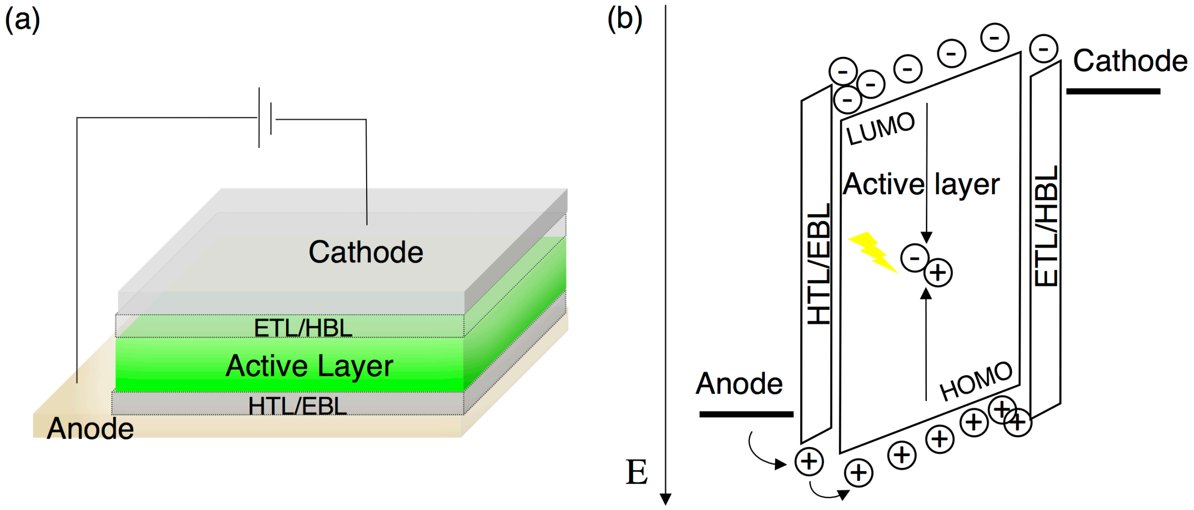

Figure 2-10. (a) A schematic illustration of the device configuration of OLED. (b) An energy diagram of OLED.

Conventional OLEDs are composed of the anode, the cathode, the active layer, the hole transport layer (the electron blocking layer), and the electron transport layer (the hole blocking layer) (Figure 2-10a). Holes are injected into the active layer, surpassing the energy barrier between the anode and HOMO level of the semiconductor (Figure 2-10b). To reduce this gap, the hole transport layer is inserted between anode and active layer so that the carrier injection becomes easier. The injected holes are confined in the active layer by the hole blocking layer. The same events take place at the cathode. Holes and electrons recombine in the active layer, resulting in the electroluminescence. Here, the applied electric field drops proportionally to the distance times dielectric constant. Therefore, the whole device cannot be too thick to operate under moderate voltages. The thickness is typically several tens to one hundred nanometers. [42,48]

2.6 Organic Devices and Ferroelectric Materials

Ferroelectric materials are occasionally incorporated into organic electronic devices. They are employed mainly to give devices switchability, but sometimes better functionality. D. M. De Leeuw *et al*. employed a ferroelectric polymer as dielectric layer in OFETs (Figure 2-11). [100]

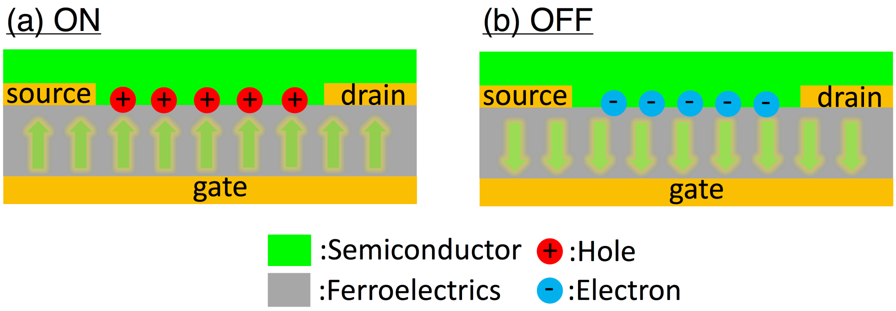

Figure 2-11. An on-state (a) and an off-state (b) of ferroelectric-gate OFETs.

They employed a p-type semiconductor as active layer. When the spontaneous dipole moments of the ferroelectric polymer align to the contact direction, holes are induced spontaneously at the interface. The channel is thus conductive even at a gate voltage of 0 V. Contrary, electrons are induced when the dipoles align to the gate direction. In this case, the channel is not conductive since the employed semiconductor is p-type. With this mechanism, they achieved the on/off ratio of 10^5 at 0 gate bias.

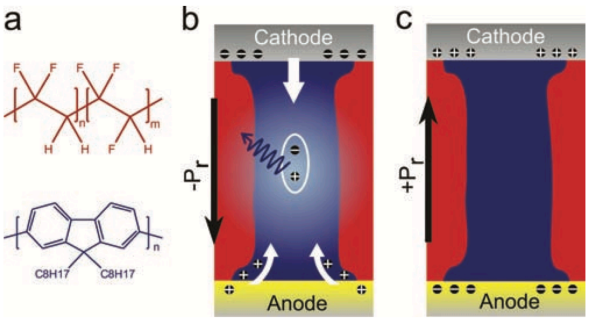

Figure 2-12. (a) Chemical structures of the employed ferroelectric polymer and semiconductor. An on-state (b) and an off-state (c) of ferroelectric material containing OLEDs. Figure reproduced with permission from ref. [101] © 2011 WILEY‐VCH Verlag GmbH & Co. KGaA, Weinheim.

The other example is an application of a ferroelectric polymer to OLEDs (Figure 2-12). [101] They employed a phase-separated film of a semiconducting polymer and a ferroelectric polymer as an active layer of OLED. In this device, the spontaneous dipole moments work as a permanent electric field. When the dipoles align from anode to cathode, the electric field helps currents to flow so that the recombination of holes and electrons is accelerated. Contrary, the electric field faces the other direction, it disturbs currents. In both cases, ferroelectric materials play a role as a switch but also contribute to increase conductivity, which is unusual for conventional OFETs and OLEDs. The similar functionality is also expected when semiconductors are ferroelectric.

2.7 Poly-(Para-Phenyleneethynylene)s

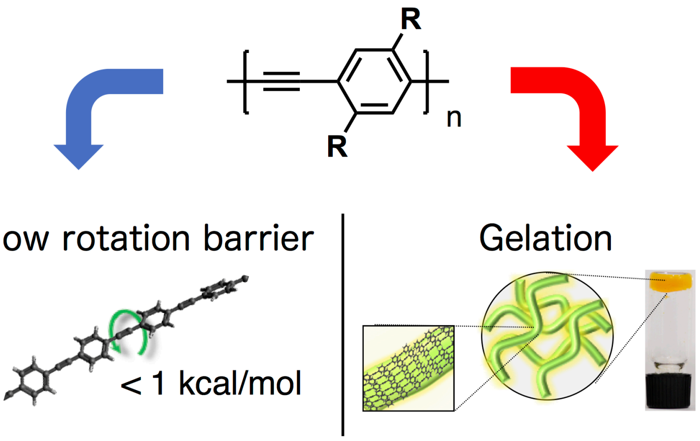

Figure 2-13. A molecular structure of PPE and its two mechanical characteristics

Poly-(*p*-Phenyleneethynylene)s (PPEs) are conjugated polymers, which contain phenyl and acetyl moieties alternatingly. [49-51] PPEs have been applied to OLEDs and OFETs. [52-54] The device performances are moderate as 2.2×10^{3} cd m^{-2} and 10^{-2} cm^{2} $V^{-1}s^{-1}$, respectively. One of the most interesting aspects of PPEs apart from the electronic properties is their mechanical properties (Figure 2-13). Since the triple bonds induce a rigid and linear backbone, high crystallinity is achieved. For this reason, PPEs occasionally form supramolecular gels by thermal saturation. [65, 66] On the other hand, the flexibility of phenyl rings around the polymer chain is also high, as the rotation energy barrier is calculated to be less than 1 kcal mol^{-1} in solution. Therefore, partial structures of PPEs are also utilized as molecular machines. [28]

3 Aim

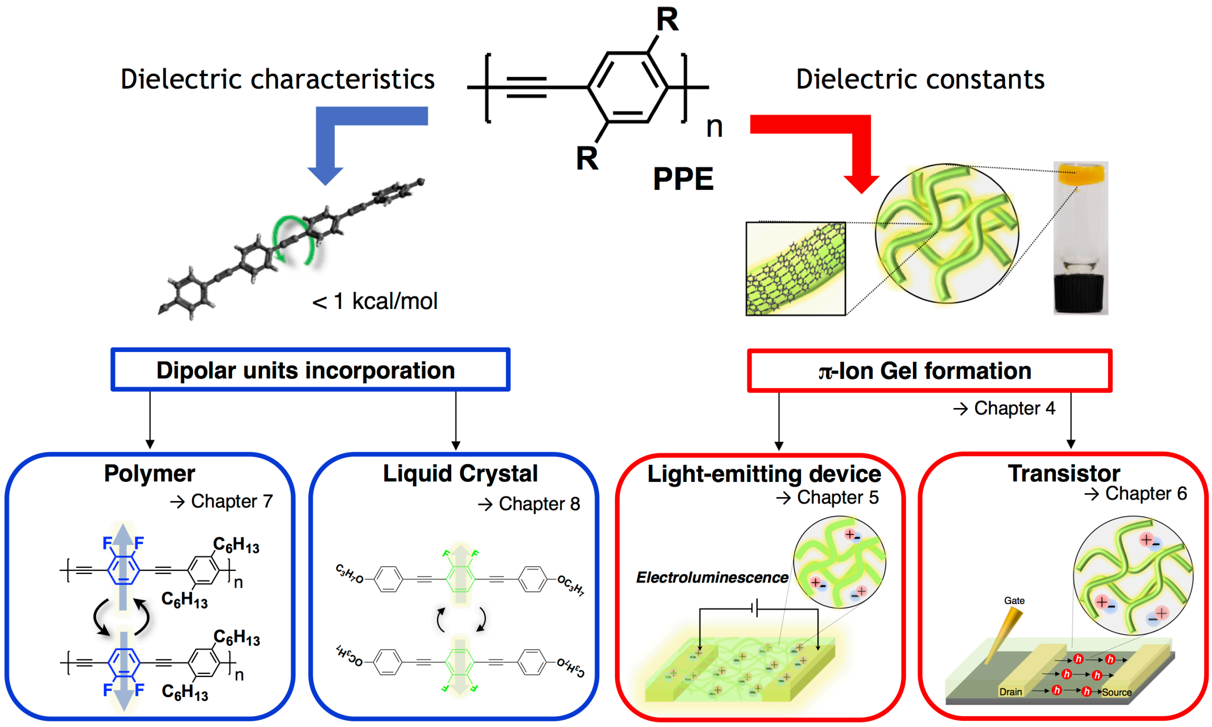

Figure 3-1. The contents tree of this thesis.

In this thesis, the dielectric behavior of PPEs is investigated and engineered to develop organic electronic devices. The context of the dielectric behavior means not only the quantity of dielectric constants but also specific dielectric characteristics under electric fields such as ferroelectricity.

Toward this goal, two main strategies are suggested, 1. molecular designs to incorporate dipolar units and 2. Forming π-ion gels. For the first strategy, the dipolar units are introduced to the PPE units (in chapter 7) and also to the PE liquid crystalline oligomers (in chapter 8) to control the bulk polarization. For the second strategy, π-ion gels, PPE gels containing an ionic liquid, are invented and developed (in chapter 4) to increase the net dielectric constant of the gel since ionic liquids display high dielectric constants. The gels are then applied to the light-emitting device (LECs, in chapter 5) and Transistors (in chapter 6). The insights about the effect of the dielectric behavior (dielectric characteristics and dielectric constants) to organic devices are the main theme of this thesis.

4 Gelation of PPEs

4.1 Motivation

Gels are a fascinating class of materials; they are spongy and porous yet can be made of wildly different organic but also inorganic or biological materials. [56-61] Gels are defined by their mechanical state and their nano or microscopic features that are typically fibril-like; gels enclose a large amount of solvent or gas (aerogel) and have a three-dimensional structure. Conjugated polymers or molecules can occasionally form gels (π-gels). The gels can display properties that are different from both of thin films but also from solutions. [61]

π-Gels are supraomlecularly built up by weak interaction and are often reversible, whereas non-conjugated gelators such as polymethacrylate or poly(acrylic acid) are often covalently cross-linked.[62-64] Therefore, one of the disadvantages of gels made of conjugated polymers is that sol–gel states are unstable and highly sensitive to the temperature.

In the case of the soluble PPE, such gel phases have been reported. [65,66] These gels were mechanically sensitive and described as fragile gels. [66] Generally, highly concentrated solutions of dialkyl-PPEs give gel-like species. These gels form from nonpolar solvents such as THF, toluene, and chloroform.

These gels are potentially useful for organic devices since they are not only frameworks filled with solvent but also semiconductors. Actually, there are some successful attempts to apply π-conjugated gels to organic photovoltaic (OPV) devices because they have an attractive configuration for OPV: nano-segregated bicontinuous structure and coplanar intermolecular packing. [66-68]

However, despite large numbers of studies on π-conjugated gels, gelation is mostly accomplished thermally, simply done by heating the conjugated polymer under consideration and cooling it down into its gel phase. In this case, a large difference of solubility upon temperature change is required. Even at room temperature, the gel still contains dissolved polymer chains in its large, solvent-filled void space; the gel is filled with solute, which gives frangibility and instability to temperature. In this chapter, the gelation using a conventional thermal approach and a novel solvent exchanging method are investigated. The insights result in the creation of “π-ion gels”.

4.2 Materials and Methods of Gelation

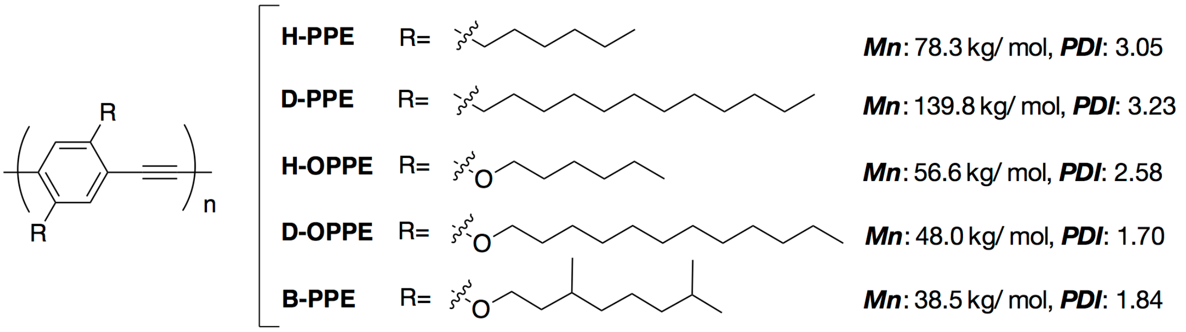

Figure 4-1. Molecular structures of poly(p-phenyleneethynylene)s (PPEs) in this study. All PPEs were synthesized by Dr. Emanuel Smaraly.

The PPEs which we investigated (Figure 4-1) in this chapter were obtained by standard Pd-catalyzed coupling of the Sonogashira type. The synthesis is already reported. [69] They are all citron- to deep-yellow-colored materials, available on a gram scale; they show molecular weights of 39−140 kg/mol and polydispersities that are in the range of 1.7−3.2. These PPEs were synthesized by Dr. Emanuel Smarsly.

Scheme 4-1. Schematic Representations of Methods for Gelation: (a) Thermally Promoted Gelation and (b) Solvent Promoted Gelation.

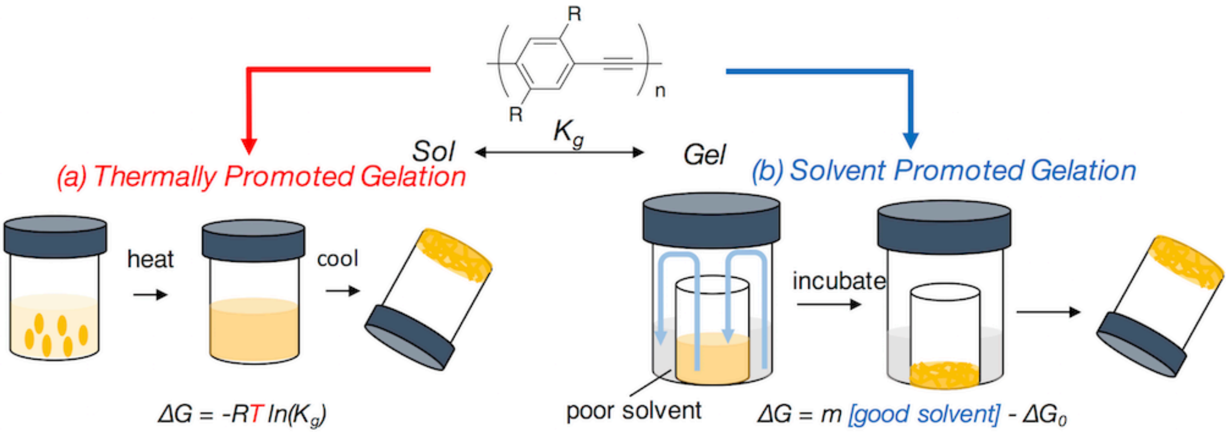

Scheme 4-1 shows the two investigated methods to prepare gels. Thermally Promoted Gelation (TOG) is known to be a conventional gelation performed by thermal saturation (scheme 4-1a). 0.5-10 mg of the PPEs were dissolved in 500 µL of THF by heating up to 80°C in a 1mL vial under air. The solution was capped and allowed to cool down slowly to room temperature and kept as it for at least 24 h in closed box at ambient temperature. Solvent Promoted Gelation is the novel method of gelation in this work. Typically, 500 µL of THF polymer solution in a 1 mL vial was placed in a 5 mL vial and filled with methanol, without capping. The 5 mL vial was closed and incubated for at least 24 h. The concentration of solution varied from 0.5 to 5 mg mL^{-1}. To confirm the gel formation, the precipitations or solutions were confirmed by simple inversion of the vials.

4.3 Results of Gel Formation

Table 4-1. Resulting Morphology of TOG

	20 mg/mL	10 mg/mL	5 mg/mL	2.5 mg/mL	1 mg/mL
D-PPE	◎	◎	-	-	-
H-PPE	◎	◎	△	-	-
D-OPPE	◎	◎	△	-	-
H-OPPE	-	-	-	-	-
B-PPE	-	-	-	-	-

◎; Rigid Gel, △; Incomplete Gel, -; No Precipitation, ×; Solid Precipitation.

Table 4-2. Resulting Morphology of SOG

	5 mg/mL	2.5 mg/mL	1 mg/mL	0.5 mg/mL
D-PPE	◎	◎	△	△
H-PPE	◎	◎	△	△
D-OPPE	◎	◎	△	△
H-OPPE	◎	◎	△	△
B-PPE	×	×	×	×

◎; Rigid Gel, △; Incomplete Gel, -; No Precipitation, ×; Solid Precipitation.

The results of gel formation of each PPE are summarized in Tables 4-1,2. D-PPE, H-PPE, and D-OPPE give good TOG gels at down to 10 mg mL^{-1} PPE concentrations in tetrahydrofuran. These gels are rigid as shown in the insets of Figure 4-2. At 5 mg mL^{-1} concentration of the PPEs, incomplete gelation is observed for either H-PPE or D-OPPE. H-OPPE. B- PPE did not form any gel phase and neither did it precipitate from tetrahydrofuran. For the solvent induced gelation (SOG) the PPEs were dissolved in THF and put into a larger vial that contained methanol. After 1 day, the methanol had diffused into the THF solution and created a gel phase, which is different from the precipitate of PPE in methanol. The diffusion of non-solvent into the THF solution of the PPE results in the formation of stable gels at 2.5 mg mL^{-1}; i.e., it is more effective than thermal gelation in the perspective of the material cost. Also, all of the PPEs form visible gels with exception of B-PPE. Insets of Figure 4-2 display the physical appearance of the gels.

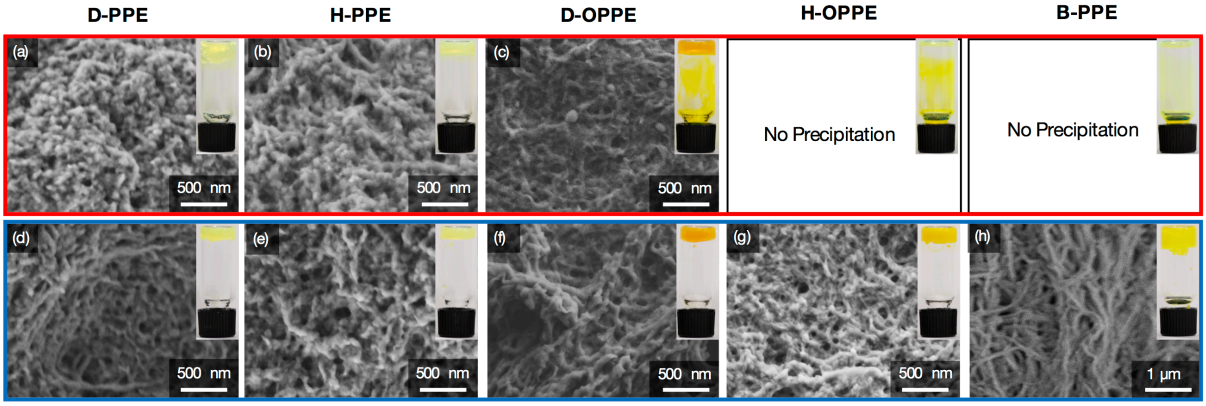

Figure 4-2. SEM micrographs of self-assembled nanostructures of (a) D-PPE, (b) H-PPE, and (c) D-OPPE prepared by thermally promoted gelation and (d) D-PPE, (e) H-PPE, (f) D-OPPE, (g) H-OPPE and (h) B-PPE prepared by solvent promoted gelation.

The gels were isolated and investigated by scanning electron microscopy (SEM) (Figure 4-2). TOG-gels and SOG-gels are similar, as all show the same type of spongy structures, even though in TOG-gels the pores seem to be more “filled”. SOG-gels show a better developed structure; particularly, the gels shown in Figure 4-2d-h have structures that are well-developed. The features are 80–100 nm in diameter and several μm long. Surprisingly, the fibers of B-PPE are the best developed ones (Figure 4-2h). Yet, precipitates of B-PPE by SOG did not give a gel. The rigid and straight nanowire structures form a powdery macroscopic material. We assume that the polymer does not incorporate solvent inside. When THF or MeOH is replaced to other good and poor solvents, gels with similar microstructures were observed (Figure A4-1), suggesting other solvent combinations should also be applicable. The solvent combinations are not investigated further because no significant dependence in the morphology is observed.

4.4 Optical Properties of TOG Gels and SOG Gels

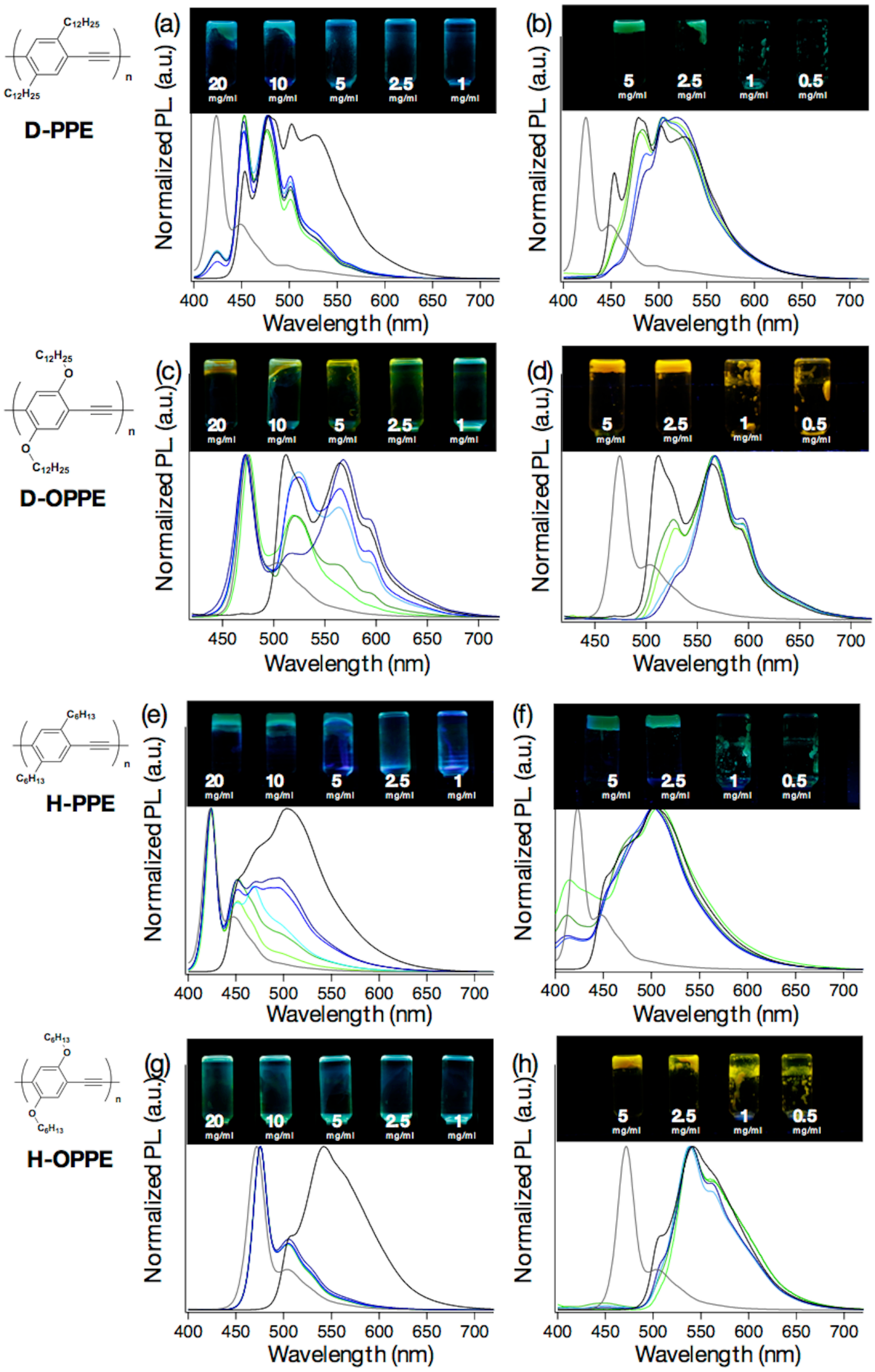

Figure 4-3. (a, c, e, g) Normalized emission spectra of thermally promoted gels of D-PPE (a), D-OPPE (c), H-PPE (e), and H-OPPE (g). The concentrations are 20 mg/mL (dark blue), 10 mg/mL (blue), 5 mg/mL (light blue), 2.5 mg/mL (dark green), and 1 mg/mL (light green), respectively. (b, d, f, h) Normalized emission spectra of solvent promoted gels of D-PPE (b), D-OPPE (d), H-PPE (f), and H-OPPE (h). The concentrations are 5 mg/mL (dark blue), 2.5 mg/mL (blue), 1 mg/mL (dark green), and 0.5 mg/mL (light green), respectively. Gray and black depict normalized emission of solutions and cast films, respectively. Insets are the fluorescent photographs of gels.

We investigated the absorption and emission of the PPEs in the different gel phases. Since structure and optical properties are strongly linked in PPEs morphology. Figure 4-3 displays the emission spectra of all of the TOG and SOG PPE gels. For the comparison, the emission spectra in solution (light gray) and in thin films (dark gray) are added. Absorption spectra are shown in Figure 4-4.

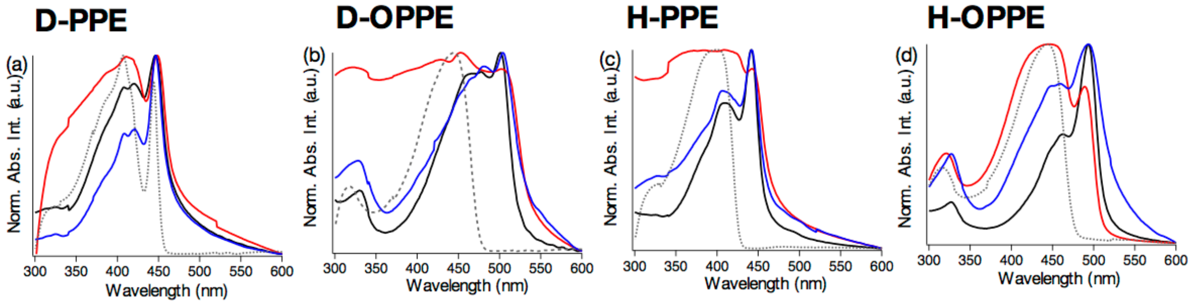

Figure 4-4. Normalized absorption spectra of thermally promoted gels and solvent promoted gels of D-PPE (a), D-OPPE (b), H-PPE (c) and H-OPPE (d). Dash grey, black, red, and blue show normalized emission of solution, cast films, thermally promoted gel (20 mg/ml), and solvent promoted gel (5 mg/ml), respectively.

The optical properties of PPEs, particularly of H-PPE and D-PPE, have been thoroughly investigated and analyzed. [70-72] PPEs attain a partially planarized conformation in the exited state when investigated in solution. In the solid, fully planarized excited states are assumed. Thin films of DPPE can retain two different states. One (usually in amorphous film) is an excimeric state emitting at 550 nm (emissive lifetime 5.9 ns), the polymer chains are planarized but disordered. The second state (usually seen in annealed thin films) is crystalline-ordered, which has a small Stokes shift, and displays a strong structured emission maximum at 450 nm. In both cases the polymer backbones are planarized, but the morphologies differ. No significant difference is observed in Absorption spectra. The emission signatures of TOG-PPEs (Figure 4-3 a,c,e,g) are carefully checked, and it is found that D-PPE features some emission assigned to residually dissolved fraction of PPE (420 nm). In H-PPE this effect is more distinct, and an increased emission of the dissolved H-PPE is observed. H-OPPE does not give thermal gels; all of the emission come from the dissolved material, while D-OPPE gives some gels, but the emission characteristics show a significant contribution of D-OPPE in solution. Only a part of the spectrum shows emission characteristics that suggest non-dissolved species.

SOG changes the situation (Figure 3b,d,f,h). D-PPE at low concentrations displays some ordered polymer chains (structured emission at 470 nm) and a solid state that is dominated by an excimeric non-ordered assembly of PPE chains (emission maximum at 550 nm). In the more concentrated Gels only the signals of excimeric species are observed, without any signals stemming from residually dissolved PPE chains. The situation is similar for other PPEs. The added non-solvent forces the PPE chains into an excimeric type gel structure. This relationship is clear when the degree of aggregation is defined and plotted.

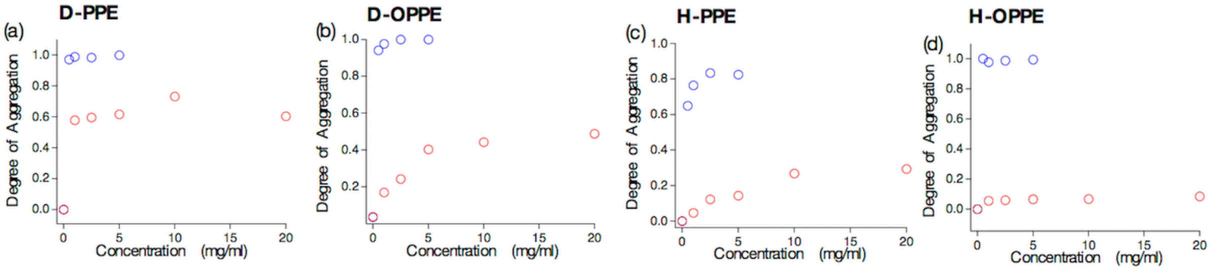

Figure 4-5. Plots of concentration versus degree of gelation of thermally promoted gels (red) and solvent promoted gels (blue) of (a) D-PPE, (b) D- OPPE, (c) H-PPE, and (d) H-OPPE.

Figure 4-5 shows the degree of aggregation with respects to TOG and SOG. The degree of aggregation(DoA) is defined by

$$\mathrm{DoA} = (X - X_{\mathrm{sol}})/(X_{\mathrm{film}} - X_{\mathrm{sol}}),\ \text{where } X = I_{\mathrm{sol}}/(I_{\mathrm{sol}} + I_{\mathrm{agg}}) \qquad \text{(eq.4-1)}$$

whereby I_{sol}, I_{agg}, X_{film}, and X_{sol} are the emission intensity at the wavelength of peak emission of the solution, emission intensity at the wavelength of peak of the cast film, the value of the cast film, and the value of the solution, respectively. The wavelengths of (I_{sol}, I_{agg}) are (423 nm, 524 nm) for D-PPE, (477 nm, 566 nm) for D-OPPE, (423 nm, 513 nm) for H-PPE, and (472 nm, 542 nm) for H-OPPE, respectively. Gel formation of the investigated PPEs is much more distinct in the SOG gels than in the TOG gels at any concentrations as mentioned above. For SOG gels we find mostly gel formation, suggesting that no dissolved single-chain polymers remain importantly.

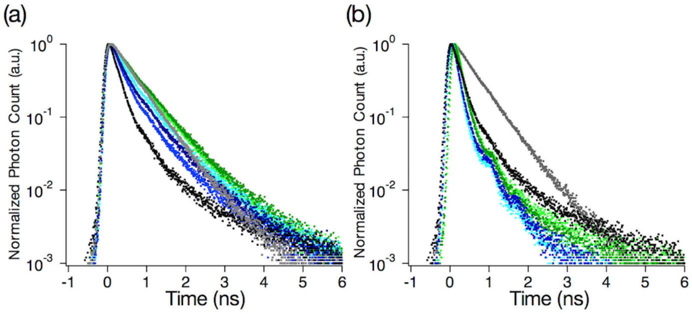

Figure 4-6. (a) Fluorescent decay profiles of TOG gels of D-OPPE at 566 nm. The concentrations are 20 mg/mL (dark blue), 10 mg/ mL (blue), 5 mg/mL (light blue), 2.5 mg/mL (dark green), and 1 mg/mL (light green), respectively. (b) Fluorescent decay profiles of SOG gels of D-OPPE at 566 nm. The concentrations are 5 mg/mL (dark blue), 2.5 mg/mL (light blue), 1 mg/mL (dark green), and 0.5 mg/ mL (light green), respectively. Gray and black traces show solutions at 1 mg/L and cast films. Table 4-3 shows the numerical values.

Table 4-3. Exponential Fitting Parameters of Fluorescent Decay Profiles of D-OPPE

Sample	t_1 / ns (f_1)	t_2 / ns (f_2)	t_{av} / ns [a]
Solution	0.52 (1.00)	-	0.52
Cast Film	0.19 (0.88)	1.60 (0.12)	0.37
20 mg/mL (TOG)	0.29 (0.85)	1.39 (0.15)	0.45
10 mg/mL (TOG)	0.24 (0.91)	1.59 (0.09)	0.37
5 mg/mL (TOG)	0.30 (0.83)	1.32 (0.17)	0.47
2.5 mg/mL (TOG)	0.47 (0.81)	1.29 (0.19)	0.63
1 mg/mL (TOG)	0.32 (0.80)	1.20 (0.20)	0.49
5 mg/mL (SOG)	0.11 (0.87)	0.67 (0.13)	0.18
2.5 mg/mL (SOG)	0.08 (0.91)	0.80 (0.09)	0.15
1 mg/mL (SOG)	0.12 (0.88)	1.00 (0.12)	0.23
0.5 mg/mL (SOG)	0.13 (0.88)	1.30 (0.12)	0.28

[a] t_{av} is defined as $(t_1f_1 + t_2f_2)/(f_1 + f_2)$.

The emission decays for D-OPPE (Figure 4-6 and Table 4-3) are investigated carefully. a mono-exponential decay of PPE solution ($\tau_{1/2}$ = 0.52 ns) is found. In cast film a bi-exponential decay with $\tau_{1/2}$ = 0.19 ns and $\tau_{1/2}$ = 1.6 ns is seen. At the low concentration, In TOG gels, a mix of lifetimes that resembles that of a cast film in the presence of PPE solution is observed. The fluorescent decay of the SOG of D-OPPE is also bimodal, but with a short component and a second one whose $\tau_{1/2}$ = 1.6 ns, resembling the decay of the cast film.

4.5 Kinetic Observations of SOG Gels

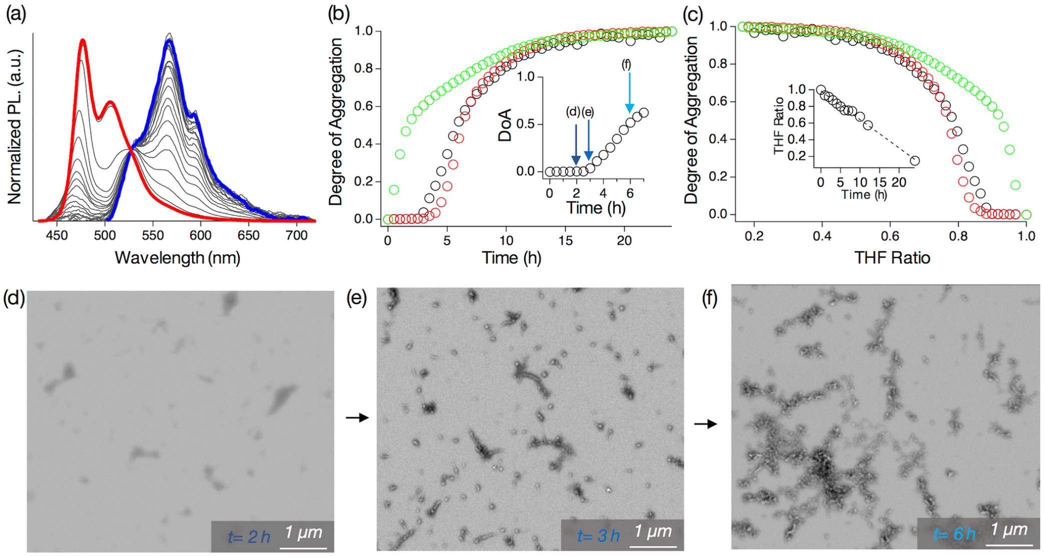

Figure 4-7. (a) Time-dependent emission spectra of SOG of D-OPPE (2.5 mg/mL). The spectra were taken every hour from 0 h (red) to 24 h (blue) and normalized at 530 nm. (b) Plots of time versus DoA of SOG gels D-OPPE with the concentrations of 1 mg/mL (red), 2.5 mg/mL (black), and 5 mg/mL (green). The insets show expanded plots of 2.5 mg/mL of (b). (c) Plots of time versus THF volume ratio determined by NMR measurement. (d–f) SEM micrographs of kinetic structures of SOG of D-OPPE at 2.5 mg/mL at t = 2 h (d), 3 h (e), and 6 h (f).

It is important to understand how the gel networks build up with time. The kinetics of solvent induced development of D-OPPE gels both by emission spectroscopy and SEM (Figure 4- 7) are investigated. After an induction period of 2 h the solvent composition has reached a threshold value of methanol and solid aggregates appear, which after around 6 h have coalesced into the strand-like gel aggregates, a hallmark of the later observed gel phases. The normalized emission spectra show an isosbestic point for the formation of the gel networks, implying a clean transformation of the unaggregated species into the gel phase. The gelation process can be followed also by the ratio of the fluorescence intensities of the two different species, aggregated and non-aggregated. In addition, the solvent ratio inside of the gel was determined by NMR (Figure 4-7c); gel formation is promoted by methanol, and the finished gel contains more than 90% of methanol after 24 h. This depends on the PPE concentration; higher concentration gives faster gelation as seen in Figure 4-7b, c. The spectra at each concentration are shown in Figure A4-2. The SEM micrographs of the developing gels were obtained by spin-coating of a suspension of samples. Samples were spin coated on Si/SiO_2 with 2000 rpm (60 s) to remove dissolved portion of polymers. From the observations, it is concluded that nuclei start to propagate into curly wormlike species at t = 6 h. The process to form the gels by SOG is a growth process, starting from several tens of nanometer-sized nuclei to the sponge-like structures (shown in Figure 4-2) *via* the intermediates shown in Figure 4-7d–f. This is typical for "nucleation and growth", which is observed in thermally promoted polymer gels as well. [73] This growing process of conjugated polymer gels has been predicted by rheological and diffraction measurements. [73,74] However, the SEM micrographs are the first direct evidence to support these observations for conjugated polymers.

4.6 Thermal Stability of Gels and Ion Gel Formation

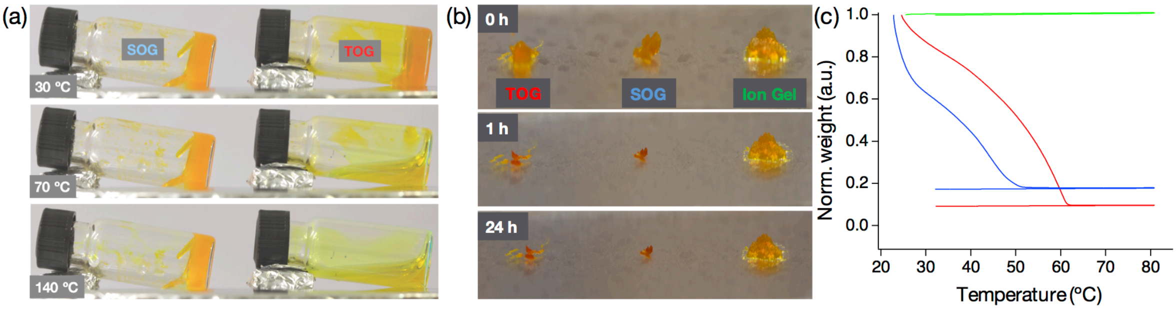

Figure 4-8. (a) Photographs of 2.5 mg/mL of SOG (left) and 10 mg/mL of TOG (right) at individual temperature (from top: 30, 70, and 140 °C). (b) Camera images of 10 mg/mL of TOG (left), 2.5 mg/mL of a SOG (middle), and an ion gel (right) at individual times after mounting on the glass substrate at ambient environment. (c) TGA trace form room temperature to 80 °C of TOG (red), SOG (blue), and ion gels (green).

Typically, gels are thermally unstable because a gel-sol transition occurs upon heating. The thermal stability test was done by following process. Both gels, prepared by SOG or by TOG, were placed on an aluminum foil coated hot plate with tightly closed caps. The temperature was increased at the rate of approximately 5 K/min. Actually, TOGs show a typical gel–sol transition upon the heating up to 70 °C (Figure 4-8a). On the other hand, no phase transition or morphological change was observed in SOGs at 70 °C and up to 140 °C, even if the concentration of the original polymer solution was a fourth of that used for TOG (2.5 and 10 mg mL^{-1}, respectively). PPEs are completely insoluble in methanol, and that is one of the advantages of SOG over TOG as it makes SOGs thermally insensitive, which is an advantage to use SOG gels.

It is found that gel infiltration is possible with SOGs but not with TOGs. When an ionic liquid (IL, tributylmethyl-ammoniumbis(trifluoromethanesulfonyl)imide) was injected into the TOG, phase separation occurred, resulting in the collapse of the gels (Figure 4-9). Note that the IL can be dissolved in pure THF. This phase separation was probably caused by incompatibility of the IL and the dissolved polymer solution, not the THF. In the case of SOG, such a phase separation was not observed and ion gel formed by evaporating the methanol.

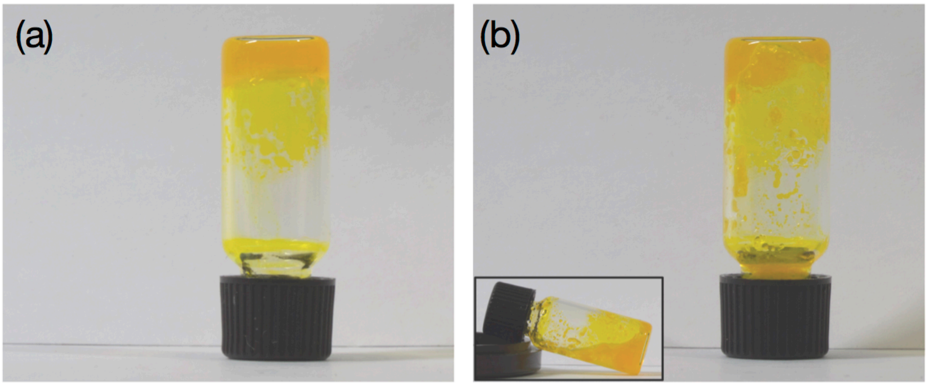

Figure 4-9. Photographs of Inverted gel of 10 mg/mL of TOG before(a) and after(b) injection of ionic liquid. Inset shows image of tilled vial after injection of ionic liquid.

Ion gels are well-known to be useful for organic devices, [75,76] and conjugated polymer ion gels have been reported. [77] However, they are assisted by gel templates such as silica precursor tetraethyl orthosilicate (TEOS) and not created directly. Pure conjugated polymer ion gels (π-ion Gels) are unknown. This ion gel shows great stability from evaporation owing to the negligible vapor pressure of IL, whereas TOG and SOG shrink soon due to the evaporation of inner solvent (Figure 4-8b). Moreover, the π-ion Gel does not show any thermogravimetric change in a TGA experiment (Figure 4-8c), indicating that the gels is never drying. These ion gels can be useful for organic devices and have a great advantage of flexibility. Hence, such a stable SOG and π-ion Gels may open a new way to approach next-generation devices. The applications are shown in next two chapters.

4.7 Short Summary of the Chapter

It is shown that PPEs form - dependent on concentration or side chain - fairly stable gels either by thermal and-better-by solvent induced gelation. The latter one gives mechanically stable gels at considerably lower concentrations and without any dissolved polymer residues in the pores. It was clarified that the obtained gel by solvent induced gelation contains more than 90% of methanol. This plays a crucial role for the thermal stability and gel's compatibility to ionic liquids. As a result, π-conjugated gels containing an ionic liquid (π-ion gels) successfully formed for the first time as far as we know. The parts of contents involving figures, tables, and text are reprinted with the permission of *Copyright © 2017, American Chemical Society.* [78]

5 LEC Application of PPE π-ion Gels

5.1 Motivation

In Chapter 4, The insights about the gelation of PPEs are discussed, leading to the formation of π-ion gels. These state of art configurations are of interest for organic electronics. In this chapter, π-ion gels are applied to light-emitting electrochemical cells (LECs).

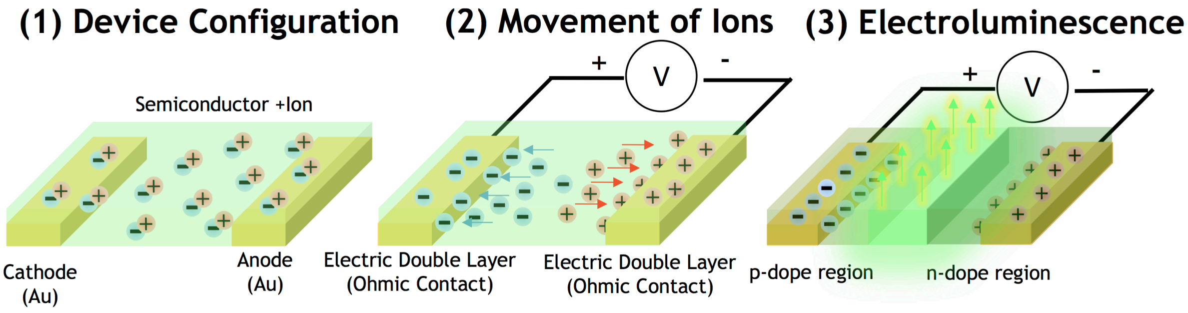

Figure 5-1. Schematic images of the working mechanism of LECs. Green: semiconductor; Grey: Ion conductor; Yellow: gold contact; plus and minus: cations and anions.

Light-emitting electrochemical cells (LECs) are light-emitting devices, but different from OLEDs for the following points. [79-81] OLEDs require thin films and typically two different energy levels of electrodes, whereas thick active layers and two stable electrodes such as gold are possible in LECs. Theoretically, the required voltage of LECs is as small as the band gap, which is lower than that of OLED. Moreover, the thickness of the active layer of an LEC can be on the µm to mm scale compared to the few tens to hundred nm required in OLEDs. [82] However, the response speed of LECs is much slower than that of OLEDs and this is the reason why LEC is rarely applied in displays. The working mechanism of LEC is the following: a mixture of ionic species and a semiconductor is prepared (Figure 5-1a). When the voltage is applied, ions dissociate and move to corresponding directions and form electric double layers on each interface, which allows for ohmic contacts (Figure 5-1b). When the interface is ohmic contact, carriers pass through as a tunnel current. This does not happen in OLEDs, where the interface between semiconductor and metal contacts is the Schottky contact. As a result, p-doped and n-doped regions invade gradually and carrier recombination occurs in between p-/n- regions. Here, it is well known that ion mobility plays a key role in response time of devices.

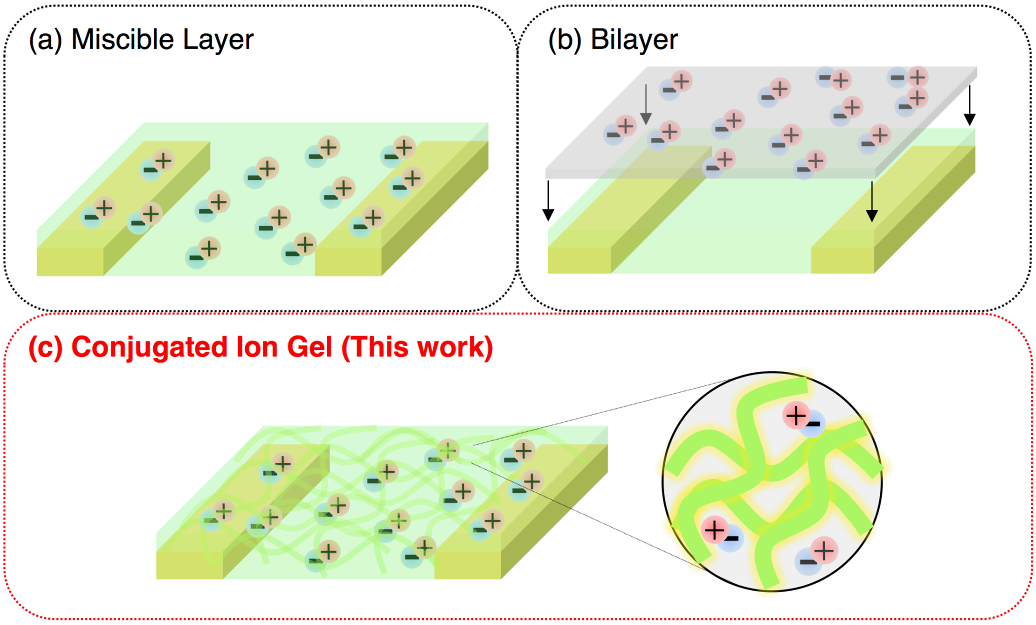

Figure 5-2. Illustrations of two types of LEC devices including, (a) a miscible active layer (b) and a bilayer. (c) Schematic illustration of concept to employ conjugated ionic gels in this work. Green: semiconductor; Grey: Ion conductor; Yellow: gold contact; plus and minus: cations and anions.

There are two types of LECs known, the miscible layer type (Figure 5-2a) and the bilayer type (Figure 5-2b). The layer of the former type contains ionic species and as a homogeneous solute the semiconductor. [79,83] A very large interface results between the semiconductor and the IL, which enables efficient doping but disturbs the bi-continuous conduction paths of ions and charge carriers, delaying the response time of the LEC. In some LEC devices, the electric double layer forms only after several tens of seconds. [80] Decreasing the response time is a challenge if the LECs are employed in display applications. The situation is different for the bilayer type (Figure 5-2b). When the ionic layer and the semiconducting layers are separated, the transport of the ionic species are achieved, which results in high ion conductivities. [84] There, the disadvantage is that the ions have to penetrate into the active layer, which can be prevented by the impermeability of the active layer. This might limit the carrier injection due to its localization of the IL to the contact line. The concept highlighted here combines the advantages of both schemes (Figure5-2c). a gel of a conjugated polymer with an IL as an active layer in LEC devices. There are two purposes behind this idea. 1. The gel fibril network creates a volume filling interface between the conjugated polymer and the IL. 2. At the same time a well segregated nano-structure exist in which the continuous IL and semiconductor networks coexist. High doping efficiency as well as improved response time are expected.

5.2 LEC Device Fabrications

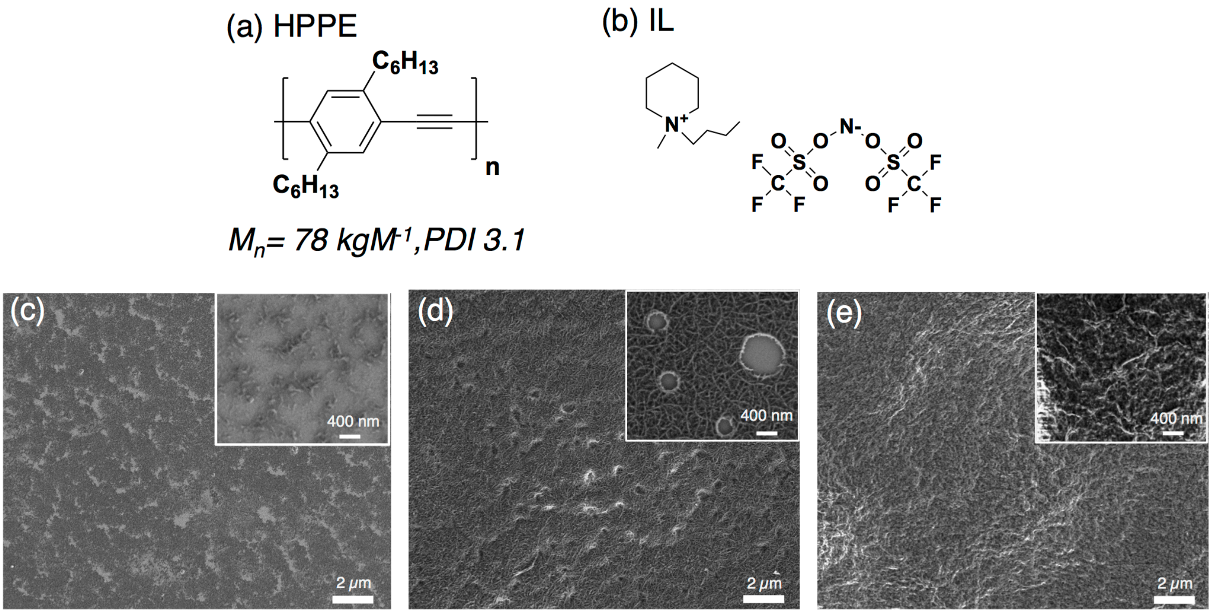

Figure 5-3. Molecular structures dihexyl-PPE and IL in this study. Mn and PDI show the number-average molecular weight and polydispersity, respectively. SEM images of (c) a SP device, (d) a DF device and (e) a gel device after removal of IL by washing process with ethanol.

Dihexyl-(poly(para-phenyleneethynylene)) (PPE) forms gels through a solvent exchange from tetrahydrofuran to methanol. [78] The PPE does not precipitate out when the exchange is performed slowly, but forms gels. In the second step methanol is exchanged with an IL under perfect solvent exchange. As IL, 1-butyl-1-methylpiperidinium bis(trifluoromethanesulfonyl-)imide was used. The gel device (gel) was prepared by gelation of the PPE on substrates with pre-fabricated finger electrodes, and subsequent infiltration of the IL as described above. Reference LECs were also prepared, using spin-coated layers (SP) and devices formed from drop cast films (DF), which are fabricated from a mixture of PPE and IL as joint solution in tetrahydrofuran. The detailed fabrication process is described in Appendix. The SEM micrographs of the dihexyl-PPE after removal of IL in each device type are shown in Figure 5-3c-e. As it is difficult to put an IL into an SEM chamber, the samples were washed with Ethanol to remove the IL before performing SEM observation. The SP displays a sub-micrometer scale phase separation and the DF displays sub-micrometer holes. We believe that these empty spaces were filled with IL, which was washed away, because the incompatibility and the insolubility of the dihexyl-PPE in IL. This problem is already known and the reason why only very few conjugated polymers (e.g. super yellow) are applied in classic LECs. [85,86,87] The gel displays a nano-segregated porous sponge structure without any large-scale phase separation due to the preparation method of the gel. The DF also displays a fibril-type structure on the surface of the polymer film, but the intercalated IL, forming an PPE / IL interface, is much less than in the gel because of the strong segregation of IL.

5.3 Functions of LEC Devices

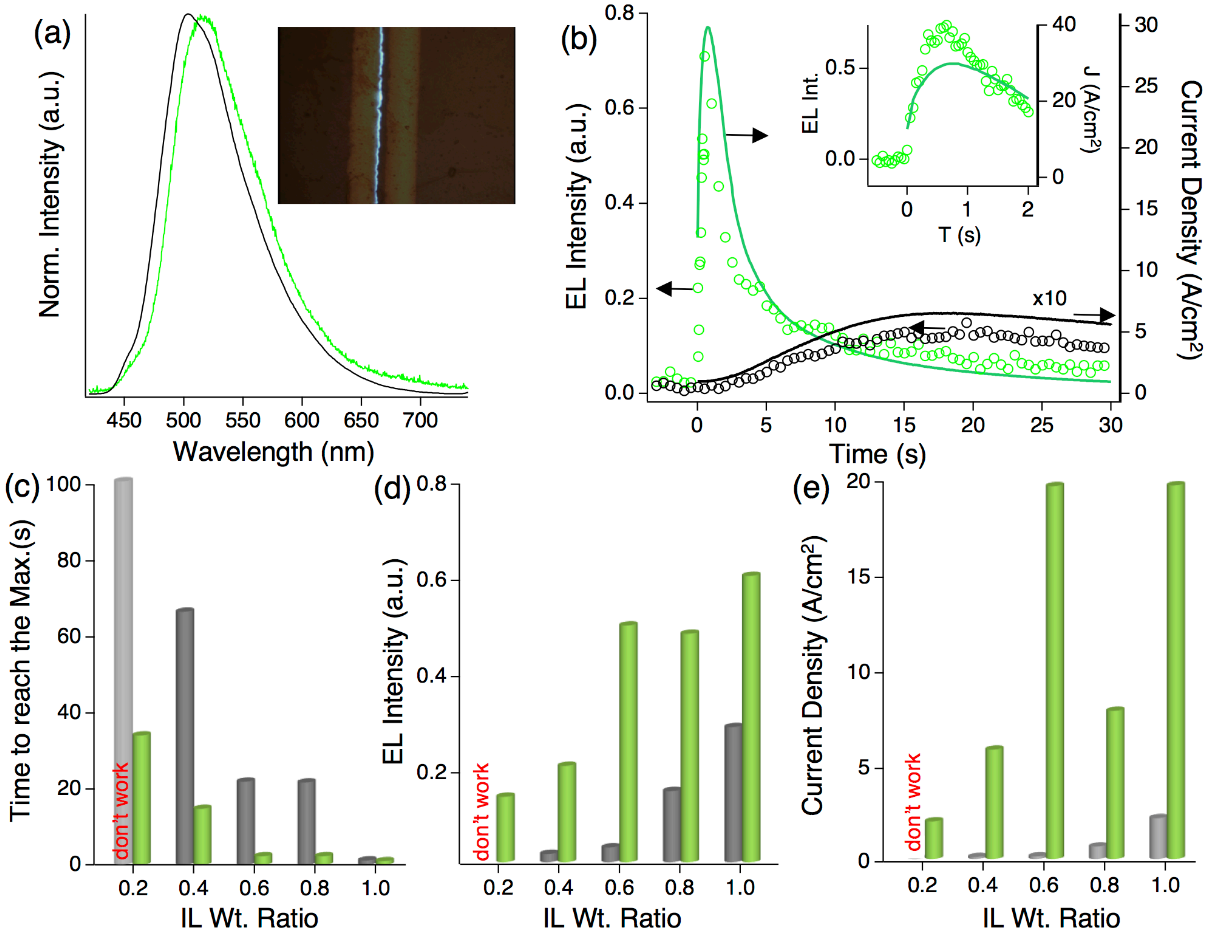

Figure 5-4. (a) Photoluminescence (black) and electroluminescence (green) spectra of a gel device. Inset shows optical image of electroluminescence. (b) EL intensity (dot) and current density (solid) as a function of time. Green and black show gel and DF, respectively. Inset shows the turn-on behavior within 0-2 s time to reach the maximum luminance(c), EL intensity(d) and maximum current density (e) as a function of IL ratio (the amount of conjugated polymer is fixed). Green and black show gel and DF devices, respectively.

Table 5-1. Values of Response time, EL intensity, current density and lifetime as a function of gel and CF devices.

	Turn-on time	Luminance	Current Density	Lifetime
gel $_{1.0}$	0.87 s (±0.21 s)	0.59 (±0.08)	19.47(± 8.0) A/cm^2	23.3 (±2.9) s
DF $_{1.0}$	1.05 s	0.28	2.13 A/cm^2	22.6 s
gel $_{0.8}$	2.03 s (±0.12 s)	0.48 (±0.29)	7.72(±0.38) A/cm^2	68.1 (±21) s
DF $_{0.8}$	19.53 s	0.14	0.65 A/cm^2	58.5 s
gel $_{0.6}$	2.03 s (±0.34 s)	0.49 (±0.16)	19.4(±11.4) A/cm^2	52.3 (±17) s
DF $_{0.6}$	19.73 s	0.03	0.13 A/cm^2	>100 s
gel $_{0.4}$	13.28 s (±3.98 s)	0.20 (±0.0)	5.7(±10.1) A/cm^2	>100 s
DF $_{0.4}$	> 100.0 s	0.02	0.10 A/cm^2	>100 s
gel $_{0.2}$	30.68 s (±6.33 s)	0.13 (±0.03)	1.96(±0.11) A/cm^2	>100 s
DF $_{0.2}$	> 100.0 s	0	0 A/cm^2	-

The electroluminescence spectrum of the gel-LEC is identical to its photoluminescence spectrum. (Figure 5-4a). The SP device does not work at all for PPEs due to the incompatibility of the PPE and the IL. [85] Figure 5-4b shows electroluminescence intensity and current density of gel and DF devices over time with an IL amount of 80% under a bias of 5 V. The electroluminescence intensity was recorded by a photodiode. The linear emission area is unknown and difficult to estimate because of the device configuration (Figure 5-4a, inset). Therefore, the determination of the absolute value of the emission intensity is not possible. The DF device displays a very slow increase in intensity and current density. It takes around 15 s for this device to reach the emission and current maxima, which is the typical switch-on time for LEC devices. [80] The maximum in the current and EL time dependency are correlated rather to the interplay between the switch-on behavior of the LEC and its degradation. The latter is related to the weak stability of the PPE. [54] In contrast to the DF device, the gel device turns on in 0.7 s to reach the maximum in emission brightness and current. The decreased switch-on time most likely results from the accelerated degradation due to the higher current densities. As seen in Fig. 5-4b the first appearance of EL of the gel device is much sooner than switch-on times for the DF devices. Thus, the electrical double layers and the doping must occur even faster than the stated 0.7 s. This will be highlighted in a later paragraph (Figure. 5-9). The switch-on behavior (Fig. 5-4b) therefore reflects therefore rather the development of the pn-junction; the gel films allow for a more efficient doping and/or charge transport than DF films. Figure 5-4c-e and Table 5-1 summarizes the time to reach the maximum luminance(c), electroluminescence intensity (d) and maximum current density(e), as a function of the ratio of IL to dihexyl-PPE (the amount of PPE is fixed). Detailed results are also summarized in FIgureA5-1. The gel devices always display faster response, higher EL intensity and current density than DF devices. A higher percentage of IL liquid results in smaller response time, higher electroluminescence intensity and current density. Due to the increasing current with increased IL content the amount of IL was not increased more than 1 weight ratio.

5.4 Step-Bias Measurements of LEC Devices

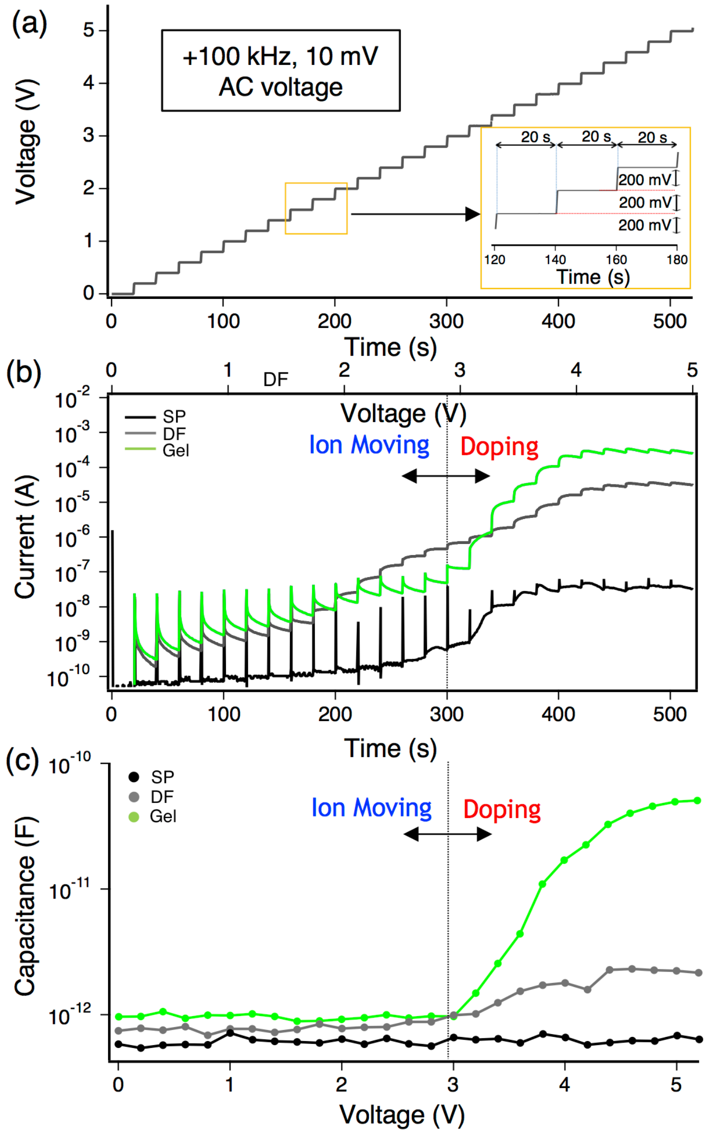

Figure 5-5. (a) Applied step DC voltage as a function of time. (b) DC current under the step DC voltage of SP (black), DF (grey) and gel (green) devices with 0.8 wt ratio of IL. (c) AC Capacitance under the step DC voltage of SP (black), DF (grey) and gel based (green) devices. The dotted line indicates the change from the region dominated by ion conduction to the region where doping and charge transport dominate the current quantity.

The obtained parameters suggest that efficient doping takes place in gel devices. To gain more detailed insights, step bias experiments are performed. [85] In this experiment, a stair-case bias with a hold time of 20 s and a step voltage of 200 mV is applied. At the same time a small 1kHz AC voltage of 10 mV amplitude is applied to obtain the device capacitance(Figure5-5a). As shown (Figure A5-4) the response of the ions at that frequency is substantial but DC-bias independent. A DC current-time graph (Figure 5-5b, Figure A5-3) displays two different regions, one region where ions move, and a doping region. At low biases, the current follows a typical charging current increasing as soon as the bias step appears and subsequently decaying exponentially. This behavior relates to the development of an electrical double layer, since it is likewise observed when only IL is electrically tested (Figure A5-2). Apparently, in an LEC only the ions can respond at that DC bias. The gel devices display a higher current than SP or DF devices, indicating an efficient movement of ions in the gel devices. When the voltage increases above the band gap of the employed semiconductor, efficient injection *via* the electric double layer occurs, resulting in significantly increased DC currents. This increase starts at a threshold voltage of 2.8V close to the band gap of dihexyl-PPE (2.75 eV). Consequently, p-, n- doping starts above 2.8 V, and the doped regions will grow with increased bias. This behavior is mirrored in the capacitance-voltage dependency (Figure 5-5c), too. The development of p- and n- doped regions narrows the intrinsic region of the semiconductor, increasing its capacitance. The increase in the device capacitance therefore also starts at 2.8 V as well. Once p-, and n- doped regions develop, the gel device has a capacitance one order of magnitude higher than that of the DF or SP devices, indicating that the doping is increased for the gel device-as concluded from Figure 5-4. It is also visible in the current values in the range of 3-5V (Figure 5-5b). The dramatically improved doping efficiency is assigned to the larger interface between the gel fibers and IL and to the µm-scale segregation of IL in the DF film. The large interface supplies the ions required for electric dou-ble layer formation and subsequent doping.

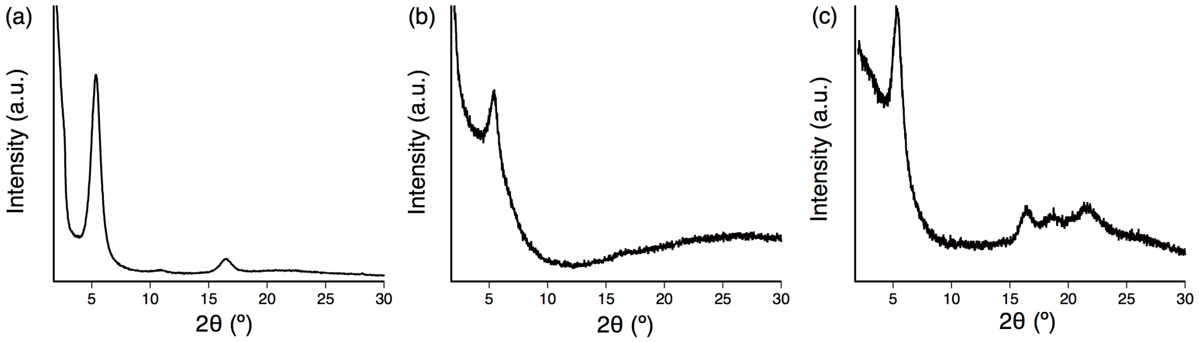

Figure 5-6. XRD patterns of (a)DF, (b) SP and (c) gel devices, respectively., 16.47~16.5 Å and 5.29~5.42 Å correspond to the lamella packing, while 4.10 Å in (c) corresponds to the perpendicular packing such as π-stacking.

Note that only gel films display a π-stacking-like signal in XRD patterns (Figure 5-6). Thus, the improved molecular packing of the PPE might also lead to better charge-carrier transport properties of the gel compared to that of DF or SP devices.

Surprisingly, the behavior in the step voltage experiment is independent on the time duration of the step. If a constant voltage is applied for 40 s or 60 s, only a minor difference in current is observed far above the threshold voltage (Figure 5-7) which is caused by degradation. The capacitance is independent of the hold time at a constant voltage.

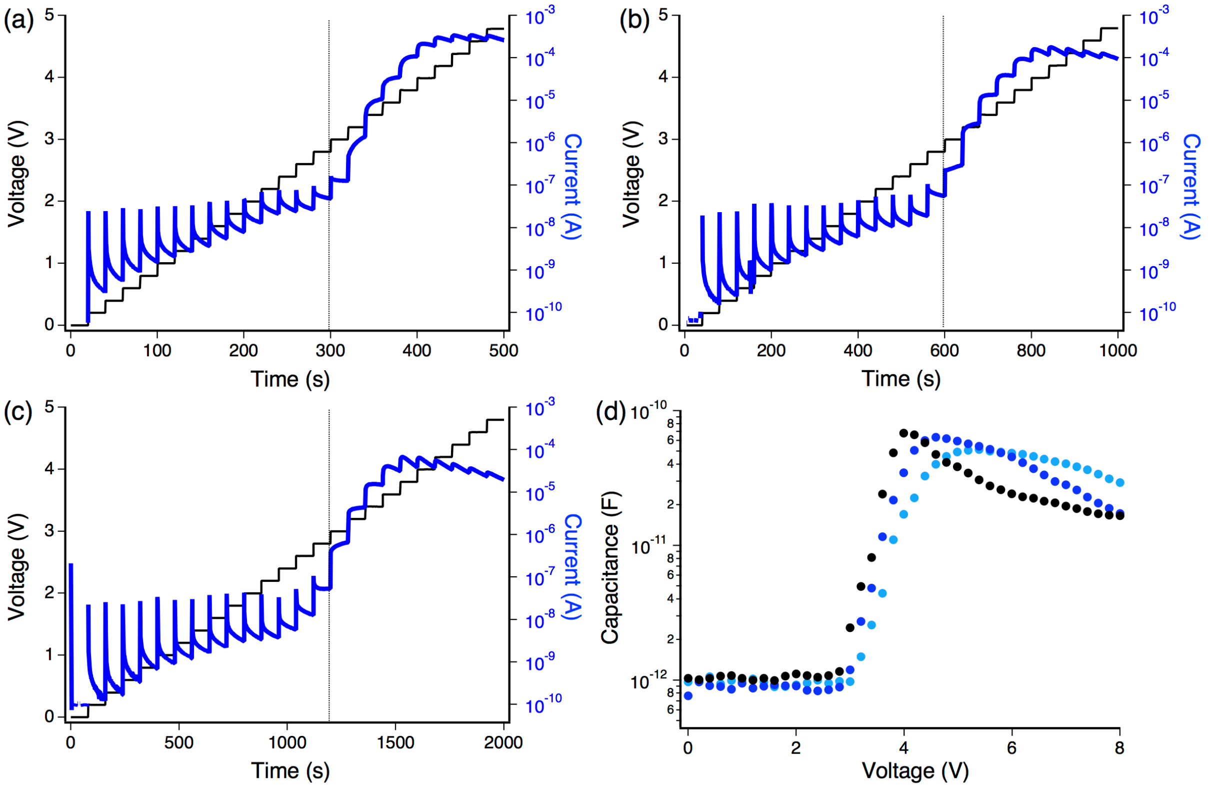

Figure 5-7. Current and applied voltage of gel $_{0.8}$ as a function of time in cases of that constant step voltage is applied for 20 s (a), 40 s (b) and 60 s (c)Dot line shows turning point of current shape. Capacitance as a function of applied voltage in cases of that constant step voltage is applied for 20 s (light blue), 40 s (blue) and 60 s (black).

The amount of IL in the gel devices dis-plays a ratio of 20% (gel$_{0.2}$), 40% (gel$_{0.4}$), 60% (gel$_{0.6}$), 80% (gel$_{0.8}$) and 100% (gel1.0 containing 50% IL and 50% PPE) with a fixed amount of PPE. Except for gel$_{0.2}$, surprisingly, all of the gel-devices also show similar results on the current and capacitance values and thresholds (Figure 5-8). With enough amount of IL i.e. more than 20% (which corresponds to 13 mol% ratio to single unit of PPE or 89.7 µL cm^{-2}) and sufficient time, all of the gel devices work equally well. The amount of IL then only affects the kinetic parameters of the device.

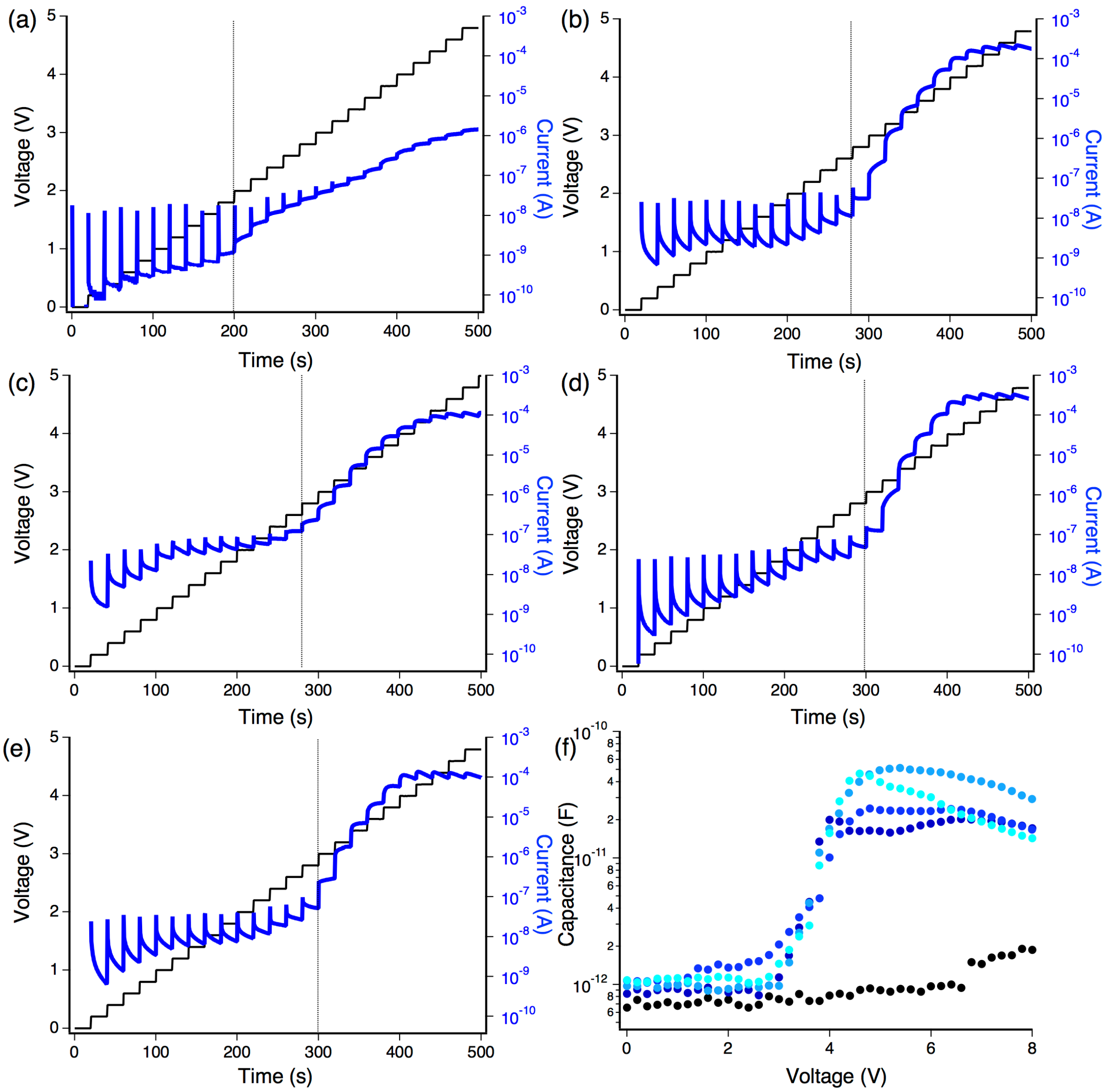

Figure 5-8. Current and applied voltage of gel$_{0.2}$ (a), gel$_{0.4}$ (b), gel$_{0.6}$ (c) gel$_{0.8}$ (d) and gel$_{1.0}$ (e) as a function of time. Dotted line shows turning point of current shape. (f) Capacitance under the step voltage as a function of IL ratio (from 0.2 to 1.0, black to light blue).

Contrary to that, DF or SP devices display IL-concentration dependent characteristics. The ratio of IL to dihexyl-PPE strongly affects phase segregation and therefore the device characteristics. The gel devices on the other hand are prepared by a templating technique (Appendix). For the gel devices, the phase segregation is predetermined by the prior gelation, before infiltrating the IL. This two-step preparation technique therefore gives devices with highly reproducible characteristics.

5.5 Impedance Measurements of LEC Devices

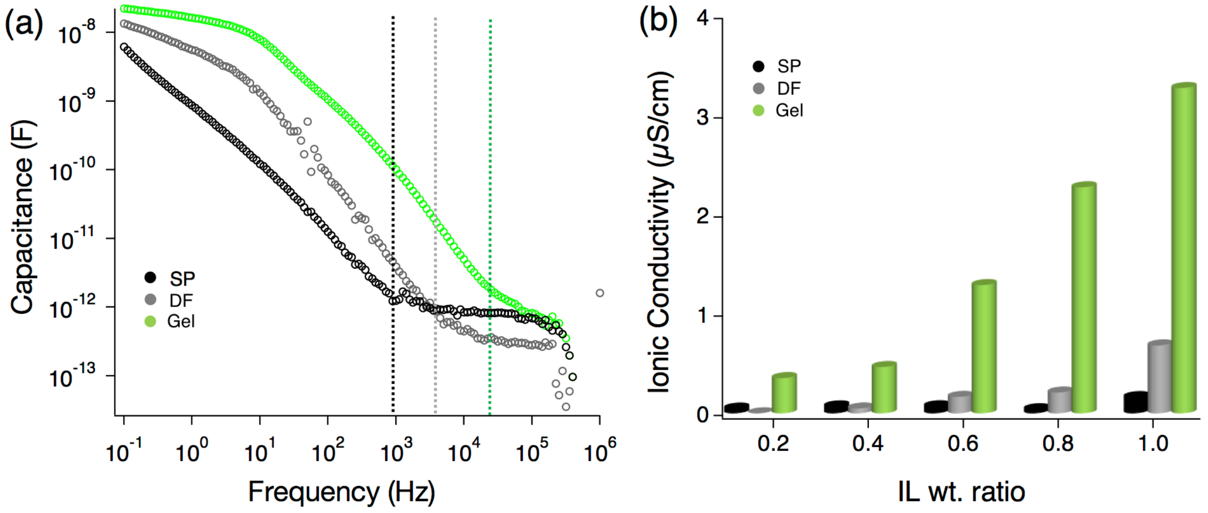

Figure 5-9. (a) Capacitance as a function of frequency of SP (black), DF (grey) and gel (green) devices at the constant voltage of 0 V to observe ion mobility only. The dotted lines display the depletion points. (b) Ionic conductivity estimated by fitting of the equivalent circuit given in the SI to the frequency dependent complex impedance. (detailed results: Figure. S9-S11, Table S2-4). Grey, black and green show SP (black), DF (grey) and gel (green) devices.

To gain insight into the kinetic parameters, we performed frequency dependent impedance measurements; a 100 mV AC voltage without DC voltage was applied for the measurements. Under these conditions, doping does not take place, and only the ion movement is observed.

When the ions respond as fast as the applied frequency of the AC voltage, the capacitance should increase due to the formation of the double layers. The capacitance of a gel devices rises below ~100 kHz and saturates around 1-10 Hz, whereas those of the DF or the SP devices only increase at frequencies below ~ 1 kHz and do not saturate (Figure 5-9a). Those results show that the ions in the gel device respond much faster than the ions in the other devices. Moreover, the shapes of the capacitance – frequency curves of the gel devices are all similar and shift, depending on the ratio of IL to dihexyl-PPE (see Figure5-11).

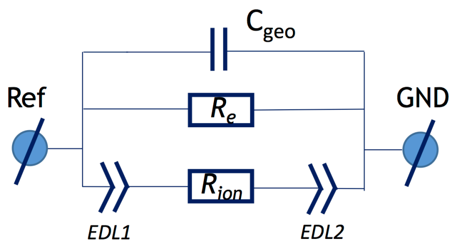

Figure 5-10. Employed equivalent circuit

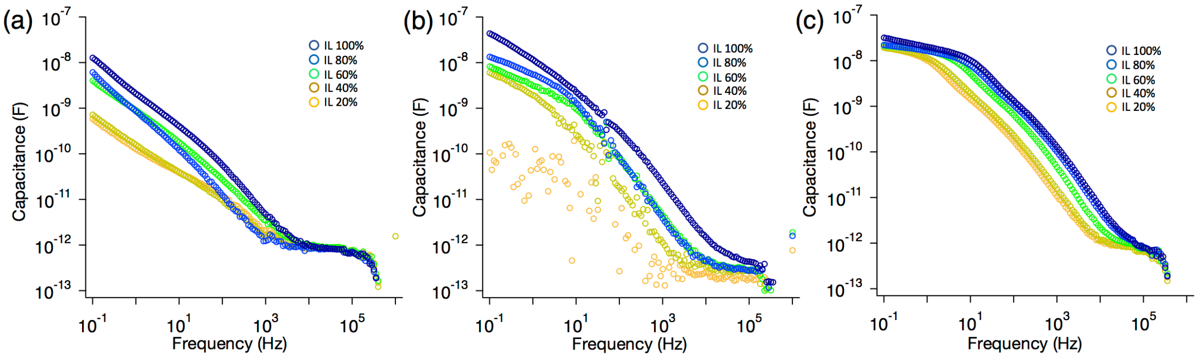

Figure 5-11. Capacitance as a function of frequency of SP (a), DF (b) and gel (c) with the constant voltage of 0V. Dark blue, blue, green, dark yellow and yellow show IL ratio of 1, 0.8, 0.6, 0.4 and 0.2, respectively.

The equivalent circuit shown in Figure 5-10 is employed as a model for the LEC devices to perform a theoretical fitting to obtain the ion-conductivity. [88] Fitting results are shown in Figures A5-5,6,7 and Tables A5-2,3,4. As seen in Figure 5-9b, the ionic conductivity of the gel devices is around one order of magnitude higher than that of DF and SP devices. Therefore, one can conclude that the appearance of first EL is indeed by orders of magnitude faster than in the DF and SP devices. The well-segregated gel structure ensures that the ionic charges can move freely towards the counter elec-trodes without being blocked by the semiconductor phase. Note that Heeger and Yang et al. employed a similar strategy to improve the response time. They employed a surfactant to make a Nanoscopically segregated active layer. [89] As a result, they achieved a response time of 50 ms for a 10-100 nm thin stacked layer. Here, it is demonstrated that a π-gel is a potent material that can self-organize into a similar system. With a sub-second response time for an electrode spacing of 40 μm, the gel performs even better.

5.6 Short Summary of the Chapter

A conjugated polymer gel based on a dihexyl-PPE is applied as active material in an LEC. The efficiently nano-segregated structure of the gel phase allows for an LEC that responds quickly, is bright and displays much lower resistance than similar devices obtained by drop cast or spin cast techniques. There are two main benefits to the gel phase: the nano-segregated structure dramatically increases the inter-face between the conjugated polymer and ionic liquid, but at the same time ensures that the ions can move freely through the open framework, i.e. allows for the counter ions to percolate. This concept should be easily transferred to other π-conjugated molecules, as long as they form gel phases from methanol as solvent, as the methanol can be easily exchanged for an ionic liquid.

6 Transistor Application of PPE π-ion Gels

6.1 Motivation

An application of π-ion gels to the light-emitting devices was demonstrated in the last chapter. The intrinsic structure of π-ion gels plays an excellent combination with the LECs and overcomes the turn-on time. It should be emphasized that it is not the only possibility of applications of π-ion gels. Here, the concept is transferred to the organic transistors.

Organic field-effect transistors (OFETs) have been of interest as components of flexible electronic circuits. [4,41] A variety of device configurations has been explored. For example, the positions of contacts and gate are optional (top or bottom). The thickness, the distance, and the width of devices are also important parameters. As dielectric materials, inorganic materials (SiO_2, Al_2O_3…), polymers (Parylene, Polyimide…) or electrolytes are available. The dielectric layer is one of the most important parameters because the device output and the quantity of induced charge carriers depend on the dielectric constant of the material; a higher dielectric constant increase drain current.

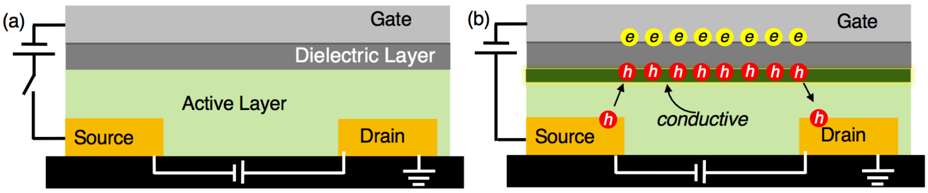

Figure 6-1. The working mechanism of OFETs.

In any type of devices mentioned above, the carrier transport takes place at a few layers of the boundary between a dielectric layer and an active layer (Figure 6-1). [90] This means that the rest of the active layer and contact thickness do not matter for the device mobility as long as the charge carriers can be injected into the active layer. The hole mobility of the OFET in the saturated regime is described as eq. 6-1 (same as eq. 2-10.)

$$\mu_{hole} = \frac{2L}{C_{2D}W}\left(\frac{\partial\sqrt{I_D}}{\partial V_G}\right)^2 \qquad (\text{eq.}\,6-1)$$

whereas μ_{hole}, L, W, C_{2D} indicate the hole mobility, the channel length, the channel width, and the capacitance per area, respectively. I_D and V_G are the drain current and the gate voltage. In eq.6-1, the channel thickness does not matter for the hole mobility. For this reason, interface engineering is emphasized. [90]

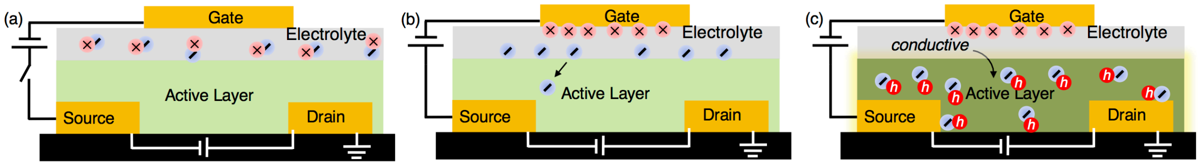

Figure 6-2. The working mechanism of OECTs.

Organic Electrochemical Transistors (OECTs) are an exception to this rule. [91-94] Although the device configuration of OECTs is the same as bottom-contact top-gate transistors with a dielectric layer of electrolytes (Figure 6-2a), the working mechanism differs. Once the gate bias is applied, ions pierce the boundary and penetrate the active layer (Figure 6-2b). As a result, the whole layer is electrochemically doped (Figure 6-2c). In this case, the conductivity is not limited to the interface, but a volumetric current flows through the whole channel. In other words, High gain transistors can be obtained simply by increasing the contact thickness. The hole mobility of OECT is defined as, [95]

$$\mu_{hole} = \frac{2Ld}{WC_{3D}}\left(\frac{\partial\sqrt{I_D}}{\partial V_G}\right)^2 \qquad (\text{eq. } 6-2)$$

Where μ_{hole}, L, W, d, C_{3D} indicate the hole mobility, the channel length, the channel width, the channel thickness, and the capacitance per volume, respectively. I_D and V_G are the drain current and the gate voltage. Especially, $\partial I_D / \partial V_G$ is called transconductance as an important parameter of OECTs. The current (transconductance) is tunable by the thickness. This is advantageous to integrate the transistors in a limited space. However, the turn-on time of OECTs is a problem as it takes several seconds. One of the reasons why high gain transistors are in demand is to get fast signals so this issue is serious. McCulloch et al., successfully engineered side chains of P3HT derivatives to give compatibility to the ions by replacing alkyl chains to ethylene glycol, resulting in dramatically shortened response time (< 1ms). [93] Yet, accelerating the response time is still challenging.

In this chapter, a new type configuration of transistors, named π-ion gel Transistor (PIGT), is suggested. π-ion gels are state of art materials that comprises nanofiber networks of a π-conjugated polymer and an enclosed ionic liquid as shown in the last two chapters. Both a conjugated polymer and an ionic liquid are continuous, so that π-ion gels are not only electrically, but also ionically conductive. The π-ion gel is employed as an active layer and also an internal gate capacitor; the coexisting ionic liquid works as a surrounding gate to every single semiconducting fiber and gives conductivity. PIGTs display a volumetric current with a high on/off ratio (~10^5). The intrinsic structure of the device allows for a response time faster than 20 μs, which is the fastest among electrochemical based transistors.

6.2 The Configuration and the Mechanism of π-Ion Gel Transistors

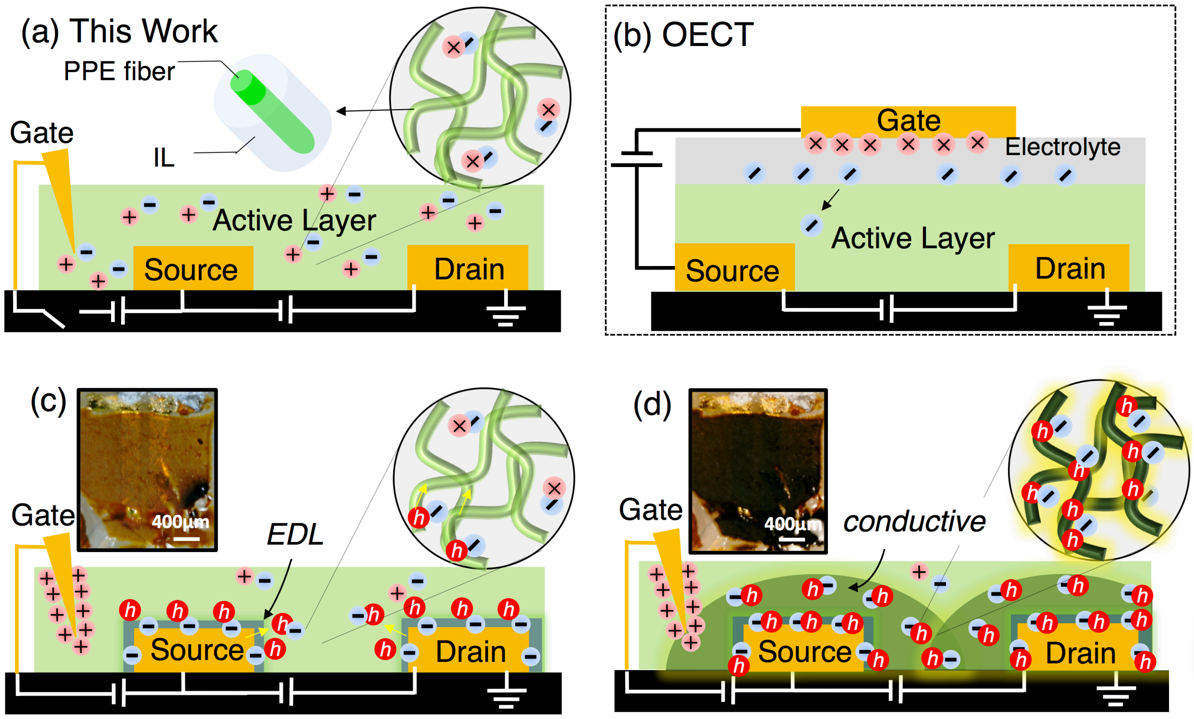

Figure 6-3. The Device configurations of PIGTs (a) and OECTs (b). When a positive bias is applied to the gate, anions accumulate on the interface of contacts and form electric double layers (c). The p-doing lasts until the whole active layer doping is accomplished (d). Insets in (c, d) show the visible appearance of undoped and doped transistors.

Here, the device configuration and the most likely possible mechanism is explained (Figure6-3). The device was prepared by a similar method with gel LEC devices. The PPE, Dihexyl-poly(para-phenyleneethynylene), formed supramolecular gel by a solvent exchanging method on the substrate with pre-fabricated finger contacts. A given amount of IL, (1-butyl-1-methylpiperidinium bis(trifluoromethanesulfonyl-)imide), was infiltrated to the gel. After the evaporation of the solvent, the resultant π-ion gel was obtained. By putting an external needle gate, a fabrication process of the transistor was done. The detailed fabrication process is shown in the Appendix. The nature of gelation allows for the nano-segregated bicontinuous structures of conjugated fibers and a surrounding ionic liquid to coexist. π-ion gels are employed as active layers in transistors. At the same time, the intercalated IL works as an internal gate. Once the gate needle is negatively biased, inner cations respond to the gate and inner anions move to the two contacts, respectively. At the boundary of the contacts and the π-ion gel, electric double layers form, allowing for ohmic contacts (Figure 6-3b). The ohmic contacts induce a p-doing and the doped region is compensated and stabilized by an excess number of anions. The p-doping starts at the contact and gradually expands until the doping in the whole layer is accomplished (Figure 6-3c). Therefore, volumetric conductivity is expected as seen in OECTs. The Channel configuration is defined as shown in Figure 6-3d. This doping process is evident from the appearance of doped devices; the whole active layer turned black (Figure 6-3, insets).

6.3 Nano Structure Observations

Before heading to the device properties, the insights about nano-scale structures are discussed.

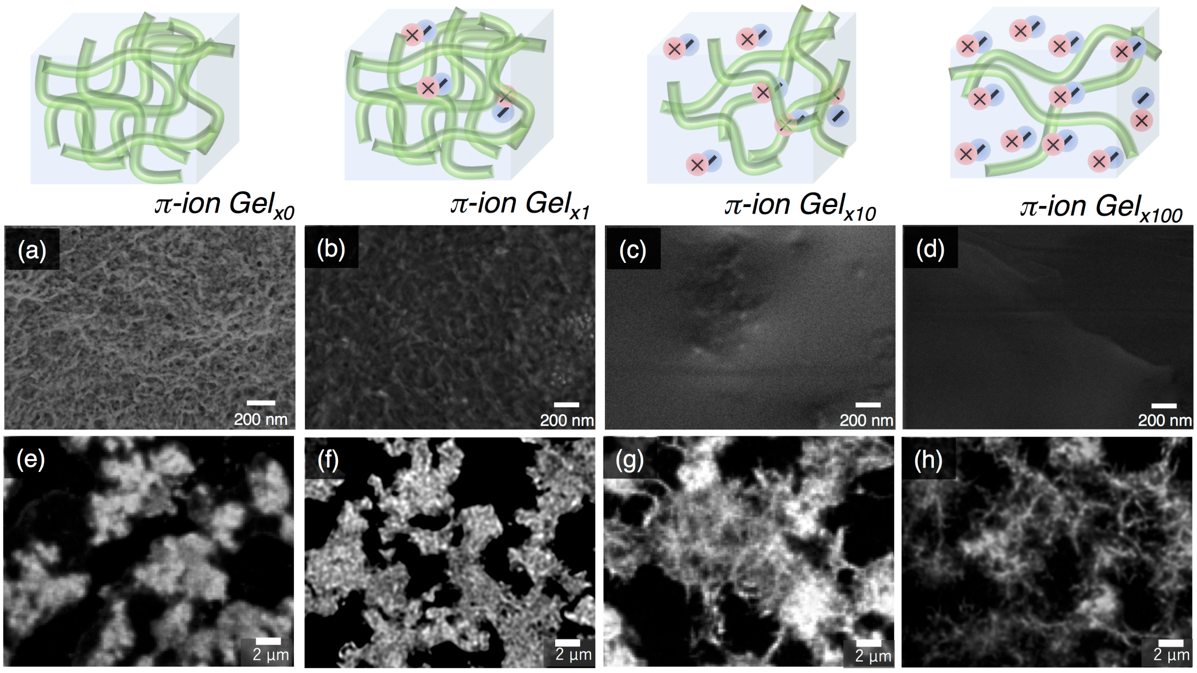

Figure 6-4. The SEM micrographs of π-ion gel $_{x0}$ (a), π-ion gel $_{x1}$ (b), π-ion gel $_{x10}$ (c) and π-ion gel $_{x100}$ (d). The Confocal fluorescent micrographs ofπ-ion gel $_{x0}$ (e), π-ion gel $_{x1}$ (f), π-ion gel $_{x10}$ (g) and π-ion gel $_{x100}$ (h) taken by Mr. Taishi Kanamaru.

π-ion gels with 4 different wt. ratios of IL were prepared and compared. According to the amount of the IL, the gels are called π-ion gel $_{x0}$ (IL wt. ratio to PPE is 0), π-ion gel $_{x1}$ (IL wt. ratio to PPE is 1), π-ion gel $_{x10}$ (IL wt. ratio to PPE is 10), andπ-ion gel $_{x100}$ (IL wt. ratio to PPE is 100), respectively. Even when the IL wt. ratio to PPE is 100, the gel geometry persists. It is amazing nature that only 1% PPE encloses 99% of the IL. Note that spin-cast or drop-cast techniques cannot access such a continuous film with the same ratio of contents because 99% of the solute is a liquid. [96] First, SEM observations were performed. When an IL is not infiltrated, the gel seems like a dried gel which is also observed in chapter 4. Sub-hundred nanometer-thick fibers are observed (Figure 6-4a). When the IL wt. ratio increases to 1, the fibers are still visible with less density (Figure 6-4b), indicating the IL is intercalated between PPE fibers. In the cases of ratios of 10 and 100, just planer surfaces are observed. These are most likely an excessive amount of IL on the surfaces of the gels since SEM detects the surface topology.

To gain insights into inner nano-structures, a confocal fluorescent microscope was utilized. Unfortunately, the theoretical limit of the resolution is 200 nm for this equipment. STED microscopy observation failed due to the wide absorption range of PPE. Nevertheless, there is some information that can be read out. The white parts depict fluorescence from PPE, not IL because the IL is non-fluorescent at the wavelength of 650 nm. Note that the black parts contain not only IL parts, but also the area unfocused due to the high surface roughness of the gel film. In the case of π-ion gel $_{x0}$, only aggregation of PPE is observed due to the high density of the PPE fibers (under resolution). In the cases of π-ion gel $_{x1,}$ π-ion gel $_{x10,}$ and π-ion gel $_{x100}$, the PPE fibers are clearly visible and the spaces between fibers become larger, depending on the amount of an IL. This is an evidence that an IL is intercalated between PPE fibers networks.

6.4 Device Properties

6.4.1 Channel Thickness Dependency -A Proof of the Volumetric Current-

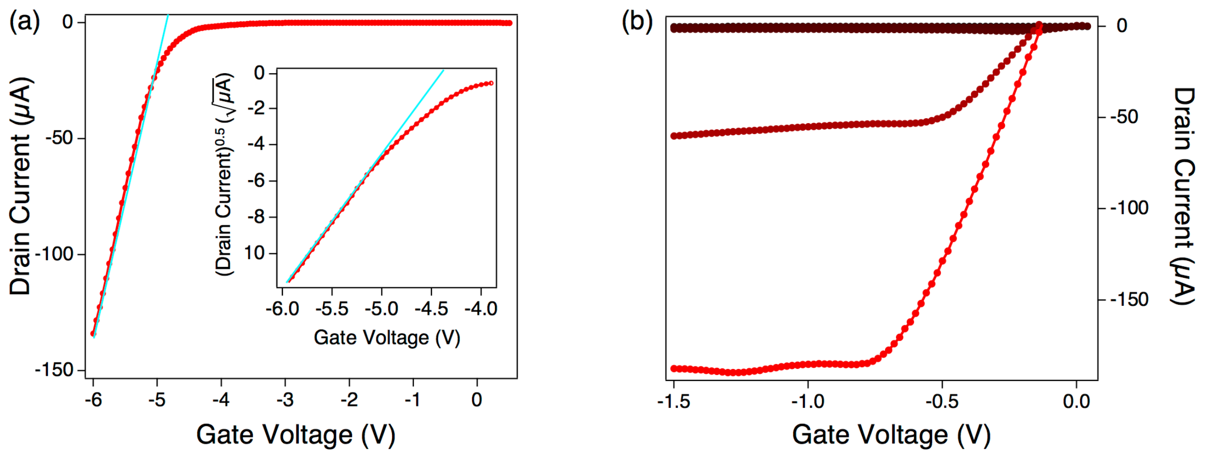

Figure 6-5. A transfer curve of π-ion gel $_{x100}$ with 160 nm thick contacts (a). The inset shows a graph of the square root of a drain current over the gate voltage. The sweeping speed is 0.5 s per 50 mV gate step. An output curve of 160 nm thick contacts(b). The gate voltage is 0V, 4V, 5V, and 6V from black to red. The sweeping speed is 0.1 s per 10 mV drain step.

When the gate is negatively biased, IL containing π-ion gel works as a transistor. Examples of a transfer curve and output curves of π-ion gels $_{x100}$ are shown in Figure 6-5. The threshold is about

V_G = -4V. In the output curve, the current saturation is observed, indicating a steady state. Note that, π-ion gels containing any ratio of IL (except 0) work as transistors although the device performances are affected by many parameters. First, the thickness dependence of the channel contacts is discussed.

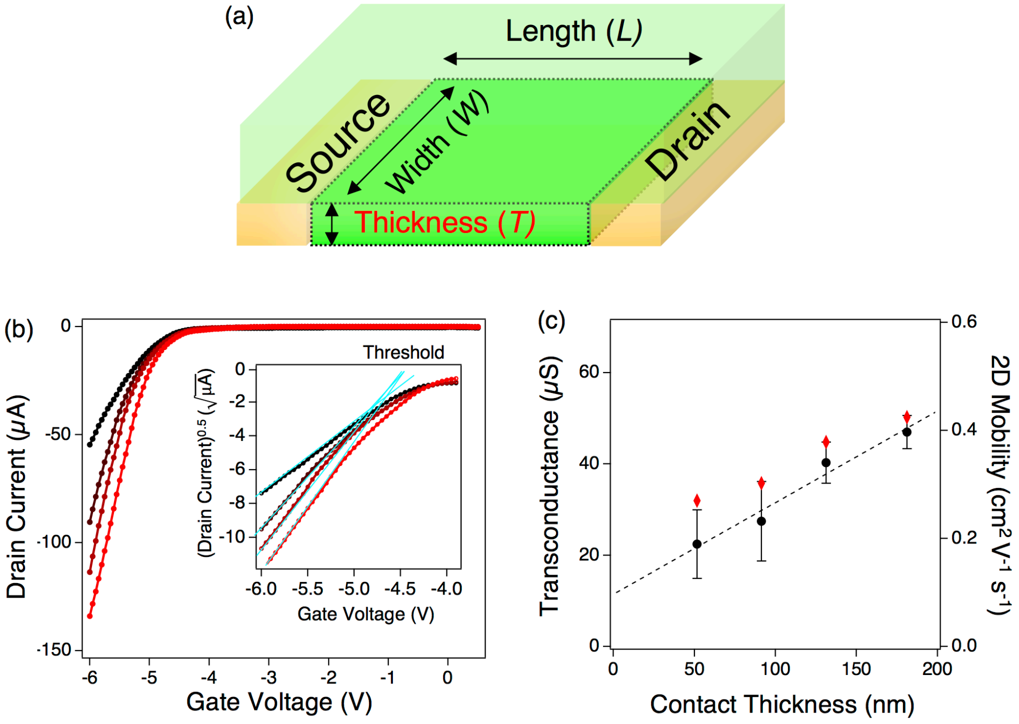

Figure 6-6. (a) The channel geometry. (b) Transfer curves of π -ion gel $_{x100}$ with 50 nm, 90 nm, 130 nm, and 180 nm (from black to red) thick contacts V_D= -1V. Inset shows a graph of the square root of drain currents over the gate voltage. (c) Transconductance and 2D mobilities as a function of the channel thickness. Black dots, red dots and error bars are the averaged values, the maximum values, and the standard deviations resulted from 5 different devices. The dot line shows a linear fit of the averaged values. The sweeping speed is 0.5 s per 50 mV step.

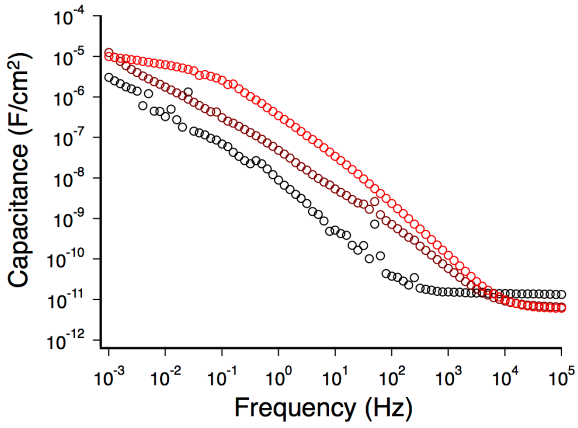

Figure 6-7. Frequency-dependent capacitance per area of π-ion gel $_{x1}$(black), π-ion gel $_{x10}$(dark red) and π-ion gel $_{x100}$(red).

The devices of π-ion gel $_{x100}$ with the different thicknesses of contacts were investigated (Figure 6-6a). At the same time, theπ-ion gels on the planer ITO substrates with different area sizes were applied frequency-dependent AC voltages and capacitance per area was obtained. (Figure 6-7, the detailed data see Appendix). The depletion point of capacitance shifts to a higher frequency when the IL ratio is larger. For example, π-ion gel $_{x100}$ shows a depletion point at 10 kHz and increases up to 100 mHz. The more IL results in higher ionic conductivity as also seen in chapter 5.

Table 6-1. Averaged [maximal] Device Parameters for the Thickness of π-ion gel $_{x100}$

Thickness (nm)	Transconductance (µS)	On/Off Ratio	2D mobility (cm^2/V s)	Current (µA) at Vg = -6
50	22.2 [31.9]	5.6 x10^3 [2.4 x10^4]	0.18 [0.26]	64.0 [74.7]
90	27.3 [35.8]	1.1 x10^4 [1.7 x10^4]	0.22 [0.30]	93.1 [120.3]
130	40.4 [45.0]	1.9 x10^4 [2.3 x10^4]	0.33 [0.37]	130.2 [143.3]
180	47.2 [50.5]	3.7 x10^4 [1.3 x10^5]	0.39 [0.42]	138.6 [169.0]

The parameters obtained by the measurements are also shown in Table 6-1. Overall performances are excellent. Especially, the on/off ratio is in a range of 10^4-10^5 under the low voltage (V_D=-1V V_G=-6V). The drain current increases with the thicker contacts while the threshold is stable (Figure 6-6b). The transfer curves are analyzed and transconductance and 2D mobilities are calculated. Note that the 2D mobility means the parameter that is calculated with the eq. 6-1 based on the OFET mechanism with the capacitance per area. Figure 6-6c tells that there is a linear correlation between the contact thickness and transconductance (2D mobilities), proving volumetric currents through the whole channel as seen in OECTs. It has to be mentioned that if a channel of the device behaves as a volumetric resistance, the mobility should be calculated by using eq.6-2 with the capacitance per volume. Therefore, the 2D mobility does not directly mean the intrinsic property of the utilized semiconductor, but the device property which is amplified by the channel thickness. The volumetric behavior of current is also seen in π-ion gel $_{x10}$ (Figure A6-1).

6.4.2 IL Ratio and Sweeping Speed Dependency

Table 6-2. Averaged [maximal] Device Parameters for the IL ratio

Device	Transconductance (μS)	On/Off Ratio	2D mobility (cm^2/V s)	Current (μA) at Vg = -6
π-ion gel $_{x1}$(fast)	0.02 [0.23]	5.9 x10^{1} [1.2 x10^{2}]	7.3 x10^{-3} [2.8 x10^{-2}]	0.3 [0.5]
π-ion gel $_{x1}$(slow)	0.03 [0.10]	2.1 x10^{2} [3.3 x10^{2}]	1.9 x10^{-2} [6.5 x10^{-2}]	0.9 [2.0]
π-ion gel $_{x10}$(fast)	0.59 [0.98]	1.9 x10^{2} [4.1 x10^{2}]	2.0 x10^{-2} [4.4 x10^{-2}]	2.6 [5.7]
π-ion gel $_{x10}$(slow)	4.10 [6.10]	1.6 x10^{3} [3.7 x10^{3}]	3.4 x10^{-2} [5.0 x10^{-2}]	12.8 [18.9]
π-ion gel $_{x100}$(fast)	22.2 [31.9]	5.6 x10^{3} [2.4 x10^{4}]	1.8 x10^{-1} [2.6 x10^{-1}]	64.0 [74.7]
π-ion gel$_{x100}$(slow)	31.7 [37.7]	3.5 x10^{3} [1.0 x10^{4}]	1.5 x10^{-1} [1.8 x10^{-1}]	76.4 [122.2]

Fast and slow mean 5 s per 50mV step and 0.5 s per 50 mV step.

Next, the influence of the IL ratios was investigated. Table 6-2 summarizes the device parameters of π-ion gels obtained from 5 different devices for each IL ratio. The higher IL ratio results in the excellent device performances such as high transconductance, On/Off ratios, 2D mobilities, and outputs even when the frequency-dependent capacitance is taken in account. Furthermore, the device parameters of π-ion gel $_{x100}$ show almost comparable properties upon a fast sweep and a slow sweep, suggesting a fast response.

Four different kinds of sweeping speeds, (0.1 s per 50 mV step, 0.5 s per 50 mV step, 1 s per 50 mV step and 5 s per 50 mV step) were conducted. The transfer curves are dependent on the sweeping speed (Figure6-8). This is normal because the capacitance of the π-ion gels depends on the frequency (Figure 6-7). According to the eq.6-1 and eq.6-2, the current is proportional to the capacitance, but the mobility should be independent of the frequency. The transfer curves are divided by the capacitance value (I_d/C) and the resulting curves are in Figure 6-8 d-f. In the case of π-ion gel $_{x1}$, the transistor does not work under a fast sweep but works under a slow sweep. Contrary to the π-ion gel $_{x1}$, π-ion gel $_{x100}$ displays almost same I_d/C curves regardless of the sweeping speed. The π-ion gel $_{x10}$ also displays resembling I_d/C curves except for the sweeping speed of 0.1 s per 50 mV step. Based on the eq. 6-1, The resulting 2D mobilities are calculated (Figure 6-9).

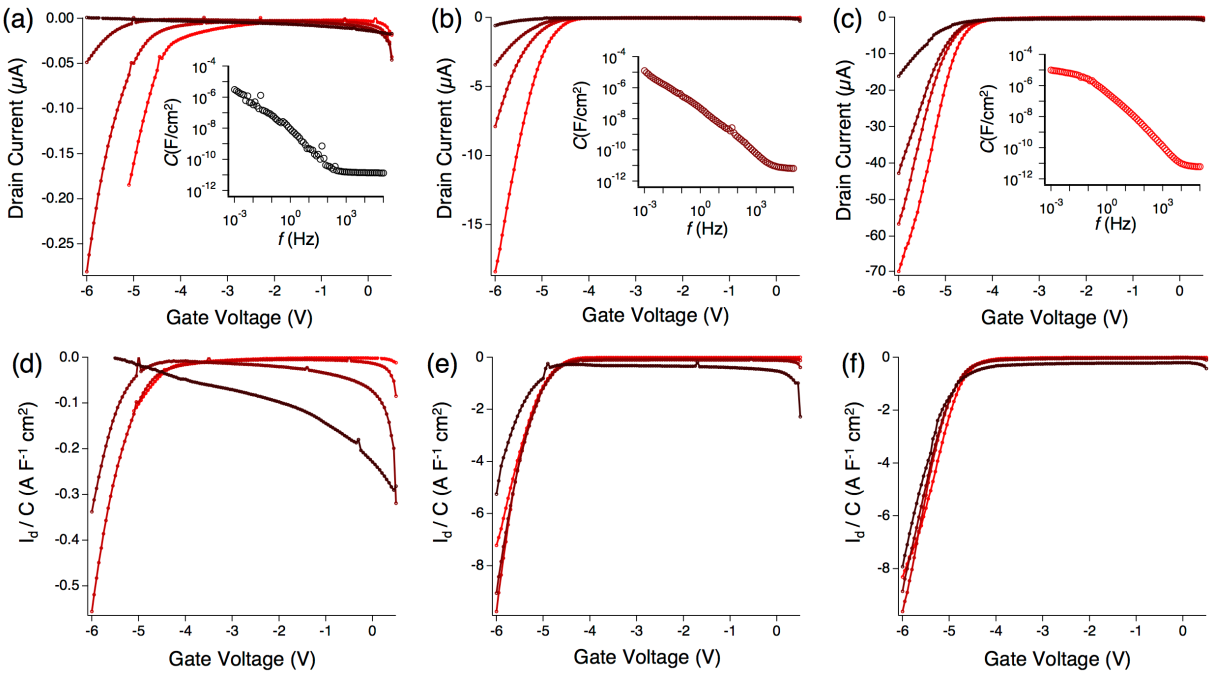

Figure 6-8. Transfer curves of π-ion gel$_{x1}$(a), π-ion gel$_{x10}$(b) and π-ion gel$_{x100}$(c) measured by the sweeping speed of 0.1 s per 50 mV step, 0.5 s per 50 mV step, 1 s per 50 mV step, and 5 s per 50 mV step from black to red. Insets are capacitance of each π-ion gel. The curves obtained by dividing Transfer curves with the corresponding capacitance value for π-ion gel$_{x1}$(d), π-ion gel$_{x10}$(e) and π-ion gel$_{x100}$(f).

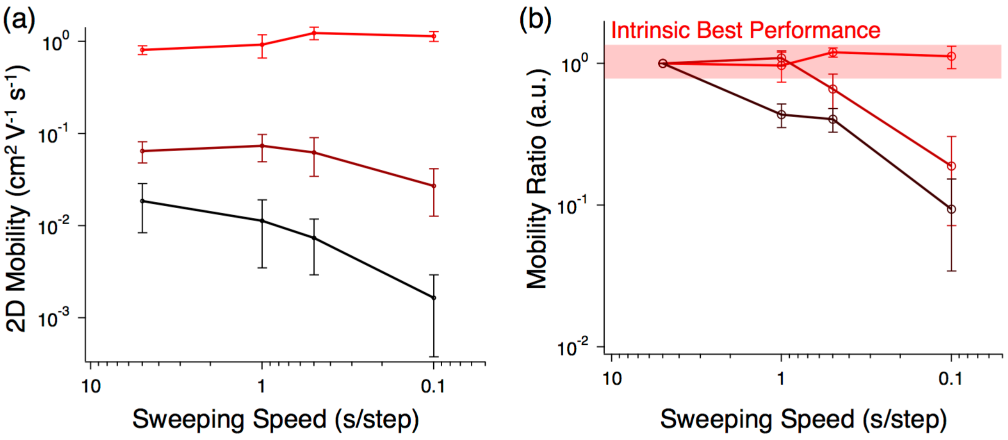

Figure 6-9. (a) 2D mobility of π-ion gel$_{x1}$(red), π-ion gel$_{x10}$(dark red) and π-ion gel$_{x100}$(red) as a function of the sweeping speed. (b) The mobility normalized at the value of 5 s per 50 mV step.

As seen in Figure 6-9 b, only the π-ion gel$_{x100}$ sustains the 2D mobilities regardless of the sweeping speed. π-ion gel$_{x10}$ and π-ion gel$_{x100}$ show the decreased mobilities as the sweeping speed increases. The decreased mobilities are due to the lack of time to reach a steady-state. These observations suggest that the response time of the π-ion gel$_{x100}$ is very fast. The IL ratio impacts on the response time. The absolute value of 2D mobilities of π-ion gel$_{x100}$ is higher than those of π-ion gel$_{x10}$ and π-ion gel$_{x1}$ (Figure6-9a). Two reasons can be suggested. One is simply that the capacitance value is high in case of a higher amount of IL, inducing more charge carriers. However, the capacitance of π-ion gels under sufficient time (e.g. 1mHz) differs just slightly so that the effect should be minor. The second reason is the net dielectric constant of the gels. Indeed, the dielectric constants of organic semiconductors are low (~ 4), in comparison to those of inorganic semiconductors, whose dielectric constants are ~12. For example, the Coulomb interaction between carriers and carrier traps is inverse-proportional to the dielectric constant; High dielectric constant media can cancel the charge carrier traps. ILs generally have dielectric constants of ILs 10-12, which are much higher than those of PPEs. The net dielectric constant should depend on the amount of a content IL. Since π-ion gel $_{x100}$ comprises 99% of IL and 1% of the polymer, high dielectric constant is assumed. It is believed that this secondary effect is major, but needs to be investigated carefully in future works.

6.5 Transient Behavior of the π-ion Gel Transistors.

The insights obtained by the sweeping speed dependency suggest that the π-ion gel $_{x100}$ responds fast. The On/Off transient behavior were investigated by measuring the drain currents after turning on and off the gate voltage.

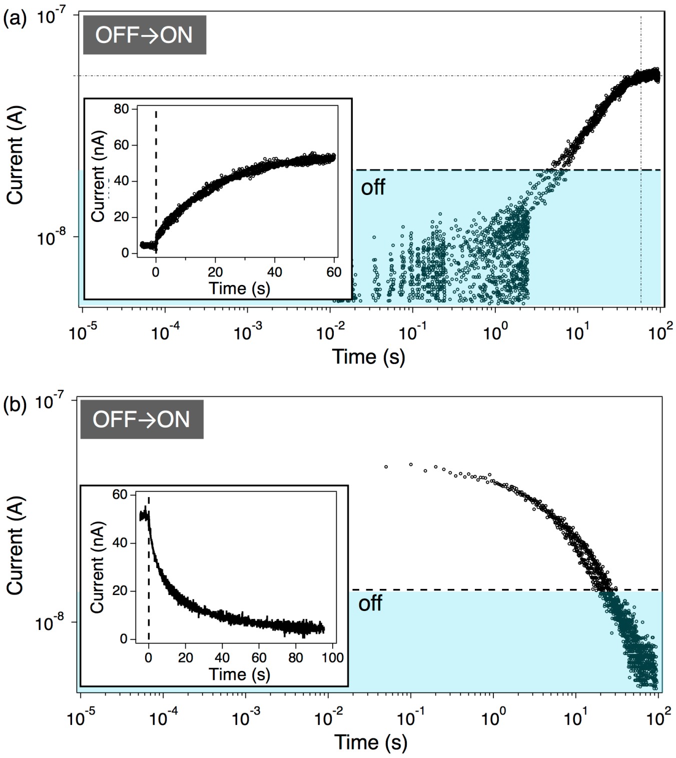

Figure 6-10. Transient behavior of the drain current (V_D=-1V) after turning on (a) and off (b) the gate voltage (V_G= -5V) in the case of π-ion gel $_{x1}$.

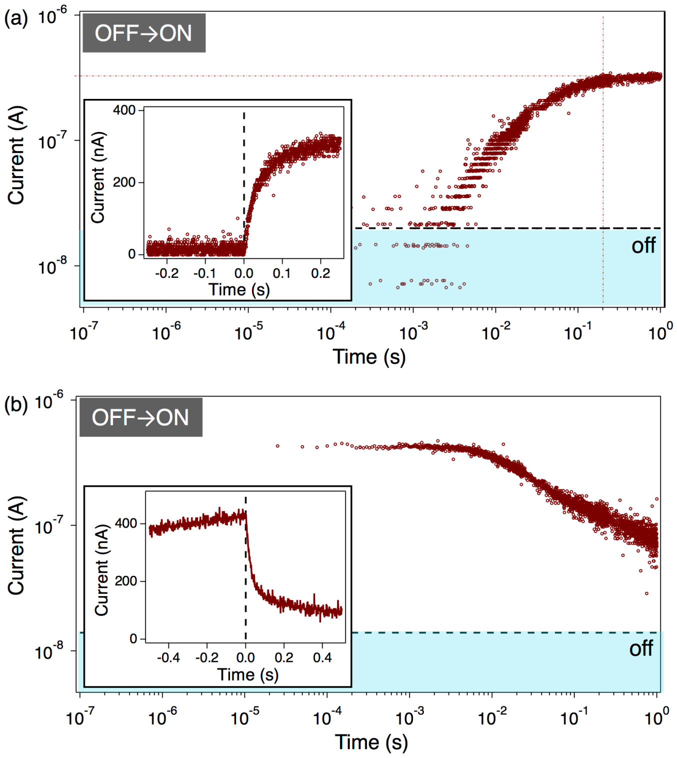

Figure 6-11. Transient behavior of the drain current (V_D=-1V) after turning on (a) and off (b) the gate voltage (V_G= -5V) in the case of π-ion gel$_{x10}$.

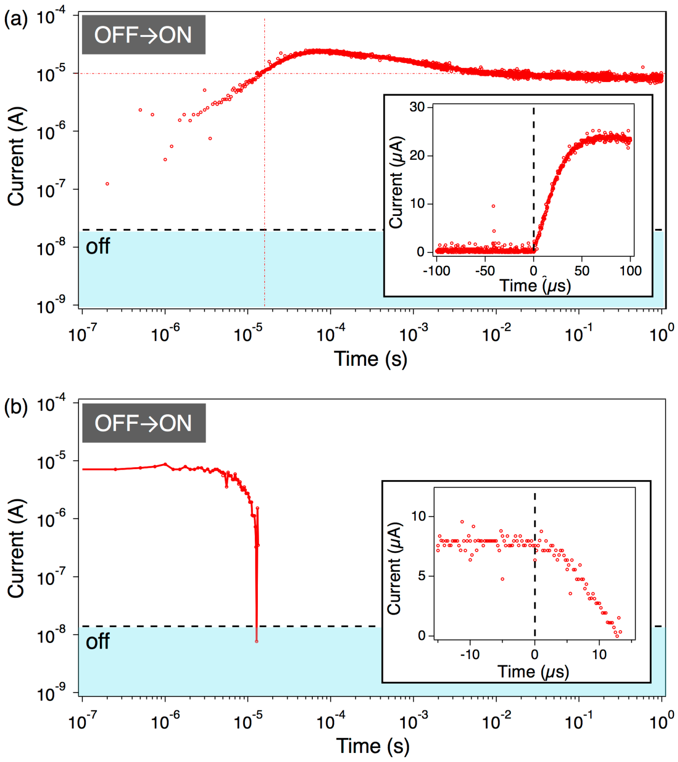

Figure 6-12. Transient behavior of the drain current (V_D=-1V) after turning on (a) and off (b) the gate voltage (V_G= -5V) in the case of π-ion gel$_{x100}$.

For the measurements, the source-gate and the resistance between source and drain are connected to the oscilloscope to read the transient current between source and drain. The resistance was carefully selected not to drop the potential more than 0.1V so that the drain voltage above 0.9 V is ensured (details see Appendix). Although a high-speed transient is measured, reading out the low current is hard due to the noise. Consequently, the off current was directly premeasured and indicated as dot lines in Figures 6-10, 11, 12.

π-ion gel $_{x1}$ shows the slow response in a range of several tens to one hundred seconds for both turn on and off (Figure6-10). This is even slower than the normal OECTs (several seconds). When the IL ratio increases, the response time is improved to several hundreds of milliseconds (Figure6-11). Surprisingly, π-ion gel $_{x100}$, the maximum amount of IL, shows the response time of only several tens of microseconds. The speed is even faster than the fastest OECT ever reported (sub-millisecond). [93] The real value of the response time is even faster than several tens microseconds because this time scale is already under the time-resolution of the setup. The power source takes several tens of microseconds to reach a commanded voltage (Figure A6-4).

Table 6-3. Response Time of Turn-on and -off

Device	Turn-on (s)	Turn-off (s)
π -ion gel $_{x1}$	6.0×10^{1}	$> 1.0 \times 10^{2}$
π -ion gel $_{x10}$	2.0×10^{-1}	5.0×10^{-1}
π -ion gel $_{x100}$	$< 2.0 \times 10^{-5}$	$< 1.0 \times 10^{-5}$

Note that Sariciftci *et al.* have already attempted the mixture film of an electrolyte and a conjugated polymer as an active layer of OFET, inspired by the LEC device geometry. [96,97] Meanwhile the mobility increased by 3 times, the device requires a high operation voltage. In that work, the mixture ratio of conjugated polymer and ions is 5 to 1, which is a much smaller amount of ions in comparison to the π-ion gel $_{x100}$ (1:100). The ratio of 1 polymer to 100 ions can be achieved by the gelation strategy.

6.6 Perspectives of PIGTs

Although the investigated advantages of the PIGTs are volumetric current and response speed, the flexibility is also a promising point which has to be focused. The devices do not require another layer for the gate so that the devices can be used in flexible printed electronic circuits. The devices made the best use of π-gels so that this work also shed light on the supramolecular chemistry. There are many reports about semiconductor gels. While PPE derivatives are the only material that forms π-ion gels so far, better materials may be found. It is desired that this work is going to be a joint of fields of device electronics and supramolecular chemistry.

6.7 Short Summary of the Chapter

The π-ion gels are utilized as a material of active layers in transistors. π-ion gels have nano-segregated bicontinuous structures. Sub hundred nanometer fibers made of a PPE enclose an IL. The space between fibers is enlarged depending on the amount of an IL. The fiber networks can enclose the 100 times larger amount of IL at the maximum. The intercalated IL works as an internal gate when a gate bias is applied. The π-ion gel works as a transistor. The device shows volumetric currents and excellent performances such as the on/off ratio of 10^5 at a gate voltage of -6V. The response time is faster than 20 µs, which is fastest among electrochemical based transistors including OECTs ever reported. [91, 93] The concept can be transferred to other fields such as printed electronics that can make the maximum use of the flexibility and absence of dielectric layers. A lot of extensional studies can be expected.

7 Ferroelectric PPEs

7.1 Motivation

Sophisticated ferroelectric organic materials are attractive, as they promise applications in the field of memory devices,[98,99] and organic electronic functions, coupled to ferroelectric behavior.[100-102] There are different mechanisms for organic ferroelectric effects that include hydrogen bonding,[33-35] liquid crystalline ordering,[36] charge-transfer complexes,[37, 38] and molecular rotation.[39,40] Among them, the most difficult type is molecular rotation based because it should rotate in the solid, which means it needs space to move, but at the same time it should be locked. Actually, there are 2 examples of this type of ferroelectric materials.

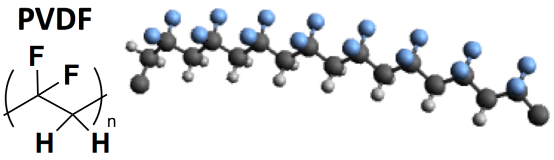

Figure 7-1. The molecular structure of Poly-vinylidene fluoride (PVDF).

The molecular rotation is most prominently described for polyvinylidene fluoride (PVDF, Figure 7-1).[103] In PVDF, the uniformly unidirectional orientation of the polymer's CF2 groups results in a permanent polarization. This principle has been employed in other polymers, including polyamides, but little is known about conjugated polymers that attain ferroelectric properties caused by molecular rotation of some of their monomeric units. In materials that contain phenylene-ethynylene (PE) units, rotation of the aryl rings modulates their optical and electronic properties; their conformational behavior is well investigated.[49-51, 104-109] PEs are planar in the solid state and their structure is static (Figure 7-2a).

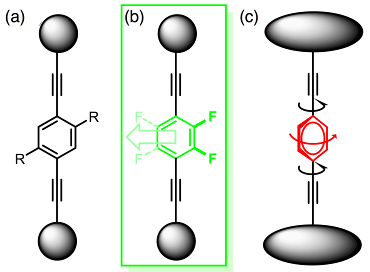

Figure 7-2. Fundamental situations for phenylene-ethynylene (PE)-based systems in the solid state. a) Static, b) dynamic and tunable by an external electric field, that is, ferroelectric, and c) dynamic, gyroscope- like. Molecular rotation is responsible for the generation of ferroelectric properties.

An exception to this rule was reported by Garcia-Garibay et al (Figure 7-3). They found that two sterically demanding molecular stoppers, localized on both side of PE units, allow the phenylene rings of PE units to rotate freely both in solution and also in the solid state (Figure 7-2c). [28, 110] They achieved thus molecular gyroscopes. The ability of a dipolar moiety to rotate will result in a macroscopic polarization upon application of an external electrical field but also in an immediate loss of the induced polarization upon removal of that field. [110]

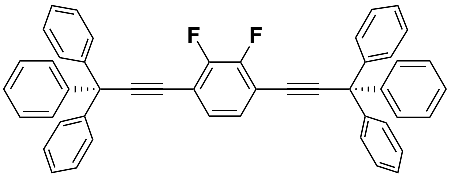

Figure 7-3. Molecular structures of the molecular gyroscope synthesized and reported by Garcia-Garibey *et al*.

To retain and switch the polarization, an appropriate but not excessive rotation barrier is required. Poly(para-phenyleneethynylene)s (PPEs), show a small rotation barrier (approximately 1 kcal mol^{-1}) [28] for the isolated molecule or in solution, but the barrier is higher in the solid state owing to the crystallinity of the material. [49-51] Consequently, employing PPE backbones seems promising as switchable materials, in which rotation is hindered but still possible upon exposure to an electric field. In this chapter, a ferroelectric PPE (Figure 7-2b), polarized at room temperature with long-lasting remanent polarization is presented.

7.2 Materials and Synthesis

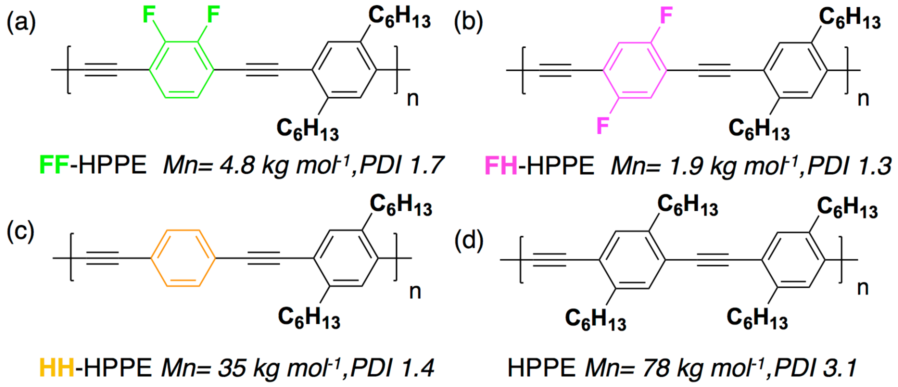

Figure 7-4. Molecular structures, number-average molecular weight (*Mn*), and polydispersity values of PPEs employed in this study.

To introduce dipoles, o-difluorobenzene rings were integrated into the PPE chain (FF-HPPE, Figure 7-4a). The reasons why o-difluorobenzene is employed are 1. its dipole moment is comparable

(2.13 Debye) with that of a unit of VDF (2.06 Debye) and 2. the rotation barrier is estimated to be enough low, 3.5 kJ mol^{-1} (almost 1 kcal mol^{-1}) upon the DFT calculation in solution. Three additional PPEs with different side chains but without dipolar moieties were also synthesized (Figure7-4. b-d). FF-HPPE was obtained by standard Sonogashira coupling of diiodo-2,3-difluorobenzene and a suitable diyne. The other PPEs were also obtained in reasonable yield as yellow powders with moderate *Mn* and polydispersity values. [111] Due to the low solubility of FF-HPPE and FH-PPE, their molecular weight is 1 order lower than other PPEs. The detailed syntheses are shown in Appendix.

7.3 The Packing Structure of PPEs

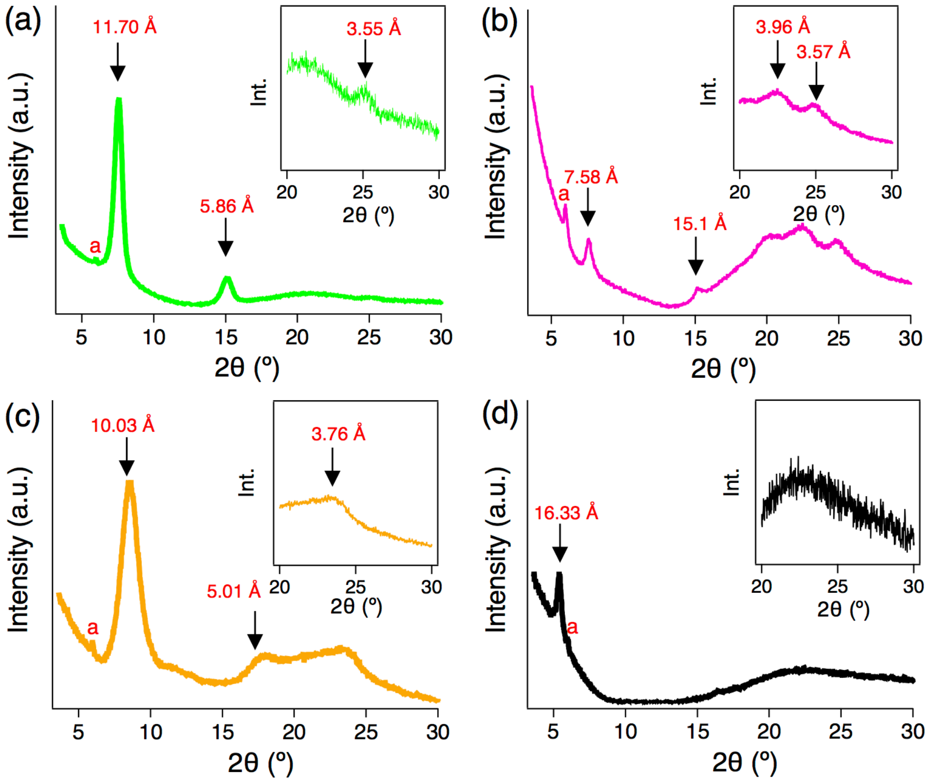

Figure 7-5. Diffractions of powder XRD patterns of the films of FH-HPPE(a) HH-HPPE(b) and HPPE(c). X-ray source: CuKα. Insets show the expanded patterns in the range of 20 °C < *2θ* < 30 °C, respectively. Peak “a” comes from the equipment.

First, the packing structures of those PPEs were investigated since the molecular packing is a key whether the ferroelectricity appears or not. The results were shown in Figure 7-5, depicting the powder diffraction patterns of the four crystalline PPEs. FF-HPPE, FH-HPPE, and HH-HPPE show higher order than HPPE. While HPPE displays a lamellar packing, other PPEs display interdigitated phases, as the main diffraction peak is shifted from 16.3 to 7.06, 10.0, and 11.7 respectively. Interdigitation is further evidenced by a second diffraction peak at twice the angle of the first. The diffraction signal at around 3.5–3.7 represents stacking distances in the PPEs. FF-HPPE, FH-HPPE, and HH-HPPE show these signals. According to those insights, one possible packing structure of FF-HPPE is shown in Figure 7-6.

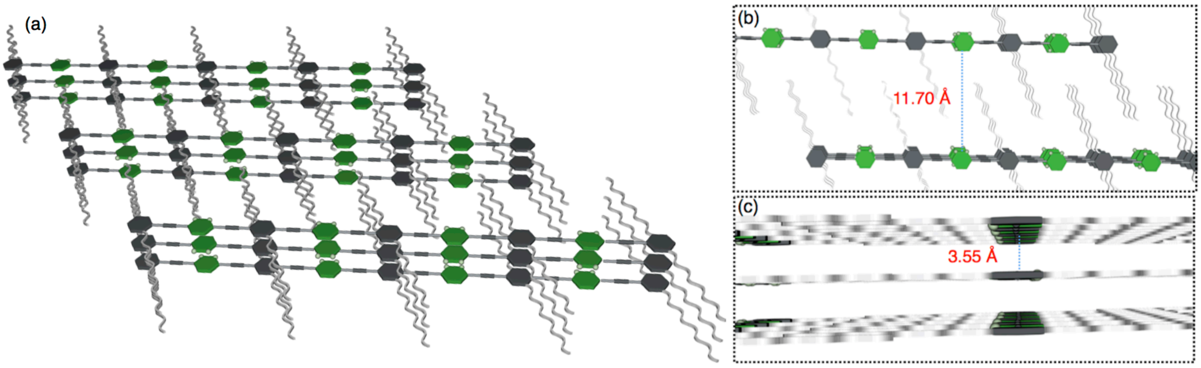

Figure 7-6. A possible packing structure of FF-HPPE. (a) over view (b) Top view and (c) side view, respectively

In the structure of FF-HPPE, the position of difluorobenzene are estimated to be syntactic or atactic, canceling each other's dipoles by dipole–dipole interaction. Nevertheless, the diffraction is broad in comparison to that of crystals of small molecules, suggesting some disorders. This is advantageous to realize the molecular rotator in solid state.

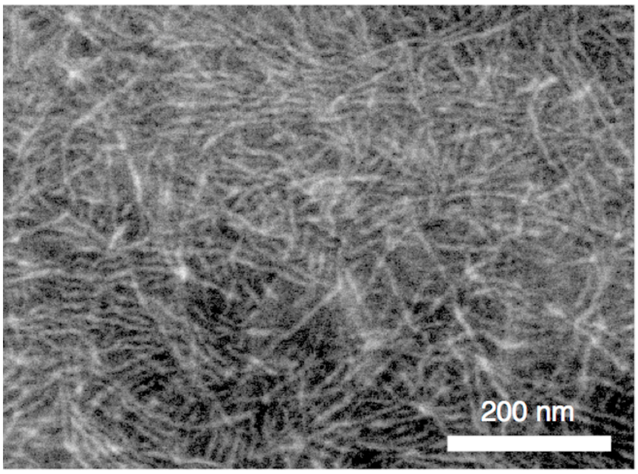

Figure 7-7. A SEM image of the surface of FF-HPPE film.

Thin films of FF-HPPE appear as a dense network of fibers, each around 10 nm thick, confirmed by SEM observation(Figure7-7). They are much thinner than the fibers made of dialkyl or dialkoxy substituted PPEs (Figure4-2). This is probably related to the lower solubility of FF-HPPE. Anyway, such a distinct fibril structure also indicates the strong crystallinity of FF-HPPE.

7.4 Temperature Depending Measurements

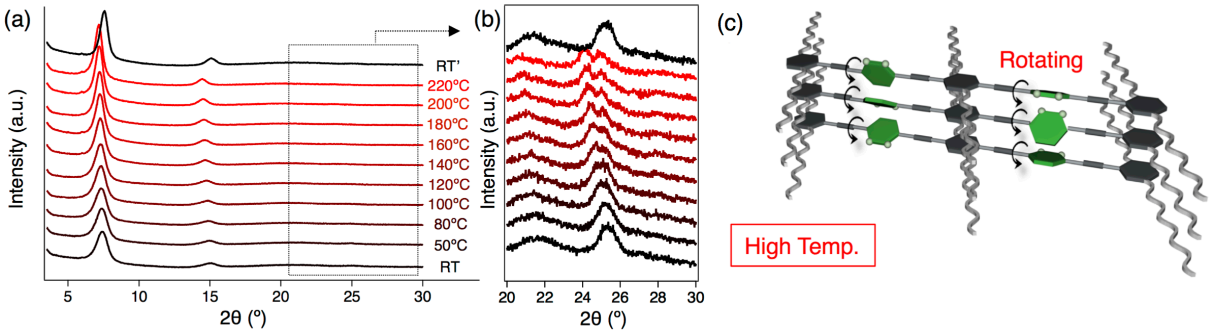

Figure 7-8. (a) XRD patterns of a film of FF-HPPE and (b) their expansion in the range of 20° < 2*θ* < 30° as a function of temperature (RT-220 °C, black to red). RT and RT' mean XRD patterns at room temperature before and after annealing. (c) A schematic of FF-HPPE at high temperature.

The temperature dependent XRD measurements were performed to observe the thermal effect on the packing structure. Upon heating to 220 °C, the structure of FF-HPPE changes (Figure 7-8). The first and secondary diffraction peaks for the alkyl packing, which corresponds to 1.17 nm, increases, moving to a lower angle value. The interlayer distance becomes larger upon heating. This is typical during annealing. [105,106] In contrast to this, the high angle peak at 25.18 °, assigned to the polymer stacking, splits from 3.55 at room temperature into two peaks of decreasing intensity at 3.70 and 3.56 at 220 °C, pointing the flip-flop motion between the canceling and aligning forms of dipoles at high temperature and rotation of the difluorobenzene units at higher temperature. Those phenomena are reversible, confirmed by the XRD patterns after cooling down to room temperature (Figure7-8b, top). The increase of the interlayer distance is also observed for other PPEs (Figure A7-1). However, the behavior of perpendicular packings of the benzene rings is hardly seen in H-PPE and FH-PPE. The stacking signal at 22° decreases upon heating and recovers upon cooling. It does not split, possibly because of the highly symmetric geometry of flexible benzene rings.

To investigate the response to an electric field of those PPEs at high temperatures, Capacitors were prepared. The PPE films were sandwiched by the patterned ITO substrates and fixed.

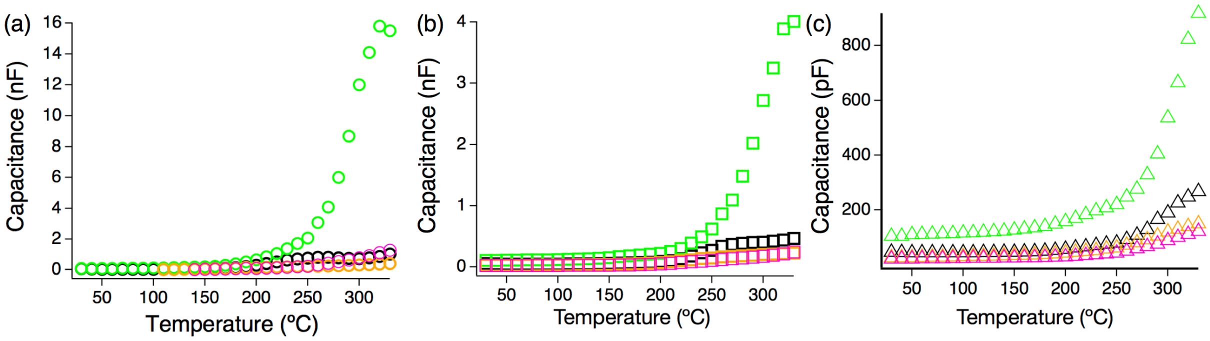

Figure 7-9. Capacitance of FF-HPPE (green), FH-HPPE (pink), HH-HPPE (orange), and HPPE (black) asa function of temperature (RT–330 8C) at 1Hz (a), 10Hz (b) and 100Hz (c).

More direct evidence of flip/rotation motion is the capacitance as a function of temperature. [39, 112] The capacitance of FF-HPPE increases with temperature and reaches its maximum at 320 °C (Figure 7-9). On the other hand, the increase of the capacitance is not pronounced in cases of other PPEs. At high temperatures, the benzene rings of FF-HPPE and HH-HPPE should be flexible. Only the o-difluorobenzenes of FF-HPPE retain the spontaneous dipoles. Consequently, FF-HPPE displays a large increase on capacitance upon heating. At the same time, the rotation barrier of FF-HPPE can be estimated by using frequency and temperature depending capacitance measurements.

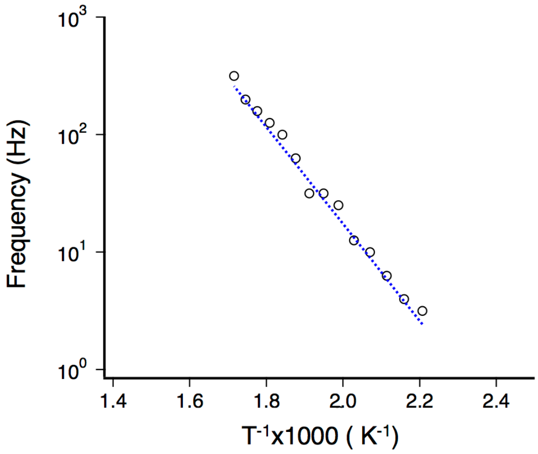

Figure 7-10. Arrhenius plot of onset frequency of capacitance of FF-HPPE as a function of temperature. The Rotation barrier plot is calculated from the equation of $\tau^{-1}=\tau_0^{-1}\exp[-E_{rot}/RT]$, where τ^{-1}, τ_0^{-1}, R, T represent onset frequency, constant value, gas constant (8.31JK^{-1} mol^{-1}) and Temperature, respectively. 18.7 kcal mol^{-1} is estimated as a result.

A rotation barrier of 18.7 kcal mol^{-1} is estimated from the Arrhenius plot of the onset frequency of capacitance as a function of temperature (Figure7-10). This value is slightly higher than that of molecular gyroscopes reported by Garcia-Garibay *et al* (10-15 kcal mol^{-1}). [28, 110] Note that they calculated from the frequency-dependent solid-state NMR so that it is not fair to compare directly. Yet, the barrier is a reasonable value to realize dipole sustainability.

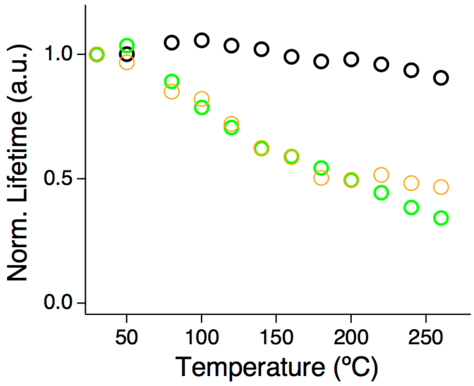

Figure 7-11. Relative photoluminescence lifetime of FF-HPPE (green) and HPPE (black) normalized by lifetime at RT.

The molecular rotation is also evident from the emission lifetime. The emission lifetime significantly decreases for FF-HPPE and HH-HPPE when going to higher temperatures, but not for HPPE (Figure7-11). Unfortunately, FH-HPPE was not applicable to this measurement due to a very short lifetime. When we take account into that the molecular rotation contributes to non-radiative decay, all PPEs except HPPE are supposed to be flexible at high temperatures. The lifetime decays are also shown in Figure A7-2.

7.5 Electronic Measurements of Capacitors of PPEs

The structural investigation and the electrical behavior of the FF-HPPE suggest a ferroelectric phase. Dielectric responses to an electric field were investigated. The PPE films were sandwiched by the patterned ITO substrates and fixed and a triangle AC voltage was applied to those samples at room temperature to polarize the film.

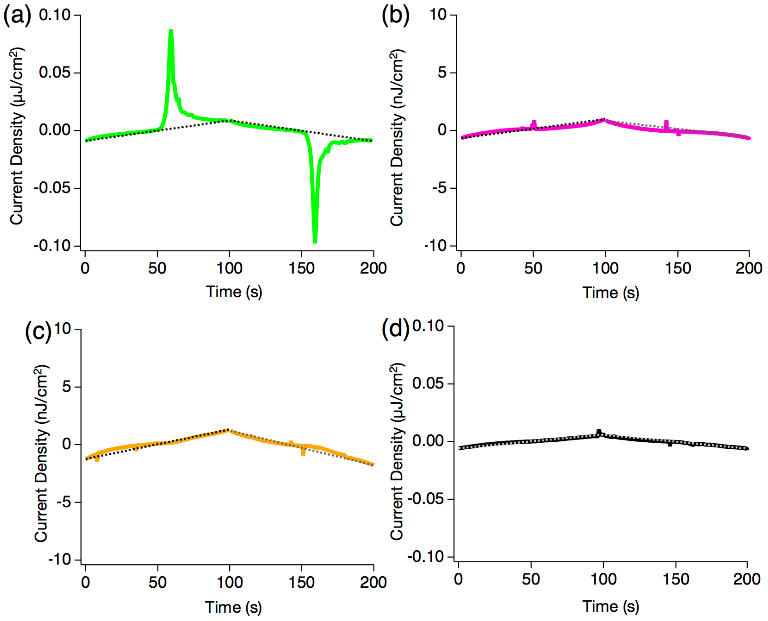

Figure 7-12. Current density–Time curves of FF-HPPE (a), FH-HPPE (b), HH-HPPE (c) and HPPE (d) applied triangle AC electric field of ± 20 V μm^{-1} at 5 mHz. Dotted lines indicate linear component of current.

The results of each PPEs' capacitors are summarized in FIgure 7-12. Apparently, only FF-HPPE has inversion currents While no polarization hysteresis was found for HH-, FH-, or HPPE derivatives. The different amplitudes of AC voltage are applied to the FF-HPPE capacitor.

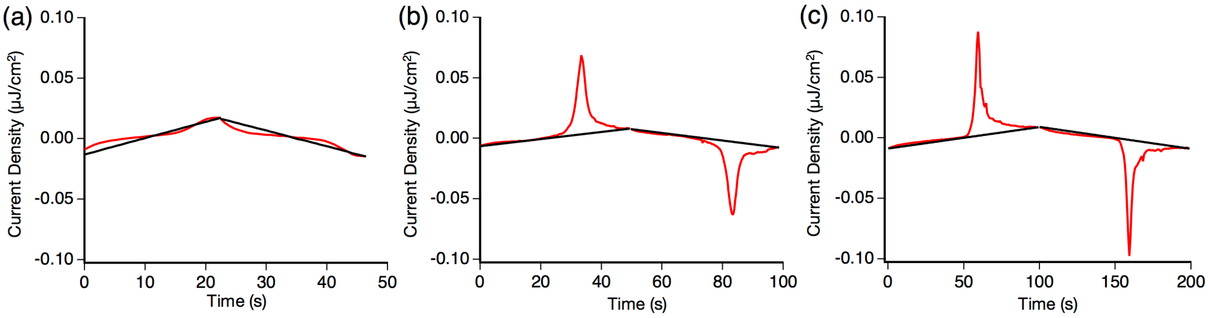

Figure 7-13. Current density–Time curves of FF-HPPE (a), FH-HPPE (b), HH-HPPE (c) and HPPE (d) applied triangle AC electric field of ± 20 V μm^{-1} at 5 mHz. Black lines indicate linear component of current (a leakage).

The obtained current density-time curves (Figure 7-13) were integrated (Figure 7-14). The linear component, which is regarded as leakage current, [113] was subtracted to get the polarization related current component.

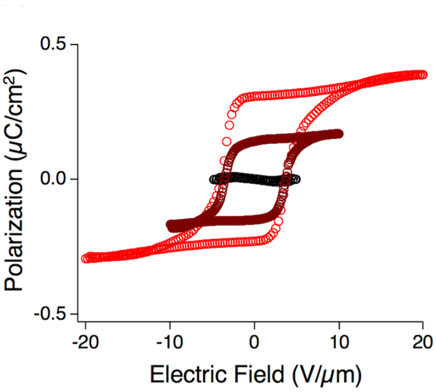

Figure 7-14. P–E hysteresis curves vs. applied triangle electric AC field of ±5 (black), ±10 (brown) and ±20 Vμm^{-1}(red) at 5×10^{-3} Hz.

Hysteretic P–E characteristics were observed for FF-HPPE when the applied voltage exceeded 5 V µm^{-1}. At 20 V µm^{-1}, this behavior was much more significant and remanent polarization (*Pr*) of circa 0.3 µC cm^{-2} was observed (Figure 7-14). Moreover, frequency dependent current density-voltage measurements were also performed.

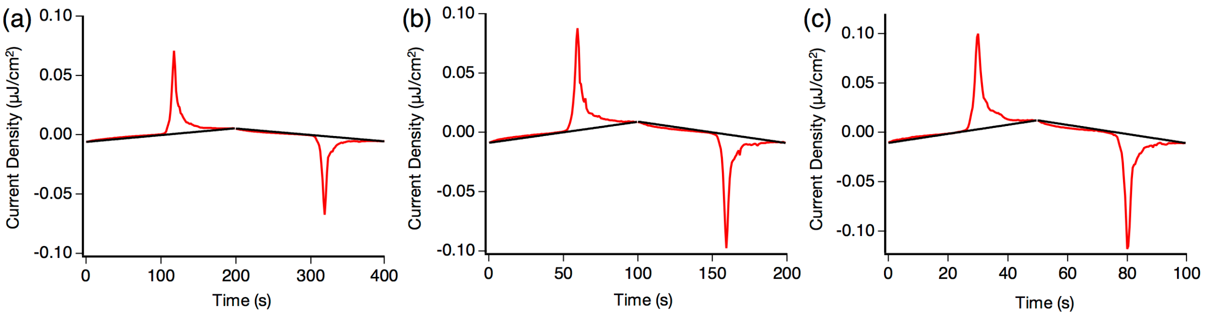

Figure 7-15. Current density–Time curves of FF-HPPE applied triangle AC electric field of ± 20 µm^{-1} at 2.5 mHz (a), 5 mHz (b) and 10 mHz (c). Black lines show linear component of current.

The results of Frequency dependent current density (Figure 7-15) were also transformed to P-E curves (Figure 7-16).

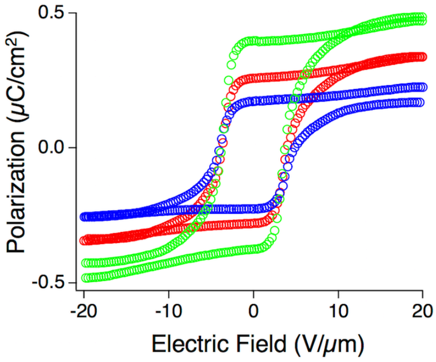

Figure 7-16. Frequency-dependent P–E curves at 2.5×10^{-3} (green), 5×10^{-3} (red), and 10×10^{-3} Hz (blue).

P–E hysteresis was found at applied AC frequencies lower than 0.01 Hz. A coercive electric field can be determined as 5.3 V µm^{-1} from the hysteresis, but the remanent polarization cannot be determined because it depends on the frequency as seen in Figure 7-16. The molecular reorientation requires time to saturate and the pure remanent polarization can be obtained when the AC voltage at a low-enough frequency is applied.

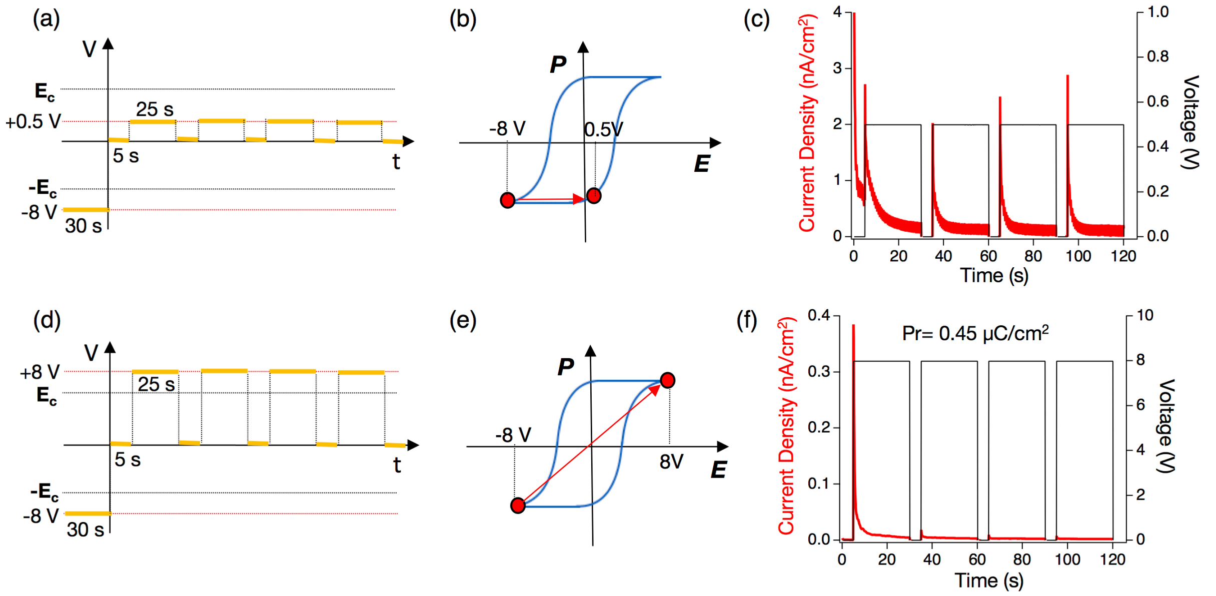

Figure 7-17. The programmed voltage and time of PUND (positive-up, negative-down) measurements (a, program-1 and d, program-2). Changes of polarization and electric field by program-1 (b) and program-2 (e). Resulted current density and applied voltage of program-1 (c) and program-2 (f) as a function of time. From the integration of (f), the Pr is calculated to be 0.45 µC cm^{-2}.

Consequently, a positive-up, negative-down (PUND), DC voltage technique for full saturation was performed to obtain the correct value (Figure 7-17). The voltage programs were set as shown Figure 7-17 a and d. After 30 s of poling with 8V and subsequent 5 s of removal, a reverse electric field was applied and the current density was recorded for 25 s. Several cycles of 5 s relaxation and electric field application resulted in Figure 7-17 c,f. When the reverse applied electric field is less than coercive electric filed, an inversion current was not observed (Figure 7-17 b,c). However, a sufficiently high inverted electric field turns polarization to the other direction, resulting in inversion current which is only seen in the first cycle (Figure 7-17 f). The difference of integrated current between first cycle and latter was used to estimate the remnant polarization of 0.45 µC cm^{-2}. This matches the result of DFT calculations, in which a value of 1.6 µC cm^{-2} was found, in particular when we take into account that the dipolar units would not align perfectly in the solid state. The remanent polarization of 0.45 µC cm^{-2} and the coercive electric field of 5.3 V µm^{-1}

compare well to that of other organic ferroelectric materials, [33, 34, 39] although the response time is relatively slow (10^{-2}–10^{-3} Hz). This is likely related to the rigid and close stacking distance.

The ferroelectric property is also conformed in the electric field dependence of the permittivity. When a material has a ferroelectric property, the permittivity increases at the coercive electric field because the dipole moments respond. As seen in Figure 7-18, only FF-HPPE shows such a butterfly hysteresis. [114] Other PPEs do not show such an electric field dependence on permittivity.

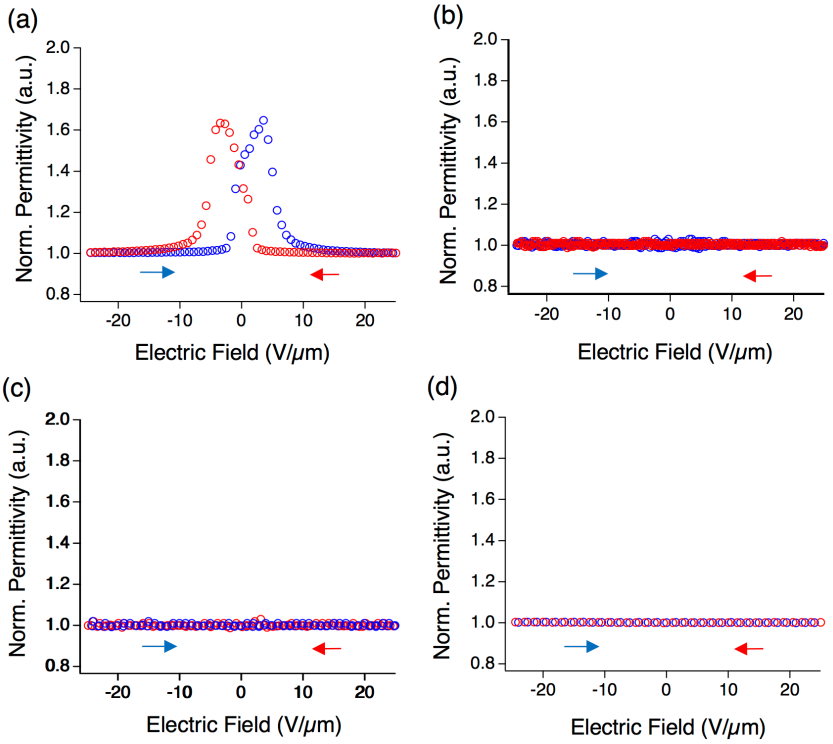

Figure 7-18. The programmed voltage and time of PUND (positive-up, negative-down) measurements (a, program-1 and d, program-2). Changes of polarization and electric field by program-1 (b) and program-2 (e). Resulted current density and applied voltage of program-1 (c) and program-2 (f) as a function of time. From the integration of (f), the Pr is calculated to be 0.45 μC cm^{-2}

7.6 Semiconducting Properties of FF-HPPE

The observed ferroelectric behavior relates to the dipolar moiety and the clamping of dipoles by the packing of neighboring PPE chains. The molecular structure of PPE is critically important for the ferroelectric behavior but provides semiconducting properties at the same time. PPEs have been employed as active layers in organic devices. and they are reported a lot. [52, 53, 115] The optoelectronic properties of the three PPEs are shown in Figure 7-19 and Tables 7-1 and 7-2. For all PPEs, typical absorption and emission spectra were found. Especially the quantum yield of FF-HPPE is 0.15 in the solid state, meaning that it is fluorescent as well as other known PPEs.

Table S1. The wavelength of Absorption maximum (Abs_{max}) and PL maximum (PL_{max}) in solution and solid states.

Polymer	Solution		Solid	
	Abs_{max} (nm)	PL_{max} (nm)	Abs_{max} (nm)	PL_{max} (nm)
FF-HPPE	389	418	420	517
FH-HPPE	390	427	434	521
HH-HPPE	393	421	432	480
HPPE	400	423	441	503

Table S2. The lifetime in solution state ($\tau_{solution}$), that in solid state (τ_{film}), their components of lifetime($\tau_{1\text{-}3}$) and corresponding fraction($f_{1\text{-}3}$), fluorescence quantum yield in solution state (ϕ_{ol}) and that in solid state(ϕ_{film})

Polymer	$\tau_{solution}$ (ns)	τ_{film} (ns)				Φ_{sol}	Φ_{film}
		τ_1 (f_1)	τ_2 (f_2)	τ_3 (f_2)	τ_{av}^a		
FF-HPPE	0.27	0.30 (0.23)	1.17 (0.56)	3.09 (0.21)	1.36	0.23	0.15
FH-HPPE	0.54	<0.01 (1)^b	-	-	0.01	0.47	0.05
HH-HPPE	0.31	0.21 (0.58)^a	1.11(0.42)	-	0.58	0.41	0.09
HPPE	0.27	0.19(0.47)	0.68(0.44)	2.85 (0.09)	0.64	0.71	0.13

^{a} τ_{av} is defined as $(\tau_1 f_1 + \tau_2 f_2 + \tau_3 f_3)/ (f_1 + f_2 + f_3)$ ^{b} Under resolution of the equipment.

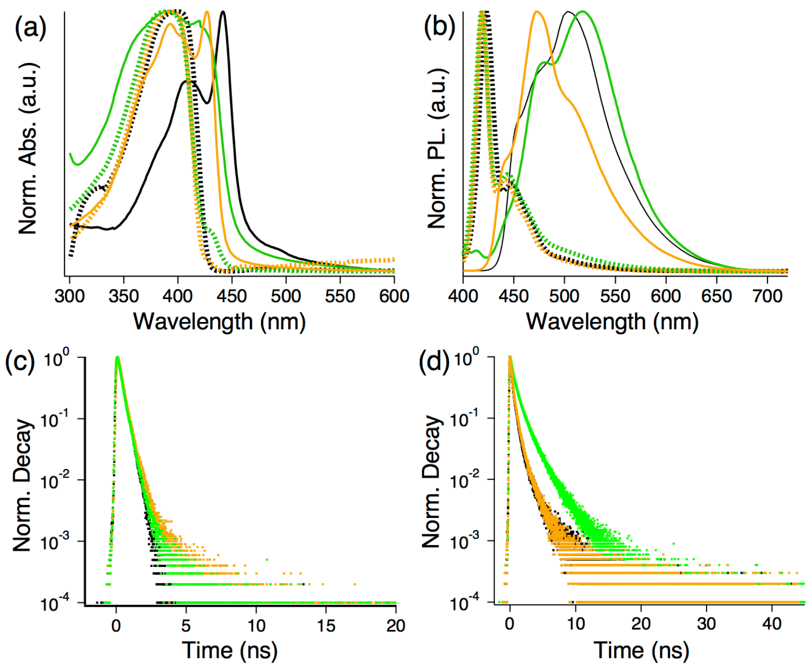

Figure 7-19. Normalized absorption (a) and photoluminescence (PL) (b) spectra of a film (solid line) and in solution (dot line) of FF-HPPE (green), FH-HPPE (pink), HH-HPPE (orange) and HPPE (black). PL decays in solution (c) and in the thin film (d) of FF-HPPE (green), FH-HPPE (pink), HH- HPPE (orange) and HPPE (black).

Since the electrical conduction of alkyl PPEs has also been investigated earlier, [52,53] electrical conduction of FF-HPPE in MIM-diodes with ITO as the contact material was investigated. In this device, two operations are performed, poling and sweeping. After the poling with 8 V for 30 s and a subsequent relaxation for 5 s, an electric field sweep from 0 V to +1 V was applied. Poling to the same and opposite direction with the voltage sweep direction are defined as sym-poling and anti-poling, respectively (Figure 7-20c). Furthermore, the several cycle measurements in Figure 7-20b are done by the same manner, but applied constant electric field of 1.6 V µm^{-1} in spite of voltage sweeping. The averaged current for 1 s is shown. The ferroelectric phase in FF-PPE results in a modulation of the measured current (Figure 7-20a,b). In sym-polarized devices, in which the direction of the dipole moment aligns with the current direction (Figure 7-20a), the current density is considerably higher than in that of the anti-polarized one. The mechanism is not clear but might stem from a change of an ohmic contact to a Schottky contact,[100] or to an induced electric field by polarization.[33] Current modulation in a simple memory device was demonstrated but is limited since the on/off ratio is only an order of magnitude. Nonetheless, the result suggests ferroelectric conjugated polymers could be useful for memory OLED, [101] memory OFET,[100] or high performance OPV.[102]

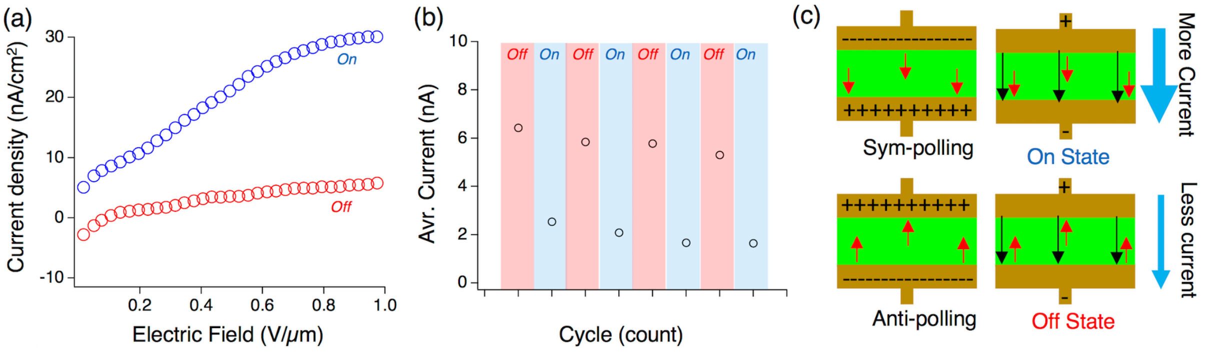

Figure 7-20. (a) Current density–electric field curve after the polarizing by 8 V (on state, blue) and 8 V (off state, red). (b) Averaged current undertheelectricfieldof1.6Vmm 1 for1safterswitchingthe polarization. (c) Schematic of sym- and anti-polarizations.

7.7 Short Summary of the Chapter

A ferroelectric PPE is prepared. Ortho-difluorinated benzenes in the PPE introduce dipole moments and the dipolar rings behave like molecular rotors at high temperature. The rotation barrier resulting from the PPE’s packing retains orientation of the molecular dipole moments at room temperature and an electrical field induces a long lasting remanent polarization; FF-PPE behaves like a ferroelectric material. The concept should be adaptable to any dipolar aromatic species incorporated into a poly(aryleneethynylene). Over all, this dynamic concept should deliver a rich harvest and add to the property-development of organic semiconductors for OLEDs, TFTs, and memory devices. The parts of contents involving figures, tables and text are reprinted with the permission of the reference. [116]

8 Liquid Crystalline PEs

8.1 Motivation

The ferroelectric conjugated polymer was successfully synthesized and applied to MIM diodes in the last chapter. It was not possible to apply the ferroelectric conjugated polymer to other organic electric devices due to the extremely low solubility. The reason why the ferroelectric materials receive the attention as device materials is that the orientation of the dipoles can work as a permanent electric field as introduced in chapter 1. The permanent electric field can accelerate currents through diodes or induce charge carriers in OFET without external voltages. [100-102] In this sense, the material does not have to be ferroelectric as long as the materials are dipole-oriented. [119, 120] To solve the solubility problem, the same concept is transferred to phenylene ethynylene (PE) oligomers to create dipole-oriented crystals in this chapter. Rigid crystals generally do not allow for the molecular rotation due to the limited space. [28] It is difficult to control the dipole-orientation in crystals directly with an electric field. If crystallization takes place while the dipole moments of molecules align, creation of dipole-oriented crystals might be possible. According to this strategy, liquid crystals (LCs) are paid attention. [117]

LCs are one of the material phases that have fluidity and molecular orientations. [117,118] The phase usually appears between a solid (crystal) phase and a liquid (isotropic) phase. Not all materials have the LC state. Molecules composed of a rigid part and a flexible part often display liquid crystalline phases. [117] The variety of LCs is versatile. Here, only smectic phases and nematic phases shall be introduced.

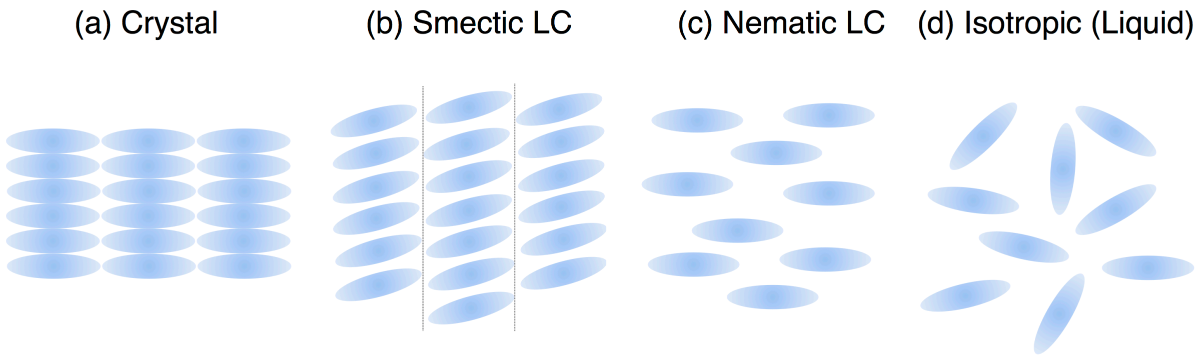

Figure 8-1. Schematic illustrations of molecules in cases of (a) crystals, (b) smectic liquid crystals, (c) nematic liquid crystals and (d) liquid.

Smectic phases and nematic phases appear when the molecules are stick-shaped. In a crystal state, the molecules pack densely and most motions of molecules such as molecular rotations are hindered (Figure 8-1a). Smectic phases appear in some molecules upon heating. In the smectic LC state, molecules are distant from each other in comparison to the crystal state. LCs gain fluidity. Accordingly, molecules can rotate in smectic phases. Yet, the molecules align in the same direction and periodicity along the long axis (the position) is kept (Figure8-1b). Further heating sometimes results in the appearance of nematic phases. In nematic phases, the fluidity increases and molecule positions become flexible, while the molecular orientations are aligned (Figure8-1c). At over the temperature of nematic phases, molecules display isotropic (liquid) states, where molecules move around and no orientation is seen (Figure8-1d).

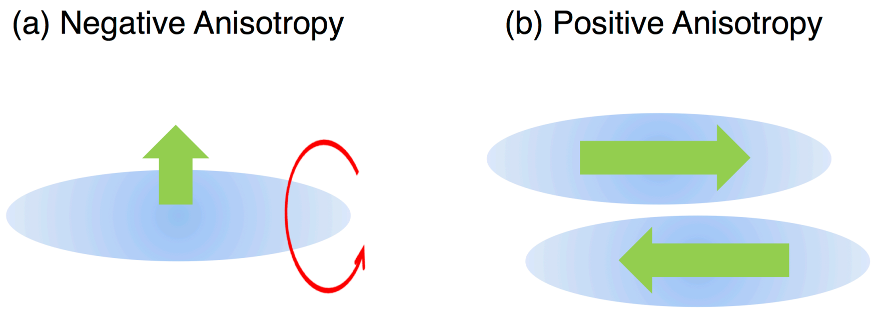

Figure 8-2. The behavior of the molecules which have a negative anisotropy (a) and positive anisotropy (b) in LC states.

If LC molecules have spontaneous dipole moments perpendicularly to the long axis (called negative anisotropy), the dipoles can respond to an electric field due to the free rotations (Figure 8-2a). However, the molecules do not keep the dipole-orientation after removal of an electric field. Ferroelectric characteristics are not achieved in this case. If the LC molecules have spontaneous dipole moments along to the long axis (called positive anisotropy), the neighboring molecules compensate the dipole by aligning to the canceling direction (Figure 8-2b). When the fluidity is small, the molecules do not respond to an electric field due to the steric hindrances. When the fluidity increases to some extent, the molecules can respond to an electric field, but the orientation is not kept after the removal of the electric field, either. For these reasons, ferroelectric characteristics hardly appear in LC phases except for some specific LC molecules,[121-123] meanwhile, LC molecules with negative anisotropy respond to an electric field. Yet, the liquid crystalline phase of negative anisotropic molecules might be beneficial to perform dipole-controlled crystallizations because molecular rotation is triggered/hindered by the temperature.

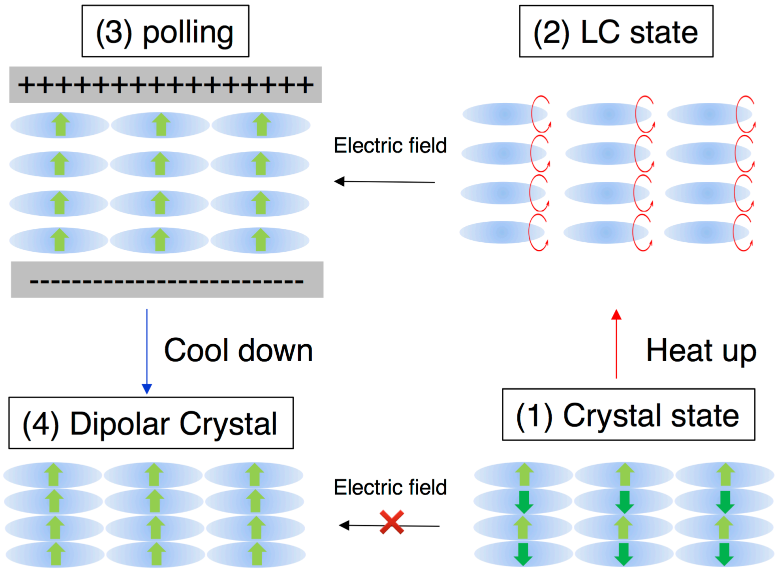

Figure 8-3. The strategy of 2D control in this chapter.

The following strategy to form dipole-oriented crystals is suggested. The strategy is named 2D-control (Figure 8-3). First, the crystals of negative anisotropic molecules have no net dipole moments due to the compensating nature. In this state, the dipoles of molecules do not respond to an electric field. *Upon* heating to the liquid crystalline state, the molecules start to rotate and poling of the dipoles can take place under an electric field. Cooling under the electric field might result in the formation of dipole-oriented crystals. If the dipolar crystals are created, the dipole-orientation should be more stable than ferroelectric materials due to the steric hindrances. To create such dipolar crystals, the liquid crystalline behavior is comprehensively studied and 2D-control is applied subsequently in this chapter.

8.2 Material and Synthesis

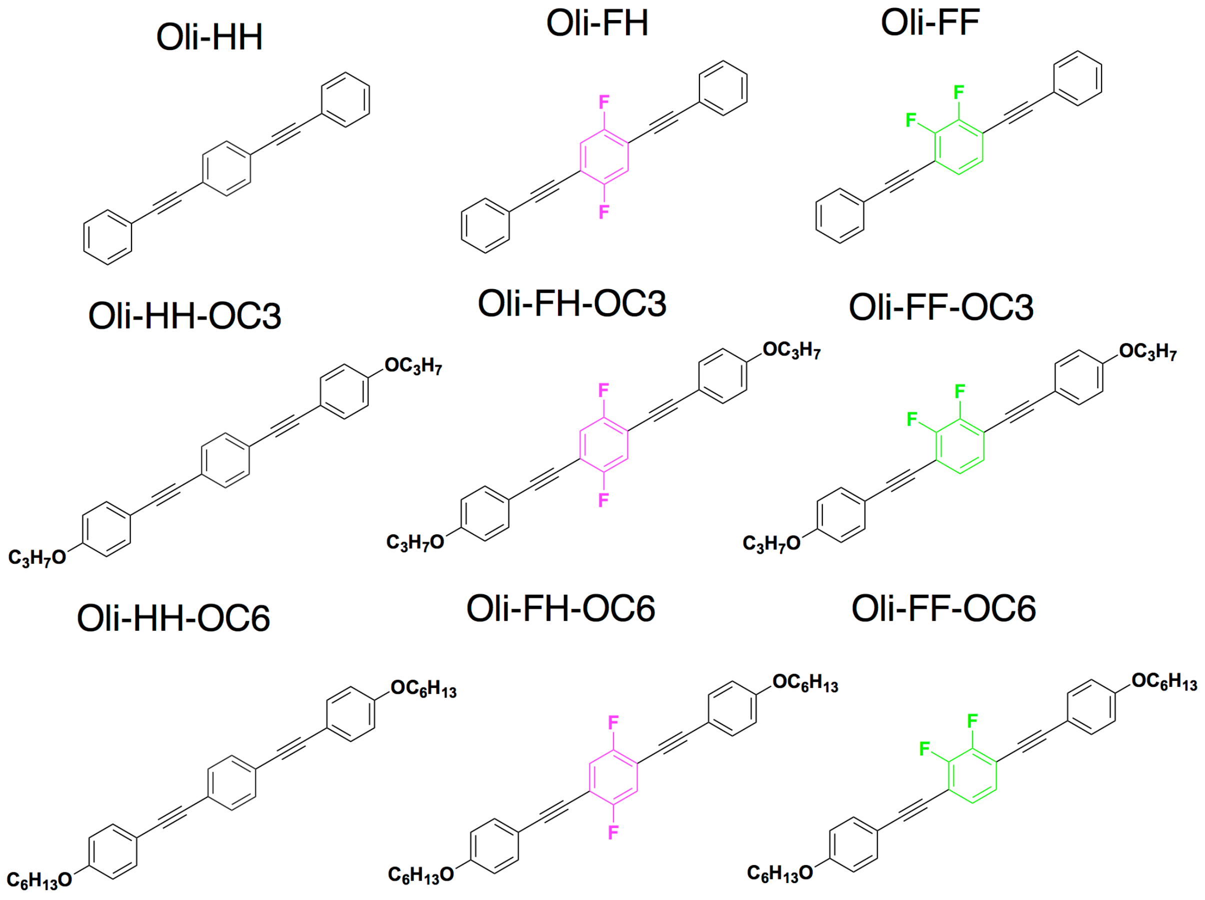

Figure 8-4. Molecular designs of synthesized PEs in this chapter.

For the comprehensive studies of phenylene ethynylene trimers (PEs), 9 different kinds of PEs were synthesized (Figure8-4, detailed syntheses in the Appendix). Non-substituted benzene, 2,6-difluorobenzene and 2,3-difluorobenzene are introduced as central cores. Only 2,3-difluorobenzene has a dipole moment (approximately 2 Debye), while non-substituted phenylene and 2,6-difluorobenzene are non-polar. As side groups, 4-propyloxy, 4-hexyloxy, and non-substituted benzenes are employed.

8.3 Crystal Structures of PEs

In this section, several examples of crystal structures of PEs are shown. The crystal structures are determined by Dr. Frank Rominger.

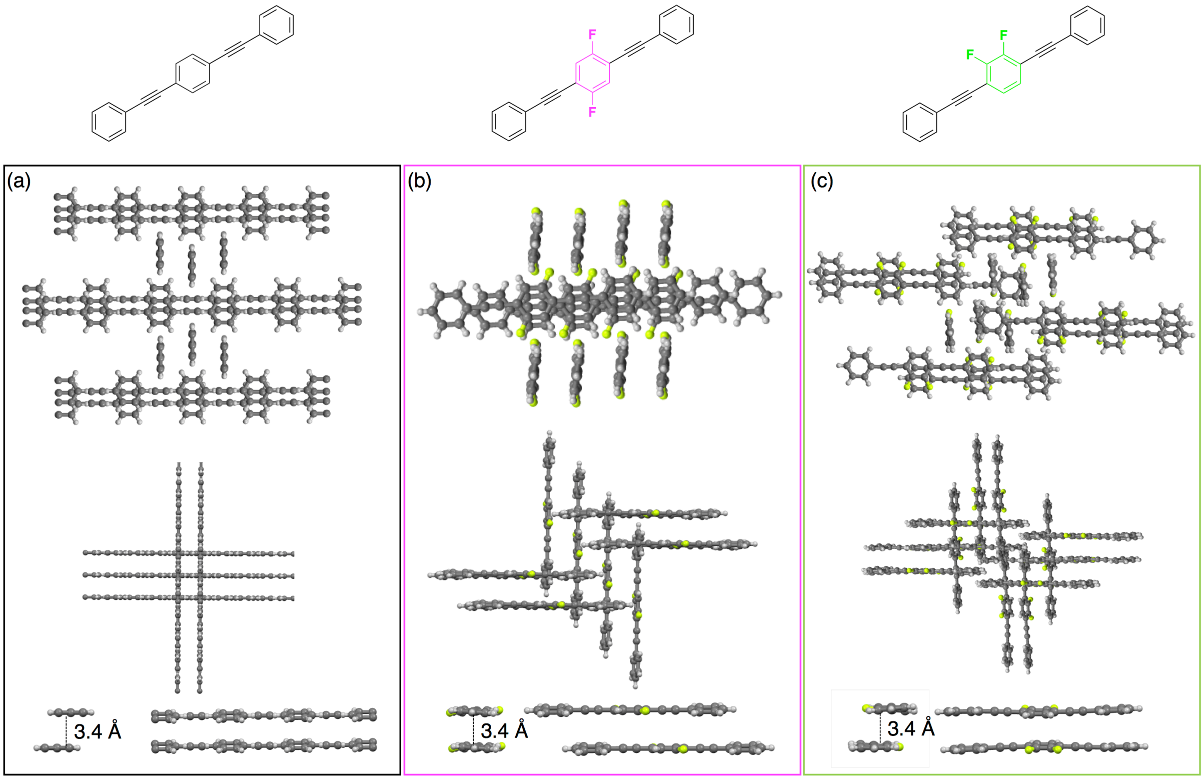

Figure 8-5. Molecular Packings of Oli-HH(a), Oli-FH(b) and Oli-FF(c), respectively. The bottom figures depict the overlap of two molecules.

First, the crystal structures of non-alkyl chain substituted PEs are shown (Figure 8-5). In all cases, molecules crystalize into grid-like structures. Phenylene ethynylene trimers often form this kind of grid structures and several examples have been reported. [124] The crystal structure has little to do with the dipoles of central cores. On the other hand, there is a slight difference in molecular overlap (Figure 8-5, bottom). When 2,6-difluorobenzene is employed, the benzene rings avoid overlapping and stay on the ethynylene bonds. This is probably resulted from the interaction between fluorine atoms at 2-position and hydrogen atoms at 5-position of the neighboring molecules. This kind of assembly is often seen in the crystal structures of 2,5- dialkoky PEs or PPEs. [125] In contrast to Oli-FH, Benzene rings of Oli-FF and Oli-HH overlap face to face. This is quite rare among derivatives of PEs and PPEs. The dipole moments of Oli-FF compensate each other, forming a net dipole moment of zero as most of the other dipolar molecules. [10,11] Note that the crystal of Oli-HH is polymeric, but that does not mean that the structure itself is polymeric. The bridging alkyne units (C4) have an occupation of only 2/3, indicating that every third unit is missing. However, this "gap" is not ordered, so that on average a "polymer" with partially occupied linkers is observed.

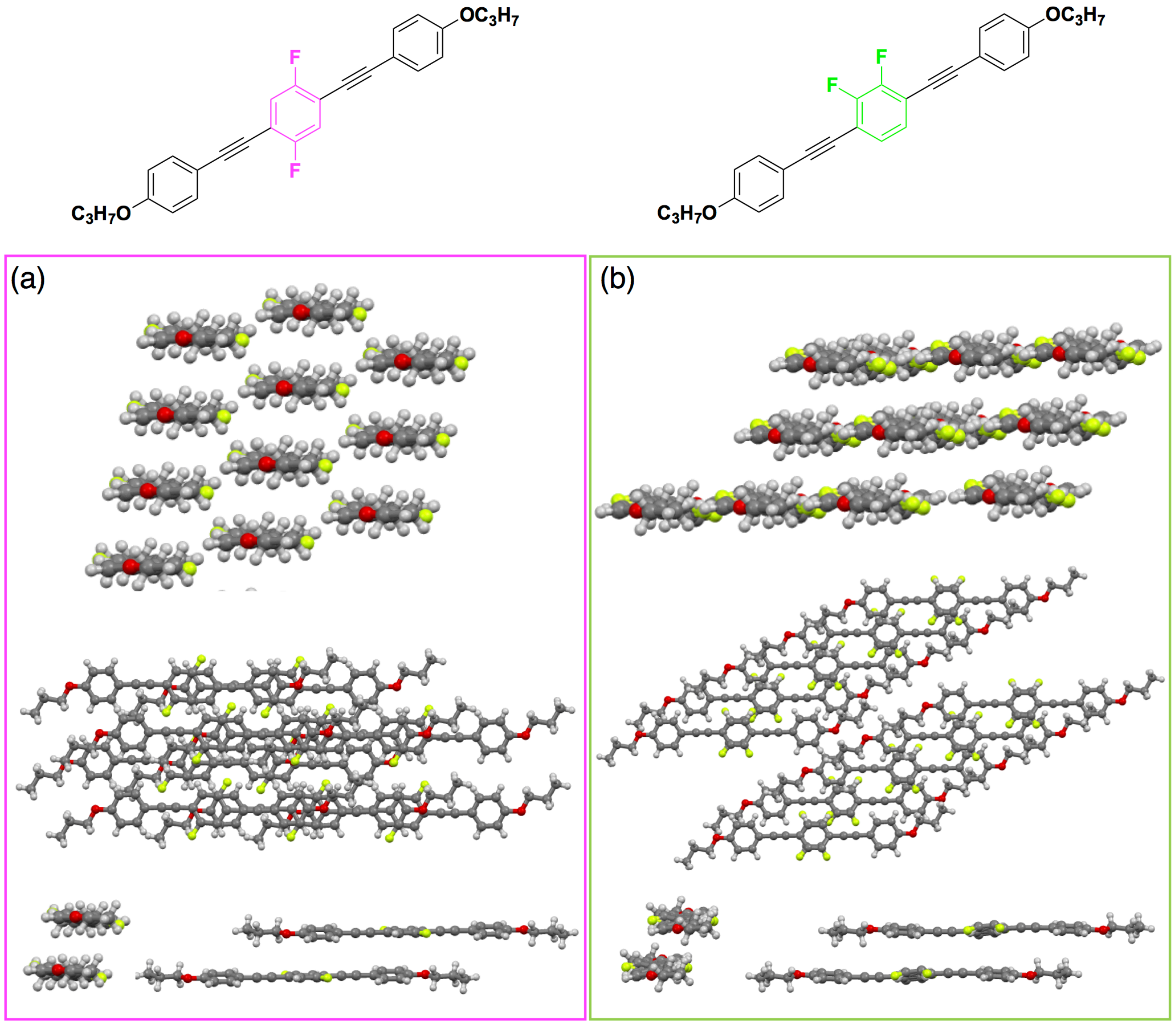

Figure 8-6. Molecular Packings of Oli-FH-OC3(a), Oli-FF-OC3(b). The bottom figures depict the overlap of two molecules.

Next, the crystal structures of 1-ethynyl-4-propyloxy substituted PEs are shown in Figure 8-6. Unfortunately, crystals of Oli-HH-OC3 were not obtained due to the low crystallinity. By introducing propyloxy side chains, the molecules face the same direction instead of grid structures. The stacks of two molecules are slipped off, not as non-substituted PEs. In both cases, the non-fluorinated benzene overlaps to the difluorobenzene. Therefore, face to face packings are observed. The positions of fluorine atoms cannot be determined in Oli-FF-OC3, so that the central core is described as tetrafluorobenzene. However, the ratio is determined 50:50. This means the net dipole moment is zero but also means that the fluoride positions are not always compensating alternatingly. This could be explained by the reduced interaction of dipoles. Apparently, the crystallization is not triggered by dipole interaction. This insight suggests the possibility to align the dipoles in a crystal.

8.4 Phase Transition Behavior of PEs

It is well known that molecular design affects the phase transition behavior. Here, the phase transition behavior is explored comprehensively. This section is separated according to the side chains since they usually dominate the transition behavior.

8.4.1 Non-substituted PEs

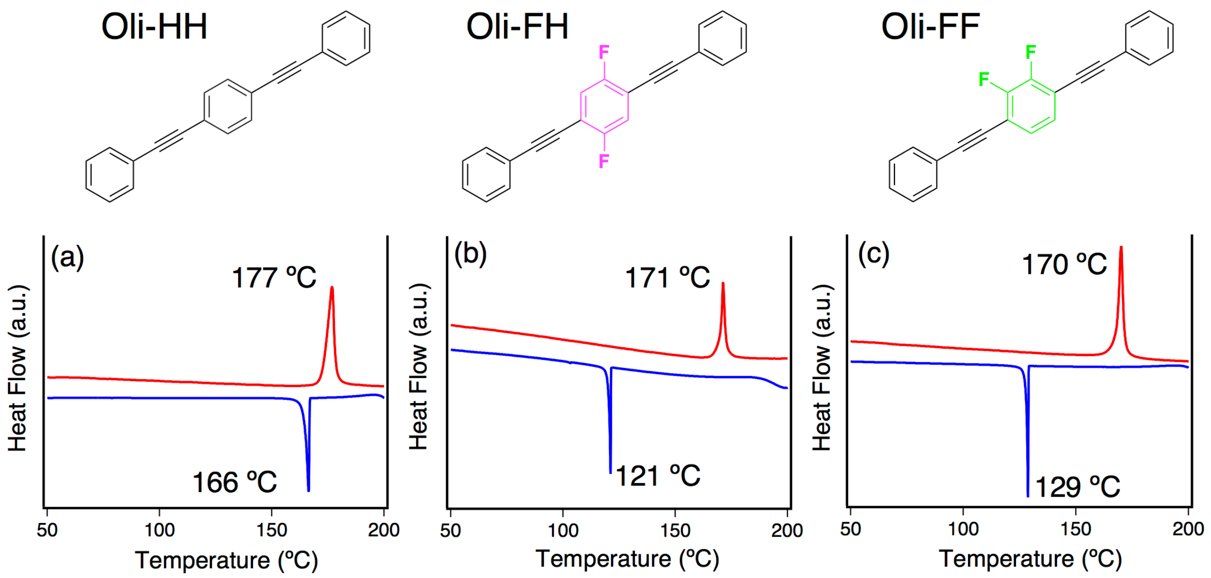

Figure 8-7. DSC traces of Oli-HH(a), Oli-FH(b) and Oli-FF(c). Red and blue lines indicate heating and subsequent cooling, respectively.

First, non-substituted PEs were investigated. In the range of room temperature to 200°C, only solid (Crystal) to liquid transitions are observed (Figure 8-7). DSC over 200°C is not investigated because it is already an isotropic liquid phase at 200 °C, confirmed by polarized optical microscopy (POM, Figure 8-8). The transition temperatures are 177°C (heating, Oli-HH), 166°C (Cooling, Oli-HH), 171°C (heating, Oli-FH), 121°C (Cooling, Oli-FH), 170°C (heating, Oli-FF) and 129 °C (Cooling, Oli-FF), respectively. The differences between the transition temperatures of heating and cooling processes are about 40-50°C in the presence of fluorine atoms, whereas, there is only 10°C difference in the absence of fluorine atoms. It is assumed that the molecular rotation of PEs in the liquid state contributes to this temperature gap. It requires time to stabilize this molecular rotation and crystalize PEs in the presence of difluorobenzene.

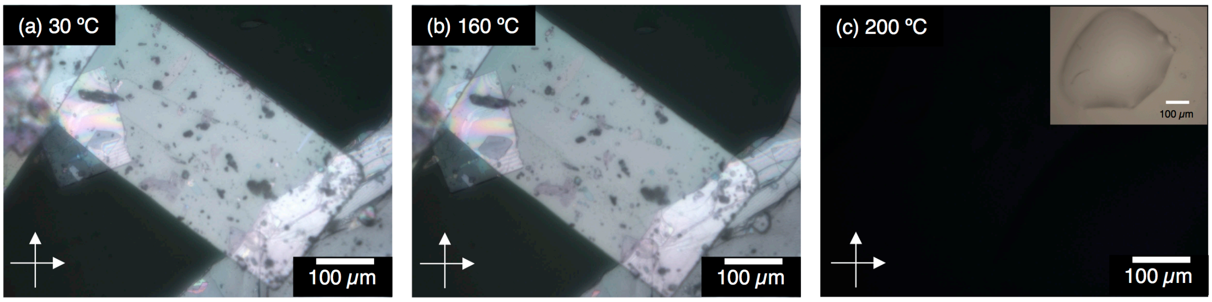

Figure 8-8. Cross polarized POM images of Oli-FF at 30 ºC(a), 160ºC(b) and 200ºC(c) during the heating process. Inset in c shows a non-polarized image of the liquid state of Oli-FF.

In Figure 8-8, polarized micrographs of Oli-FF at different temperatures are shown. There is no difference in the appearances at room temperature and 160ºC. This result is in accordance with that of DSC. At over 170ºC, the crystal melts and no polarized image can be seen, indicating an isotropic phase. Oli-FH and Oli-HH also show same the behavior and the POM images are in Figures A8-1,2.

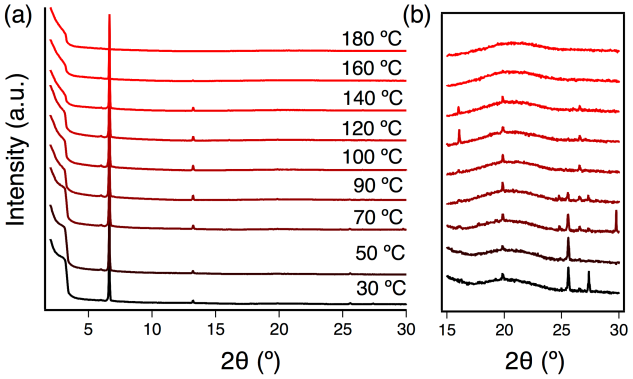

Figure 8-9. (a) XRD diffractions of Oli-FF at different temperatures from 30ºC (black)-200 ºC(Red) by 20 ºC. The range of 15-30 º is enlarged (b).

The XRD diffractions at different temperatures were measured in the case of Oli-FF (Figure8-9). There is a clear difference above and below 170ºC, confirming the same insights obtained from POM and DSC. It is definitely a solid to liquid transition. There is some difference especially between 25º-27º at 70ºC-90ºC. These peaks are assigned to the perpendicular packings to the benzene planer rings. The intensity of peaks decreases as elevating temperature in the crystal phase, meaning that the molecules are disordered at the higher temperatures. This tendency suggests weak π-π interactions in the crystal. Interestingly, a peak at around 6º increases *upon* heating, meaning that the interlayer crystallinity is increased. The observation gives an insight that the dominant force to support the crystal structure is not perpendicular packing to the π-π planes, but interlayer interactions. The transition behavior of non-substituted PEs is summarized in Figure 8-10.

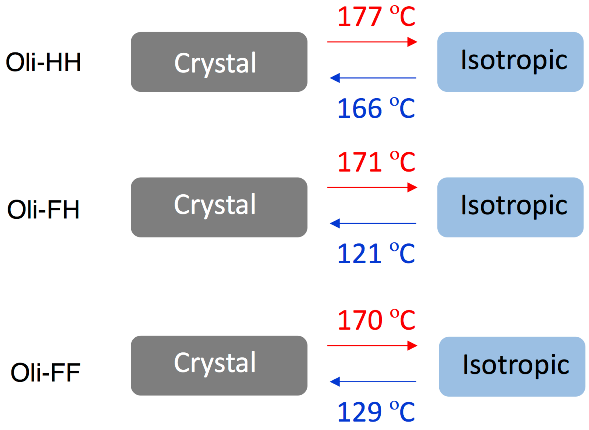

Figure 8-10. The Summary of phase transitions of non-substituted PEs

8.4.2 1-ethynyl-4-propyloxybenzene PEs

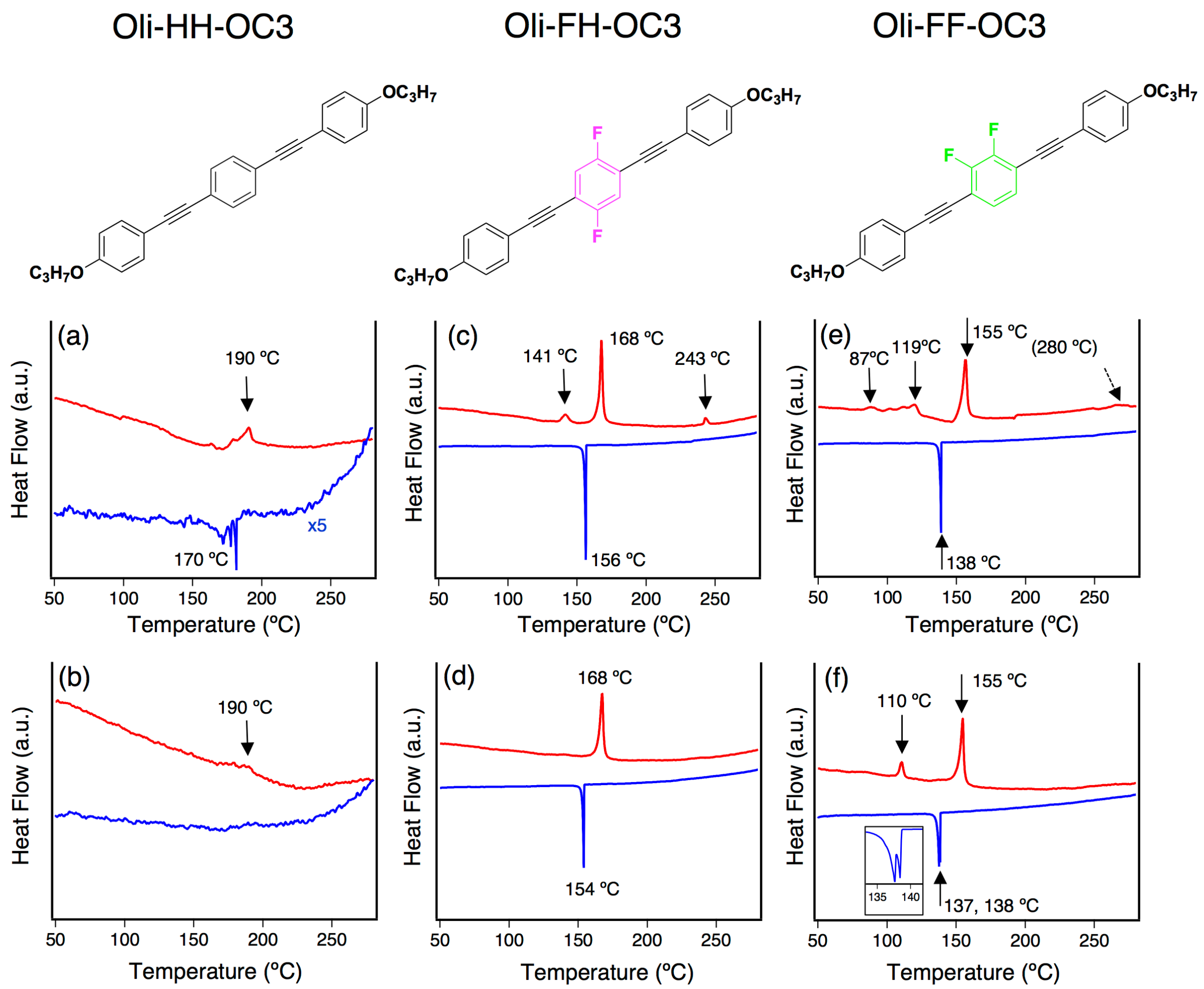

Figure 8-11. First cycles of DSC traces of Oli-HH-OC3(a), Oli-FH-OC3(c) and Oli-FF-OC3(e) and second cycles of DSC traces of Oli-HH-OC3(b), Oli-FH-OC3(d) and Oli-FF-OC3(f). Red and blue lines indicate heating and subsequent cooling, respectively.

Next, 1-ethynyl-4-propyloxybenzene is introduced as a side group. The DSC trances are shown in Figure 8-11. Contrary to the non-substituted cases, the phase transitions are different, depending on the central core. POM observations identified the phases. In the absence of fluorine atoms (Oli-HH-OC3), the compound does not form crystals at room temperature due to the low crystallinity. However, the amorphous phase transfers to the liquid crystalline phase (nematic) at 190°C. The DSC traces of Oli-HH-OC3 are poor due to the small energetic difference and limitation of the sample amount, although the transition is seen. This is also confirmed by the POM observations (Figure 8-12). The nematic phase disappears at 300°C. The nematic phase does not appear on cooling, suggesting decomposition of Oli-HH-OC3 at 300°C.

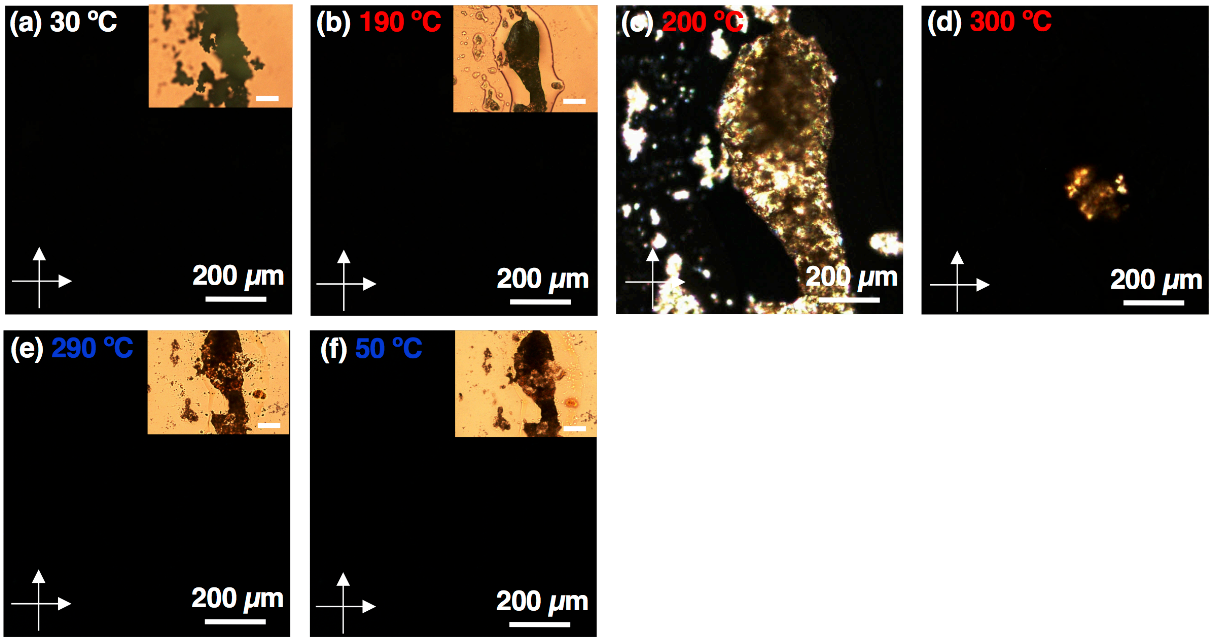

Figure 8-12. POM micrographs of Oli-HH-OC3 at different temperatures of 30°C(a), 190°C(b), 200°C(c), 300°C(d), 290°C(e), and 50°C (g). Insets show the images of non-polarized microscopy with a scale bar of 200 μm. Red temperature and blue temperature mean heating process and cooling process, respectively.

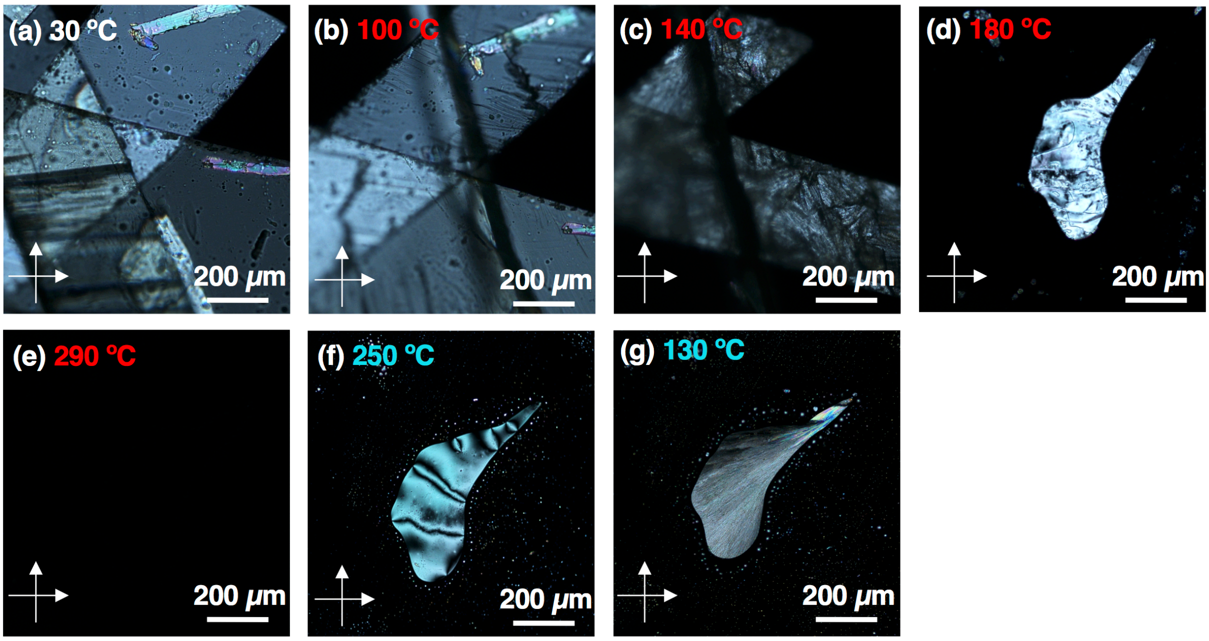

Figure 8-13. POM micrographs of Oli-FF-OC3 crystal at different temperatures of 30°C(a), 100°C(b), 140°C(c), 180°C(d), 290°C(e), 250°C(f) and 130°C (g). Red temperature and blue temperature mean heating process and cooling process, respectively.

In the case of Oli-FF-OC3, the behavior is more complicated. The peak at 87°C is only seen in the first cycle. This is assigned to another crystal state since there is no difference on the POM micrographs (Figure 8-13 a,b). *Upon* heating, the edge of the crystal is slightly soft (Figure 8-8c). This is a smectic phase. Subsequently, the smectic liquid crystal obtains more fluidity, but still sustains the polarization at 180°C (Figure 8-13d). This is a nematic liquid crystalline state. At 290°C, no cross-polarized image can be seen, indicating an isotropic state. When it cools down, the nematic state appears again. After 138°C, a crystalline or a smectic state appears. Oli-FH-OC3 shows a similar behavior except for the absence of the smectic phase confirmed by DSC and POM (Figure A8-3).

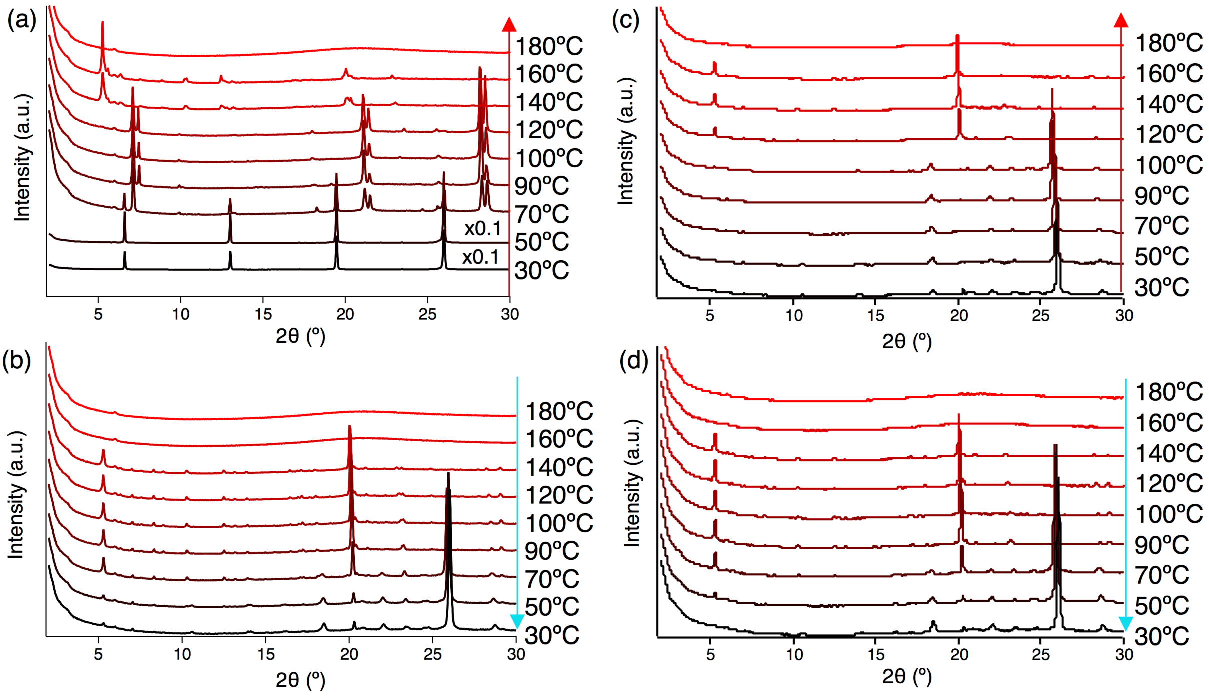

Figure 8-14. The first cycle of XRD diffractions of Oli-FF-OC3 crystal upon a heating(a) and cooling(b). The second cycle of XRD diffractions of Oli-FF-OC3 upon heating(c) and cooling(d).

To gain more insights into these complicated behavior, 2 cycles of XRD diffractions upon heating and cooling were measured (Figure 8-14). In the first heating, a transition from crystal to another crystal takes place at 50~90°C, a transition from crystal to smectic liquid crystal takes place at 120-140°C and smectic to nematic transition at 160-180°C takes place, respectively, although nematic phase does not show any diffraction. These phase transitions almost coincide with the data obtained by DSC and POM, but there is a slight difference through a cooling process. After the transition from nematic to smectic or crystal, no other transition is confirmed by POM or DSC. However, there is a clear difference between 70°C~50°C in XRD diffractions. This is assigned to the smectic liquid crystal to crystal transition as the smectic liquid crystal is highly ordered and energetically comparable to the crystal state. It is assumed that the reason why heat flow is not observed in DSC is due to the comparable energy difference between the smectic liquid crystal and the crystalline phase. The phase transition behavior of propyloxy PEs is summarized in Figure 8-15.

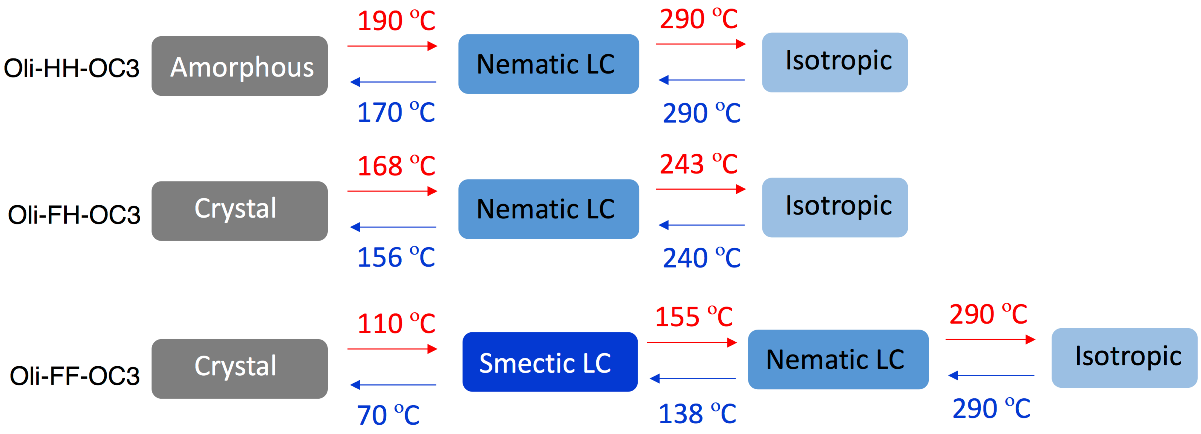

Figure 8-15. The summary of phase transitions of propyloxy-substituted PEs

8.4.3 1-ethynyl-4-hexyloxybenzene PEs

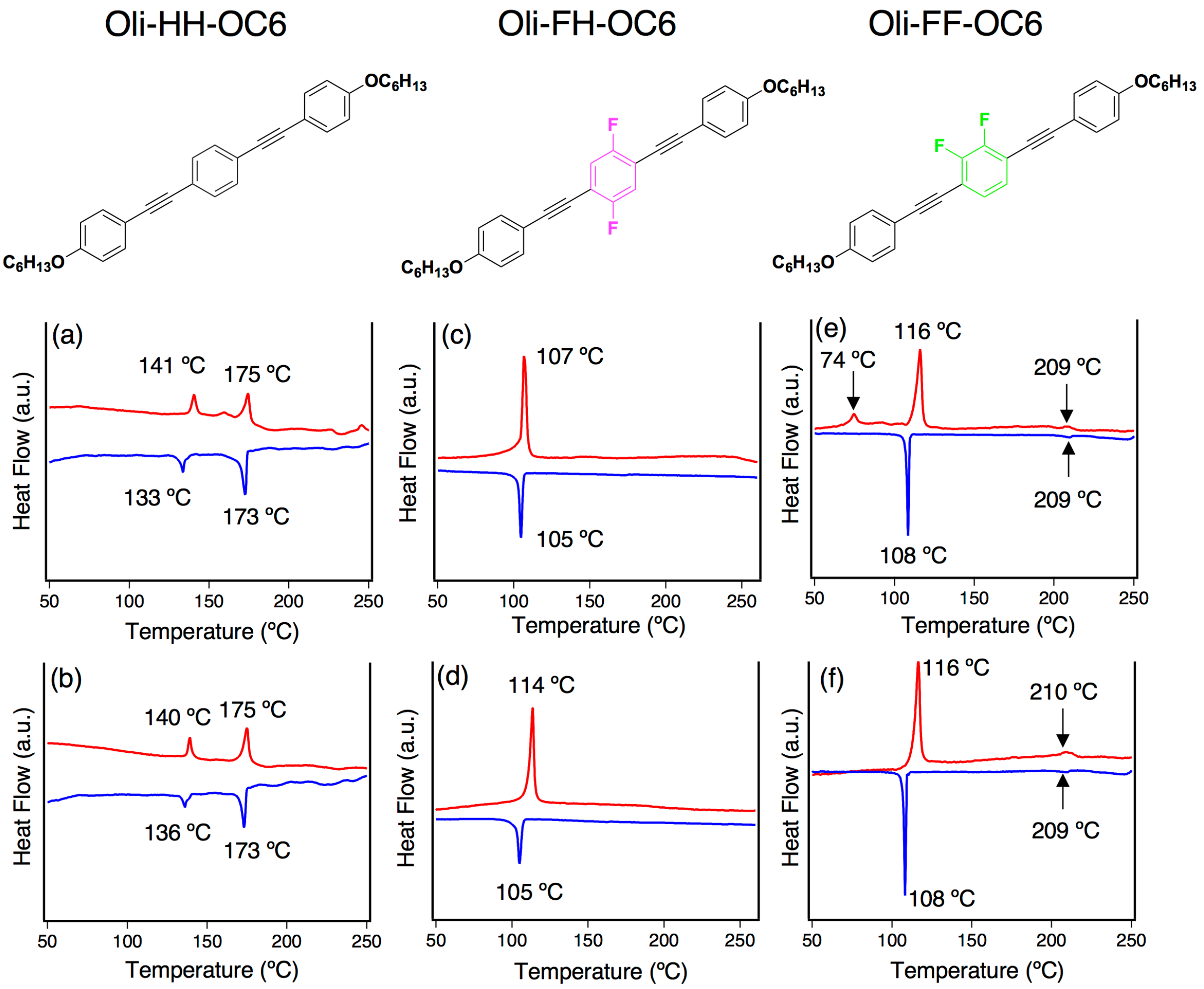

Figure 8-16. First cycles of DSC traces of Oli-HH-OC6(a), Oli-FH-OC6(c) and Oli-FF-OC6(e) and second cycles of DSC traces of Oli-HH-OC6(b), Oli-FH-OC6(d) and Oli-FF-OC6(f). Red and blue lines indicate heating and subsequent cooling, respectively.

When the alkoxy chains are extended to hexyl, the transition temperatures decrease in all cases (Figure 8-16) as generally known.[126] These three molecules have 3 transition states, a crystalline state, a nematic liquid crystal state, and an isotropic state (a liquid state). Interestingly, there is little difference in transition temperatures of heating and cooling, contrary to the cases of non-substituted PEs and propyloxy PEs. This means that the kinetic state, triggered by molecular rotation, is short when the PEs have long alkyl chains. Alkyl chains dominate the transition behavior. In the DSC trace of Oli-FH-OC6, the nematic to isotropic transition is not seen, although it is confirmed by the POM observation. In cases of Oli-FF-OC6 and Oli-FH-OC6, the transition behavior is similar to the cases of propyloxy-PEs. A crystal phase, a nematic phase, and an isotropic phase are seen (Figures 8-16, A8-5). Only in the case of Oli-HH-OC6, the smectic phase appeared, confirmed by both DSC and POM (Figure A8-4)

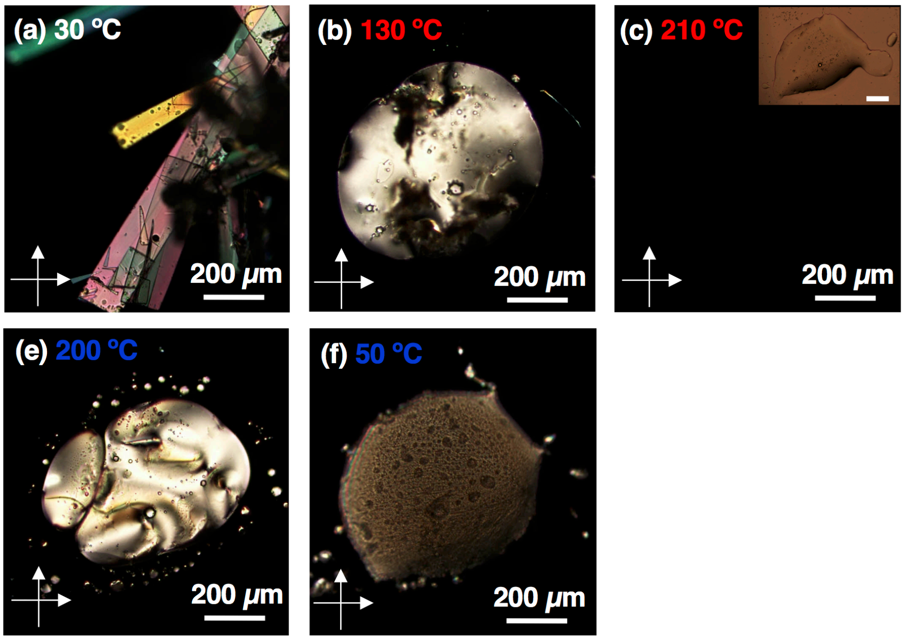

Figure 8-17. POM micrographs of Oli-FF-OC6 at different temperature of 30ºC (a), 130ºC (b), 210ºC (c), 200ºC (e) and 50ºC (f). The inset shows the images of the non-polarized microscopy. Red temperature and blue temperature mean heating process and cooling process, respectively. An inset shows the image of non-polarized microscopy with a scale bar of 200 μm.

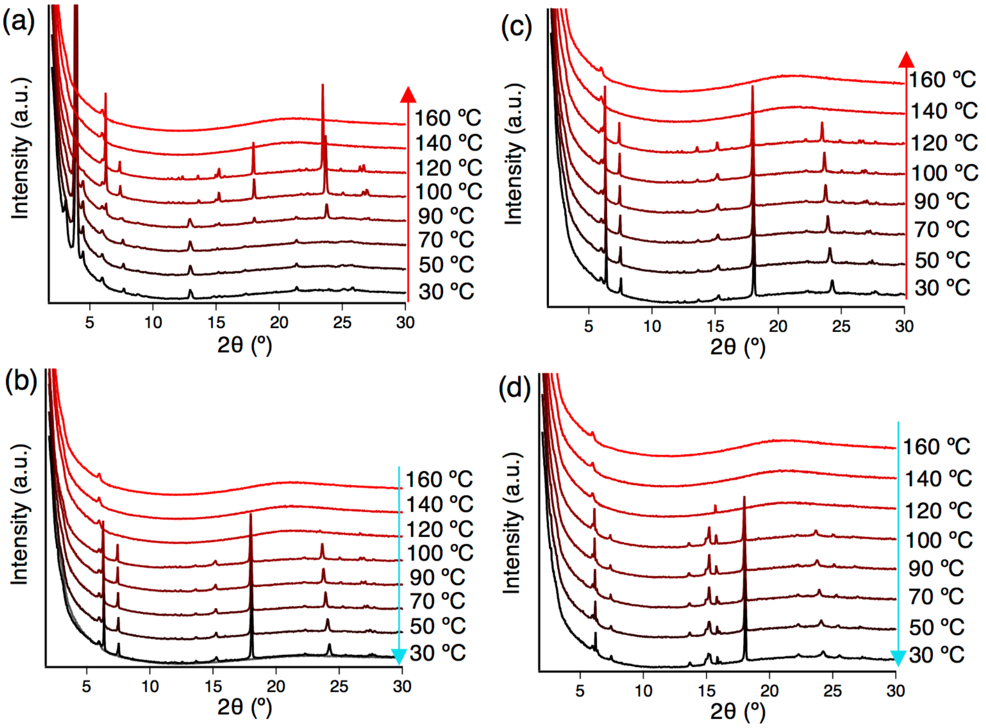

Figure 8-18. The first cycle of XRD diffractions of Oli-FF-OC6 crystal upon heating(a) and cooling(b). The second cycle of XRD diffractions of Oli-FF-OC6 upon heating(c) and cooling(d).

XRD diffractions of Oli-FF-OC6 were also measured (Figure 8-18). At 70-90°C, a crystal to another crystal transition is seen only in the first heating. a crystal to nematic transition is seen at 120-140°C in both heating processes and a nematic to crystal transition is also seen in both cooling processes. These insights are not contradictory to the insights obtained by POM and DSC. The phase transition behavior of Hexyloxy PEs is summarized in Figure 8-19.

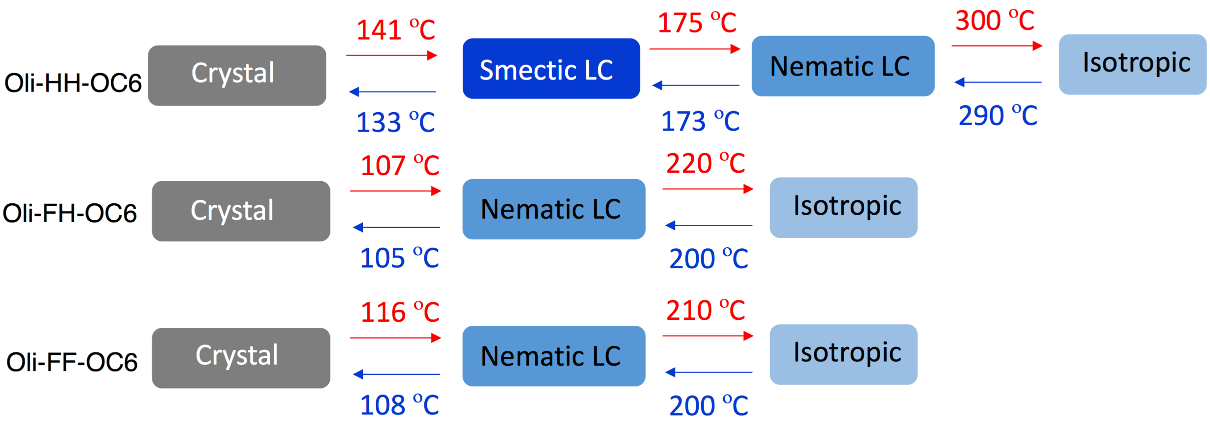

Figure 8-19. The first cycle of XRD diffractions of Oli-FF-OC6 crystal upon a heating(a) and cooling(b). The second cycle of XRD diffractions of Oli-FF-OC6 upon heating(c) and cooling(d).

8.5 Dielectric Responses

The liquid crystalline materials were put into the two ITO glasses to be capacitors and dielectric responses were measured. The capacitor configuration and the fabrication method are in figure A8-6 and Appendix, respectively. The capacitance of different frequencies was measured.

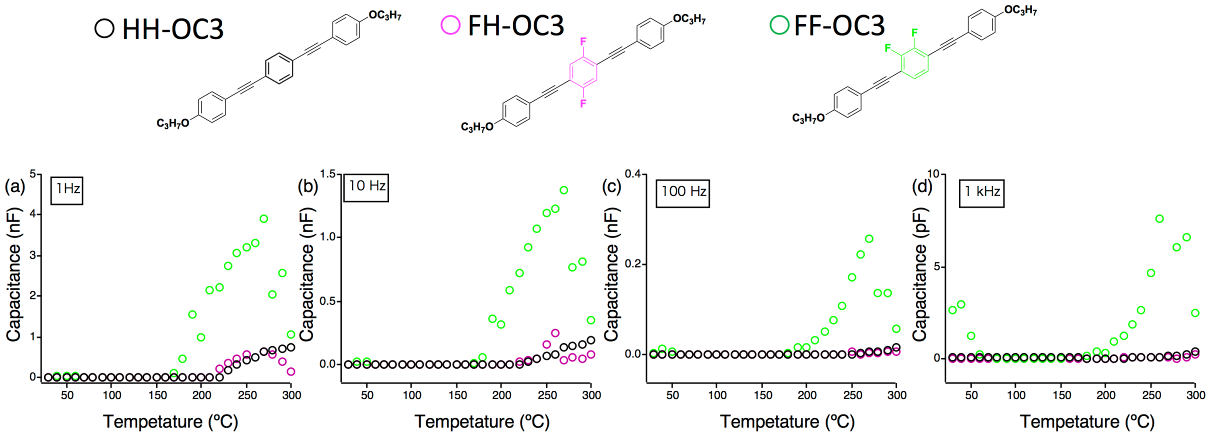

Figure 8-20. The capacitance as a function of temperature at the frequency of 1Hz(a), 10Hz(b), 100Hz(c) and 1kHz (d). Black, green and purple circles indicate Oli-HH-OC3, Oli-FH-OC3, and Oli-FF-OC3.

As shown in Figure 8-20, the dielectric capacitance of Oli-FF-OC3 begins to increase at 150-160°C, which corresponds to the temperature of the smectic to nematic transition and reaches its maximum at 270°C. When the temperature is higher than that, the capacitance decreases again.

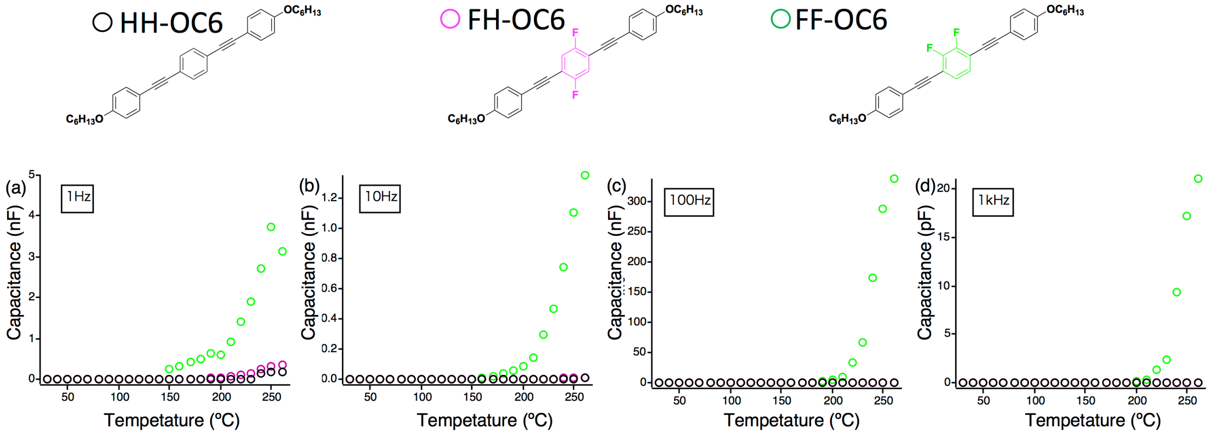

Figure 8-21. The capacitance as a function of temperature at the frequency of 1Hz(a), 10Hz(b), 100Hz(c) and 1kHz. Black, green and purple circles indicate Oli-HH-OC6, Oli-FH-OC6, and Oli-FF-OC6.

In the case of Hexyloxy substituted PEs, only Oli-FF-OC6 shows high capacitance in the range of nematic (and also isotropic) phases. Apparently, the increase of capacitance is correlated to the presence of dipoles of the central core (Figure 8-21).

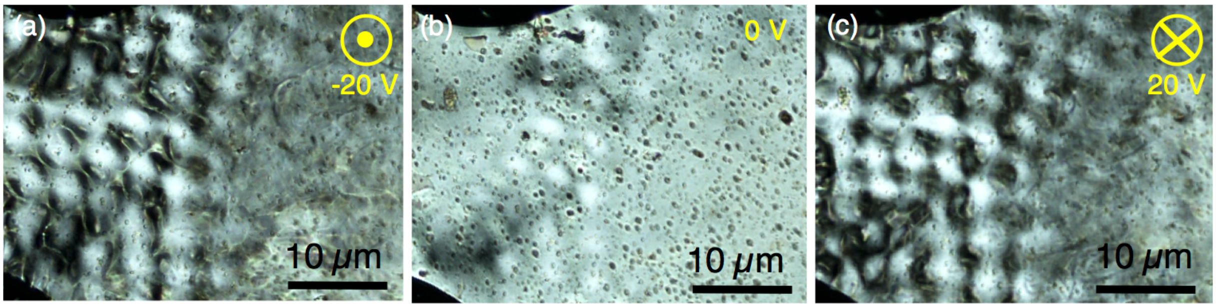

Figure 8-22. POM micrographs of Oli-FF-OC3 at 180℃ under the electric field of -20 V(a), 0V (b), 20V (c).

The dielectric anisotropy of Oli-FF-OC3 is negative. Therefore, the electric field does not induce dynamic structural movements. As seen in Figure 8-22, an electric field to the perpendicular to the ITO substrate makes the texture different, but it is not what can be expected in positively anisotropic liquid crystals. [117] If the positively anisotropic liquid crystal is biased, the molecules stand to the out of plane direction and a dark image can be seen, which is not the case in Oli-FF-OC3. When the dielectric response is taken in account, dipoles of Oli-FF-OC3 and Oli-FF-OC6 respond to the electric field while the molecules lie on the substrates.

8.6 Currents in Polarized PEs

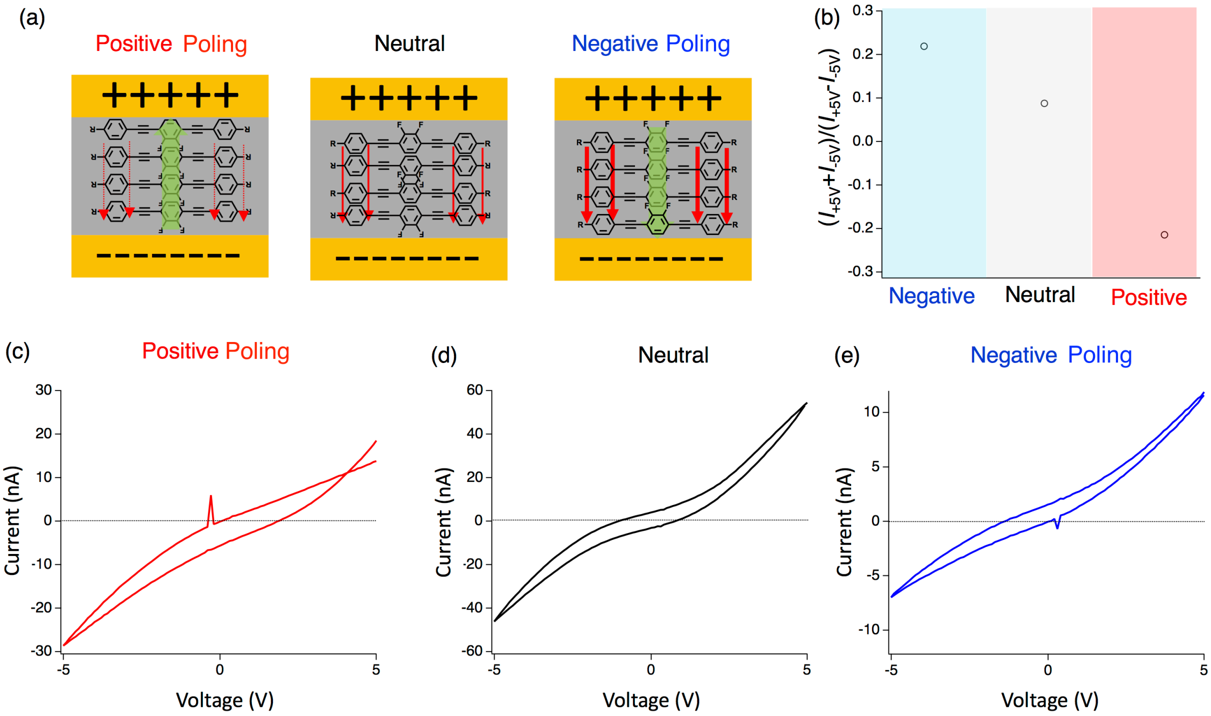

Figure 8-23. Current measurements under the poling at high temperature. (a) schematic illustrations of suggested polarization behavior after the poling treatment at high temperature. Green and red arrows mean dipole moments of compound and current, respectively. (b) The ratio of current at +/- electric field upon the poling treatments. The current upon a voltage sweep after the positive poling(c), the negative poling(e) and without poling (d).

The POM observations under an electric field suggest that the spontaneous dipoles of Oli-FF-OC3 can be controlled by the poling at high temperature. The treatment of “2D control” was applied to the compound to obtain the dipole-oriented crystal. 2D-control is the treatment that is controlled by the electric field and the temperature. The capacitor was heated up to smectic liquid crystalline state (140°C) and cooled down to room temperature under the ± 10 V/μm electric field to obtain the dipole-oriented solid materials (Figure 8-23). The current was measured *upon* a voltage sweep of ± 5 V at room temperature. When the compound is positively polarized, more current flows at minus voltage than at a plus voltage (Figure 8-23c). In contrast, more current flows at plus voltage than at minus voltage when the compound is negatively polarized (Figure 8-23d). The reference sample, which is not polarized at liquid crystalline state, shows isotropic currents at plus and minus voltages. The ratios of current at a positive and a negative voltage are shown (Figure 8-23b). The current quantity is not controlled because the fluid nature of liquid crystalline state affects the area size connected to the ITO plates. Yet, the current ratios suggest the net dipole orientations of Oli-FF-OC3 in the crystalline state (Figure 8-24). However, more control experiments are required to prove the dipole orientation.

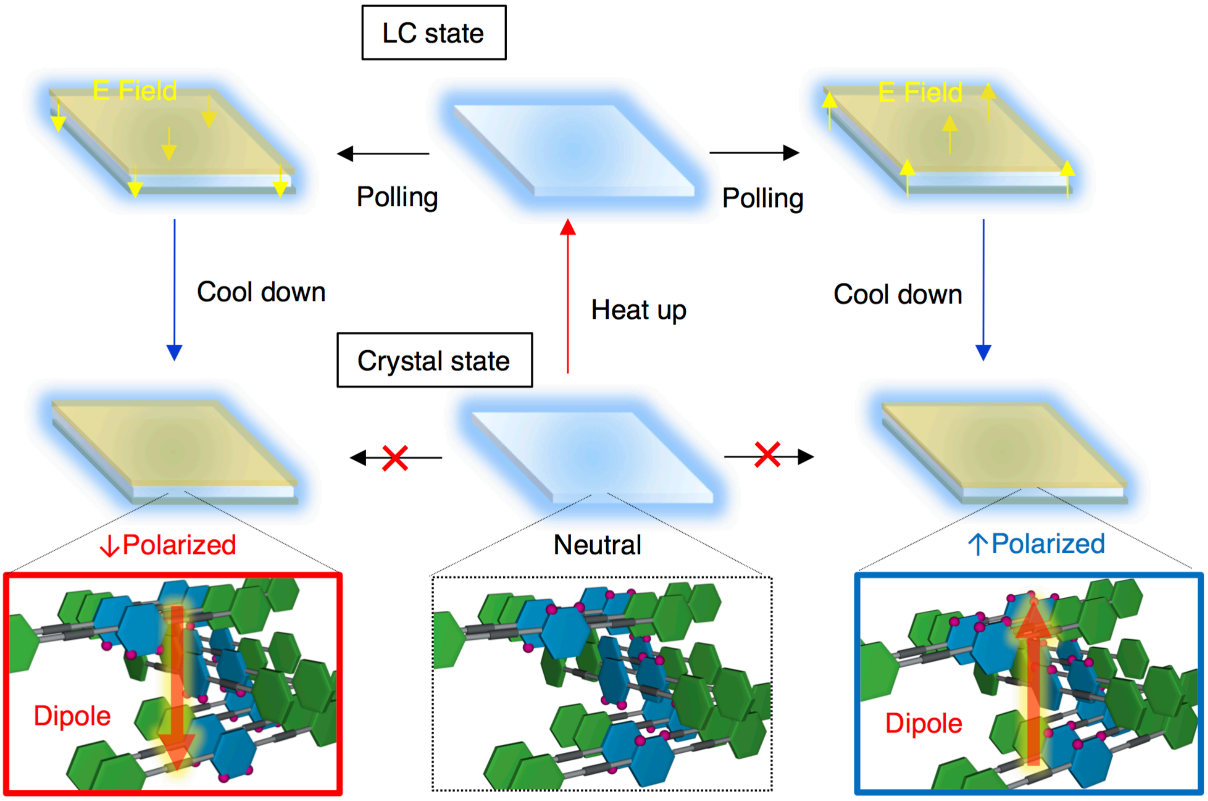

Figure 8-24. Schematic illustration of 2D control of dipole-orientation.

8.7 Short Summary of the Chapter

The phase transitions of PE oligomers are comprehensively investigated. PEs without alkoxy chains display simple crystalline to isotropic transitions. PEs with alkoxy chains display phase transitions to a nematic liquid crystalline state. Moreover, some PEs show transitions to the smectic liquid crystal. The dipolar PEs which contain *o*-difluorobenzene display the strong increase of capacitance at the liquid crystalline state, suggesting the response of dipolar units to an electric field. Poling at liquid crystalline temperature and subsequent cooling (2D-control) result in the formation of the dipole-oriented crystal, proved by the current anisotropy at negative and positive voltage. The dipole-control *via* electric field and temperature is useful to create stable piezoelectric materials. [114]

9 Conclusion

In this thesis, two main topics are discussed. The first topic is about π-ion gels and their applications to light-emitting devices and transistor devices.

In chapter 4, the gelation behavior is comprehensively investigated and the solvent exchange method is invented. As a result, π-ion gels, which are composed of an ionic liquid and a PPE, were formed successfully. The gels are non-volatile and display great thermal stability. Ionic liquids are of high dielectric constants. Therefore, many applications in electric devices are suggested.

In chapter 5, the π-ion gels are applied to light-emitting electrochemical cells. The bicontinuous structure of π-ion gels gives two advantages. The nano-segregation of conjugated polymer and ionic liquid allows for the distinct passways of ion and carrier conductions, resulting in the faster response (0.7-2 s) in comparison to the conventionally fabricated LECs (~15s). Moreover, the large interface between ionic liquid and conjugated polymer improves the doping efficiency as seen in the one order of magnitude increased capacitance. Owing to this effect, LECs based on the π-ion gels display 4 times brighter luminance and 10 times larger current density (~20 A/cm^2 at 5V). The concept to use gel geometry for LECs is demonstrated.

In chapter 6, π-ion gels are applied to a new type of transistor devices, named π-ion gel transistors (PIGTs). The π-ion gel is composed of 99% ionic liquid and 1% didodecyloxy-PPE. PIGTs display a high on/off ratio at low voltage operations. The device displays a volumetric current, that flows through a whole channel. More importantly, PIGTs respond as fast as 20 µs owing to the bi-continuous structures. The response time is the fastest among electrochemical based transistors. The high dielectric constant gives further benefits in carrier mobilities.

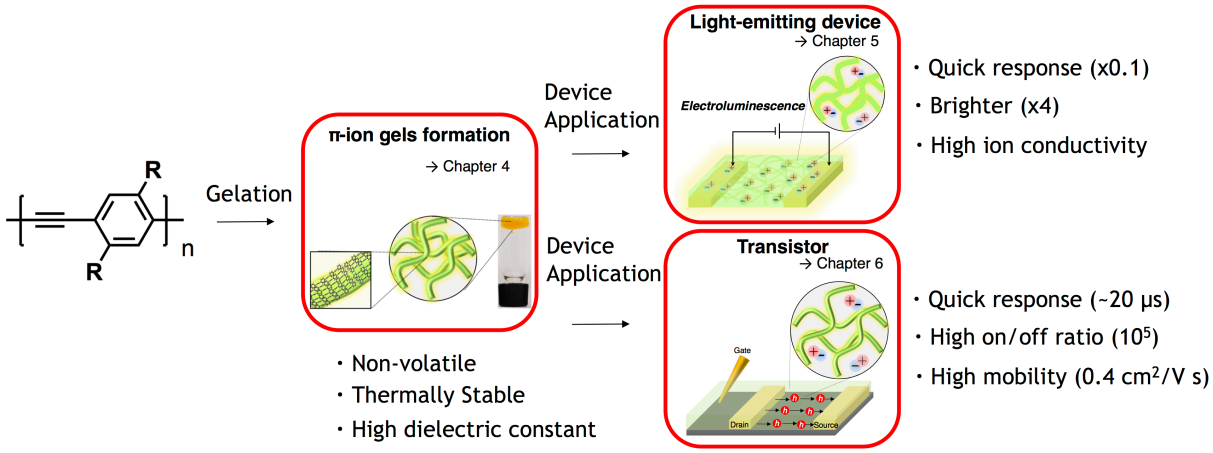

Figure 9-1. a work tree of the strategy "π-ion gels and their application"

The second topic is the molecular design to control the spontaneous dipole moments of molecules. The dipole moment in solid-state can behave as a permanent electric field, which is useful for device applications.

In chapter 7, the dipolar units of *o*-difluorobenzene are incorporated into PPE and a ferroelectric phase is achieved. Upon an electric field, polarization is induced. Anisotropic currents flow through a MIM diode, as a result. This is the first example of the ferroelectric conjugated polymers based on molecular rotation.

In chapter 8, the same concept is introduced to phenylene-ethynylene oligomers. Some oligomers display liquid crystalline state. 2D-control, which operates the electric field and the temperature, results in the formation of dipolar-oriented crystals, where anisotropic current flows.

The combination of phenylene-ethynylene derivatives and *o*-difluorobenznene introduces new dielectric properties such as ferroelectric characteristics and dipole-orientations.

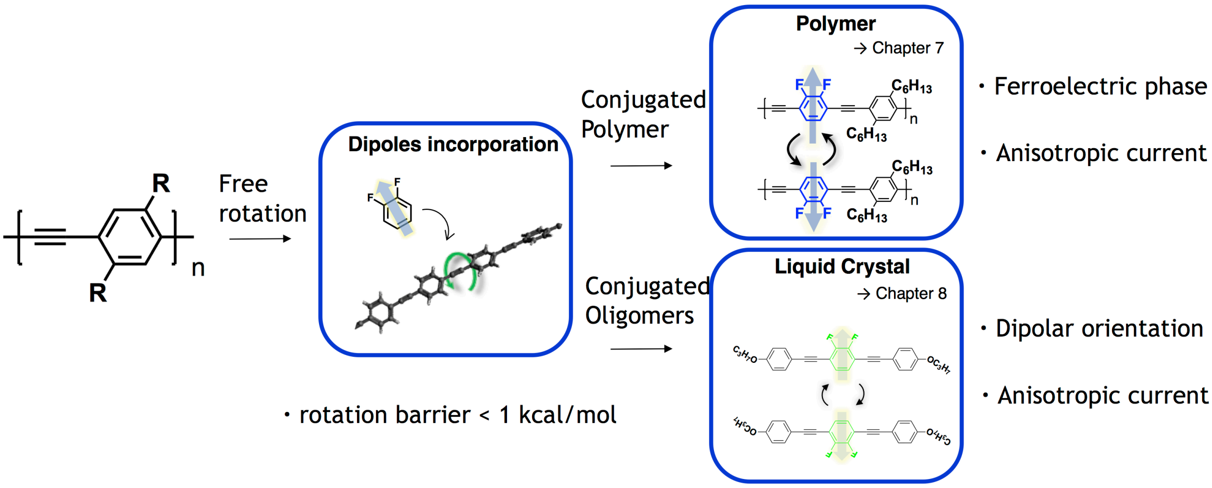

Figure 9-2. a work tree of the strategy “incorporation of dipolar units to conjugated molecules”

The strategies of those investigations are straightforward and the insights obtained can be transferred to other applications. As the conclusion of this thesis, dielectric behavior, which means both the quantity of dielectric constants and the variety of dielectric characteristics, makes large impacts on the versatile device performances and are worth to be investigated further. π-ion gels are intrinsically flexible and should be applied to printed electronic devices and wearable electronic devices. The *o*-difluorobenzene containing PPEs and PEs are also beneficial for organic electronic devices e.g. OLEDs since the dipole moments in solid can control the movement of carriers. It is desired that this thesis will contribute to future developments of organic electronics.

10 Bibliography

[1] D. D. Eley, *Nature* **1948**, *4125*, 819.

[2] H. Akamatu, H. Inokuchi, *J. Chem. Phys.* **1950**, *18*, 810.

[3] F. Ebisawa, T. Kurokawa, S.Nara, *J. Appl. Phys.* **1983**, *54*, 3255.

[4] H. Sirringhaus, *Adv.Mater.***2014**, *26*, 1319.

[5] T. Sekitani, Y. Noguchi, K. Hata, T. Fukushima, T. Aida, T. Someya, *Science*, **2008**, *321*, 1468.

[6] Nikkei Electronics **2004**, *16th Feb.*, 11.

[7] A.S. D. Sandanayaka, T. Matsushima, F. Bencheikh, S. Terakawa, W. J. Potscavage Jr., C. Qin, T. Fujihara, K. Goushi, J.-C. Ribierre, C. Adachi, *Appl. Phys. Express*, **2019,** *12*, 061010.

[8] H. Iino, T. Usui, J. Hanna, *nat. comm.* **2015**, 6, 3571.

[9] S. Koser *"*Rationalization of Structure-Property-Relationships of Modified (Hetero-)Acenes in Organic Electronics", *Ruprecht-Karls University,* **2018**, Heidelberg.

[10] J. Wudarczyk, G. Papamokos, V. Margaritis, D. Schollmeyer, F. Hinkel, M. Baumgarten, G. Floudas, K. Müllen, *Angew. Chem. Int. Ed.* **2016**, *55*, 3220.

[11] J. Wudarczyk, G. V. Papamokos, T. Marszalek, T. Nevolianis, D. Schollmeyer, W. Pisula, G. Floudas, M. Baumgarten, K. Müllen *ACS Appl. Mater. Interfaces*. **2017**, *9*, 20527.

[12] A. J. Heeger, N. S. Sariciftci, E. B. Namdas, "Semiconducting and Metallic Polymers", Oxford University Press **2010.**

[13] B.G. Yacobi, "*Semiconductor Materials: An Introduction to Basic Principles"*, Springer **2003**.

[14] H. Dong, X. Fu, J. Liu, Z. Wang, W. Hu, *Advanced Materials,* **2013**, *25*, 6158.

[15] B. Kumar, B. K. Kaushik, Y. S. Negi, *Polymer Reviews,* **2014**, *54*, 33.

[16] T. Sakanoue, H. Sirringhaus *Nat Mater*, **2010**, *9*, 736.

[17] M. E. Gershenson, V. Podzorov, A. F. Morpurgo, *Rev. Mod. Phys.* **2006**, *78*, 973.

[18] A. Nenashev, J. Oelerich, S. Baranovskii, *J. Phys. Condens. Matter,* **2015,** 27, 093201.

[19] R. A. Marcus, *J.Chem.Phys.***1956**, *24*, 966.

[20] R. A. Marcus, *J.Chem.Phys.***1956**, *24*, 979.

[21] V. Coropceanu, J. Cornil, D. A. da Silva Filho, Y. Olivier, R. Silbey and J.-L. Brédas, *Chem. Rev.* **2007**, *107*, 926.

[22] J. L. Brédas, J. P. Calbert, D. A. da Silva Filho, and J. Cornil, *PNAS* **2002**, *99*, 5804.

[23] Barbara P.F., *J. Phys. Chem*. **1996**, *100*,13148.

[24] Jortner, J. and Freed, K.F. J. Chem. Phys. **1970**, *52*, 6272.

[25] N. Seiki, Y. Shoji, T. Kajitani, F. Ishiwari, A. Kosaka, T. Hikima, M. Takata, T. Someya, T. Fukushima, *Science* **2015**, *348*, 1122.

[26] D. Abbaszadeh, A. Kunz, G. A. H. Wetzelaer, J. J. Michels, N. I. Crăciun, K. Koynov, I. Lieberwirth, P. W. M. Blom, *Nat. Mater.,***2016**, 15, 628

[27] Engineering ToolBox, (2010). Relative Permittivity - the Dielectric Constant. [online] Available at: https://www.engineeringtoolbox.com/relative-permittivity-d_1660.html

[28] Z. Dominguez, H. Dang, M. J. Strouse, M. A. Garcia-Garibay, J. Am. Chem. Soc. **2002**, *124*, 7719.

[29] S. Horiuchi, Y. Tokura, *Nat. Mat.* **2008**, *7*, 357.

[30] R. C. G.Naber, K. Asadi, P. W. M Blom, D. M. de Leeuw, B. de Boer, *Adv. Mater.* **2010**, *22*, 933

[31] J. C. Scott, L. D. Bozano, *Adv. Mater*. **2007**, *19*,1452.

[32] Q. D. Ling, D. J. Liaw, C. X. Zhu, D. S. H. Chan, E.T. Kang, K. G. Neoh, *Prog. Polym. Sci.* **2008**, *33*, 917.

[33] H. Anetai, Y. Wada, T. Takeda, N. Hoshino, S. Yamamoto, M. Mitsuishi, T. Takenobu, T. Akutagawa, *J. Phys. Chem. Lett.* **2015**, *6*, 1813.

[34] Y. Shishido, H. Anetai, T. Takeda, N. Hoshino, S. Noro, T. Nakamura, T. Akutagawa, *J. Phys. Chem. C* **2014**, *118*, 21204.

[35] D. Majumdar, S. K. Saha, *Appl. Phys. Lett*. **2010**, *96*, 18311.

[36] K. Akagi, H. Goto, H. Shirakawa, *Synth. Met.* **1997**, *84*, 313.

[37] E. Collet, M. H. Leḿee-Cailleau, M. B-L. Cointe, H. Cailleau, M. Wulff, T. Luty, S. Koshihara, M. Meyer, L. Toupet, P. Rabiller, S. Techert, *Science* **2003**, *300*,612.

[38] M. Pandeeswar, S. P. Senanayak, K. S. Narayan, T. Govindaraju, *J. Am. Chem. Soc.,* **2016**, *138*, 8259.

[39] T. Akutagawa, H. Koshinaka, D. Sato, S. Takeda, S. Noro, H. Takahashi, R. Kumai, Y. Tokura, T. Nakamura, *Nat. Mat.* **2009**, *8*, 342.

[40] D.-W. Fu, W. Zhang, H.-L. Cai, Y. Zhang, J. Ge, R.-G. Xiong, S. D. Huang, *J. Am. Chem. Soc*. **2011**, *133*, 12780.

[41] H. Sirringhaus, *Adv. Mater.* **2005**, *17*, 2411.

[42] A. Salehi, X. Fu, D.-H. Shin, F. So, A*dv. Funct. Mater.* **2019***, 29,* 1808803.

[43] B. Kippelen and J.-L. Brédas, *Energy Environ. Sci.* **2009**, *2*, 251.

[44] Y. Na, F. S. Kim, *Chem. Mater.* **2019**, *31,* 4759.

[45] M. J. Panzer, C. D. Frisbie, *Adv. Mater.* **2008**, *20*, 3177.

[46] H. H. Choi, K. Cho, C. D. Frisbie, H. Sirringhaus V. Podzorov, *Nat. Mater.* **2018**, *17*, 2.

[47] https://www.samsung.com/de

[48] J. H. Burroughes, D. D. C. Bradley, A. R. Brown, R. N. Marks, K. Mackay, R. H. Friend, P. L. Burns, A. B. Holmes, *Nature* **1990**, *347*, 539.

[49] U. H. F. Bunz, *Chem. Rev.* **2000**, *100*, 1605.

[50] U. H. F. Bunz, *Macromol. Rapid Commun*. **2009**, *30*, 772.

[51] U. H. F. Bunz, *Adv. Polym. Sci.* **2005**, *177*, 1.

[52] H. Dong, S. Jiang, L. Jiang, Y. Liu, H. Li, W. Hu, E. Wang, S. Yan, Z. Wei, W. Xu, X. Gong, *J. Am. Chem. Soc.*, **2009**, *131*, 17315.

[53] S. Schmid, A. K. Kast, R. R. Schröder, U. H. F. Bunz, C. Melzer, *Macromol. Rapid Commun*. **2014**, *35*, 1770.

[54] E. Smarsly, D. Daume, F. Braig, S. Koser, E. Dörsam, U.H.F. Bunz, *J. Mater. Chem. C*, **2018**, *6*, 11002.

[55] D. Perahia, R. Traiphol, U. H. F. Bunz, *J. Chem. Phys.* **2002**, *117*, 1827.

[56] D. K. Kumar, J. W. Steed, *Chem. Soc. Rev.* **2014**, *43*, 2080.

[57] A. Ajayaghosh, S. J. George, *J. Am. Chem. Soc.* **2001**, *123*, 5148.

[58] F. Würthner, C. Bauer, V. Stepanenko, S. Yagai, *Adv. Mater.* **2008**, *20*, 1695.

[59] S. Yagai, M. Ishii, T. Karatsu, A. Kitamura, *Angew. Chem., Int. Ed.* **2007**, *46*, 8005.

[60] S. Yagai, M. Higashi, T. Karatsu, A. Kitamura, *Chem. Mater.* **2004**, *16*, 3582.

[61] S. J. Ananthakrishnan, E. Varathan, N. Somanathan, V. Subramanian, A. B. Mandal, J. D. Sudha, R. Ramakrishnan, *J. Mater. Chem. C* **2014**, *2*, 9035.

[62] S. Sasaki, Y. Sugita, M. Tokita, T. Suenobu, O. Ishitani, G. Konishi, *Macromolecules* **2017**, *50*, 3544.

[63] F. Ishiwari, H. Hasebe, S. Matsumura, F. Hajjaj, N. Horii-Hayashi, M. Nishi, T. Someya, T. Fukushima, *Sci. Rep.* **2016**, *6*, 247275.

[64] K. Morishima, F. Ishiwari, S. Matsumura, T. Fukushima, M. Shibayama, *Macromolecules* **2017**, *50*, 5940.

[65] W. Y. Huang, S. Matsuoka, T. K. Kwei, Y. Okamoto, *Macromolecules* **2001**, *34*, 7166.

[66] D. Perahia, R. Traiphol, U. H. F. Bunz, *J. Chem. Phys.* **2002**, *117*, 1827.

[67] V. S. Nair, R. D. Mukhopadhyay, A. Saeki, S. Seki, A. Ajayaghosh, *Sci. Adv.* **2016**, *2*, e1600142.

[68] M. Koppe, C. J. Brabec, *Macromolecules* **2009**, *42*, 4661.

[69] U. H. F. Bunz, K. Müllen, J. R. Reynolds, T. Masuda, *R. Soc. Chem. Ser.* **2014**, 156.

[70] U. H. F. Bunz, J. M. Imhof, R. K. Bly, C. G. Bangcuyo, L. Rozanski, D. A. Vanden Bout, *Macromolecules* **2005**, *38*, 5892.

[71] M. I. Sluch, A. Godt, U. H. F. Bunz, M. A. Berg, *J. Am. Chem. Soc*. **2001**, *123*, 6447.

[72] L. T. Liu, D. Yaron, M. A. Berg, *J. Phys. Chem. C* **2007**, *111*, 5770.

[73] P. D. L. Iglesia, D. C. Pozzo, *Soft Matter* **2013**, *9*, 11214.

[74] M. Koppe, C. J. Brabec, **2009**, *42*, 4661.

[75] T. P. Lodge, T. Ueki, *Acc. Chem. Res.* **2016**, *49*, 2107.

[76] J. H. Cho, J. Lee, Y. Xia, B. Kim, Y. He, M. J. Renn, T. P. Lodge, *Nat. Mater.* **2008**, *7*, 900.

[77] R. C. Evans, P. C. Marr, *Chem. Commun.* **2012**, *48*, 3742.

[78] S. Kushida, E. Smarsly, L. Veith, I. Wacker, R. R. Schröder, U. H. F. Bunz, *Macromolecules* **2017**, *50*, 7880.

[79] Q. B. Pei, G. Yu, C. Zhang, Y. Yang, A. Heeger, *Science*, **1995**, *269*, 1086.

[80] J. Mindemarkab, L. Edman, *J. Mater. Chem. C,* **2016**, *4*, 420.

[81] S. B. Meier, D. Tordera, A. Pertegás, C. Roldán-Carmona, E. Ortí, H.J. Bolink, *Materials Today*, **2014**, *17*, 217.

[82] J.-H. Shin, L. Edman, *J. Am. Chem. Soc.,* **2006**, *128*, 15568.

[83] Q. B. Pei, Y. Yang, G. Yu, C. Zhang, A. J. Heeger, *J. Am. Chem. Soc.,* **1996**, *118*, 3922.

[84] A. Sandström, P. Matyba, O. Inganäs, L. Edman, *J. Am. Chem. Soc.,* **2010**, *132*, 6646

[85] T. Sakanoue, F. Yonekawa, K. Albrecht, K. Yamamoto, T. Takenobu, *Chem. Mater*. **2017**, *29*, 6122.

[86] F. Habrard, T. Ouisse, O. Stephan, M. Armand, M. Stark, S. Huant, E. Dubard, J. Chevrier, *J. Appl. Phys.,* **2004**, *96*, 7219.

[87] F. Habrard,; T. Ouisse, O. Stéphan, *J. Phys. Chem. B,* **2006**, *110*, 15049.

[88] A. Munar, A. Sandström, S, Tang, L. Edman, *Adv. Funct. Mater.* **2012**, *22*, 1511.

[89] Y. Cao, G. Yu, A. J. Heeger, C. Y. Yang, *Appl. Phys. Lett*. **1996**, *68*, 3218.

[90] M. Fahlman, S. Fabiano, V. Gueskine, D. Simon, M. Berggren, X. Crispin, *Nat. Rev. Mater.,* **2019**, 4, 627.

[91] J. Rivnay, S. Inal, A Salleo, R. M. Owens, M. Berggren, G. G. Malliaras, *Nat. Rev. Mater.*, **2018**, *3*, 17086.

[92] A. Laihoa, L. Herlogssona, R. Forchheimerb, X. Crispina, M. Berggren, *Proc. Natl Acad. Sci. USA,* **2011**, *108*, 15069.

[93] A. Giovannittia, D.-T. Sbirceaa, S. Inal, C. B. Nielsena, E. Bandielloe, D. A. Hanifif, M. Sessoloe, G. G. Malliarasb, I. McCulloch, J. Rivnay, *Proc. Natl Acad. Sci. USA*, **2016**, *113*, 12017.

[94] J. D. Yuen, A. S. Dhoot, E. B. Namdas, N. E. Coates, M. Heeney, I. McCulloch, D. Moses, A. J. Heeger, *J. Am. Chem. Soc.,* **2007**, *129*, 14367.

[95] J. Rivnay, P. Leleux, M. Ferro, M. Sessolo, A. Williamson, D. A. Koutsouras, D. Khodagholy, M. Ramuz, X. Strakosas, R. M. Owens, C. Benar, J.-M. Badier, C. Bernard, G. G. Malliaras, *Sci. Adv.* **2015**, *1*, e1400251.

[96] Y. Na, F. S. Kim, *Chem. Mater.* **2019**, *31*, 4759.

[97] C. Yumusak, M. Abbas, N. S. Sariciftci, *J. Luimin.* **2013**. *134*. 107.

[98] J. C. Scott, L. D. Bozano, *Adv. Mater.* **2007**, *19*, 1452.

[99] Q. D. Ling, D. J. Liaw, C. X. Zhu, D. S. H. Chan, E. T. Kang, K. G. Neoh, *Prog. Polym. Sci.* **2008**, *33*, 917.

[100] R. C. G. Naber, C. Tanase, P. W. M. Blom, G. H. Gelinck, A. W. Marsman, F. J. Touwslager, S. Setayesh, D. M. De **Leeuw**, *Nat.Mater.* **2005**, *4*, 243.

[101] K. Asadi, P. W. M. Blom, D. M. De Leeuw, *Adv. Mater.* **2011**, *23*, 865.

[102] Y. Yuan, T. J. Reece, P. Sharma, S. Poddar, S. Ducharme, A. Gruverman, Y. Yang, J. Huang, *Nat. Mater.* **2011**, *10*, 296.

[103] A. J. Lovinger, Science **1983**, *220*, 1115.

[104] U. H. F. Bunz, J. N. Wilson, C. Bangcuyo, *ACS Symp. Ser.* **2005**, *888*, 147.

[105] U. H. F. Bunz, J. M. Imhof, R. K. Bly, C. G. Bangcuyo, L. Rozanski, D. A. van Vanden Bout, *Macromolecules* **2005**, *38*, 5892.

[106] M. Levitus, K. Schmieder, H. Ricks, K. D. Shimizu, U. H. F. Bunz, M. A. Garcia-Garibay, *J. Am. Chem. Soc.* **2001**, *123*, 4259.

[107] A. Beeby, K. Findlay, P. J. Low, T. B. Marder, *J. Am. Chem. Soc.* **2002**, *124*, 8280.

[108] T. Miteva, L. Palmer, L. Kloppenburg, D. Neher, U. H. F. Bunz, *Macromolecules* **2000**, *33*, 652.

[109] J. Kim, T. M. Swager, *Nature* **2001**, *411*, 1030.

[110] T.-A. V. Khuong, J. E. NuÇez, C. E. Godinez, M. A. Garcia-Garibay, *Acc. Chem. Res.* **2006**, *39*, 413.

[111] K. B. Woody, J. E. Bullock, S. R. Parkin, M. D. Watson, Macromolecules **2007**, *40*, 4470.

[112] S. Nishihara, T. Akutagawa, D. Sato, S. Takeda, S, Noro, T. Nakamura, *Chem. Asian J.* **2007**, *2*, 1083.

[113] D. Miyajima, F. Araoka, H. Takezoe, J. Kim, K. Kato, M. Takata, T. Aida, *Science* **2012**, *336*, 209.

[114] K. Asadi, M. A. van der Veen, *Eur. J. Inorg. Chem*. **2016**, 4332.

[115] C. Weder, C. Sarwa, A. Montali, C. Bastiaansen, P. Smith, *Science* **1998**, *279*, 835.

[116] S. Kushida, E. Smarsly, N. M. Bojanowski, I. Wacker, R. R. Schrçder, O. Oki, Y. Yamamoto, C. Melzer, U. H. F. Bunz, *Angew. Chem. Int. Ed.* **2018**, *57*, 17019.

[117] J. W. Goodby, P. J. Collings, T. Kato, C. Tschierske, H. Gleeson, P. Raynes, "Handbook of Liquid Crystals" **2014,** Wiley-VCH, Weinheim

[118] D. Pauluth, K, Tarumi, *J. Mater. Chem.*, **2004**, *14*, 1219.

[119] Y. Noguchi, N. Sato, Y. Tanaka, Y. Nakayama, H. Ishii, *Appl. Phys. Lett.* **2008,** *92*, 203306.

[120] Y. Noguchi, Y. Miyazaki, Y. Tanaka, N. Sato, Y. Nakayama, T. D. Schmidt, W. Brütting, H. Ishii, *J. Appl. Phys.* **2012**. *111*, 114508.

[121] D. A. Coleman, J. Fernsler, N. Chattham, M. Nakata, Y. Takanishi, E. Körblova, D. R. Link, R.-F. Shao, W. G. Jang, J. E. Maclennan, O. Mondainn-Monval, C. Boyer, W. Weissflog, G. Pelzl, L.-C. Chien, J. Zasadzinski, J. Watanabe, D. M. Walba, H. Takezoe, N. A. Clark, *Science,* **2003,** *301*, 1204.

[122] A. Seki, Y. Funatsu M. Funahashi, *Phys. Chem. Chem. Phys.*, **2017**, *19*, 16446.

[123] Y. Funatsu, A. Sonoda, M. Funahashi, *J. Mater. Chem. C,* **2015**, *3*, 1982.

[124] S. W. Watt, C. Dai, A. J. Scott, J. M. Burke, R. L. Thomas, J. C. Collings, C. Viney, W. Clegg, T. B. Marder, *Angew. Chem. Int. Ed.* **2004**, *43*, 3061.

[125] U. H. F. Bunz, V. Enkelmann, L. Kloppenburg, D. Jones, K. D. Shimizu, J. B. Claridge, H.-C. zur Loye, G. Lieser., *Chem. Mater.* **1999**, *11*, 1416.

[126] T. Yatabe, Y. Suzuki Y. Kawanishi, *J. Mater. Chem.*, **2008**, *18*, 4468.

11 Appendix

11.1 Appendix to the Chapter 4

11.1.1 Experimental Section of Chapter 4

Unless otherwise noted, reagents and solvents were used as received from Aldrich Chemical Co. Ltd, Tokyo Chemical Industry Co. Ltd., and the chemical store at the Organisch-Chemisches Institut of the University of Heidelberg or from commercial laboratory suppliers. Polymers were synthesized and published previously. [54] Photoabsorption and PL spectra were recorded on a JASCO V-660 spectrophotometer and a JASCO FP-6500 spectrofluorometer, respectively. Fluorescence lifetimes τ were acquired by an exponential fit according to the least mean square with commercially available software HORIBA Scientific Decay Data Analyses 6 (DAS6) version 6.4.4. The luminescence decays were recorded with a HORIBA Scientific Fluorocube single photon counting system operated with HORIBA Scientific DataStationversion 2.2. Scanning electron microscopy images were taken with Zeiss Ultra 55. Thermogravimetry analysis (TGA) measurements were carried out with TGA/DSC1 STARe System of Mettler Toledo. All photographs were taken with Canon EOS 7D.

Synthesis All of the PPEs are literature known and prepared by the Sonogashira coupling of dialkoxydiethynylbenzenes or dialkyl- diethynylbenzenes to the corresponding dialkoxydiiodobenzenes or dialkyldiiodobenzenes, respectively, according to ref 25.

Thermally Promoted Gelation. 0.5–10 mg of the PPEs was dissolved in 500µL of THF by heating up to 80°C in a 1mL vial under air. The solution was capped and allowed to cool down slowly to room temperature and let it sit for at least 24 h in closed box at ambient temperature.

Solvent Promoted Gelation. 500 µL of THF polymer solution in a 1 mL vial was placed in a 5 mL vial and filled with methanol, without capping. The 5 mL vial was closed and incubated for at least 24 h. The concentration of solution varied from 0.5 to 5 mg/mL.

Gel Test. Gel formation was confirmed by simple inversion of the vials.

Scanning Electron Microscopy (SEM) Measurement. Typically, pieces of the gels were mounted on Si/SiO2 wafer and dried overnight under vacuum. The wafer was fixed on an aluminum plate by silver ink. The images were taken with accelerating voltage and working distance of 1.5 kV and

3 mm, respectively. For measurements of Figure 4-7d−f, the samples were spin-coated onto Si/SiO2 with 2000 rpm (60 s) to remove the dissolved portion of polymers.

Emission and Absorption Measurements. Photoemission spectra were taken from the vials as prepared. For absorption spectra measurements, samples were spread on a glass plate with the spacer of 50 µm and enclosed with a second glass plate. To avoid the evaporation, the two plates were enclosed by tape, and the spectra were measured as soon as possible. The drop-cast films were prepared by casting and drying a small amount of a 1 mg/mL PPE-containing solution onto a glass plate. The reference solution spectra were taken from a 1 µg/mL solution in a 1 mm quartz cell. The same reference samples were also used for the lifetime measurements.

Temperature Stability Test. The temperature stability test of the samples shown in Figure 4-8a was done as follows. Both gels, prepared by SOG or by TOG, were placed on an aluminum foil coated hot plate with tightly closed caps. The temperature was increased at the rate of approximately 5 K/min.

Ion Gel Formation. 2.5 mg/mL SOG was prepared. 300 µL of the ionic liquid tributylmethylammoniumbis(trifluoromethanesulfonyl)- imide was injected on top of the gel layer, and the vial was incubated for 1 day without a cap. The solvent but not the ionic liquid evaporated, and the pure ionic liquid gels formed.

11.1.2 Appendix Figures of Chapter 4

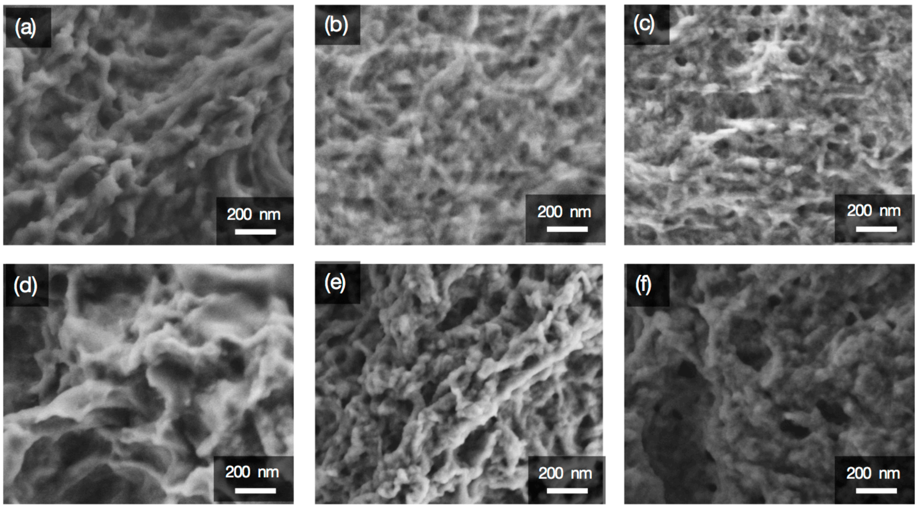

Figure A4-1. SEM Micrographs of self-assembled nano-structures of solvent promoted gel of D-PPE with the combinations of THF – MeOH (a), THF - Acetnitrile (b), THF – Acetone (c), CHCl3- MeOH (d), CHCl3- Acetnitrile (e), and CHCl3- Acetone (f).

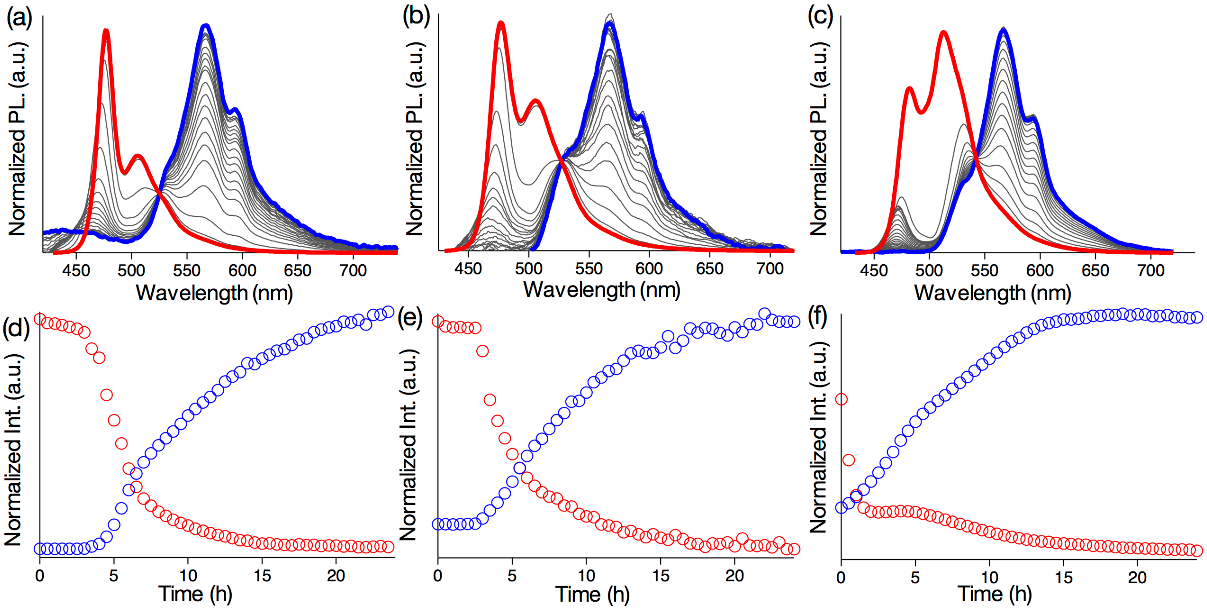

Figure A4-2. Time depending emission spectra of solvent promoted gel of D-OPPE with the concentrations of 1 mg/ml (a), 2.5 mg/ml (b, same data with Fig. 5a), and 5 mg/ml (c). The spectra were taken every hour from 0h (red) to 24h (blue) and normalized at 525 nm, 530 nm and 542 nm, respectively. Plots of Time versus emission intensity at 477 nm (red) and 566 nm (blue) of solvent promoted gel of D-OPPE with the concentrations of 1.0 mg/ml (d), 2.5 mg/ml (e), and 5 mg/ml (f).

11.2 Appendix to the Chapter 5

11.2.1 Experimental Section of Chapter 5

Unless otherwise noted, reagents and solvents were used as received from Aldrich Chemical Co. Ltd, Tokyo Chemical Industry Co. Ltd., and the chemical store at the Organisch-Chemisches Institut of the University of Heidelberg or from commercial laboratory suppliers. Number-average (M_n) and weight-average (M_w) molecular weights and polydispersities (PDI, M_w/M_n) were determined by GPC versus polystyrene standards at room temperature in chloroform with PSS-SDV columns (8.0 mm x 30.0 mm, 5 µm particles, 102 -, 103 - and 105 - Å pore size) on a Jasco PU-2050 GPC unit equipped with a Jasco UV-2075 UV- and a Jasco RI-2031 RIdetector. Photoabsorption and PL spectra were recorded on a JASCO V-660 spectrophotometer and a JASCO FP-6500 spectrofluorometer, respectively. Scanning electron microscopy images were taken with Zeiss Ultra 55, Inlens detector, line averaged scanning mode, accelerating voltage of 1.5 kV. Variable temperature powder XRD patterns were recorded on a RIGAKU model Miniflex600 diffractometer with a CuKα radiation source (40 kV and 15 mA), equipped with model D/Tex Ultra2-MF high-speed 1D detector. Electroluminescence measurements were performed on a homemade photodiode stage connected to FEMTO current amplifier (model: DHPCA-100) and Agilent Technologies digital storage oscilloscope (DSO-X 3014A). Current measurements were performed on a Keithley 2636B system source meter. Step bias measurements and Impedance measurements for ion conductance were performed with a Solartron analytical Modulab MAT equipping MHV100. The synthesis of the conjugated polymer, Poly-((para-phenyleneethynylene) with Dihexyl side chain (dihexyl-**PPE**) is reported in previous publication.(S1)

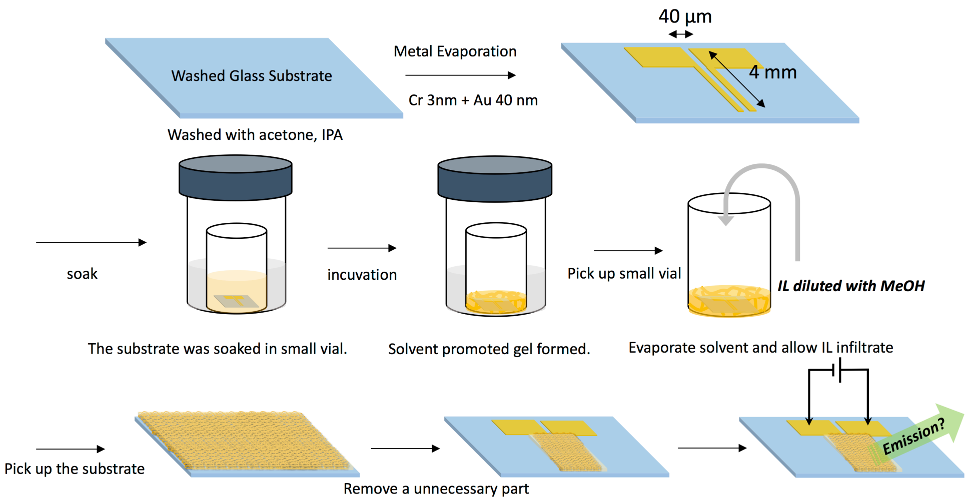

SchemeA5-1 Preparation protocol of PPE gel-based device.

Gel Device Fabrication. An 1.2 cm x 1.2 cm large glass substrate was washed with acetone and isopropanol in an ultrasonication. Chromium (3 nm) and gold (40 nm) were thermally evaporated onto the substrate in vacuum to fabricate the lateral finger electrodes. The configuration is 4 mm of length and 40 µm of width, respectively. The substrate was soaked in a small vial with a solution of PPE in tetrahydrofuran (2.5 mg mL-1, 400 µL) without capping. The small vial was put into large vial with 1 mL of methanol; the larger vial was closed. Incubation for one day results in solvent exchange with gel formation. A given amount of ionic liquid in 100 µL of methanol solution was slowly added to the gel in methanol, not to mechanically break the gel. The methanol was removed by evaporation typically for two to three days. The substrate was picked up and the gel fractions apart from the contacts were removed. The devices were held under vacuum before the measurements for 15 min. All the processes were done in the glovebox (O2: < 3 ppm. H2O: < 1 ppm.). The schematic protocol is shown(SchemeA5-1).

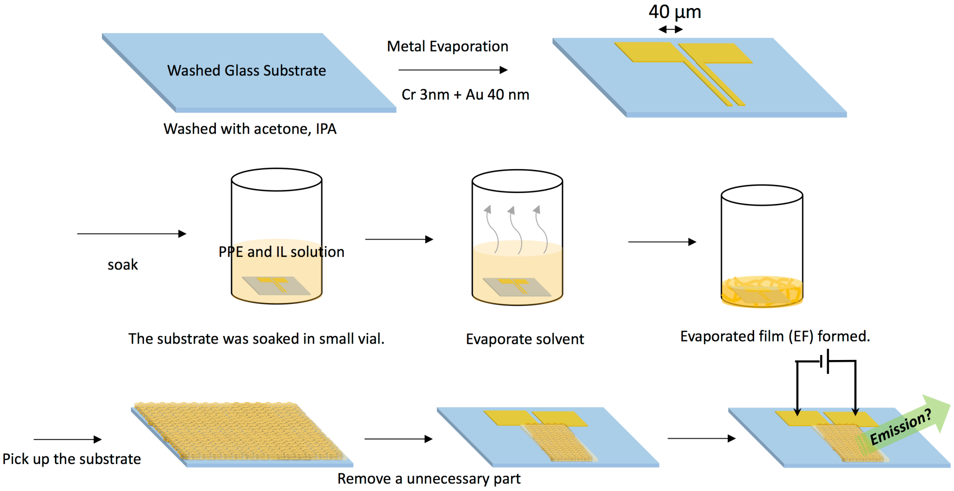

SchemeA5-2 Preparation protocol of the drop-casting film device (DF).

DF Device Fabrication. The fabrication processes of the Au electrodes are same as above. The substrate was soaked in a small vial with PPE (2.5 mg mL-1, 400 µL) and the ionic liquid in tetrahydrofuran solution was added without capping. The THF evaporated and a thin film formed in one to two days. The devices were held under vacuum before the measurements for 15 min. All the processes were done in the glovebox (O2: < 3 ppm. H2O: < 1 ppm.). The schematic protocol is shown(Scheme A5-2).

SP Device Fabrication. The fabrication processes of electrodes are same above. The PPE (8 mg mL-1) and the ionic liquid in tetrahydrofuran solution were spin cast on the substrate with the parameter of 1000 rpm. The devices were held under vacuum before the measurements for 15 min. All the processes were done in the glovebox (O2: < 3 ppm. H2O: < 1 ppm.).

Electroluminescence and Current Density Measurements. A power source was connected to the prepared device and oscilloscope. A photodiode was placed on the device and was connected to the amplifier and oscilloscope as well. The applied bias and electroluminescence (EL) were synchronized on the oscilloscope and current density and EL were measured depending on the time. The response time was defined as the time to reach the maximum luminance. Lifetime is defined as the time to reach 20% luminance relative to the maximum luminance. The luminance was measured on basis of the current of the photo diode. 3 independent devices were measured and the averaged value is shown in Figure2c-e in case of gel devices.

Step Bias Measurements. Step DC voltage (every 200 mV, typically 20 s) with a superimposed AC voltage (10 mV, 1 kHz) was applied from 0V to 5 V directly to the devices. The DC current density and AC capacitance as a function of DC voltage were recorded.

Ion Conductivity Measurements. 100 mV AC voltage as a function of frequency (1 MHz - 100 mHz) was applied to the devices. Real and imaginary value of capacitance were obtained. By fitting with the equivalent circuit [88] (Figure A5-10), the ion conductivity was estimated. Fitting results are shown in Figure S9-11.

11.2.2 Appendix Figures of Chapter 5

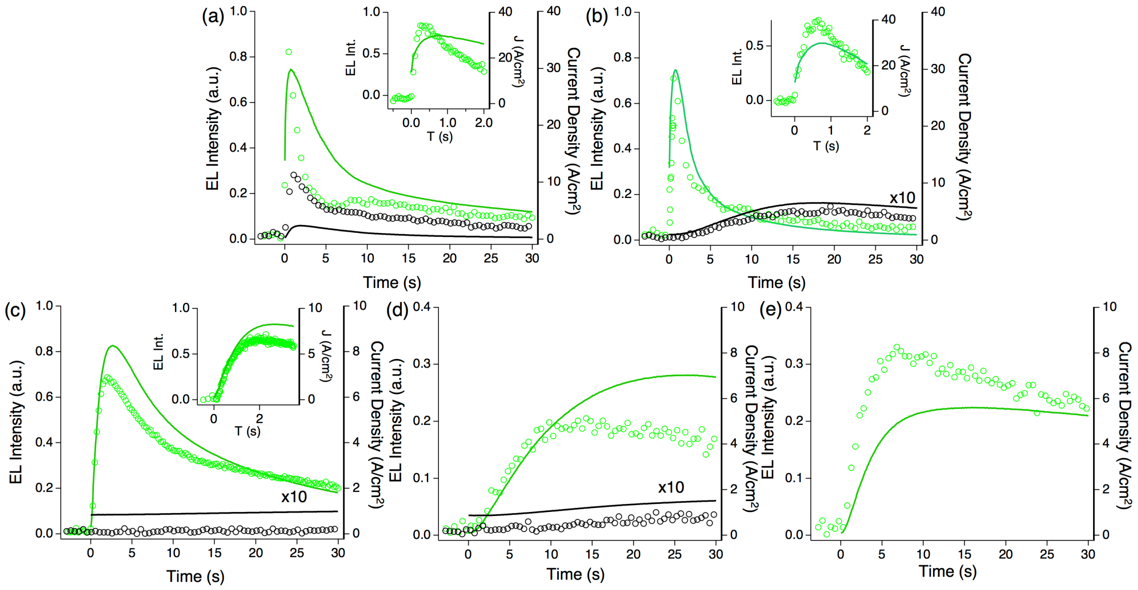

Figure A5-1. EL intensity (dot) and current density (solid) of devices as a function of time. Green and black show Gel and DF, respectively. IL ratio is 1.0 (a), 0.8 (b), 0.6 (c), 0.4 (d) and 0.2 (e). The current density of DF0.8, DF0.6 and DF0.4 is multiplied by 10 times.

Table A5-1. Values of Response time, EL intensity, current density and lifetime as a function of Gel and CF devices.

	Turn-on time	Luminance	Current Density	Lifetime
Gel$_{1.0}$	0.87 s (±0.21 s)	0.59 (±0.08)	19.47(± 8.0) A/cm^2	23.3 (±2.9) s
DF$_{1.0}$	1.05 s	0.28	2.13 A/cm^2	22.6 s
Gel$_{0.8}$	2.03 s (±0.12 s)	0.48 (±0.29)	7.72(±0.38) A/cm^2	68.1 (±21) s
DF$_{0.8}$	19.53 s	0.14	0.65 A/cm^2	58.5 s
Gel$_{0.6}$	2.03 s (±0.34 s)	0.49 (±0.16)	19.4(±11.4) A/cm^2	52.3 (±17) s
DF$_{0.6}$	19.73 s	0.03	0.13 A/cm^2	>100 s
Gel$_{0.4}$	13.28 s (±3.98 s)	0.20 (±0.0)	5.7(±10.1) A/cm^2	>100 s
DF$_{0.4}$	> 100.0 s	0.02	0.10 A/cm^2	>100 s
Gel$_{0.2}$	30.68 s (±6.33 s)	0.13 (±0.03)	1.96(±0.11) A/cm^2	>100 s
DF$_{0.2}$	> 100.0 s	0	0 A/cm^2	-

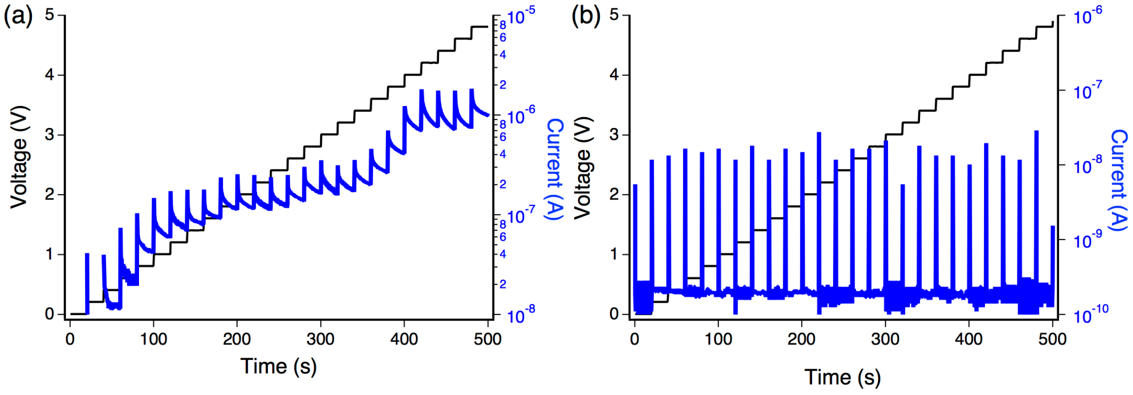

Figure A5-2. Current and applied voltage of IL (a) and Gel without IL (b) as a function of time.

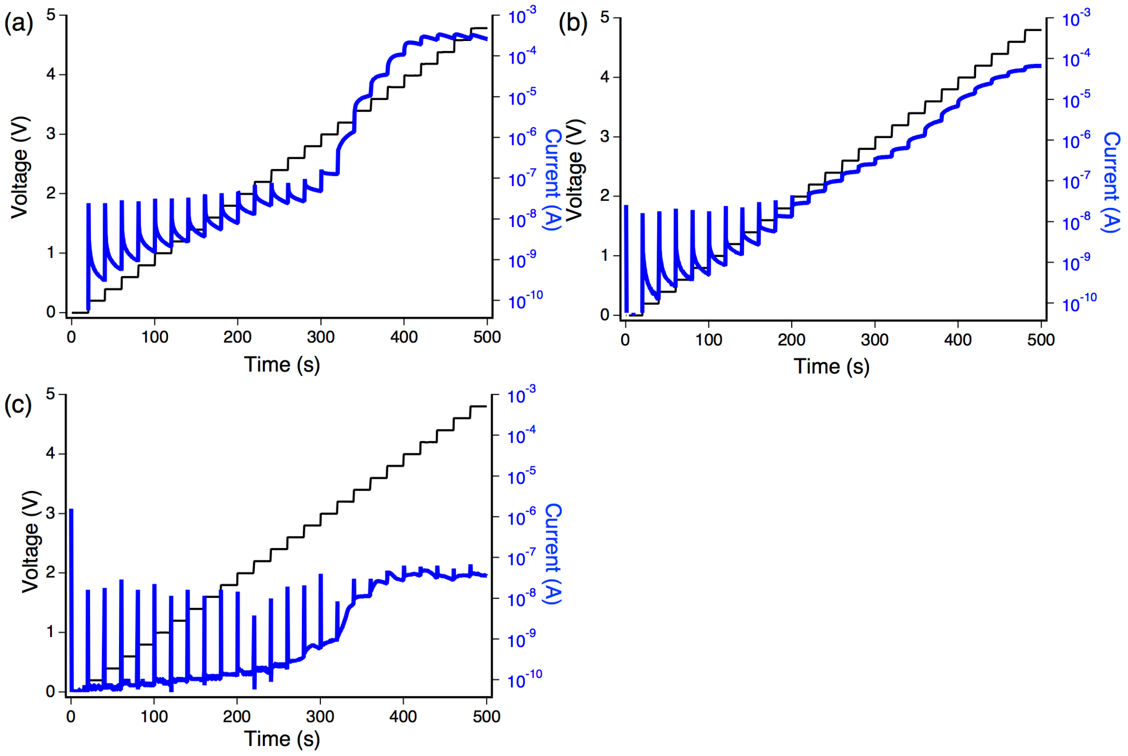

Figure A5-3. Current and applied voltage of Gel (a), DF(b) and SP (c) as a function of time. IL wt. ratio is 0.8 for all.

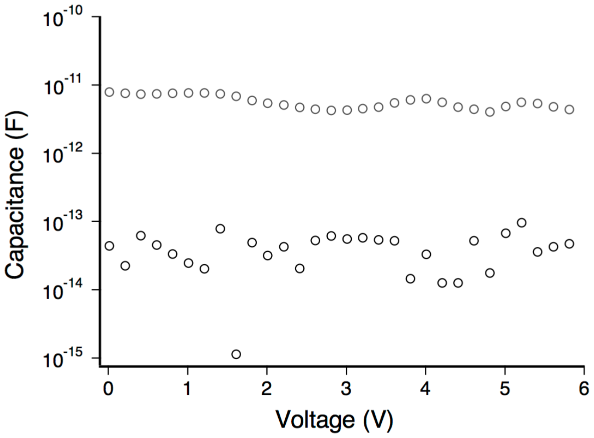

Figure A5-4. Capacitance of IL (gray) and Gel0 as a function of applied DC voltage measured at 1 kHz Hz. AC amplitude was 10 mV.

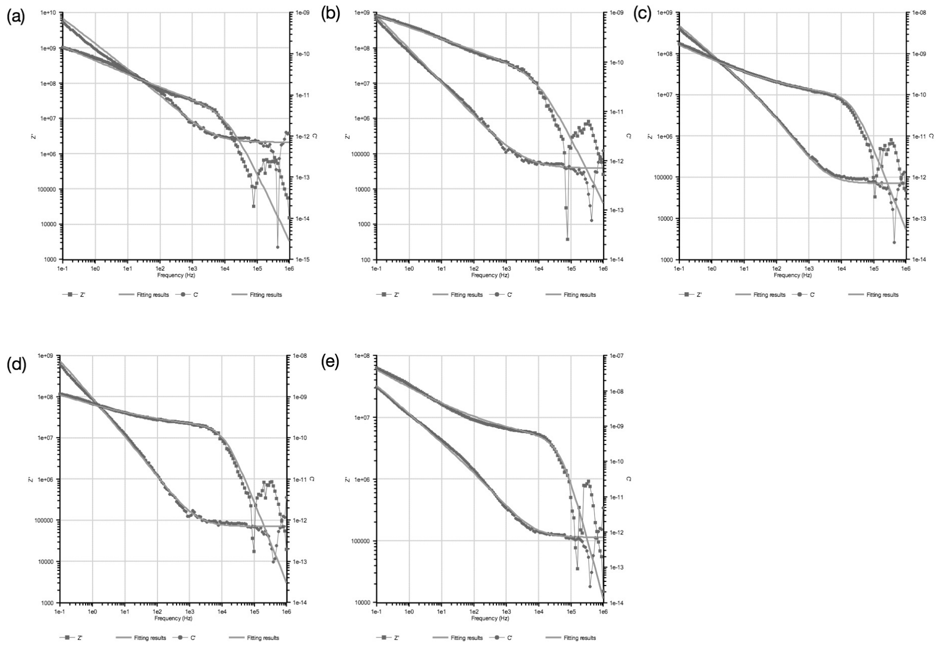

Figure A5-5. Impedance, capacitance and the best fitted result of SP devices as a function of frequency. IL ratio is 0.2 (a), 0.4 (b), 0.6 (c), 0.8 (d) and 1 (e), respectively.

Table A5-2. The best fitted parameters of Gel devices. Re and C_{geo} are estimated from non-IL device and fixed 130 G Ω and 0.9 pF, respectively.

IL ratio	**R_{ion}**	**CPE1 (EDL1)**		**CPE2 (EDL2)**	
		TDI	Phide	TDI	Phide
0.2	1.90 MΩ	5.9×10^{-8}	0.42	2.7×10^{-8}	1
0.4	1.44 MΩ	6.3×10^{-8}	0.45	2.6×10^{-8}	1
0.6	0.52 MΩ	1.6×10^{-7}	0.40	2.3×10^{-8}	1
0.8	0.30 MΩ	1.9×10^{-7}	0.42	2.4×10^{-8}	0.97
1.0	0.25 MΩ	3.7×10^{-7}	0.35	3.4×10^{-8}	0.89

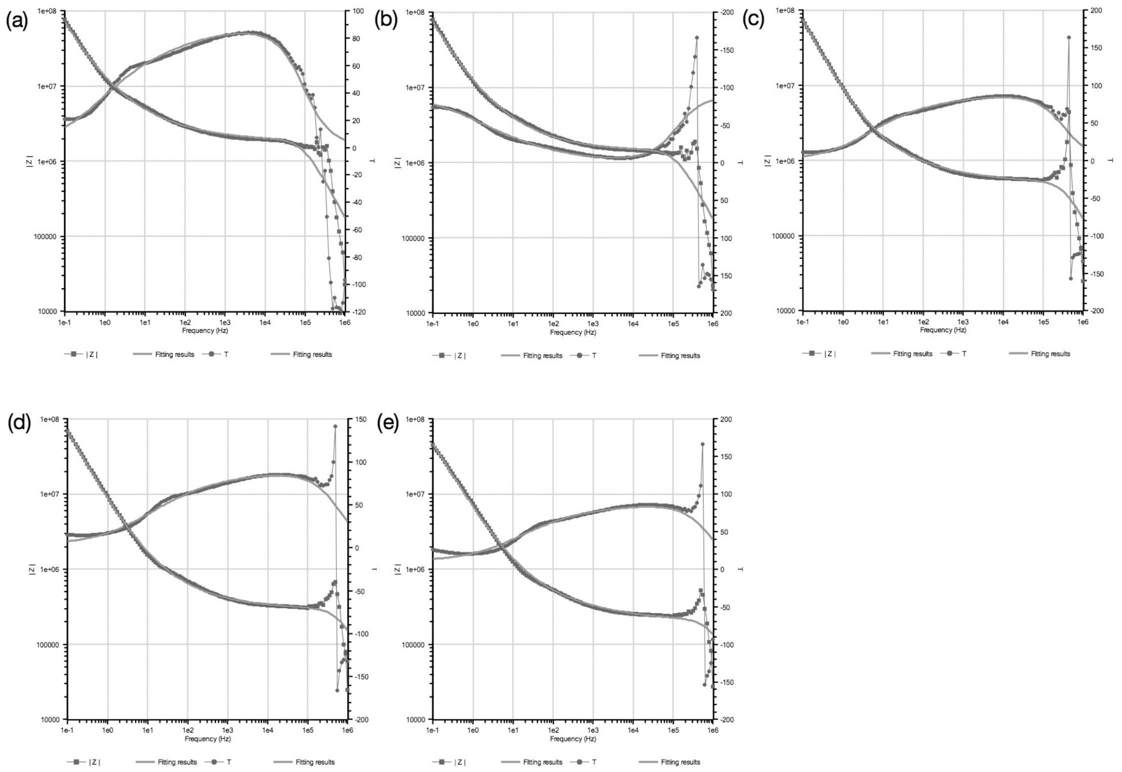

Figure A5-6. Impedance, capacitance and the best fitted result of Gel devices as a function of frequency. IL ratio is 0.2 (a), 0.4 (b), 0.6 (c), 0.8 (d) and 1 (e), respectively.

.

Table A5-3. The best fitted parameters of Gel devices. R_e and C_{geo} are estimated from non-IL device and fixed 130 G Ω and 0.9 pF, respectively.

IL ratio	**R_{ion}**	**CPE1 (EDL1)**		**CPE2 (EDL2)**	
		TDI	Phide	TDI	Phide
0.2	1.90 MΩ	5.9×10^{-8}	0.42	2.7×10^{-8}	1
0.4	1.44 MΩ	6.3×10^{-8}	0.45	2.6×10^{-8}	1
0.6	0.52 MΩ	1.6×10^{-7}	0.40	2.3×10^{-8}	1
0.8	0.30 MΩ	1.9×10^{-7}	0.42	2.4×10^{-8}	0.97
1.0	0.25 MΩ	3.7×10^{-7}	0.35	3.4×10^{-8}	0.89

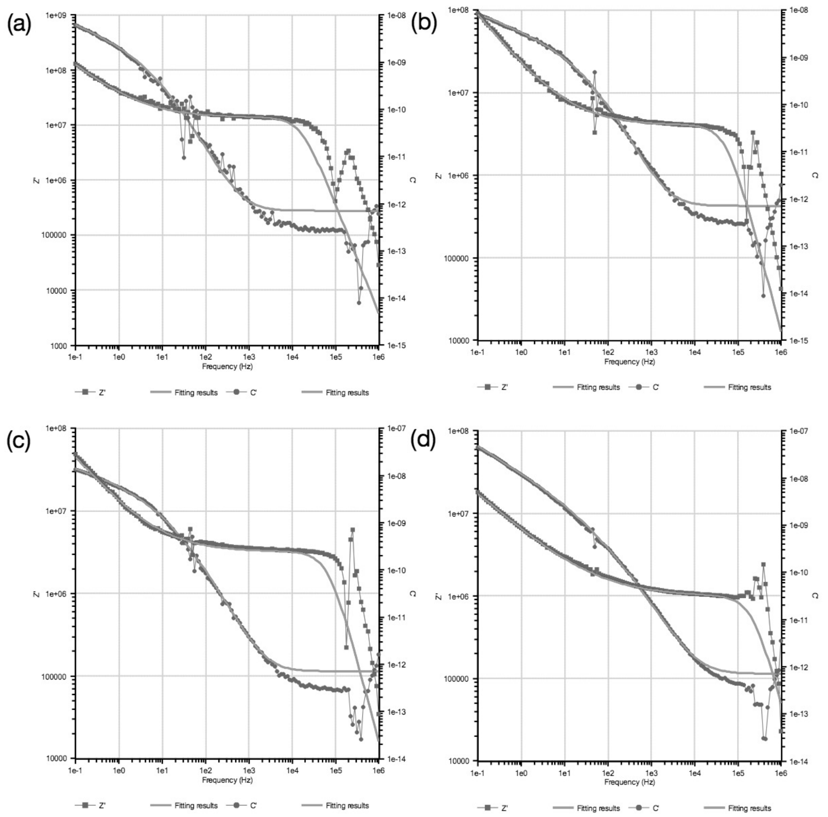

Figure A5-7. Impedance, capacitance and the best fitted result of DF devices as a function of frequency. IL ratio is 0.4 (a), 0.6 (b), 0.8 (c) and 1.0 (d), respectively.

Table A5-4. The best fitted parameters of DF devices. R_e and C_{geo} are estimated from non-IL device fixed 200 G Ω and 0.7 pF, respectively.

IL ratio	**R_{ion}**	**CPE1 (EDL1)**		**CPE2 (EDL2)**	
		TDI	Phide	TDI	Phide
0.4	13.7 MΩ	6.7 x10^{-9}	0.63	2.6 x10^{-5}	1
0.6	4.05 MΩ	9.5 x10^{-9}	0.48	1.3 x10^{-6}	0.64
0.8	3.20 MΩ	1.8 x10^{-8}	0.61	4.6 x10^{-8}	1
1.0	0.98 MΩ	5.4 x10^{-8}	0.48	1.3 x10^{-6}	1

11.3 Appendix to the Chapter 6

11.3.1 Experimental Section of Chapter 6

Unless otherwise noted, reagents and solvents were used as received from Aldrich Chemical Co. Ltd, Tokyo Chemical Industry Co. Ltd., and the chemical store at the Organisch-Chemisches Institut of the University of Heidelberg or from commercial laboratory suppliers. Number-average (M_n) and weight-average (M_w) molecular weights and polydispersities (PDI, M_w/M_n) were determined by GPC versus polystyrene standards at room temperature in chloroform with PSS-SDV columns (8.0 mm x 30.0 mm, 5 µm particles, 102-, 103- and 105- Å poresize) on a Jasco PU-2050 GPC unit equipped with a Jasco UV-2075 UV- and a Jasco RI-2031 RI detector. Photoabsorption and PL spectra were recorded on a JASCO V-660 spectrophotometer and a JASCO FP-6500 spectrofluorometer, respectively. Scanning electron microscopy images were taken with Zeiss Ultra 55, line averaged scanning mode, accelerating voltage of 1.5 kV. Transistor measurements were performed with a Keithley 4200-SCS. Transient drain current measurements were performed with the resistance across the source and drain. The voltage drop and gate voltage were monitored with the Agilent Technologies digital storage oscilloscope (DSO-X 3014A). The observations of confocal microscopy were performed with Leica TCS SP8 confocal microscope, microscope stand (Leica DMi8, inverted microscope) Laser (White light laser, E 470-670 nm) Objective lens (HC PL APO 100x/1.40 STED White Oil) Software (Leica Application Suite 3), and Image processer (Huygens deconvolution pro).The capacitance measurements were performed with a Solartron analytical Modulab MAT equipping MHV100. The thickness measurements are performed with a profilometer (DektakXT, Bruker). The synthesis of the conjugated polymer, Poly-((para-phenyleneethynylene) with Dihexyl side chain (dihexyl-**PPE**) is reported in previous publication. [54] Dihexyl-(poly(p-phenyleneethynylene)s) and 1-Butyl-1-methylpiperidinium Bis(trifluoromethanesulfonyl-)imide are employed as a conjugated polymer and an ionic liquid, respectively.

Device Fabrications. A 2.5 cm x 2.5 cm large glass substrate was washed with acetone and isopropanol in an ultrasonication. Chromium (3 nm) and gold (optimal thickness) were thermally evaporated onto the substrate in vacuum to fabricate the lateral finger electrodes. The substrate was cut to 4 pieces of 1.2 cm x1,2 cm substrates. The configuration of electrodes is 2 mm of length and 40 µm of width, respectively. The substrate was soaked in a small vial with a solution of PPE in tetrahydrofuran (5 mg mL^{-1}, 400 µL) without capping. The small vial was put into large vial with 1 mL of methanol; the larger vial was closed. Incubation for one day results in solvent exchange with gel formation. A given amount of ionic liquid (2 mg for πI-Gel$_{x1}$, 20 mg for πI-Gel$_{x10}$ and 200 mg for πI-Gel$_{x100}$) in 100 µL of methanol solution was slowly added to the gel in methanol, not to mechanically break the gel. The methanol was removed by evaporation typically for two to three days. The substrate was picked up and the gel fractions were cut apart. The devices were held under vacuum before the measurements for 15 min. All the processes were done in ambient and measurement were performed in a glovebox (O2: < 3 ppm. H2O: < 1 ppm.). The schematic protocol is shown (SchemeA6-1).

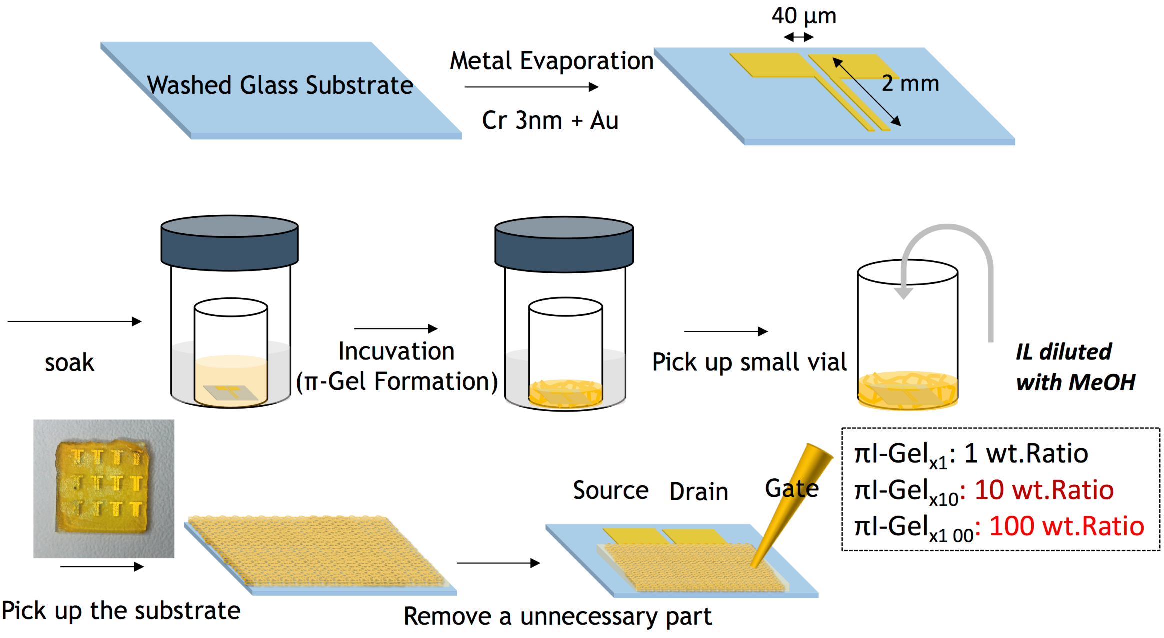

Scheme A6-1 The Preparation protocol of the πI-gel devices.

SEM Observations. The same fabrication protocol of πI-Gel devices is applied on the Si/SiO2 substrates in glovebox. The samples were put in vacuum for 15 min. The substrates were fixed on an aluminum plate by silver ink. The images were taken with accelerating voltage and working distance of 1.5 kV and 3 mm, respectively. The detector of SE2 mode was employed.

Confocal Microscope Observations. The same fabrication protocol of πI-Gel devices is applied on the thin cover glasses. The cover glasses were put on the slide glass to sandwich the gels. The cover glass side was observed.

Electronic Measurements for Contact Thickness Dependent Measurements. The drain voltage of -1 V was applied while a sweeping of gate voltage from 1 V to -6 V. The sweeping speed of gate voltage was 0.5 s per 50 mV for πI-Gel$_{x100}$ and 10 s per 50 mV for πI-Gel$_{x10}$.

Electronic Measurements for Sweeping Speed Dependent Measurements. The drain voltage of -1 V was applied while a sweeping of gate voltage from 1 V to -6 V. The sweeping speed of gate voltage was 0.1 s, 0.5 s, 1 s and 5 s per 50 mV step voltage.

Capacitance Measurements. The same fabrication protocol of πI-Gel devices is applied on the pre-patterned ITO substrates. The capacitance was measured with 2 or 3 different domain sizes of ITO samples and normalized by the area. The averaged value of capacitance per area is employed.

Transient Drain Current Measurements. The resistance was settled between the source and the drain. The oscilloscope was connected to the resistance and gate. The resistance was determined not to exceed the voltage drop of 100 mV. The voltage drop was translated to the current.

11.3.2 Appendix Figures of chapter 6

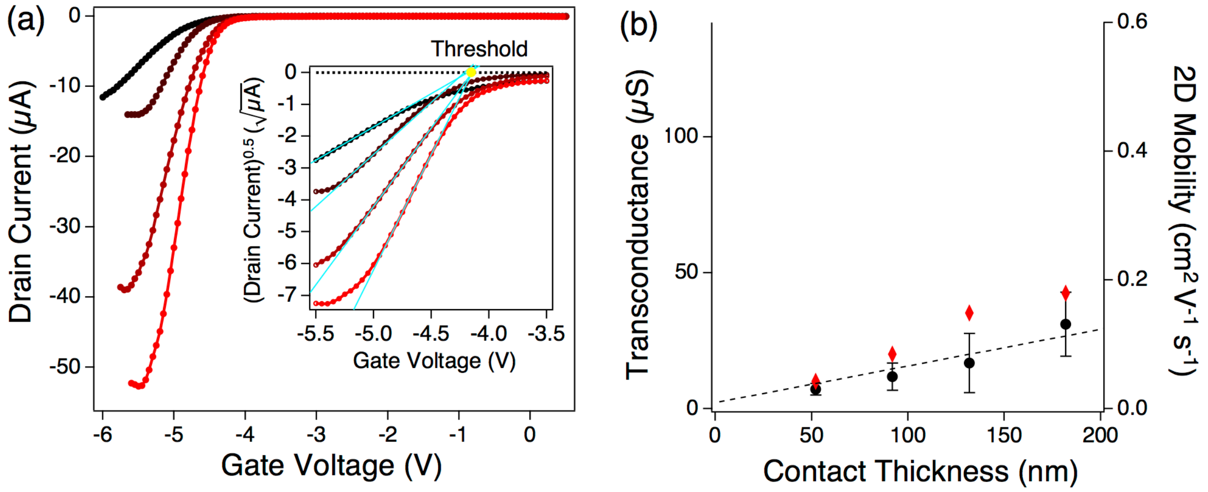

Figure A6-1 (a) Transfer curves of πI-Gel$_{x10}$ with 50 nm, 90 nm, 130 nm and 180 nm (from black to red) thick contacts V_D= -1V. Inset shows a graph of the square root of drain currents over the gate voltage. (b) The transconductances and the 2D mobility as a function of the channel thickness. Black dots, red dots and error bars are averaged values, maximum values and standard deviations resulted from 5 different devices. Dot line shows linear fit of the averaged values. The sweeping speed is 10 s per 50 mV step.

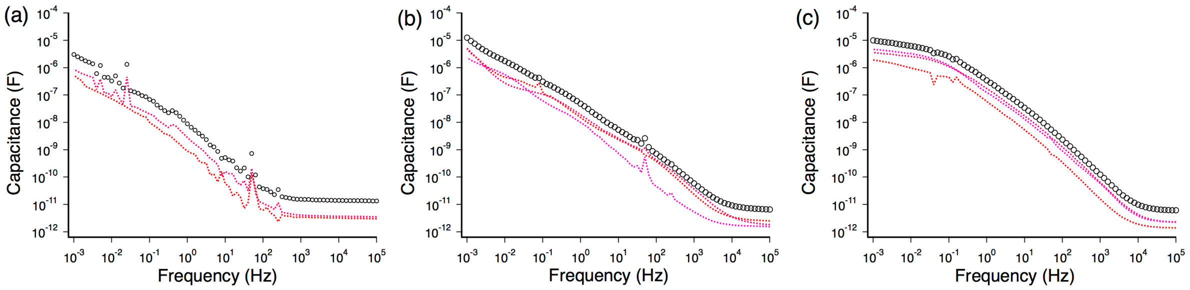

Figure A6-2 Frequency dependent capacitance of πI-Gel$_{x1}$(a), πI-Gel$_{x10}$(b) and πI-Gel$_{x100}$(c) with different sizes of area. Blank circles indicate the averaged capacitance per area.

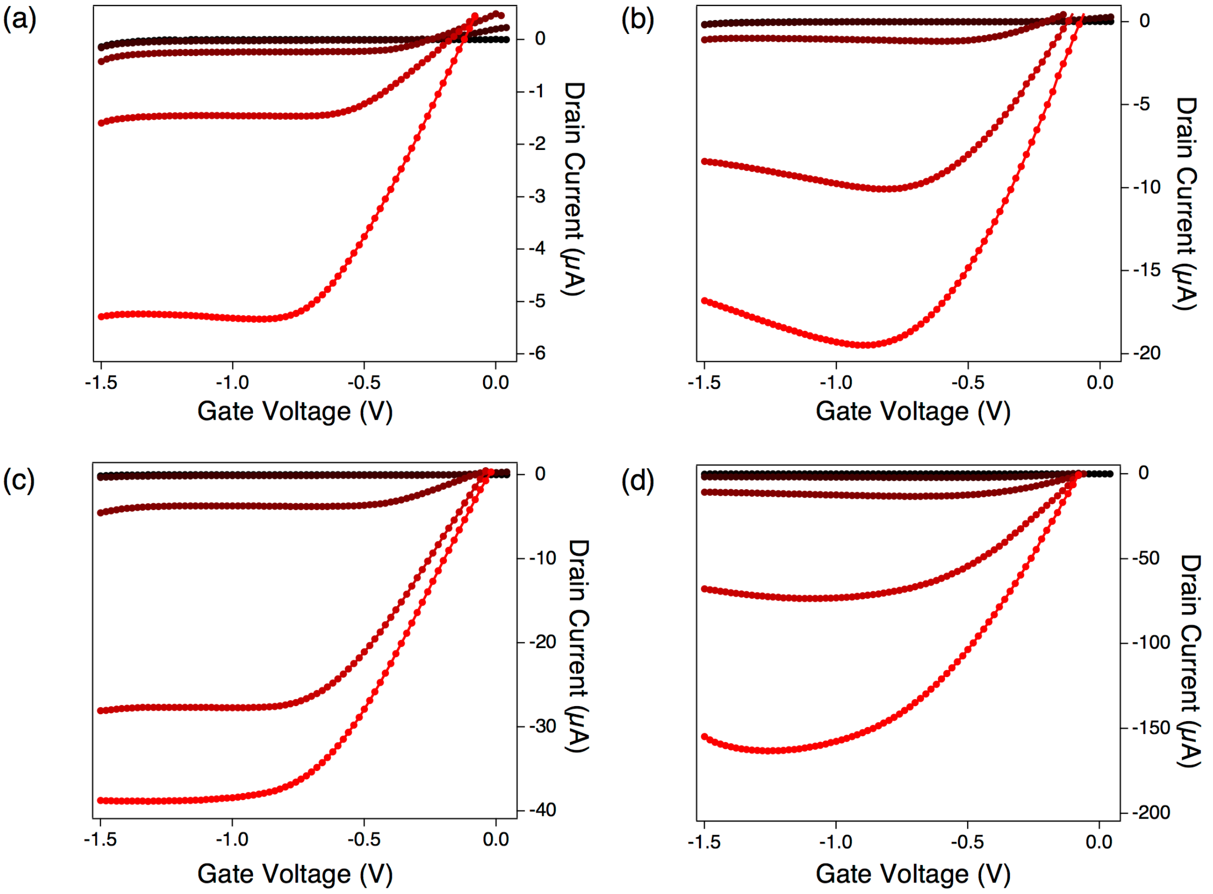

Figure A6-3 Output curves with 50 nm thick contacts(a), 90 nm thick contacts(b), 130 nm thick contacts(c) and 180 nm thick contacts (d). The gate voltage is 0V, 4V, 5V and 6V from black to red. The sweeping speed is 0.1 s per 10 mV drain step.

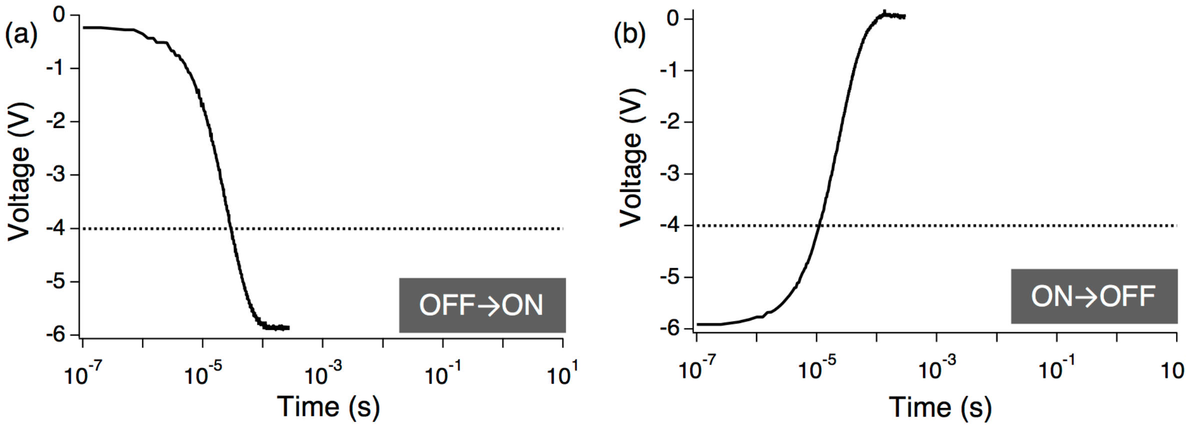

Figure A6-4 The turn-on (a) and –off (b) responses of the setup

11.4 Appendix to the Chapter 7

11.4.1 Experimental Section of Chapter 7

Unless otherwise noted, reagents and solvents were used as received from Aldrich Chemical Co. Ltd, Tokyo Chemical Industry Co. Ltd., and from commercial laboratory suppliers. Flash column chromatography was carried out using silica gel S (0.032 mm-0.062 mm), purchased from Sigma Aldrich. ^{1}H-NMR spectra were recorded at room temperature, at 70°C or 100 °C on the following spectrometers: Bruker Avance III 400 (400 MHz). ^{13}C-NMR spectra were recorded at room temperature or 70°C on the Bruker Avance III 600 (151 MHz). The data were interpreted as first order spectra. The spectra were recorded in $CDCl_3$ or 1,2-dichloroethane-d_4 as indicated in each case. All NMR spectra were integrated and processed using the ACD/Spectrus Processor. Number-average (M_n) and weight-average (M_w) molecular weights and polydispersities (Đ, M_w/M_n) were determined by GPC versus polystyrene standards at room temperature in chloroform with PSS-SDV columns (8.0 mm x 30.0 mm, 5 µm particles, 102 -, 103 - and 105 - Å pore size) on a Jasco PU-2050 GPC unit equipped with a Jasco UV-2075 UV- and a Jasco RI-2031 RIdetector. Photoabsorption and PL spectra were recorded on a JASCO V-660 spectrophotometer and a JASCO FP-6500 spectrofluorometer, respectively. Fluorescence lifetimes τ were acquired by an exponential fit according to the least mean square with commercially available software from HORIBA Scientific Decay Data Analyses 6 (DAS6) version 6.4.4. IR spectra were recorded on a JASCO FT/IR-4100. Substances were applied as a film, solid or in solution. Processing of data was done using the software JASCO Spectra Manager™. The photoluminescence decays were recorded with a HORIBA Scientific Fluorocube single photon counting system operated with a HORIBA Scientific DataStationversion 2.2. Density functional theory (DFT) calculation to obtain theoretical remnant polarization was performed at the B3LYP/6-31G(d) level with the Spartan program. Scanning electron microscopy images were taken with Zeiss Ultra 55, Inlens detector, line averaged scanning mode, accelerating voltage of 1.5 kV. Variable temperature powder XRD patterns were recorded on a RIGAKU model Miniflex600 diffractometer with a CuKα radiation source (40 kV and 15 mA), equipped with model D/Tex Ultra2-MF high-speed 1D detector. Electronic measurements including Current-Voltage-Time, Capacitance as a function of voltage and temperature, poling switching and PUND were performed with either a Solartron analytical Modulab MAT equipping a MHV100 or Keithley 2636B system source meter with a heat stage in ambient condition.

Synthesis HPPE, 1,4-dihexyl-2,5-diiodobenzene and 1,4-diethynyl-2,5-dihexylbenzene were synthesized by Dr. Emanuel Smarsly and the synthesis is reported.[54]

Synthesis of FF-HPPE. 2,3-Difluoro-1,4-diiodobenzene (543 mg, 1.48 mmol), 1,4-diethynyl-2,5-dihexylbenzene (436 mg, 1.48 mmol) and the catalyst standard solution (0.5 mL; 0.2 mol% Pd, 0.4 mol% Cu) were stirred in a mixture of degassed toluene (4.93 mL) and degassed piperidine (4.35 mL) at 80 °C for 3 d. The catalyst standard solution was prepared from (Ph3P)2PdCl2 (14.0 mg, 20.0 µmol), CuI (7.62 mg, 40.0 µmol) and degassed piperidine (5.0 mL). Purification of the polymer was carried out by reprecipitation from toluene and methanol for 2 times. FF-HPPE was obtained as a yellow solid (555 mg, 86.3%). The Mn was estimated to be 4.8 kg mol–1 with Đ = 3.1. TGA-DSC shows phase transformation or decomposition at 326 °C; 1H NMR (400 MHz, Cl2CDCDCl2 at 100oC): δ = 7.51 (br, 2H), 7.33 (br, 2H), 2.85-3.05 (br, 4H), 1.75-1.95 (br, 4H), 1.30-1.60 (br, 12H), 0.9- 1.05 (br, 6H) ppm. 13C NMR (151 MHz, Cl2CDCDCl2 at 70oC): δ = 151.94 150.25 (JC-F = 253.5 Hz), 143.1, 132.9, 127.6, 122.8, 114.5, 96.8, 86.8, 34.4, 31.9, 30.9, 29.4, 22.8, 14.3 ppm.

Scheme 7-1. Synthetic scheme of FF-HPPE

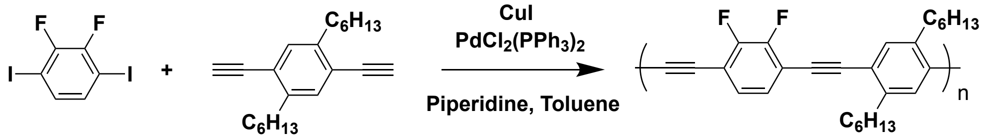

Synthesis of HH-HPPE. 1,4-Diiodobenzene (100 mg, 303 µmol), 1,4-diethynyl-2,5-dihexylbenzene (89 mg, 303 µmol) and the catalyst standard solution (0.5 mL; 0.2 mol% Pd, 0.4 mol% Cu) were stirred in a mixture of degassed toluene (2 mL) and degassed piperidine (1 mL) at 75 °C for 150 min. The catalyst standard solution was prepared from (Ph3P)2PdCl2 (14.0 mg, 20.0 µmol), CuI (7.62 mg, 40.0 µmol) and degassed piperidine (5.0 mL). Purification of the PPE was carried out by reprecipitation from Toluene and methanol for 2 times. FF-HPPE was obtained as a yellow solid (80 mg, 66.2%). The Mn was estimated to be 1.6 kg mol–1 with Đ = 1.68. 1H NMR (400 MHz, Cl2CDCDCl2 at 100ºC): δ = 7.58 (br, 4H), 7.44 (br, 2H), 2.70-3.00 (br, 4H), 1.65-1.95 (br, 4H), 1.30-1.60 (br, 12H), 0.85-1.05 (br, 6H) ppm. 13C NMR (151 MHz, Cl2CDCDCl2 at 70ºC): δ = 142.7, 132.7 131.7, 123.6, 122.9, 94.3, 91.0, 86.7, 34.4, 31.9, 30.8, 29.5, 22.8, 14.3 ppm.

Scheme 7-2. Synthetic scheme of HH-HPPE

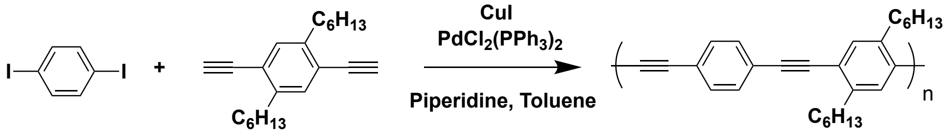

Synthesis of FH-HPPE. 1,4-diethynyl-2,5-difluorobenzene (48.8 mg, 0.3 mmol), 1,4-dihexyl-2,5-diiodobenzene (150 mg, 0.3 mmol) and the catalyst standard solution (0.5 mL; 0.2 mol% Pd, 0.4 mol% Cu) were stirred in a mixture of degassed tetrahydrofran (1 mL) and degassed piperidine (0.8 mL) at 75 °C for 3 d. The catalyst standard solution was prepared from (Ph3P)2PdCl2 (14.0 mg, 20.0 µmol), CuI (7.62 mg, 40.0 µmol) and degassed piperidine (5.0 mL). Purification of the polymer was carried out by reprecipitation from toluene and methanol for 2 times. FH-HPPE was obtained as a yellow solid. The Mn was estimated to be 1.9 kg mol–1 with Đ = 1.3. 1H NMR (400 MHz, Cl2CDCDCl2 at 100ºC): δ = 6.89-7.50 (br, 4H), 3.15-2.25 (br, 2H), 1.30-1.80 (br, 16H), 0.9-1.05 (br, 6H) ppm. 13C NMR (151 MHz, Cl2CDCDCl2 at 70ºC): δ = 159.32 157.66 (JC-F = 253.5 Hz), 143.5, 132.9, 119.5, 113.6, 109.9, 96.9, 86.9, 34.4, 31.9, 30.9, 29.4, 22.8, 14.3 ppm. This synthesis was performed with Mr. Maximilian N. Bojanowski.

Scheme 7-3. Synthetic scheme of FH-HPPE

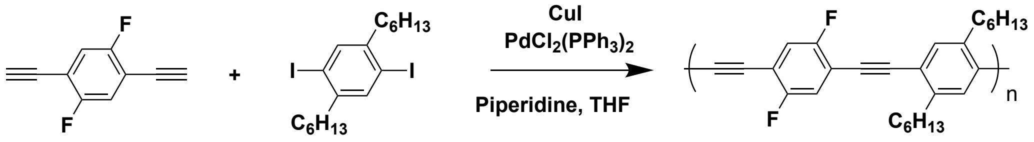

11.4.2 Appendix Figures of Chapter 7

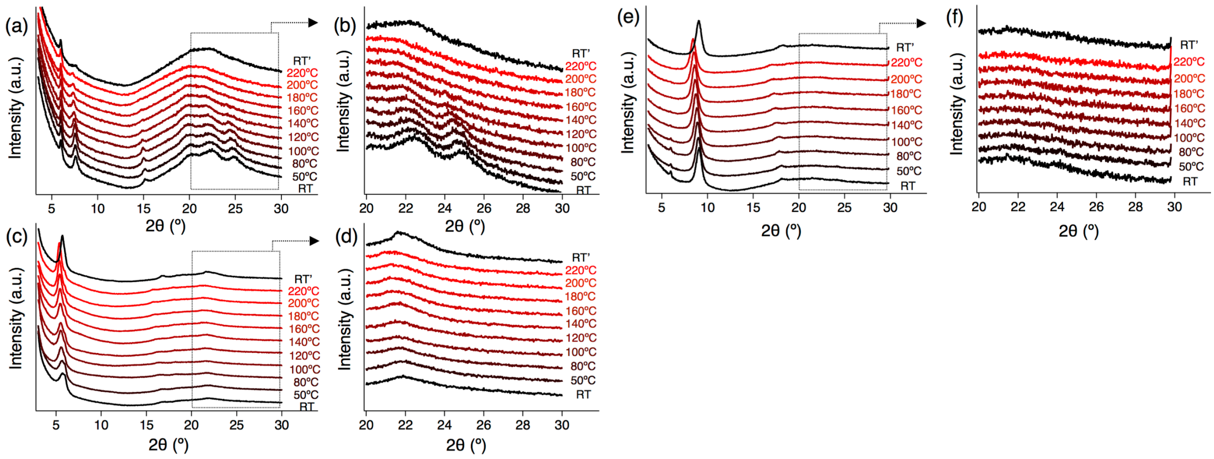

Figure A7-1. (a) XRD patterns of the films of FH-HPPE (a) HH-HPPE (c) and HPPE (e) and their expansion (b, d, f) on the range of 20° < 2θ < 30°(b) as a function of temperature (30-220°C, black to red). RT and RT' means XRD pattern at 30°C before and after thermal annealing at 220 °C, respectively.

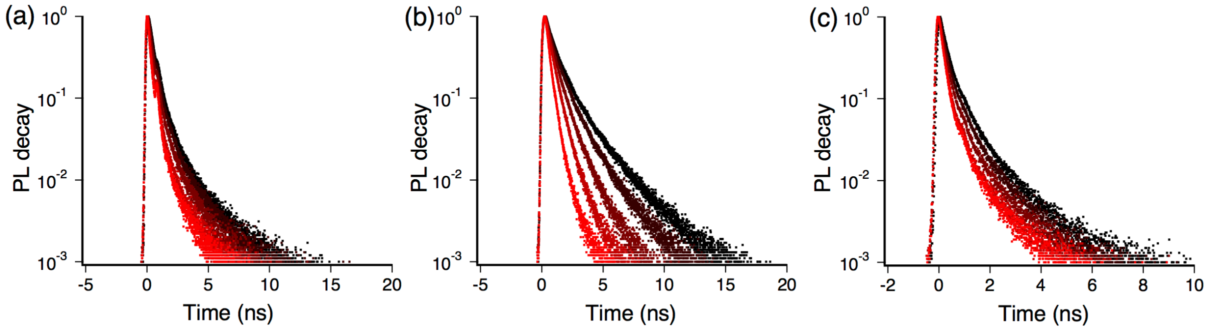

Figure A7-2. Temperature dependence of the PL decay profiles (30°C, 100°C, 160°C, 220°C and 260°C from black to red) of HPPE (a), FF-HPPE (b) and HH-HPPE(c)

11.5 Appendix to the Chapter 8

11.5.1 Experimental Section of Chapter 8

Unless otherwise noted, reagents and solvents were used as received from Aldrich Chemical Co. Ltd, Tokyo Chemical Industry Co. Ltd., and from commercial laboratory suppliers. Flash column chromatography was carried out using silica gel S (0.032 mm-0.062 mm), purchased from Sigma Aldrich. ^{1}H-NMR spectra were recorded at room temperature on the g spectrometer of Bruker Avance III 400 (400 MHz). ^{13}C-NMR spectra were recorded at room temperature on the Bruker Avance III 600 (151 MHz). The data were interpreted as first order spectra. The spectra were recorded in $CDCl_3$. All NMR spectra were integrated and processed using the ACD/Spectrus Processor. Scanning electron microscopy images were taken with Zeiss Ultra 55, line averaged scanning mode, accelerating voltage of 1.5 kV. Variable temperature powder XRD patterns were recorded on a RIGAKU model Miniflex600 diffractometer with a CuKα radiation source (40 kV and 15 mA), equipped with model D/Tex Ultra2-MF high-speed 1D detector. Differential scanning calorimetry (DSC) measurements were carried out with TGA/DSC STARe System of Mettler Toledo with the scanning speed of 5 K/min. Polarized micrographs were recorded on a Nikon Eclipse LV100POL microscope with included a camera and a heat stage. Electronic measurements including POM observations under an electric field and current measurements under poling switching were performed with either a Solartron analytical Modulab MAT equipping a MHV100 or Keithley 2636B system source meter.

POM Observation under an Electric Field. Two ITO plates were prepared and put on a hot plate. Methanol suspension of 1µm silica beads was put on an ITO plate at 100 ^{o}C to evaporate the methanol. The LC material was out on the ITO plate and a pre-heated another ITO plate was put on it to sandwich the compound at the LC temperature. Subsequently, the hot plate is cooled down to the room temperature to have a capacitor. The capacitor was put on the heat stage under the polarized microscope. The device configuration is shown in Figure A8-6.

Poling Treatment at LC Temperature. Two ITO plates were prepared and put on a hot plate. 200 nm thick parylene C was evaporated on both ITO as spacers. 0.6 mm x 6 mm space was cut. Methanol suspension of 1µm silica beads was put on an ITO plate at 100 ^{o}C to evaporate the methanol. The LC material was out on the ITO plate and a pre-heated another ITO plate was put on it to sandwich the compound at the LC temperature. Subsequently, the hot plate is cooled down to the room temperature to have a capacitor. The capacitor was heated up to smectic liquid crystal state (140 °C) and ±25 V/µm DC voltage was applied. Keeping the electric field, the capacitor was cooled down to the room temperature.

Synthesis of Oli-HH

Scheme A8-1. Synthetic scheme of Oli-HH

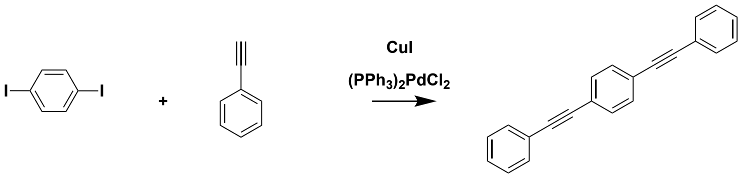

1,4-diiodobenzene (500 mg, 1.52 mmol) was dissolved in Piperidine (1.5 mL) and Toluene (3 mL) under nitrogen. Bubbling took place for 30 min before adding ethynylbenzene (310 mg, 3.03 mmol). Then, bis-(triphenylphosphine) palladium dichloride (21 mg, 0.03 mmol) and copper iodide (2.9 mg, 0.015 mmol) were added. The mixture was stirred for 24 hours at room temperature. The resulted mixture was purified by chromatography using PE as eluent to obtain (1,4-bis(phenylethynyl)benzene) (310 mg, 73.5%). ^{1}H NMR (400 MHz, $CDCl_3$): δ = 7.33-7.40 (m, 6H), 7.50-7.57 (m, 8H) ppm. ^{13}C NMR (151 MHz, $CDCl_3$): δ = 131.69 131.80, 128.54, 123.22, 91.39, 89.27 ppm.

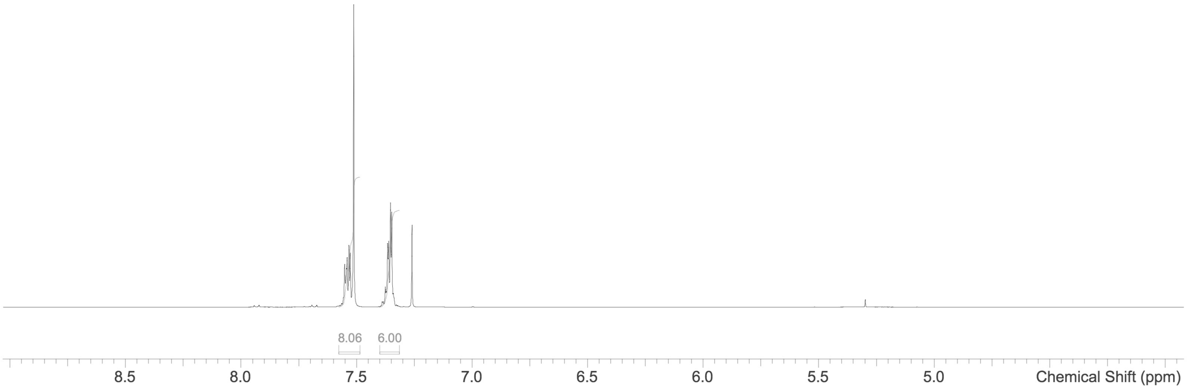

Chart A8-1. ^{1}H NMR Chart of Oli-HH in $CDCl_3$

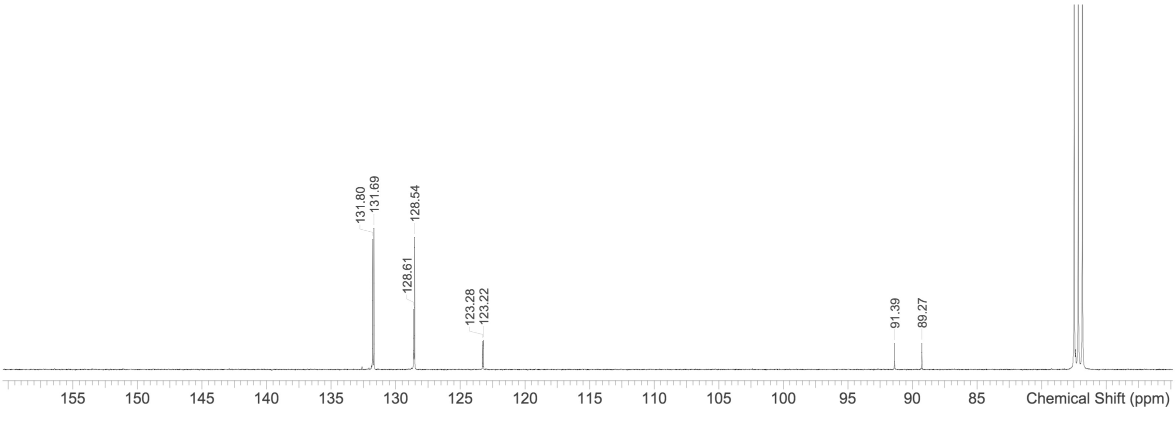

Chart A8-2. ^{13}C NMR Chart of Oli-HH in $CDCl_3$

Synthesis of Oli-FH

Scheme A8-2. Synthetic scheme of Oli-FH

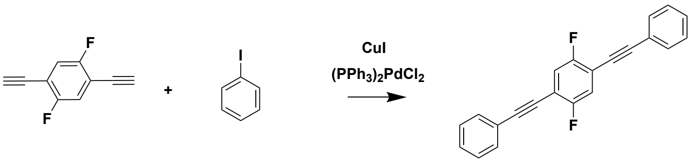

1,4-diethynyl-2,5-difluorobenzene (200 mg, 1.23 mmol) was dissolved in Piperidine (1.5 mL) and Toluene (3 mL) under nitrogen. Bubbling took place for 30 min before adding iodobenzene (755 mg, 3.70 mmol). Then, bis-(triphenylphosphine) palladium dichloride (17.3 mg, 0.024 mmol) and copper iodide (4.7 mg, 0.025 mmol) were added. The mixture was stirred for 24 hours at room temperature. The resulted mixture was purified by chromatography using PE as eluent and recrystallization to obtain ((2,5-difluoro-1,4-phenylene)bis(ethyne-2,1-diyl))dibenzene (106 mg, 27.3%). ^{1}H NMR (400 MHz, $CDCl_3$): δ = 7.14-7.18 (tr, 2H), 7.20-7.35 (m, 6H) ppm, 7.46-7.53 (m 4H). ^{13}C NMR (151 MHz, $CDCl_3$): δ = 159.45, 156.93, 131.81, 129.10, 128.45, 122.29, 119.37(q), 113.23(tr), 96.94, 81.67 ppm.

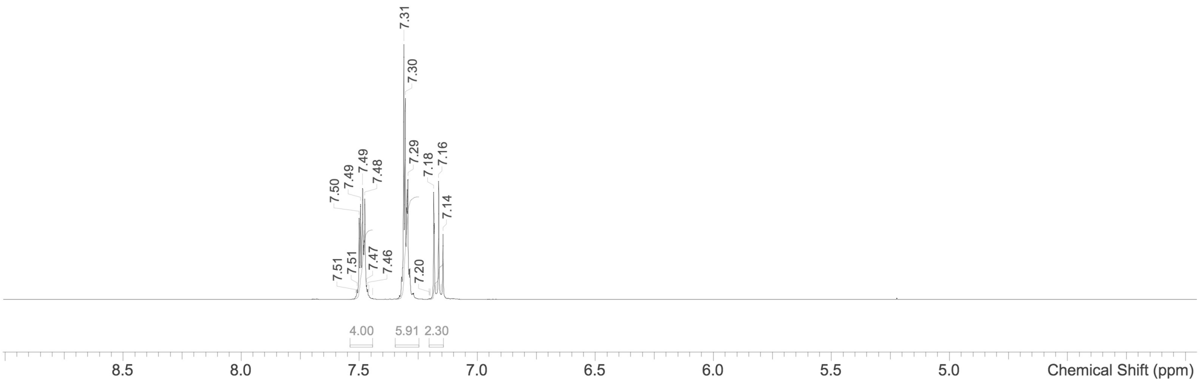

Chart A8-3. ^{1}H NMR Chart of Oli-FH in $CDCl_3$

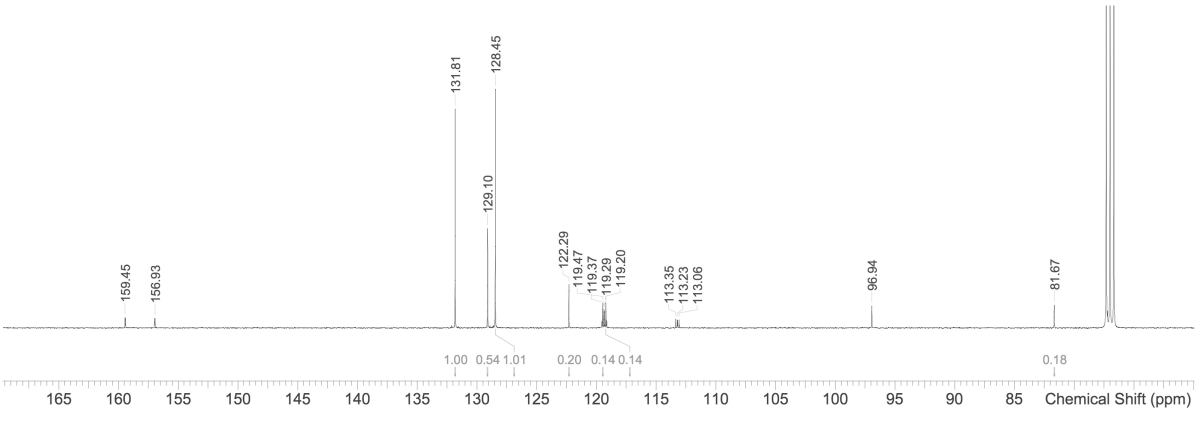

Chart A8-4. ^{13}C NMR Chart of Oli-FH in $CDCl_3$

Synthesis of Oli-FF

Scheme A8-3. Synthetic scheme of Oli-FF

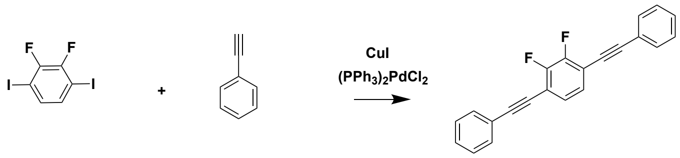

2,3-difluoro-1,4-diiodobenzene (400 mg, 1.09 mmol) was dissolved in Piperidine (1.5 mL) and Toluene (3 mL) under nitrogen. Bubbling took place for 30 min before adding ethynylbenzene (335 mg, 3.28 mmol). Then, bis-(triphenylphosphine) palladium dichloride (15.3 mg, 0.022 mmol) and copper iodide (4.2 mg, 0.022 mmol) were added. The mixture was stirred for 24 hours at room temperature. The resulted mixture was purified by chromatography using PE/CH_2cl_2 as eluent and recrystallization to obtain ((2,3-difluoro-1,4-phenylene)bis(ethyne-2,1-diyl))dibenzene (106 mg, 30.8%). ^{1}H NMR (400 MHz, $CDCl_3$): δ = 7.16-7.18 (m, 2H), 7.29-7.32 (m, 6H) ppm, 7.46-7.53 (m 4H). ^{13}C NMR (151 MHz, $CDCl_3$): δ = 152.41-152.26(d), 149.87-149.72(d), 131.96, 129.23, 128.61, 127.58, 114.22(q), 97.31, 81.67 ppm.

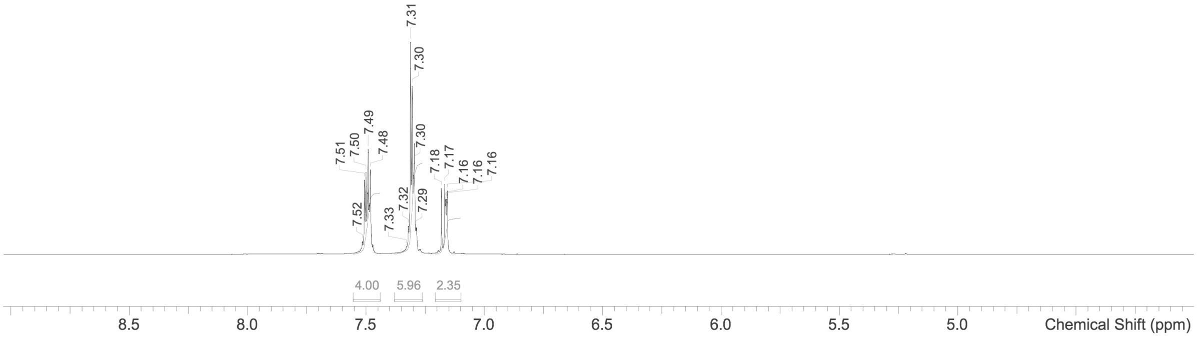

Chart A8-5. ^{1}H NMR Chart of Oli-FF in $CDCl_3$

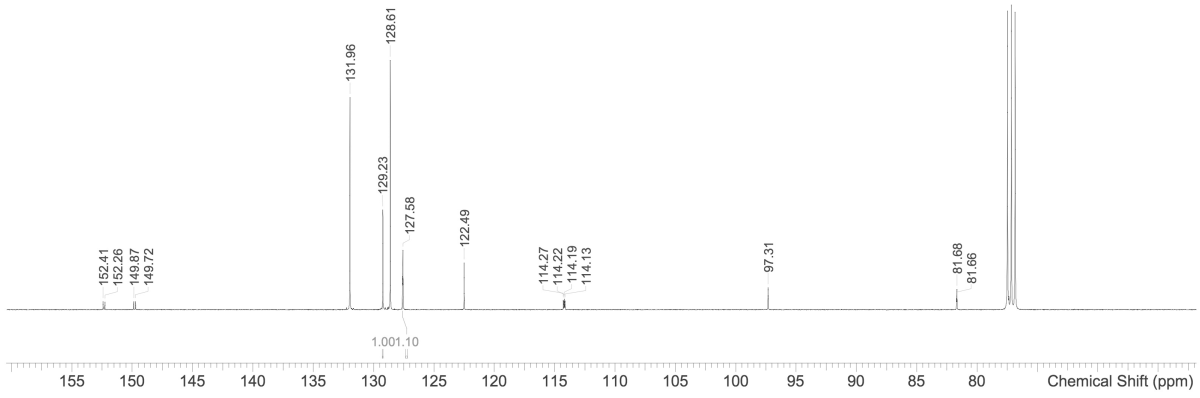

Chart A8-6. ^{13}C NMR Chart of Oli-FF in $CDCl_3$

Synthesis of Oli-HH-OC3

Scheme A8-4. Synthetic scheme of Oli-HH-OC3

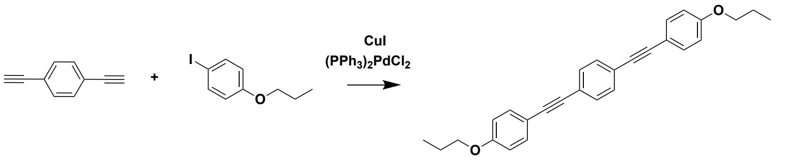

1,4-diethynylbenzene (70 mg, 0.05 mmol) was dissolved in Piperidine (1 mL) and Toluene (1.5 mL) under nitrogen. Bubbling took place for 30 min before adding 1-iodo-4-propoxybenzene (320 mg, 1.22 mmol). Then, bis-(triphenylphosphine) palladium dichloride (7.8 mg, 0.011 mmol) and copper iodide (2.1 mg, 0.011 mmol) were added. The mixture was stirred for 24 hours at room temperature. The resulted mixture was purified by chromatography using PE as eluent to obtain 1,4-bis((4-propoxyphenyl)ethynyl)benzene (32 mg, 14.6%). ^{1}H NMR (400 MHz, $CDCl_3$): δ = 1.03-1.06 (tr, 6H), 1.78-1.87 (m, 4H),3.93-3.96 (tr, 4H), 6.86-6.88 (d,4H), 7.44-7.48 (m,8H) ppm. ^{13}C NMR (151 MHz, $CDCl_3$): δ = 159.54, 133.22, 131.47, 123.27, 115.11, 114.75, 91.42, 88.04, 69.75, 22.69, 10.64 ppm.

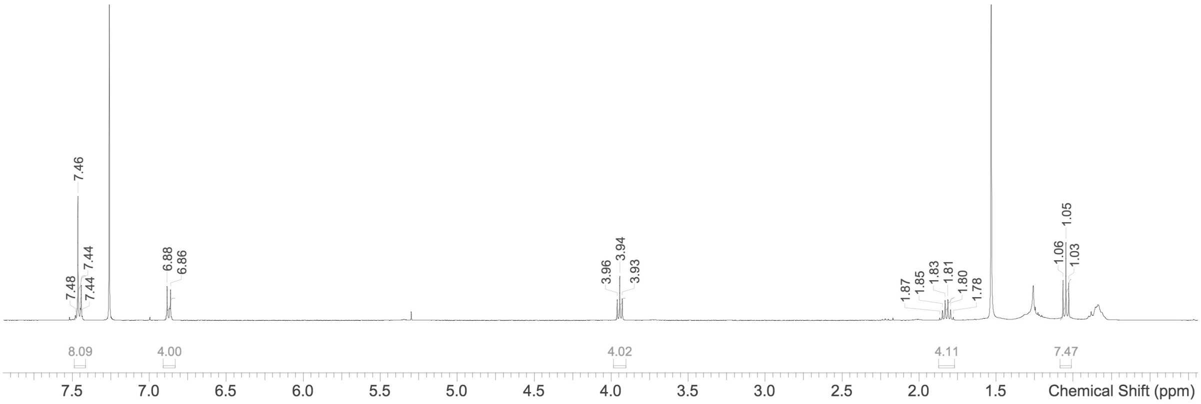

Chart A8-7. ^{1}H NMR Chart of Oli-HH-OC3 in $CDCl_3$

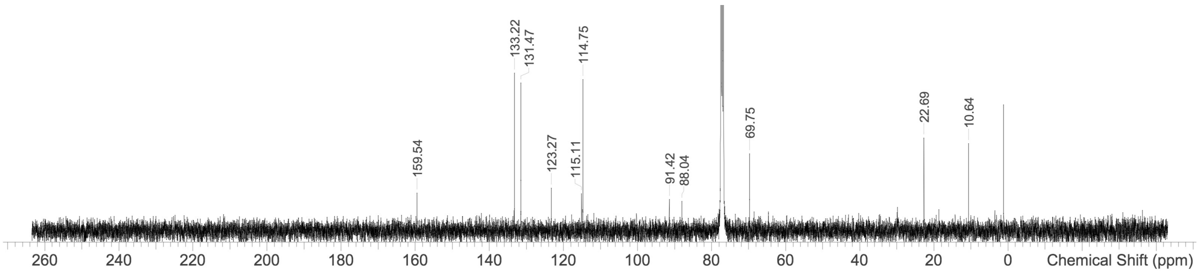

Chart A8-8. ^{13}C NMR Chart of Oli-HH-OC3 in $CDCl_3$

Synthesis of Oli-FH-OC3

Scheme A8-5. Synthetic scheme of Oli-FH-OC3

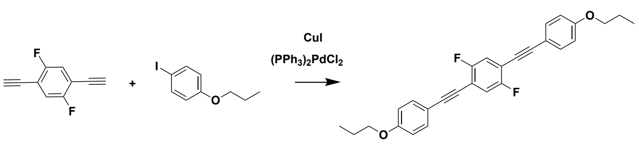

1,4-diethynyl-2,5-difluorobenzene (80 mg, 0.49 mmol) was dissolved in Piperidine (1 mL) and Toluene (1.5 mL) under nitrogen. Bubbling took place for 30 min before adding 1-iodo-4-propoxybenzene (284 mg, 1.09 mmol). Then, bis-(triphenylphosphine) palladium dichloride (6.9 mg, 0.009 mmol) and copper iodide (1.8 mg, 0.009 mmol) were added. The mixture was stirred for 24 hours at room temperature. The resulted mixture was purified by chromatography using PE as eluent to obtain 4,4'-((2,5-difluoro-1,4-phenylene)bis(ethyne-2,1-diyl))bis(propoxybenzene) (87 mg, 40.9%). ^{1}H NMR (400 MHz, $CDCl_3$): δ = 1.01-1.07 (tr, 6H), 1.78-1.87 (m, 4H),3.93-3.97 (tr, 4H), 6.87-6.89 (d,4H), 7.17-7.21 (tr,2H) 7.46-7.50 (m,4H) ppm. ^{13}C NMR (151 MHz, $CDCl_3$): δ = 160.02, 159.46, 156.99, 133.48, 119.39-119.06(m), 114.8, 114.29, 113.41-113.12(tr), 97.28, 80.74, 69.77, 22.66, 10.62 ppm.

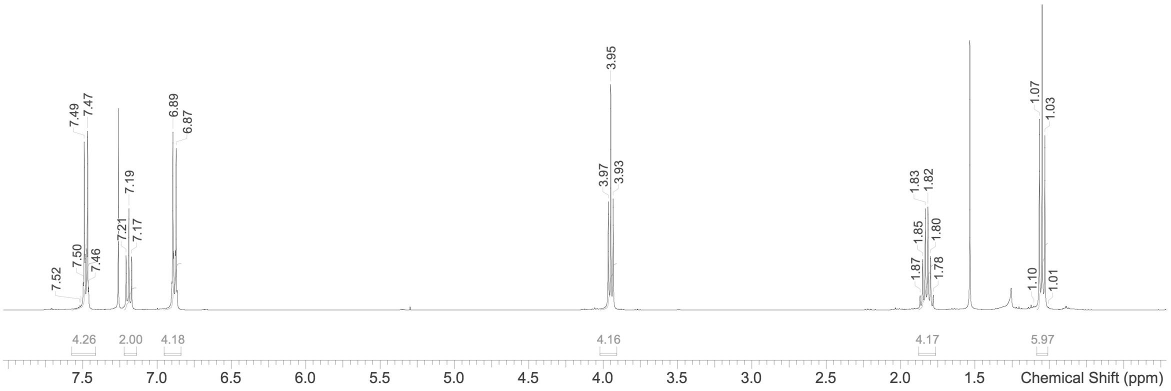

Chart A8-9. ^{1}H NMR Chart of Oli-FH-OC3 in $CDCl_3$

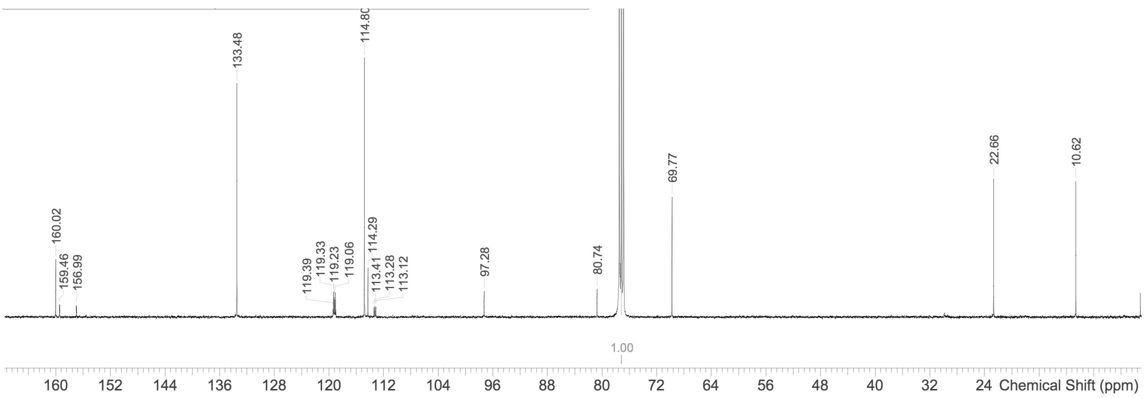

Chart A8-10. ^{13}C NMR Chart of Oli-FH-OC3 in $CDCl_3$

Synthesis of Oli-FF-OC3

Scheme A8-6. Synthetic scheme of Oli-FF-OC3

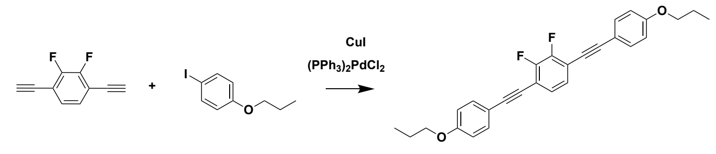

1,4-diethynyl-2,3-difluorobenzene (110 mg, 0.68 mmol) was dissolved in Piperidine (1 mL) and Toluene (1.5 mL) under nitrogen. Bubbling took place for 30 min before adding 1-iodo-4-propoxybenzene (390 mg, 1.49 mmol). Then, bis-(triphenylphosphine) palladium dichloride (9.5 mg, 0.013 mmol) and copper iodide (2.6 mg, 0.013 mmol) were added. The mixture was stirred for 24 hours at room temperature. The resulted mixture was purified by chromatography using PE/$CHCl_3$ as eluent to obtain 4,4'-((2,3-difluoro-1,4-phenylene)bis(ethyne-2,1-diyl))bis(propoxybenzene) (130.3 mg, 44.6%). ^{1}H NMR (400 MHz, $CDCl_3$): δ = 1.03-1.07 (tr, 6H), 1.78-1.85 (m, 4H),3.94-3.97 (tr, 4H), 6.87-6.90 (d,4H), 7.18-7.19 (tr,2H) 7.47-7.50 (d,4H) ppm. ^{13}C NMR (151 MHz, $CDCl_3$): δ = 160.01, 152.25, 149.57, 133.47, 127.35, 114.81, 114.36, 97.48, 80.58, 69.78, 22.67, 10.63 ppm.

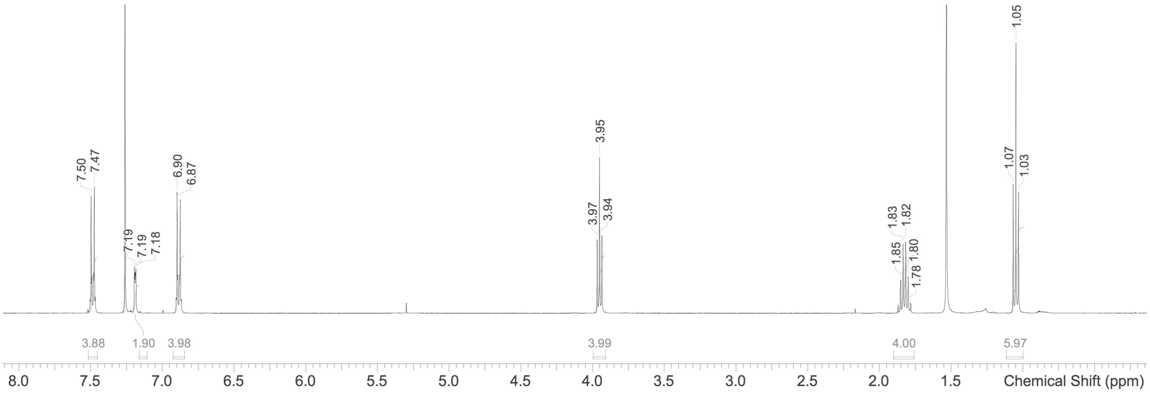

Chart A8-11. ^{1}H NMR Chart of Oli-FF-OC3 in $CDCl_3$

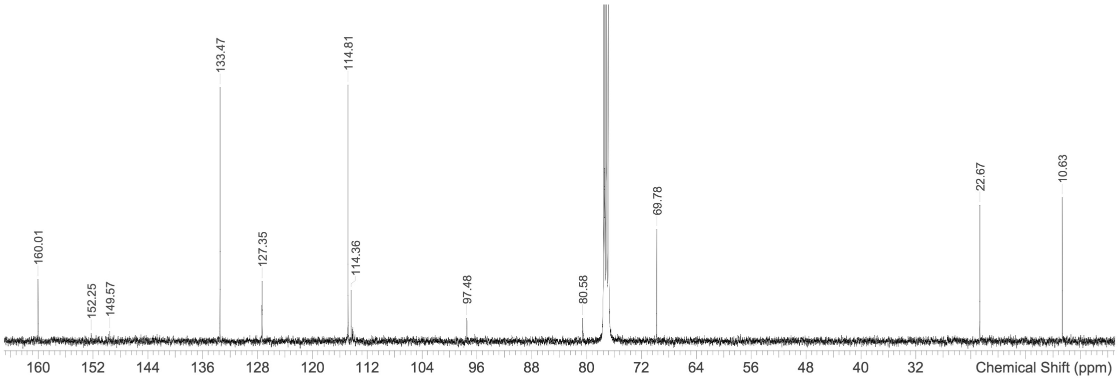

Chart A8-12. ^{13}C NMR Chart of Oli-FF-OC3 in $CDCl_3$

Synthesis of Oli-HH-OC6

Scheme A8-7. Synthetic scheme of Oli-HH-OC3

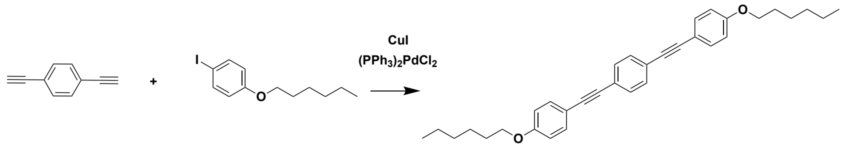

1,4-diethynylbenzene (60 mg, 0.47mmol) was dissolved in Piperidine (1 mL) and Toluene (1.5 mL) under nitrogen. Bubbling took place for 30 min before adding 1-(hexyloxy)-4-iodobenzene (318 mg, 1.05 mmol). Then, bis-(triphenylphosphine) palladium dichloride (6.7 mg, 0.009mmol) and copper iodide (1.8 mg, 0.009 mmol) were added. The mixture was stirred for 24 hours at room temperature. The resulted mixture was purified by chromatography using PE as eluent and recrystallization to obtain 1,4-bis((4-(hexyloxy)phenyl)ethynyl)benzene (113 mg, 49.3%). ^{1}H NMR (400 MHz, $CDCl_3$): δ = 0.90-0.93 (tr, 6H), 1.33-1.49 (br, 12H), 1.76-1.83 (m, 4H), 3.96-3.99 (tr, 4H), 6.85-6.89 (d,4H), 7.44-7.48 (m,8H) ppm. ^{13}C NMR (151 MHz, $CDCl_3$): δ = 159.54, 133.21, 131.46, 123.26, 115.08, 114.74, 91.42, 88.03, 68.27, 31.72, 29.32, 25.85, 22.74, 14.16 ppm.

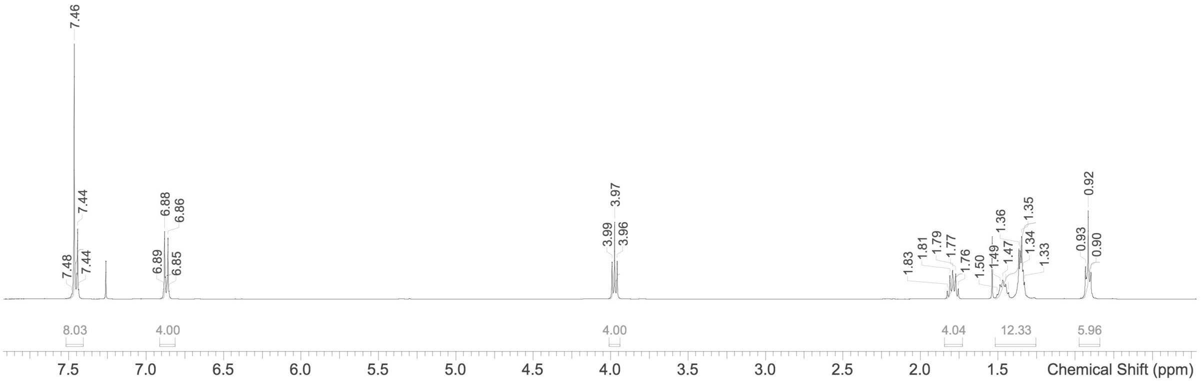

Chart A8-13. ^{1}H NMR Chart of Oli-HH-OC6 in $CDCl_3$

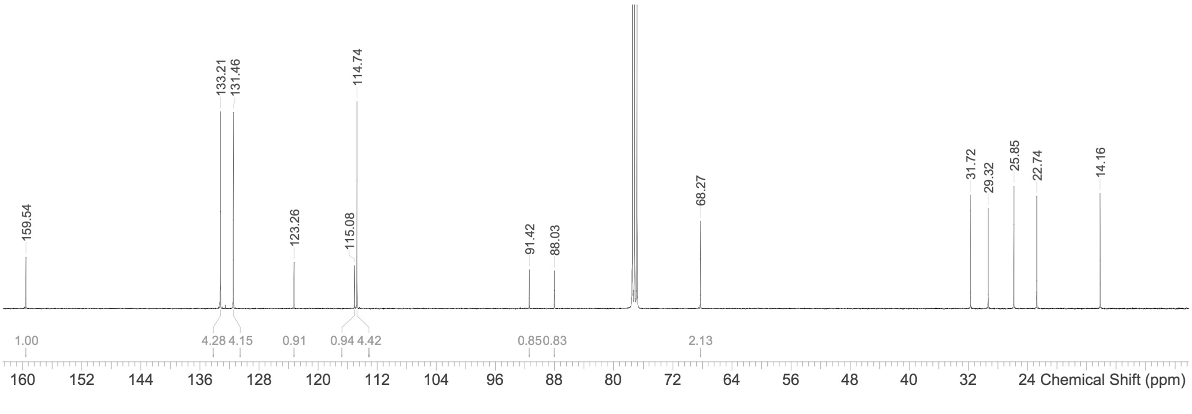

Chart A8-14. ^{13}C NMR Chart of Oli-HH-OC6 in $CDCl_3$

Synthesis of Oli-FH-OC6

Scheme A8-9. Synthetic scheme of Oli-FH-OC3

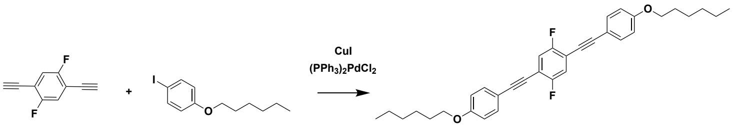

1,4-diethynyl-2,5-difluorobenzene (80 mg, 0.49mmol) was dissolved in Piperidine (1 mL) and Toluene (1.5 mL) under nitrogen. Bubbling took place for 30 min before adding 1-(hexyloxy)-4-iodobenzene (330 mg, 1.09 mmol). Then, bis-(triphenylphosphine) palladium dichloride (6.9 mg, 0.01 mmol) and copper iodide (1.9 mg, 0.01 mmol) were added. The mixture was stirred for 24 hours at room temperature. The resulted mixture was purified by chromatography using PE as eluent and recrystallization to obtain 4,4'-((2,5-difluoro-1,4-phenylene)bis(ethyne-2,1-diyl))bis((hexyloxy)benzene) (87.7 mg, 34.6%). ^{1}H NMR (400 MHz, $CDCl_3$): δ = 0.90-0.93 (tr, 6H), 1.33-1.50 (br, 12H), 1.76-1.83 (m, 4H), 3.96-4.00 (tr, 4H), 6.87-6.89 (d,4H), 7.17-7.21 (tr,2H), 7.46-7.49 (d, 4H) ppm. ^{13}C NMR (151 MHz, $CDCl_3$): δ = 160.03, 159.43, 156.99-156.95(d), 133.47, 119.38-119.05 (m) 114.8, 114.27, 113.41-113.12, 97.29, 80.74, 68.31, 31.72, 29.29, 25.84, 22.74, 14.16 ppm.

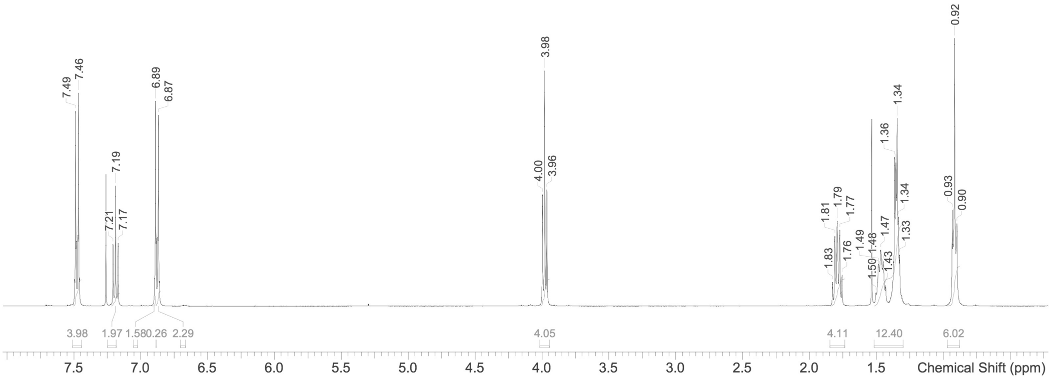

Chart A8-15. ^{1}H NMR Chart of Oli-FH-OC6 in $CDCl_3$

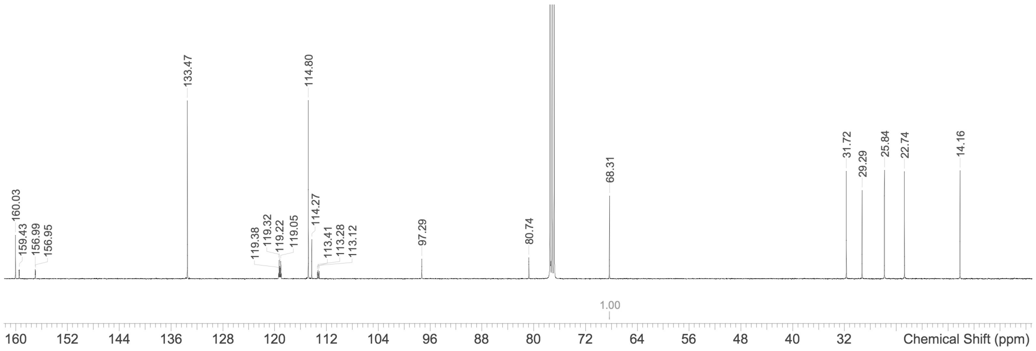

Chart A8-16. ^{13}C NMR Chart of Oli-FH-OC6 in $CDCl_3$

Synthesis of Oli-FF-OC6

Scheme A8-9. Synthetic scheme of Oli-FF-OC3

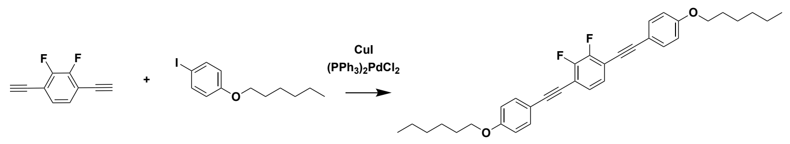

1,4-diethynyl-2,3-difluorobenzene (40 mg, 0.24mmol) was dissolved in Piperidine (1 mL) and Toluene (1.5 mL) under nitrogen. Bubbling took place for 30 min before adding 1-(hexyloxy)-4-iodobenzene (165 mg, 0.54 mmol). Then, bis-(triphenylphosphine) palladium dichloride (3.5 mg, 0.005 mmol) and copper iodide (1.0 mg, 0.005 mmol) were added. The mixture was stirred for 24 hours at room temperature. The resulted mixture was purified by chromatography using PE as eluent and recrystallization to obtain 4,4'-((2,3-difluoro-1,4-phenylene)bis(ethyne-2,1-diyl))bis((hexyloxy)benzene) (56.7 mg, 44.6%). ^{1}H NMR (400 MHz, CDCl$_3$): δ = 0.90-0.93 (tr, 6H), 1.33-1.45 (br, 12H), 1.50-1.83 (m, 4H), 3.97-4.00 (tr, 4H), 6.87-6.89 (d,4H), 7.18-7.19 (tr,2H), 7.47-7.49 (d, 4H) ppm. ^{13}C NMR (151 MHz, CDCl$_3$): δ = 160.01, 152.24, 149.71, 133.46, 127.34, 114.80, 114.33, 97.49, 80.57, 68.31, 31.72, 29.29, 25.84, 22.74, 14.16 ppm.

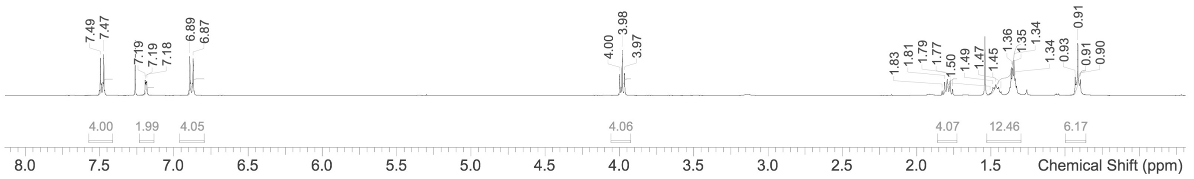

Chart A8-17. ^{1}H NMR Chart of Oli-FF-OC6 in CDCl$_3$

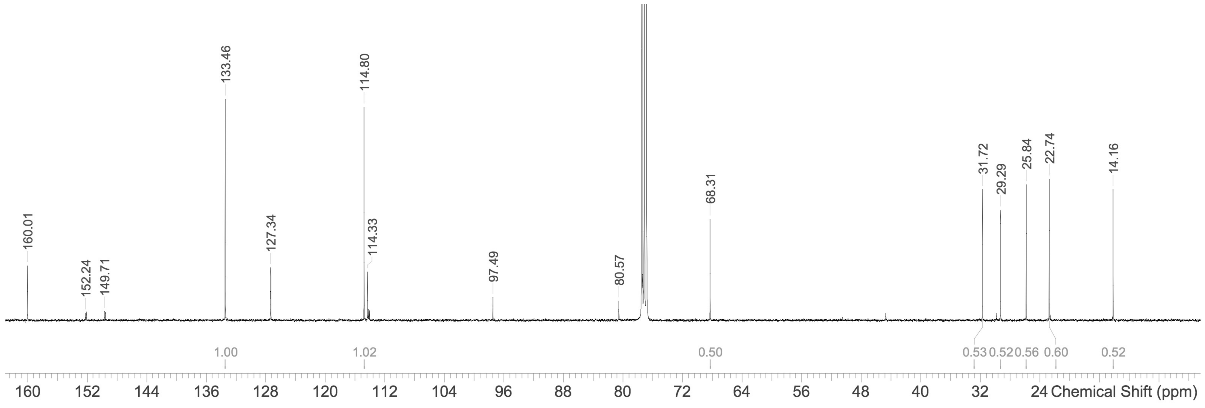

Chart A8-18. ^{13}C NMR Chart of Oli-FF-OC6 in CDCl$_3$

Crystal Structure of Oli- FF

Table A8-1: Crystal data and structure refinement for Oli-FF.

Identification code	soh1	
Empirical formula	$C_{22}H_{12}F_2$	
Formula weight	314.32	
Temperature	200(2) K	
Wavelength	0.71073 Å	
Crystal system	monoclinic	
Space group	$P2_1/c$	
Z	4	
Unit cell dimensions	a = 13.447(3) Å	α = 90 deg.
	b = 9.466(2) Å	β = 91.147(5) deg.
	c = 11.988(3) Å	γ = 90 deg.
Volume	1525.7(6) $Å^3$	
Density (calculated)	1.37 g/cm^3	
Absorption coefficient	0.09 mm^{-1}	
Crystal shape	lamina	
Crystal size	0.179 x 0.162 x 0.036 mm^3	
Crystal colour	colourless	
Theta range for data collection	1.5 to 23.0 deg.	
Index ranges	$-14 \le h \le 14$, $0 \le k \le 10$, $0 \le l \le 13$	
Reflections collected	2123	
Independent reflections	2123 (R(int) = ?)	
Observed reflections	1122 ($I > 2\sigma(I)$)	
Absorption correction	Semi-empirical from equivalents	
Max. and min. transmission	0.96 and 0.70	
Refinement method	Full-matrix least-squares on F^2	
Data/restraints/parameters	2123 / 0 / 219	
Goodness-of-fit on F^2	0.93	
Final R indices (I>2sigma(I))	R1 = 0.060, wR2 = 0.115	
Largest diff. peak and hole	0.22 and -0.25 $eÅ^{-3}$	

Crystal Structure of Oli- FH

Table A8-2: Crystal data and structure refinement for Oli-FH

Identification code	soh3	
Empirical formula	$C_{22}H_{12}F_2$	
Formula weight	314.32	
Temperature	200(2) K	
Wavelength	0.71073 Å	
Crystal system	monoclinic	
Space group	$P2_1/n$	
Z	2	
Unit cell dimensions	a = 4.8376(7) Å	α = 90 deg.
	b = 14.954(2) Å	β = 92.575(5) deg.
	c = 10.5624(17) Å	γ = 90 deg.
Volume	763.3(2) $Å^3$	
Density (calculated)	1.37 g/cm^3	
Absorption coefficient	0.09 mm^{-1}	
Crystal shape	plank	
Crystal size	0.298 x 0.073 x 0.031 mm^3	
Crystal colour	yellow	
Theta range for data collection	2.4 to 24.7 deg.	
Index ranges	$-5 \le h \le 5$, $-17 \le k \le 17$, $-12 \le l \le 12$	
Reflections collected	4642	
Independent reflections	1304 (R(int) = 0.0628)	
Observed reflections	751 ($I > 2\sigma(I)$)	
Absorption correction	Semi-empirical from equivalents	
Max. and min. transmission	0.96 and 0.79	
Refinement method	Full-matrix least-squares on F^2	
Data/restraints/parameters	1304 / 0 / 114	
Goodness-of-fit on F^2	1.01	
Final R indices (I>2sigma(I))	R1 = 0.049, wR2 = 0.105	
Largest diff. peak and hole	0.16 and -0.17 $eÅ^{-3}$	

Crystal Structure of Oli- FH

Table A8-3: Crystal data and structure refinement for Oli-HH

Identification code	soh2	
Empirical formula	$C_{22}H_{14}$	
Formula weight	278.34	
Temperature	200(2) K	
Wavelength	0.71073 Å	
Crystal system	tetragonal	
Space group	$I4_1/amd$	
Z	2.67	
Unit cell dimensions	a = 6.9611(13) Å	α = 90 deg.
	b = 6.9611(13) Å	β = 90 deg.
	c = 19.995(4) Å	γ = 90 deg.
Volume	968.9(4) $Å^3$	
Density (calculated)	1.27 g/cm^3	
Absorption coefficient	0.07 mm^{-1}	
Crystal shape	lance	
Crystal size	0.340 x 0.114 x 0.096 mm^3	
Crystal colour	orange	
Theta range for data collection	3.1 to 26.4 deg.	
Index ranges	$-7 \le h \le 8$, $-8 \le k \le 5$, $-24 \le l \le 24$	
Reflections collected	1570	
Independent reflections	293 (R(int) = 0.0243)	
Observed reflections	227 ($I > 2\sigma(I)$)	
Absorption correction	Semi-empirical from equivalents	
Max. and min. transmission	0.96 and 0.88	
Refinement method	Full-matrix least-squares on F^2	
Data/restraints/parameters	293 / 9 / 25	
Goodness-of-fit on F^2	1.21	
Final R indices (I>2sigma(I))	R1 = 0.040, wR2 = 0.096	
Largest diff. peak and hole	0.14 and -0.13 eÅ^{-3}	

Crystal Structure of Oli- FH

Table A8-4: Crystal data and structure refinement for Oli-FF-OC3

Identification code	soh4	
Empirical formula	$C_{28}H_{24}F_2O_2$	
Formula weight	430.47	
Temperature	110(2) K	
Wavelength	1.54178 Å	
Crystal system	Triclinic	
Space group	P-1	
Z	1	
Unit cell dimensions	a = 5.7798(6) Å	α = 93.237(8) deg.
	b = 7.4015(7) Å	β = 96.390(8) deg.
	c = 13.9517(14) Å	γ = 111.801(8) deg.
Volume	547.61(10) Å^3	
Density (calculated)	1.30 g/cm^3	
Absorption coefficient	0.75 mm^{-1}	
Crystal shape	plate	
Crystal size	0.680 x 0.110 x 0.048 mm^3	
Crystal colour	yellow	
Theta range for data collection	6.4 to 66.9 deg.	
Index ranges	$-6 \le h \le 4$, $-8 \le k \le 8$, $-16 \le l \le 16$	
Reflections collected	3826	
Independent reflections	1831 (R(int) = 0.0274)	
Observed reflections	1614 (I > 2\s(I))	
Absorption correction	Spherical	
Max. and min. transmission	0.81 and 0.81	
Refinement method	Full-matrix least-squares on F^2	
Data/restraints/parameters	1831 / 0 / 173	
Goodness-of-fit on F^2	1.06	
Final R indices ($I>2\sigma(I)$)	R1 = 0.060, wR2 = 0.154	
Largest diff. peak and hole	0.29 and -0.30 eÅ^{-3}	

Crystal Structure of Oli- FH

Table A8-5: Crystal data and structure refinement for Oli-FH-OC3

Identification code	soh5	
Empirical formula	$C_{28}H_{24}F_2O_2$	
Formula weight	430.47	
Temperature	200(2) K	
Wavelength	1.54178 Å	
Crystal system	triclinic	
Space group	$P\bar{1}$	
Z	1	
Unit cell dimensions	a = 7.7466(7) Å	α =100.017(7) deg.
	b = 8.2419(7) Å	β = 93.287(7) deg.
	c = 8.7866(7) Å	γ = 96.687(7) deg.
Volume	546.96(8) Å^3	
Density (calculated)	1.31 g/cm^3	
Absorption coefficient	0.76 mm^{-1}	
Crystal shape	needle	
Crystal size	0.110 x 0.044 x 0.038 mm^3	
Crystal colour	colourless	
Theta range for data collection	5.5 to 72.4 deg.	
Index ranges	$-9 \leq h \leq 9$, $-9 \leq k \leq 10$, $-10 \leq l \leq 10$	
Reflections collected	7485	
Independent reflections	2099 (R(int) = 0.0355)	
Observed reflections	1460 ($I > 2\sigma(I)$)	
Absorption correction	Semi-empirical from equivalents	
Max. and min. transmission	1.63 and 0.60	
Refinement method	Full-matrix least-squares on F^2	
Data/restraints/parameters	7485 / 0 / 147	
Goodness-of-fit on F^2	1.04	
Final R indices (I>2sigma(I))	R1 = 0.069, wR2 = 0.186	
Largest diff. peak and hole	0.21 and -0.24 eÅ^{-3}	

11.5.3 Appendix Figures of Chapter 8

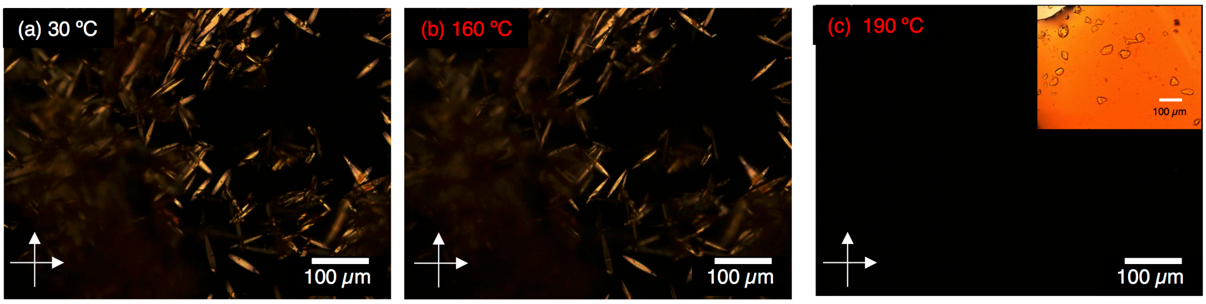

Figure A8-1. Cross polarized POM images of Oli-HH at 30 ºC(a), 160ºC(b) and 200ºC(c) during heating process. Inset in c shows non-polaerized image of liquid state of Oli-FF.

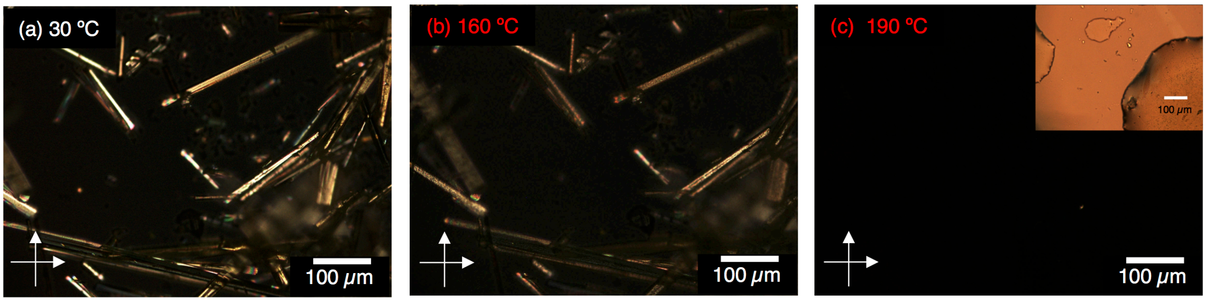

Figure A8-2. Cross polarized POM images of Oli-FH at 30 ºC(a), 160ºC(b) and 200ºC(c) during heating process. Inset in c shows non-polaerized image of liquid state of Oli-FF.

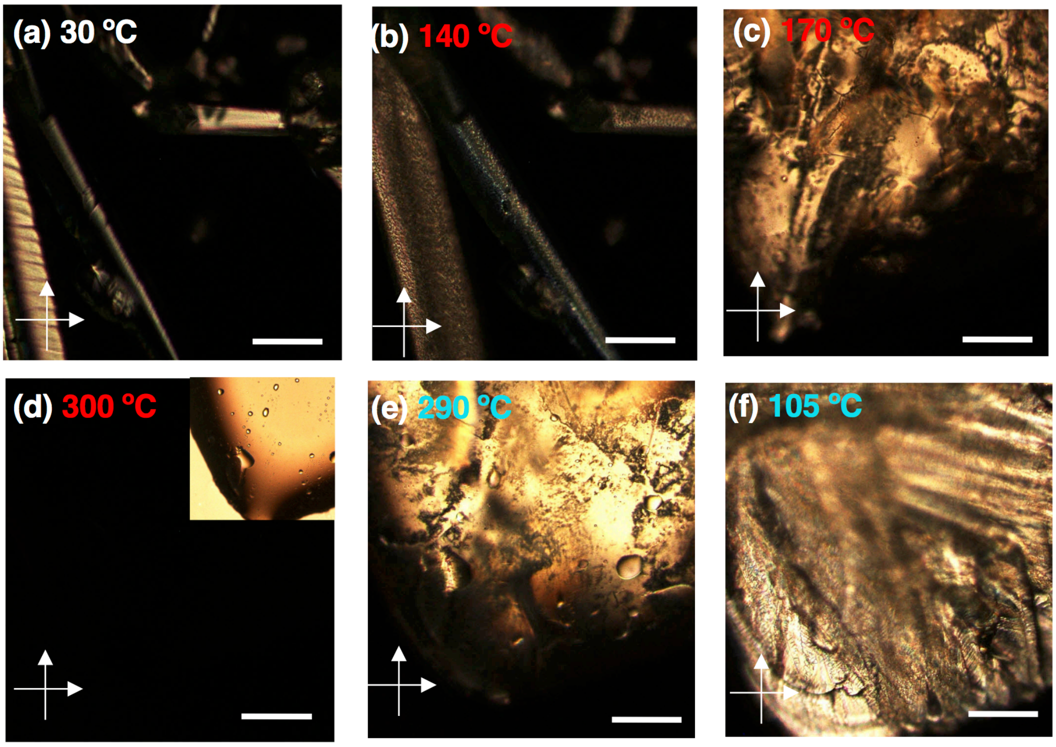

Figure A8-3. Cross polarized POM images of Oli-FH-OC3 at 30 ºC(a), 140ºC(b), 170ºC(c) and 300ºC(d) upon a heating, 290ºC(e) and 105ºC(f) upon a cooling. Inset in c shows the non-polarized image.

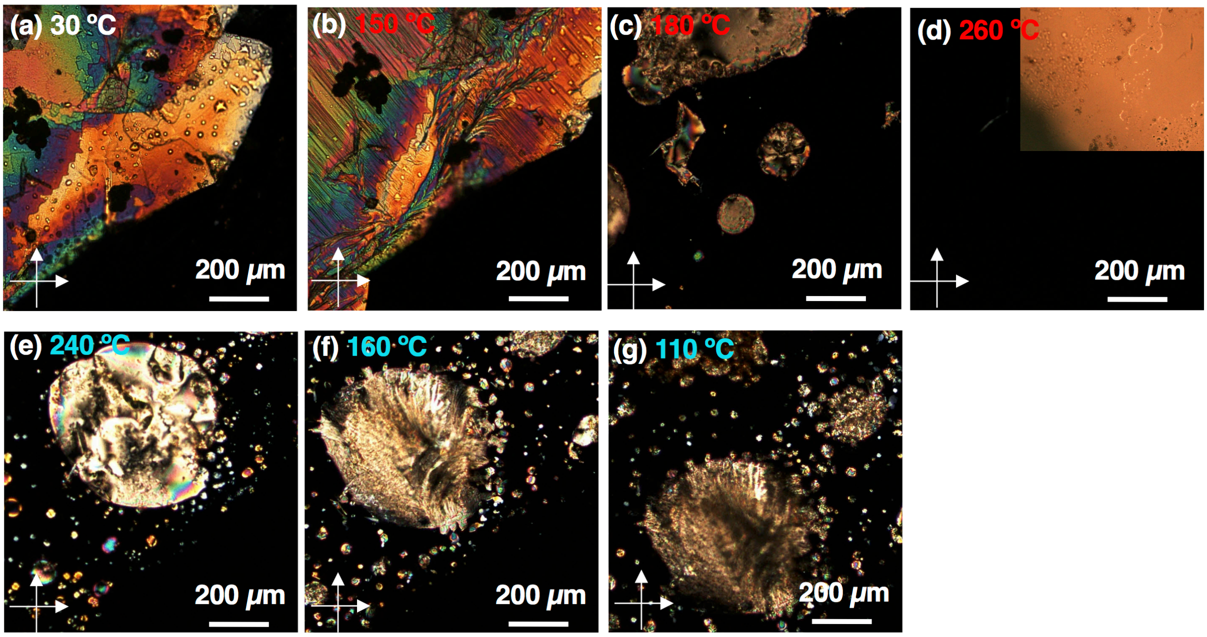

Figure A8-4. POM micrographs of Oli-HH-OC6 at different temperature of 30ºC(a), 150ºC(b), 180ºC(c), 260ºC (d), 240ºC (f), 160ºC(f) and 110ºC(g). Insets show the images non-polarized microscopy. Red temperature and blue temperature mean heating process and cooling process, respectively.

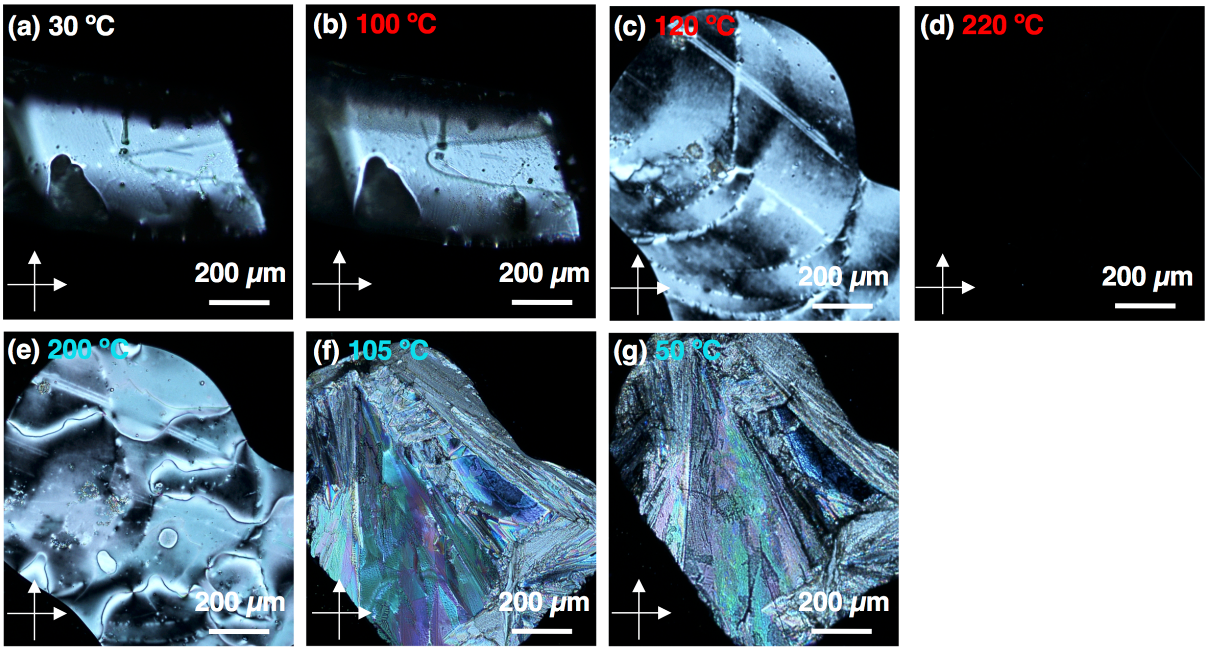

Figure A8-5. POM micrographs of Oli-FH-OC6 at different temperature of 30ºC(a), 100ºC(b), 120ºC(c), 220ºC (d), 200ºC (f), 105ºC(f) and 50ºC(g). Red temperature and blue temperature mean heating process and cooling process, respectively.

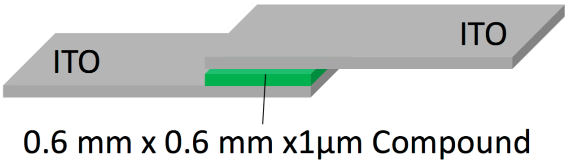

Figure A8-6. The capacitor configuration for the dielectric response measurements. The detailed Device fabrication process is in experimental.

12 Abbreviations and Units

Abbreviations

μ	charge carrier mobility
2D	two-dimensional
3D	three-dimensional
A	area
a.u.	arbitrary units
abs	Absorption
AC	alternating current
Avr.	averaged
br	broad
C	capacitance
C_{geo}	geometric capacitance
C_{2d}	capacitance per area
C_{3d}	capacitance per volume
$CHCl_3$	chloroform
d	channel thickness of a transistor
DC	direct current
DCM	Dichlormethan
DF	drop cast film
DoA	Degree of aggregation
DSC	differential scanning calorimetry
e	electron
E	electric field
E_b	Coulomb energy interaction
ε	dielectric constant
ε_0	dielectric constant in vacuum
ε_r	relative dielectric constant

em	Emission
eq	*equivalents*
et al.	and coworkers (*et alii*)
EBL	electron blocking layer
EDL	electric double layer
EL	electroluminescence
ETL	electron transport layer
FET	field-effect transistor
G	Gibbs free energy
GND	grounded
HOMO	highest occupied molecular orbital
HBL	hole blocking layer
HTL	hole transport layer
I	current
I_d	drain current
I_g	gate current
IL	ionic liquid
Int.	intensity
ITO	indium tin oxide
J	current density
k_B	Boltzmann coefficient
L	channel length of a transistor
LC	liquid crystal
LEC	light-emitting electrochemical cell
LUMO	lowest unoccupied molecular orbital
MIM	metal-insulator-metal
NMR	nuclear magnetic resonance spectroscopy
OECT	organic electrochemical transistor
OFET	organic field-effect transistor

OLED	organic light-emitting diode
OPV	organic photovoltaic
OLED	organic light-emitting diode
P	polarization
πI-gel	π-ion gel
PDI	polydispersity index
PIGT	π-ion gel transistor
PL	photoluminescence
POM	polarized optical microscopy
PPE	phenylene ethylene
PPE	poly(phenylene ethylene)
PUND	positive-up, negative-down
PVDF	polyvinylidene difluoride
R	resistance
r	radius
Si	silicon
SiO_2	silicon dioxide
SOG	solvent promoted gelation
SP	spin cast film
T	temperature
TOG	thermally promoted gelation
θ	angle
UV	ultraviolet
V	voltage
V_d	drain voltage
V_g	gate voltage
vis	visible
V_{th}	threshold voltage
W	channel width of a transistor
X	volume ratio
XRD	X-ray radiation diffraction

Units

º	degrees
ºC	degrees Celsius
m	meter
A	ampere
Å	angstrom
C	coulomb
cd	Candela
eV	electronvolt
F	farad
G	giga
g	gram
h	hours
Hz	hertz
k	kilo
L	liter
M	mega
m	milli
μ	micro
min	minutes
mol	mole
n	nano
p	pico
ppm	parts per million
rpm	revolutions per minute
V	volt
W	watt

13 Acknowledgements

First and foremost, I would like to express my sincere appreciation to my supervisor, **Prof. Dr. Uwe H. F. Bunz**, for his generous support and guidance during my Ph.D. study. If I did not meet him in Tsukuba 2014, I would miss great opportunities here in Heidelberg. I am proud to be his academic child. I would also like to thank **Prof. Dr. Petra Tegeder** for kindly accepting to be my second referee.

I wish to extend my sincere thanks to **Dr. Emanuel Smarsly**, **Maximilian Bojanowski**, **Dr. Christian Melzer**, **Dr. Karl-Philipp Strunk**, **Dr. Silke Koser**, **Sebastian Kebrich** and **Maximilian Krings** for fruitful collaborations, expert discussions, kind encouragements, and pleasant atmosphere in Lab 2.10 and Melzer lab. Without their contributions to my thesis, the dissertation would not be accomplished.

I would also like to thank **Dr. Sebastian Intorp, Dr. Manuela Casutt** and **Dr. Jinsong Han** for sharing their work and fruitful collaborations. Those experiences extended my knowledge.

I would like to thank **Dr. Stefanie Schmid** and **Dr. Jan Freudenberg** for many supports and kind help especially when I started working in Heidelberg.

I would like to thank **Dr. Kai Seehafer**, **Kerstin Windisch**, **Kerstin Brödner**, **Olena Tverskoy** and **Dr. Olaf Skibbe** (CAM) for the daily support of research works.

I would like to thank **Thomas Wiesner, Nikolai Hippchen**, **Maximilian Bojanowski**, and **Sebastian Intorp** for the careful correction of this dissertation.

I would like to thank my collaborators, **Prof. Dr. Rasmus R. Schröder**, **Dr. Irene Wacker** and **Lisa Veith** (Bioquant and CAM) for the bits of help on electron beam microscopy observations and **Prof. Dr. Yohei Yamamoto** and **Osamu Oki** (Univ. of Tsukuba) for the assistance of XRD measurements and **Taishi Kanamaru** (COS) for the confocal microscope observations.

I am grateful to **DAAD** for the financial supports for 3.5 years.

I would like to thank **all other members of the Bunz group** for a pleasant atmosphere and occasional parties, heartwarming encouragements and education of German cultures (also Chinese cultures).

I would like to thank the football club **ASC Neuenheim** and all the involved people for offering a special place and brilliant time. ASC is like my home in Germany. My life in Germany was more fruitful than that a Ph.D. student usually experiences.

I would like to thank **Maika Stephanie Nezu** for the support on the way of Ph. D. study.

I would like to thank **the Japanese researchers' community "Ikea-kai"** for sharing time to speak in Japanese and group "**Tea-sensing**" for relaxed time.

I would like to thank my talented cousin, **Arata Tojo** for drawing the cover picture and inside picture of this dissertation.

Last but not least, I am deeply grateful for the consistent supports of **all my family (Masami, Makiko, Mizuki, and Jun)**.

I would like to dedicate this dissertation to my beloved grandfather **Yasuhiko Tojo,** who passed away before the dissertation is accomplished. I am proud to have been born as his grandson.

Eidesstattliche Versicherung gemäß § 8 der Promotionsordnung der Naturwissenschaftlich-Mathematischen Gesamtfakultät der Universität Heidelberg

1. Bei der eingereichten Dissertation zu dem Thema "Controlling the Dielectric Behavior of Organic Electronic Devices" handelt es sich um meine eigenständig erbrachte Leistung.

2. Ich habe nur die angegebenen Quellen und Hilfsmittel benutzt und mich keiner unzulässigen Hilfe Dritter bedient. Insbesondere habe ich wörtlich oder sinngemäß aus anderen Werken übernommene Inhalte als solche kenntlich gemacht.

3. Die Arbeit oder Teile davon habe ich bislang nicht an einer Hochschule des In- oder Auslands als Bestandteil einer Prüfungs- oder Qualifikationsleistung vorgelegt.

4. Die Richtigkeit der vorstehenden Erklärung bestätige ich.

5. Die Bedeutung der eidesstattlichen Versicherung und die strafrechtlichen Folgen einer unrichtigen oder unvollständigen eidesstattlichen Versicherung sind mir bekannt.

Ich versichere an Eides statt, dass ich nach bestem Wissen die reine Wahrheit erklärt

und nichts verschwiegen habe.

Heidelberg, 13. März 2020

Ort, Datum Unterschrif